Western Graduate&PostdoctoralStudies

Western University
Scholarship@Western

Electronic Thesis and Dissertation Repository

1-17-2024 10:00 AM

Development of pH-Weighted Magnetic Resonance Imaging in the Spinal Cord: Application in Degenerative Cervical Myelopathy

Alicia E. Cronin, *The University of Western Ontario*

Supervisor: Bartha, Robert, *The University of Western Ontario*
Co-Supervisor: Duggal, Neil, *The University of Western Ontario*
A thesis submitted in partial fulfillment of the requirements for the Doctor of Philosophy degree in Medical Biophysics
© Alicia E. Cronin 2024

Follow this and additional works at: https://ir.lib.uwo.ca/etd

Part of the Medical Biophysics Commons

Recommended Citation

Cronin, Alicia E., "Development of pH-Weighted Magnetic Resonance Imaging in the Spinal Cord: Application in Degenerative Cervical Myelopathy" (2024). *Electronic Thesis and Dissertation Repository*. 9918.
https://ir.lib.uwo.ca/etd/9918

This Dissertation/Thesis is brought to you for free and open access by Scholarship@Western. It has been accepted for inclusion in Electronic Thesis and Dissertation Repository by an authorized administrator of Scholarship@Western. For more information, please contact wlswadmin@uwo.ca.

Abstract

Degenerative cervical myelopathy (DCM) is a degenerative disease of the spinal cord that can lead to neurological dysfunction. It has been hypothesized that ischemia and hypoxia in the spinal cord at the site of compression could impact functional recovery after decompression surgery. Unfortunately, direct in-vivo quantification of hypoxia and ischemia in the spine has been limited in humans. Magnetic resonance imaging (MRI) can be utilized to measure hypoxia indirectly in soft tissue. Specifically, chemical exchange saturation transfer (CEST) is an MRI contrast that can be derived from the transfer of magnetization from selectively excited endogenous protons to bulk water protons. This exchange process is pH-dependent and can be exploited to produce a pH-weighted CEST contrast called amine/amide concentration independent detection (AACID). Hypoxia can decrease the pH of tissue.

For the first time in DCM patients, the severity of spinal cord compression was correlated with functional brain activity changes, suggesting that hypoxic injury in the spinal cord may contribute to cortical reorganization in the motor areas of the brain. The results from this study provided the motivation for this thesis to develop three-dimensional (3D) AACID CEST pH-weighted MRI at the clinically relevant field strength of 3.0T in the healthy brain and spinal cord and then to demonstrate the feasibility of pH-weighted imaging in the spinal cord of DCM patients. Furthermore, the reproducibility of spinal cord AACID CEST MRI was quantified and found to have the greatest reproducibility at the center of the 3D volume when incorporating a B_1-inhomogeneity correction.

In conclusion, this dissertation demonstrates the process of developing a 3D pH-weighted CEST MRI contrast at the clinically relevant field strength of 3.0T in the cervical spinal cord. This work includes initially exploring how the severity of cord compression affects brain functional activity, optimizing the CEST sequence at 3.0T, evaluating the reproducibility of the AACID measurement in both the healthy brain and cervical spinal cord and initial utilization in the spinal cord of people with DCM. This dissertation lays the groundwork to determine if hypoxia is occurring in the spinal cord of DCM patients and if it is a measure of neurological outcome.

Keywords

Magnetic Resonance Imaging, Task-Based functional MRI, Cortical Reorganization, Chemical Exchange Saturation Transfer, Degenerative Cervical Myelopathy, Spinal Cord, pH Imaging

Summary for Lay Audience

Degenerative cervical myelopathy (DCM) is a progressive disease of the spine that leads to compression, causing disruptions in hand function and walking and may lead to paralysis. Surgery is often the treatment recommended for DCM patients. Unfortunately, some patients continue to decline after surgery, and it is difficult to predict who. A new measure of outcome is needed to identify which patients will improve from decompression surgery and to determine when surgery should be performed. Compression of the spine might reduce the blood supply and oxygen available to the tissue, and this might affect how patients respond to decompression surgery. This thesis investigates and develops a way to non-invasively create images of the spine using magnetic resonance imaging (MRI) that is sensitive to changes in the tissue caused by a lack of oxygen. Specifically, such tissue becomes acidic, decreasing the tissue pH.

In DCM patients, a spinal cord compression measure was developed and compared to changes in brain activity observed when performing a hand-based task. The study found that patients who had more severely compressed spinal cords also tended to show more brain activation, suggesting that injury to the spinal cord caused by a lack of oxygen could cause adaptations to occur in the brain to compensate for the injury.

This study motivated the development of a specialized MRI measurement that is sensitive to tissue acidity using clinically available MRI scanners. This technique has been previously utilized to detect changes in tissue acidity in animal models of stroke and cancer but has never been implemented in humans. Before assessing changes in tissue acidity in the spinal cord of DCM patients, the technique was fine-tuned and tested in the healthy human brain and cervical spinal cord. Measurement reproducibility was evaluated in the healthy brain and cervical spinal cord, demonstrating the feasibility of the method. Preliminary testing also demonstrated that the spinal cord of DCM patients may be acidic at the site of spinal cord compression.

The research in this thesis lays the groundwork for future research in DCM patients to determine if tissue acidity can be used to predict functional outcome after surgery.

Co-Authorship Statement

The following thesis contains materials from previously published and submitted manuscripts (Chapters 2 and 4). In addition, material from the third and fourth manuscript are in preparation for submission (Chapters 3 and 5). All Chapters (excluding Chapter 1) of this thesis contain original research studies completed in collaboration with a team of authors. Acknowledgements of the contributions from myself and others to this work are described below for each project.

The material in Chapter 2 has been published in *Brain Communications*, in a manuscript entitled 'Spinal Cord Compression is Associated with Brain Plasticity in Degenerative Cervical Myelopathy' (2021; Volume 3, Issue 3, pages 1-12. https://doi.org/*10.1093*/*braincomms*/*fcab131*.). Co-authors for this manuscript were Alicia E Cronin, Sarah A Detombe, Camille A Duggal, Neil Duggal, and Robert Bartha. As the first author, I was involved in the data collection, data analysis, interpretation, and preparation and submission of the manuscript. Sarah Detombe was involved in patient recruitment and imaging data collection. Camille Duggal assisted with spinal cord compression data analysis for reproducibility. Neil Duggal was responsible for clinical assessments of all DCM patients. Robert Bartha and Neil Duggal were responsible for study conception and design and provided guidance on data interpretation and manuscript revisions.

The material contained in Chapter 3 is in preparation for submission in a manuscript entitled 'Reproducibility of 3D Chemical Exchange Saturation Transfer (CEST) Contrasts in the Healthy Brain at 3T'. Co-authors for this manuscript were Alicia E Cronin, Patrick Liebig, Sarah A Detombe, Neil Duggal, and Robert Bartha. As the first author, I was involved in software creation, protocol design, subject recruitment, data collection, data analysis, interpretation, and preparation of the manuscript. Patrick Liebig provided guidance on data analysis and CEST development and implementation. Sarah Detombe provided guidance on data interpretation. Robert Bartha assisted in the design of the study and provided guidance and support in the analysis and interpretation of the data. Robert Bartha and Neil Duggal provided critical review and revision of the manuscript.

The material contained in Chapter 4 has been published in *NMR in Biomedicine*, in a manuscript entitled 'Reproducibility of 3D pH-Weighted Chemical Exchange Saturation Transfer Contrast in the Healthy Cervical Spinal Cord' (2024; pages 1-13. doi:10.1002/nbm.5103). Co-authors for this manuscript were Alicia E Cronin, Patrick Liebig, Sarah A Detombe, Neil Duggal, and Robert Bartha. As the first author, I was involved in protocol design, subject recruitment, data collection, data analysis, interpretation, and preparation of the manuscript. Patrick Liebig provided guidance on data analysis and CEST development and implementation. Sarah Detombe provided guidance on data interpretation. Robert Bartha assisted in the design of the study and provided guidance and support in the analysis and interpretation of the data. Robert Bartha and Neil Duggal provided critical review and revision of the manuscript.

The material contained in Chapter 5 is in preparation for submission in a manuscript entitled 'Spinal Cord pH-weighted CEST MRI Suggests Hypoxia in Degenerative Cervical Myelopathy'. Co-authors for this manuscript were Alicia E Cronin, Patrick Liebig, Sarah A Detombe, Neil Duggal, and Robert Bartha. As the first author, I was involved in protocol design, patient recruitment, data collection, data analysis, interpretation, and preparation of the manuscript. Patrick Liebig provided guidance on data analysis and CEST development and implementation. Sarah Detombe provided guidance on data interpretation. Robert Bartha assisted in the design of the study and provided guidance and support in the analysis and interpretation of the data. Neil Duggal was responsible for clinical assessments of all DCM patients. Robert Bartha and Neil Duggal provided critical review and revision of the manuscript.

Acknowledgments

First, I am extremely grateful to my supervisors, Dr. Rob Bartha and Dr. Neil Duggal. Rob – thank you for answering that initial email I sent as an undergrad looking for a supervisor to teach me about MRI. Thank you for all the support and encouragement over the last five years. Your patience and endless positivity during the many challenges have been invaluable. I am grateful for everything you have taught me, which has been crucial in my journey to become a better researcher and person. Neil – thank you for taking the time to help me learn about impactful scientific writing. Without your initial phone call during my first attempt at writing a manuscript, I would still be floundering when writing. I am also grateful for all our conversations about the spinal cord and DCM – coming from a background in physics, these discussions have been invaluable.

To my advisory committee, Dr. Corey Baron. Thank you for invaluable scientific discussions and for providing guidance throughout my graduate career. Problems we had been stuck on for months were solved quickly when bouncing ideas off you.

To the Natural Sciences and Engineering Research Council of Canada - thank you for supporting my research over the years.

Thank you to the staff and scientists of the Centre of Functional and Metabolic Mapping (CFMM) and Robarts – without this large team, none of this research would be possible. Thank you for the laughs throughout the years and all the potluck lunches. I would particularly like to thank Scott Charlton and Oksana Opalevych for the numerous MRI scans, whether it be on myself, egg whites, or patients. Thank you to Sarah Detombe – your guidance with data interpretation has been invaluable, and I always looked forward to chatting with you during the MRI scans.

Thank you to all the students at CFMM – I always looked forward to our lunch breaks and the laughter that came with them. To the members of the Bartha Lab, in particular, Maryam, Dana, Jack, Helma, and Pauline - thank you for the guidance and thoughtful discussions throughout the years. Thank you for making the lab a great workplace and always being

willing to listen to me rant while on our walks to get coffee. You all have truly made my graduate career memorable.

To all the friends I have made in Grad School – thank you for all the amazing memories we have together. I am eternally grateful for everyone's friendship and constant encouragement throughout the years. I always looked forward to our times together, whether it be at Grad Club, playing boardgames, or going for a much-needed night out. Thanks especially to my roommate Simran – you have been an incredible friend, and even though not much work was accomplished whenever we were together, I would not have made it through my Ph.D. without you. To my hometown friends Brianna, Madison, Sydney, Naomi, Kaitlyn, and Hannah – thank you for the constant support, laughter, and friendship over the years. I am grateful for the friendship we still have and will cherish it for years to come. Thank you for always having the time to hang out on weekends and the silly videos and photos sent in our group chat that always brighten my day.

Finally, thank you to my family, especially my Mom and Dad. You have constantly been supportive of everything I've done, and I'm exceptionally grateful for you. Thank you for all the sacrifices you have made over the years to help us achieve our dreams. Thank you for always picking up the phone and saying precisely what I needed to hear. Thank you for inspiring me at an early age to value science and education. Dad - thank you for suggesting I take physics in Grade 11 – my life would look a little different without that push. Special thanks to Poe - you have been the best dog a girl could ask for. Your constant energy and love always puts a smile on my face. Sorry to Mom and Dad for the constant FaceTime calls where I make you focus the video on Poe and I just watch him.

Dedicated to my family

Table of Contents

Abstract ii

Summary for Lay Audience iv

Co-Authorship Statement v

Acknowledgments vii

Table of Contents x

List of Tables xvi

List of Figures xvii

List of Supplementary Tables xxv

List of Supplementary Figures xxvi

List of Appendices xxviii

List of Symbols, Acronyms, and Abbreviations xxix

Chapter 1 1

1 Introduction 1

1.1 Spinal Cord 1

1.1.1 Spinal Cord Structure 1

1.1.2 Spinal Cord Blood Supply 4

1.2 Degenerative Cervical Myelopathy 5

1.2.1 Pathophysiology and Pathobiology of DCM 6

1.2.2 Clinical Assessment 9

1.2.3 Diagnostics Using Imaging 11

1.2.4 Management 12

1.2.5 Predictors of Outcome 13

1.3 Ischemia and Hypoxia 14

1.3.1 Reperfusion Injury 15

1.3.2 Acidity measured by pH 15
1.3.3 Imaging of pH 19
1.4 Introduction to Magnetic Resonance Imaging (MRI) 21
1.4.1 Magnetic Moments 21
1.4.2 Excitation 25
1.4.3 Relaxation 28
1.4.4 Signal Detection and Localization 29
1.5 Functional MRI 33
1.5.1 Neurovascular Coupling 33
1.5.2 Hemoglobin 35
1.5.3 Blood oxygen level-dependent (BOLD) contrast 35
1.5.4 Hemodynamic Response 36
1.5.5 fMRI Applications in DCM and Spinal Cord Injury 37
1.6 Chemical Exchange Saturation Transfer 39
1.6.1 CEST Mechanism 39
1.6.2 Z-Spectrum/CEST Spectrum 43
1.6.3 CEST Contrast 45
1.6.4 Proton Exchange Rate and pH 46
1.6.5 Endogenous pH Measurements 47
1.6.6 Amine/Amide Concentration Independent Detection 49
1.6.7 Nuclear Overhauser Enhancement 52
1.6.8 Spinal Cord MR Imaging Challenges 58
1.6.9 CEST in the Spinal Cord 59
1.6.10 CEST Reproducibility 60
1.7 Thesis Overview 60
Chapter 2 63

2 Spinal Cord Compression is Associated with Brain Plasticity in Degenerative Cervical Myelopathy 63

2.1 Introduction 63

2.2 Materials and Methods 65

2.2.1 Participants and Clinical Evaluation 65

2.2.2 Imaging Protocol 65

2.2.3 Study Design 66

2.2.4 Imaging Processing 66

2.2.5 Statistical Analysis 67

2.3 Results 68

2.4 Discussion 80

2.5 Conclusion 83

2.6 Acknowledgements 84

2.7 Funding 84

2.8 Supplementary Materials 85

2.8.1 Results 85

Chapter 3 92

3 Reproducibility of 3D Chemical Exchange Saturation Transfer (CEST) Contrasts in the Healthy Brain at 3T 92

3.1 Introduction 92

3.2 Material and Methods 94

3.2.1 Phantom Preparation 94

3.2.2 Participants 94

3.2.3 Image Acquisition 94

3.2.4 CEST Postprocessing 96

3.2.5 Statistics 98

3.3 Results 99

3.4 Discussion 110
3.5 Conclusion 114
3.6 Acknowledgements 115
3.7 Funding 115
3.8 Supplementary Materials 116
3.8.1 CEST Acquisition 116
3.8.2 Fitting 116
Chapter 4 118
4 Reproducibility of 3D pH-Weighted Chemical Exchange Saturation Transfer Contrast in the Healthy Cervical Spinal Cord 118
4.1 Introduction 118
4.2 Methods 120
4.2.1 Participants 120
4.2.2 Imaging Acquisition 121
4.2.3 CEST Postprocessing 122
4.2.4 Statistics 124
4.3 Results 125
4.4 Discussion 131
4.5 Conclusion 135
4.6 Acknowledgements 135
4.7 Funding 136
4.8 Supplementary Materials 137
4.8.1 CEST Acquisition 137
4.8.2 Fitting 137
4.8.3 Results 140
Chapter 5 143

5 Spinal Cord pH-weighted CEST MRI Suggests Hypoxia in Degenerative Cervical Myelopathy 143

5.1 Introduction 143

5.2 Materials and Methods 145

5.2.1 Subjects 145

5.2.2 Imaging Acquisition 145

5.2.3 CEST Data Processing 147

5.2.4 Compression Measurement 149

5.2.5 Statistics 149

5.3 Results 149

5.4 Discussion 155

5.5 Conclusion 160

5.6 Acknowledgements 160

5.7 Funding 160

5.8 Supplementary Materials 161

5.8.1 CEST Acquisition 161

5.8.2 Fitting 161

Chapter 6 164

6 Conclusions 164

6.1 Thesis Summary 164

6.1.1 Spinal cord compression is associated with brain plasticity in degenerative cervical myelopathy 164

6.1.2 Reproducibility of 3D Chemical Exchange Saturation Transfer (CEST) Contrasts in the Healthy Brain at 3T 165

6.1.3 Reproducibility of 3D pH-Weighted Chemical Exchange Saturation Transfer Contrast in the Healthy Cervical Spinal Cord 166

6.1.4 Spinal Cord pH-weighted CEST MRI Suggests Hypoxia in Degenerative Cervical Myelopathy 167

6.2 Thesis Significance and Impact 168
6.3 Future Directions 169
6.3.1 CEST Image Acquisition Improvements 169
6.3.2 DCM Study Continuation 171
References 173
Appendices 192
Curriculum Vitae 203

List of Tables

Table 1.1: The modified Japanese Orthopaedic Scale (mJOA), modified with permission from Benzel *et al*. (20). 10

Table 2.1: Demographic data and clinical characteristics of patients with DCM 71

Table 3.1: Summary of the mean values in both gray matter and white for each of the four contrasts (amine/amide concentration independent detection (AACID), Amide*, MTRRexδamide, and MTRRexδNOE) at each time point (with standard deviation). 106

Table 5.1: Demographic data and clinical characteristics of patients with degenerative cervical myelopathy (DCM). 147

List of Figures

Figure 1.1: Anatomy of the spinal cord, showing the nerve pairs and vertebrae throughout the spinal cord. This figure was reproduced and modified with permission from Ahuja *et al.* (4) 3

Figure 1.2: Schematic view of the blood supply of the spinal cord stemming from the aorta. *a.* stands for artery and *n.* stands for nerve. This figure was used with permission from Bosmia *et al.* (5)..... 5

Figure 1.3: Flow graph of the pathophysiological process of degenerative cervical myelopathy (DCM). Static factors can cause stenosis of the spinal cord (narrowing of the cross-sectional area of the spinal cord), which is further exacerbated by dynamic factors during movement. This can cause compression of the spinal cord which can result in the disruption of the blood-spinal cord barrier (BSCB) via endothelial cell dysfunction or ischemia/hypoxia through regional malperfusion and vessel deformation. Both can eventually activate the apoptotic pathways, causing neuronal and oligodendroglial cell death. This figure was adapted with permission from Badhiwala *et al.* (8)..... 8

Figure 1.4: Sagittal T_2-weighted MRI (acquired on a Siemens 3.0 T MAGNETOM Prisma Fit, 3D spin-echo sequence, repetition time (TR)/echo time (TE) = 1400/136 ms, 64 slices, isotropic resolution of 0.8 mm^3) of the spinal cord of a DCM patient. Arrow indicates presence of spinal cord compression. 12

Figure 1.5: Schematic diagram of pH homeostasis. Normal cellular glucose metabolism in normoxic (blue) and hypoxic (red) conditions. The hypoxic pathway contributes to proton and lactate production. MCT – monocarboxylate transporters..... 17

Figure 1.6: A. Protons spin in random orientation in the absence of a magnetic field. B. In the presence of a magnetic field (B_0), the proton spins have a slight excess of magnetic moments aligned in parallel to the external field, leading to a net magnetization M_0. 23

Figure 1.7: Protons spin in the rotating reference frame. A. In the presence of an external magnetic field (B_0), the protons tend to orient either parallel or anti-parallel with B_0, leading to a net magnetization vector ($Mz0$). B. Upon the application of an RF excitation pulse along

the x′-axis, protons become evenly distributed between parallel and anti-parallel orientations and phase in alignment along the y′-axis. Figure was recreated from de Graaf with permission (84). 26

Figure 1.8: A. Blood flow during rest; oxygen is extracted from the hemoglobin at a constant rate. B. Blood flow during neural activity; glucose and oxygen consumption triggers an increase in blood flow and the dilation of the capillary, overcompensating for the oxygen being extracted. The BOLD contrast occurs due to changes in the relative concentration of deoxyhemoglobin. 34

Figure 1.9: At the stimulus onset, an initial dip occurs, leading to a temporary increase in deoxyhemoglobin (dHb) concentration due to heightened oxygen consumption. In response to the elevated demand for glucose and oxygen, both cerebral blood flow and blood volume increases. This surplus of oxygen exceeds the actual consumption, resulting in a relative decrease in dHb and elevation in BOLD signal. Once the activity subsides, the BOLD signal decreases below baseline, a phenomenon referred to as post-stimulus undershoot. This occurs due to the blood flow decreasing more rapidly than cerebral blood volume. 37

Figure 1.10: Schematic illustration of the basic chemical exchange saturation transfer (CEST) MRI principles. Solute protons (red) are saturated at their specific resonance frequency by a radiofrequency (RF) saturation pulse. This saturation is transferred to bulk water at exchange rate k_{SW} and non-saturated protons (blue) return. After a period of time, the CEST effect becomes visible on the water signal and is an indirect measure of the solute concentration and the rate of exchange. 40

Figure 1.11: An example of a CEST spectrum. The CEST peak (or CEST effect) is observed at 5ppm, highlighted with the red arrow. The peak due to direct saturation of the bulk water protons by the RF saturation pulse is demonstrated at 0 ppm. 44

Figure 1.12 An example of one pixel's CEST spectrum fitted using a 6-pool model. 45

Figure 1.13: Schematic diagram demonstrating the effect of pH on the amine and amide CEST effects. The top schematic demonstrates both the amide and amine proton pools that are chemically shifted from the bulk water pool. The bottom schematic demonstrates CEST spectra measured at different pH (6.0, 6.5, and 7.0), showing the amide and amine pH

dependent changes highlighted in blue and purple, respectively. This figure has been adapted with permission from McVicar *et al.* (129). 52

Figure 1.14: Schematic diagram illustrating the different mutual spin flips that are the pathways corresponding to the NOE. A. Energy level diagram for a dipolar coupled two spin system, I spin population difference of 5. B. A double quantum transition involves a pair of spin-up nuclei flipping to spin-down, or vice-versa, and causes an increase in the signal of the proton of interest. When spin S relaxes back to equilibrium, the coupled spin I flips from higher energy to the ground state, increasing the population difference (i.e., difference of 7). C. Zero order quantum transitions involve the flipping of a pair of opposite spins and causes a decrease in the signal of the proton of interest. When spin S relaxes back to equilibrium, the coupled spin I flips from low energy to the ground state, decreasing the population difference (i.e., difference of 3). 54

Figure 1.15: Schematic illustrating the irradiation if a nonexchangeable proton pool with a radiofrequency (RF) pulse, which causes the bulk water pool signal to decrease through relayed nuclear Overhauser effect (rNOE). This figure has been recreated and adapted with permission from Zhou *et al.* (134) 56

Figure 2.1: Volume of compression measurement. A: T_2-weighted image of the cervical spinal cord of a DCM patient showing the segmented cord in red, with the compression site displayed on the inset. B: Line graph displaying the area of each axial slice of the segmented cord, from inferior to superior, with the coloured region the total compression volume measurement. C: Dot plot of rater agreement, with an ICC of 0.977 for inter-rater reliability, first rater achieving an intra-rater reliability ICC of 0.996, and the second rater achieving an intra-rater reliability ICC of 0.967. 69

Figure 2.2: Left hand tapping BOLD signal and volume of compression. A: The correlation between the % BOLD signal of the contralateral M1 and the spinal cord compression volume. B: The correlation between the % BOLD signal of the contralateral S1 and the spinal cord compression volume. C: The correlation between the % BOLD signal of the contralateral PMC and the spinal cord compression volume. D: The correlation between the % BOLD signal of the contralateral SMA and the spinal cord compression volume. 73

Figure 2.3: Left hand tapping volume of activation and volume of compression. A: The correlation between the VOA of the contralateral M1 and the spinal cord compression volume. B: The correlation between the VOA of the contralateral S1 and the spinal cord compression volume. C: The correlation between the VOA of the contralateral PMC and the spinal cord compression volume. D: The correlation between the VOA of the contralateral SMA and the spinal cord compression volume. 74

Figure 2.4: Right hand tapping BOLD signal and volume of compression. A: The correlation between the % BOLD signal of the contralateral M1 and the spinal cord compression volume. B: The correlation between the % BOLD signal of the contralateral S1 and the spinal cord compression volume. C: The correlation between the % BOLD signal of the contralateral PMC and the spinal cord compression volume. D: The correlation between the % BOLD signal of the contralateral SMA and the spinal cord compression volume. 76

Figure 2.5: Right hand tapping volume of activation and volume of compression. A: The correlation between the VOA of the contralateral M1 and the spinal cord compression volume. B: The correlation between the VOA of the contralateral S1 and the spinal cord compression volume. C: The correlation between the VOA of the contralateral PMC and the spinal cord compression volume. D: The correlation between the VOA of the contralateral SMA and the spinal cord compression volume. 77

Figure 2.6: The association between the neurological function in DCM patients measured by the mJOA score and spinal cord compression volume. 78

Figure 2.7: Correlation between % BOLD signal and mJOA. A: The correlation between the % BOLD signal of the contralateral M1when tapping with the left hand and neurological function of the CSM patients measured by the mJOA score. B: The correlation between the % BOLD signal of the contralateral M1 when tapping with the right hand and the mJOA score. C: The correlation between the % BOLD signal of the contralateral S1 when tapping with the left hand and the mJOA score. D: The correlation between the % BOLD signal of the contralateral S1 when tapping with the right hand and the mJOA score. 79

Figure 3.1: A: Axial T_1-weighted slice of the brain of a healthy participant corresponding to the center of the 3D volume (slice 4). The same T_1-weighted axial image with overlayed B:

segmented gray matter (black), white matter (grey), and cerebrospinal fluid (white) regions of interest; C: amine/amide concentration independent detect (AACID) Z-Score map; D: Amide* Z-Score map; E: MTRRexδamide Z-Score map, and F: MTRRexδNOE Z-Score map..... 100

Figure 3.2: A. B_1 amplitude optimization using egg white phantoms (values represent mean amide signal of control egg white phantom map ± standard deviation of the map), demonstrating maximized amide signal amplitude at B_1 = 0.5 μT. Although all phantoms demonstrated a similar pattern of change as a function of pH, only data from the four phantoms that encompass the physiological pH range are shown. B. Average amine/amide concentration independent detection (AACID) maps (slices = 8) for the ten egg white phantoms ranging in pH from 5.82-9.17 when using a B_1 amplitude of 0.5 μT. C. The correlation between the measured AACID value and the pH of each egg white phantom, demonstrating a significant linear relationship ($p < 0.001$, $r = -0.98$). The line of best fit has a slope of -0.176. pH accounts for 97% of the total variation in AACID. The inset represents the data in the physiological range, also demonstrating a significant linear relationship ($p < 0.05$, $r = -0.91$) and slope of -0.236. AACID values represent the mean AACID value of each phantom map ± standard deviation of the map. 101

Figure 3.3: A. B_1 amplitude optimization in the human brain in three healthy participants (values represent mean amide signal of the three volunteers ± standard deviation), showing maximum amide signal amplitude at B_1 = 0.5 μT. B. Axial slice amide signal amplitude map through the brain of one healthy participant using B_1 amplitude = 0.5 μT. 103

Figure 3.4: A: Mean amide/amine concentration independent detection (AACID) values (with standard deviation) for gray matter (GM) and white matter (WM), with WM significantly greater than GM ($p < 0.0001$). B. Mean MTRRexδamide values (with standard deviation) for GM and WM, with GM significantly greater than WM ($p < 0.05$). C. Mean Amide* values (with standard deviation) for GM and WM, with GM significantly greater than WM ($p < 0.0001$). D. Mean MTRRexδNOE values (with standard deviation) for GM and WM, with WM significantly greater than GM ($p < 0.0001$). Means were calculated from all subjects and both time points (24 measurements). 105

Figure 3.5: A. Axial CEST image of one slice (corresponding to the center of the 3D volume) of one healthy participant. B-C. Amide/amine concentration independent detection (AACID) map of the same healthy participant for the first scan (B) and second scan (C), with both overlayed onto the corresponding T_1-weighted axial slice. 107

Figure 3.6: Histograms of the four different calculated contrasts of one healthy participant (amide/amine concentration independent detection (AACID), Amide*, MTRRexδamide, and MTRRexδNOE) for both the scan (pink) and rescan (blue) conditions. The top row shows the histograms for the gray matter region-of-interests (ROIs), while the bottom row shows the histograms for the white matter ROIs. The overlap of the two scans is demonstrated in purple and visually, the histograms show good reproducibility between scans for all calculated contrasts. 107

Figure 3.7: A. Mean between-subject coefficients of variation (CV) for each calculated contrast for both gray matter (GM) and white matter (WM). Between-subject CV values represent the mean ± standard error of the mean across the 12 participants (averaged over the two time points). B. Mean within-subject CV for each calculated contrast for both GM and WM. Within-subject CV values represent the mean ± standard error of the mean between the two time points (averaged across the 12 participants). C. Mean percent difference for each calculated contrast for both GM and WM. Percent difference represents the mean ± standard error of the mean between the two time points (averaged across the 12 participants). 109

Figure 4.1: A. Sagittal T_2-weighted image of the cervical spinal cord of a healthy participant showing the segmented and labelled spinal cord levels (C2-C6), with the positions of corresponding CEST slices of interest overlayed in yellow. B-D. Axial oblique CEST images from the same participant corresponding to slices 5, 7, and 10 respectively in the 3D volume, shown by the yellow outlines in panel A. Each CEST image shows the spinal cord ROI outlined in white. The ROI was created by transforming the segmented cord into the CEST space. E-G. Amine/amide concentration independent detection (AACID) maps of the spinal cord corresponding to slices 5, 7, and 10, overlayed onto the corresponding T_2-weighted anatomical axial oblique image. H-J. Average raw CEST spectra (blue points) for all pixels within the cord in slices 5, 7, and 10, respectively, with the average 6-pool Lorentzian model fitted line overlayed. 126

Figure 4.2: Mean between-subject coefficients of variation (CV) for each of the post-processing schemes at each spinal cord level (C2-C6). Between-subject CV values represent the mean ± standard deviation across the 12 participants (averaged over the two time points). 127

Figure 4.3: A. Mean within-subject coefficients of variation (CV) for each of the post-processing schemes at each spinal cord level (C2-C6). Within-subject CV values represent the mean ± standard error of the mean between the two time points (averaged across the 12 participants). B. Mean within-subject absolute amine/amide concentration independent detection (AACID) difference for each post-processing scheme at each spinal cord level (C2-C6). Absolute AACID difference values represent the mean difference ± standard deviation between the two time points (averaged across the 12 participants). A typical AACID value is ~1.5 in healthy spine. 129

Figure 4.4: A. Mean absolute amine/amide concentration independent detection (AACID) difference between the two time points (with standard deviation) comparing the four different post-processing schemes at the spinal cord levels C3, C4, and C5. The B_1 correction significantly decreased AACID changes across time (adjusted p-value = 0.002) compared to no correction. Neither the signal drift correction nor the combined correction showed any improvement compared to no correction. B. Mean AACID difference between the two time points (with standard deviation) for all participants comparing the different post-processing schemes at spinal cord levels C3, C4, and C5. 130

Figure 4.5: Average amine/amide concentration independent detection (AACID) values (with standard deviation) within different spinal cord levels. No significant differences in AACID values were observed between the cervical spinal cord levels for the B_1 correction post-processing scheme. Similar results were obtained for combined correction, signal drift correction alone, and when using no correction (not shown). 131

Figure 5.1: A. Sagittal T_2-weighted image of the cervical spinal cord of a degenerative cervical myelopathy (DCM) patient, with the position of CEST slice 7 overlayed in dotted yellow. B. Amine/amide concentration independent detection (AACID) map of the compressed spinal cord of the DCM patient, overlayed onto the corresponding T_2-weighted anatomical axial oblique image. C. Average raw CEST spectrum (blue points) for all pixels

within the cord in slice 7 of the DCM patient, with the average 6-pool Lorentzian model fitted line overlayed. D. Sagittal T_2-weighted image of the cervical spinal cord of a healthy control, with the position of CEST slice 7 overlayed in dotted yellow. E. AACID map of the spinal cord, corresponding to slice 7, overlayed onto the corresponding T_2-weighted anatomical axial oblique image. F. Average raw CEST spectrum (purple points) for all pixels within the cord in slice 7 of the healthy control, with the average 6-pool Lorentzian model fitted line overlayed. 151

Figure 5.2: Mean single slice amine/amide concentration independent detection (AACID) (with standard deviation) corresponding to the compression site for degenerative cervical myelopathy (DCM) patients (n = 9), a single slice above the compression (slice 3) (n = 6), and a single slice below the compression (slice 11) (n = 6). No significant differences were observed throughout the spinal cord of DCM patients. 152

Figure 5.3: Mean amine/amide concentration independent detection (AACID) (with standard deviation) corresponding to the single slice at the compression site for degenerative cervical myelopathy (DCM) patients (n = 9), slices 6-8 for the younger healthy controls (n = 24), and slices 6-8 for older healthy controls (n = 5). DCM patients had a significantly higher AACID value than younger controls (p = 0.03). 154

Figure 5.4: The correlation measured between the amine/amide concentration independent detection (AACID) value at the spinal cord compression of degenerative cervical myelopathy (DCM) patients and the associated spine compression volume, demonstrating a nonsignificant linear relationship (p = 0.17, r = 0.51). 155

List of Supplementary Tables

Supplementary Table 2.1: The measurements of the spinal cord compression volume (mm^3) found for each rater 90

Supplementary Table 3.1: Offsets (measured in ppm) sampled to acquired Z-spectrum for all healthy participants (read left to right, top to bottom) 116

Supplementary Table 3.2: Starting points and boundary values of all fit parameters of the five-pool Lorentzian fit. Chemical shift (δ) and FWHM (Γ) are given in ppm. 117

Supplementary Table 4.1: Offsets (measured in ppm) sampled to acquired Z-spectrum for all healthy participants (read left to right, top to bottom), with non-saturated scan (S_0) of 100 ppm interleaved after every third frequency offset. 137

Supplementary Table 4.2: Starting points and boundary values of all fit parameters of the six-pool Lorentzian fit. Chemical shift (δ) and FWHM (Γ) are given in ppm. 139

Supplementary Table 4.3: Summary of the mean between-subject coefficients of variation (CV), within-subject CV, and absolute amine/amide concentration independent detection (AACID) difference for each spinal cord level (C2-C6) for all post-processing schemes (averaged across the 12 healthy participants ± standard deviation). 140

Supplementary Table 4.4: Summary of the mean amine/amide concentration independent detection (AACID) for each time point (with standard deviation), comparing the four different post-processing schemes for each spinal cord level (C2-C6). 142

Supplementary Table 5.1: Offsets (measured in ppm) sampled to acquired Z-spectrum for all patients and healthy controls (read left to right, top to bottom), with non-saturated scan (S_0) of 100 ppm interleaved after every third frequency offset. 161

Supplementary Table 5.2: Starting points and boundary values of all fit parameters of the six-pool Lorentzian fit. Chemical shift (δ) and FWHM (Γ) are given in ppm. 163

List of Supplementary Figures

Supplementary Figure 2.1: fMRI activation map variations associated with spinal cord compression severity. A: Participant with a significant compression site (white arrow). B: A symptomatic participant with a lesser degree of spinal cord compression (white arrow). C: The corresponding fMRI activation map (left hand tapping) for the participant with severe compression. D: The corresponding fMRI activation map (left hand tapping) for the participant with less compression. 85

Supplementary Figure 2.2: Left hand tapping BOLD signal and volume of compression. A: The correlation between the % BOLD signal of the cerebellum and the spinal cord compression volume. B: The correlation between the % BOLD signal of putamen and the spinal cord compression volume. C: The correlation between the % BOLD signal of the caudate and the spinal cord compression volume. D: The correlation between the % BOLD signal of the thalamus and the spinal cord compression volume. 86

Supplementary Figure 2.3: Left hand tapping volume of activation (VOA) and volume of compression. A: The correlation between the VOA of the cerebellum and the spinal cord compression volume. B: The correlation between the VOA of putamen and the spinal cord compression volume. C: The correlation between the VOA of the caudate and the spinal cord compression volume. D: The correlation between the VOA of the thalamus and the spinal cord compression volume. 87

Supplementary Figure 2.4: Right hand tapping BOLD signal and volume of compression. A: The correlation between the % BOLD signal of the cerebellum and the spinal cord compression volume. B: The correlation between the % BOLD signal of putamen and the spinal cord compression volume. C: The correlation between the % BOLD signal of the caudate and the spinal cord compression volume. D: The correlation between the % BOLD signal of the thalamus and the spinal cord compression volume. 88

Supplementary Figure 2.5: Right hand tapping volume of activation (VOA) and volume of compression. A: The correlation between the VOA of the cerebellum and the spinal cord compression volume. B: The correlation between the VOA of putamen and the spinal cord compression volume. C: The correlation between the VOA of the caudate and the spinal

cord compression volume. D: The correlation between the VOA of the thalamus and the spinal cord compression volume..... 89

List of Appendices

Appendix A – Ethics Approval 192

Appendix B - Copyright Permissions 194

List of Symbols, Acronyms, and Abbreviations

2D	2-Dimensional
3D	3-Dimensional
γ	Gyromagnetic ratio
δ	Chemical Shift (ppm)
AACID	Amine/amide concentration independent detection
ANOVA	One-way analysis of variance
APT	Amide proton transfer
AREX	Apparent exchange-dependent relaxation
ASA	Anterior Spinal Artery
B_0	Main magnetic field strength (T)
B_1	RF pulse magnetic field strength (T)
BOLD	Blood oxygen level-dependent
BW	Bandwidth
CEST	Chemical exchange saturation transfer
CNS	Central Nervous System
CSF	Cerebrospinal fluid
CV	Coefficient of variation
DCM	Degenerative cervical myelopathy
dHb	Deoxygenated Hemoglobin

FA	Flip Angle
FID	Free Induction Decay
FLASH	Fast low angle shot
FLIRT	FMRIB's Linear Image Registration Tool
fMRI	Functional magnetic resonance imaging
FSL	FMRIB Software Library
GM	Gray matter
GRAPPA	Generalized autocalibrating partially parallel acquisitions
GRASSP-M	Graded Redefined Assessment of Strength, Sensibility, and Prehension – Version Myelopathy
Hb	Hemoglobin
HCl	Hydrochloric acid
HDR	Hemodynamic Response
ICC	Intraclass correlation coefficient
k_w	Dissociation constant of water
M_0	Net Magnetization
M1	Primary motor cortex
mJOA	Modified Japanese Orthopaedic Association
MPRAGE	Magnetization-prepared rapid acquisition gradient echo
MRI	Magnetic resonance imaging

MT	Magnetization transfer
MTR	Magnetization Transfer Ratio
M_z	Bulk Water Magnetization
NH	Amide
NH_2	Amine
NOE	Nuclear Overhauser Enhancement
p	Pearson's correlation coefficient
pK_w	Ionization constant of water
PMC	Premotor Cortex
ppm	Parts per million
PSA	Posterior Spinal Artery
RF	Radiofrequency
S_0	Non-Saturated
S1	Primary somatosensory cortex
SCT	Spinal Cord Toolbox
SMA	Supplementary motor area
T_1	Longitudinal relaxation time
T_2	Transverse relaxation time
T_2*	apparent transverse relaxation
t_{delay}	Interpulse delay

TE	Echo Time
TI	Inversion Time
t_{pulse}	Radiofrequency pulse length
TR	Repetition Time
μ	Magnetic moment
VOA	Volume of activation
WASSR	Water saturation shift referencing
WM	White matter

Chapter 1

1 Introduction

This introductory chapter provides the necessary information to understand the topics presented in the other subsequent chapters of this thesis. A brief overview is presented of the cervical spinal cord structure and vasculature, degenerative cervical myelopathy and the need to find a measure of outcome in these patients, and how ischemia and hypoxia could present itself in the spinal cord. In addition, the fundamentals of magnetic resonance imaging (MRI) and functional MRI (fMRI) and chemical exchange saturation transfer (CEST) techniques are thoroughly explained.

1.1 Spinal Cord

1.1.1 Spinal Cord Structure

The spinal cord is an important component of the central nervous system (CNS). The CNS has both ascending sensory and descending motor tracts that transfer information from the brain, down the spinal cord to target muscles, or from muscles to the brain. The spinal cord is within the spinal canal and surrounded by cerebrospinal fluid (CSF). In adults, the spine has 33 vertebrae which protect the spinal cord from damage. These vertebrae are separated by cartilage disks that cause a buffer to any force caused by movements. Together, the vertebrae and cartilage form the spinal column. The spinal cord is comprised of four different regions: cervical (7 vertebrae, 8 nerve pairs), thoracic (12 nerve pairs and vertebrae), lumbar (5 nerve pairs and vertebrae), sacral (5 nerve pairs and fused vertebrae), and coccyx (1 nerve pair and 3-5 fused vertebrae) (1). There are 31 segments of the spinal cord, which are defined by the 31 pairs of nerves exiting the cord (2). Dorsal and ventral roots enter and leave the vertebral column, respectively. Dorsal roots allow sensory information from all over the body to be relayed to the spinal cord, while the ventral roots allow motor information to exit the spinal cord to movement-related muscles (2).

Internally, the spinal cord has white matter in the periphery, gray matter within and a small canal with CSF in the centre. The gray matter is butterfly-shaped and is

divided into four main columns: dorsal, intermediate column, lateral, and ventral. The dorsal horn is primarily comprised of sensory nuclei, which receive and process sensory information. The intermediate column and lateral horn are comprised of autonomic neurons related to visceral and pelvic organs. The ventral horn is comprised of motor neurons that innervate skeletal muscle. Specifically, in the cervical region, the spinal cord has motor and sensory neurons related to the upper limbs. Surrounding the gray matter butterfly is white matter, which mainly contains glial cells and myelinated axons from sensory or motor neurons. In the peripheral region of the spinal cord, the axons can either carry sensory information from the brain down the body to control movements (descending pathways) or carry sensory information from the body upward toward the brain (ascending pathways) (3).

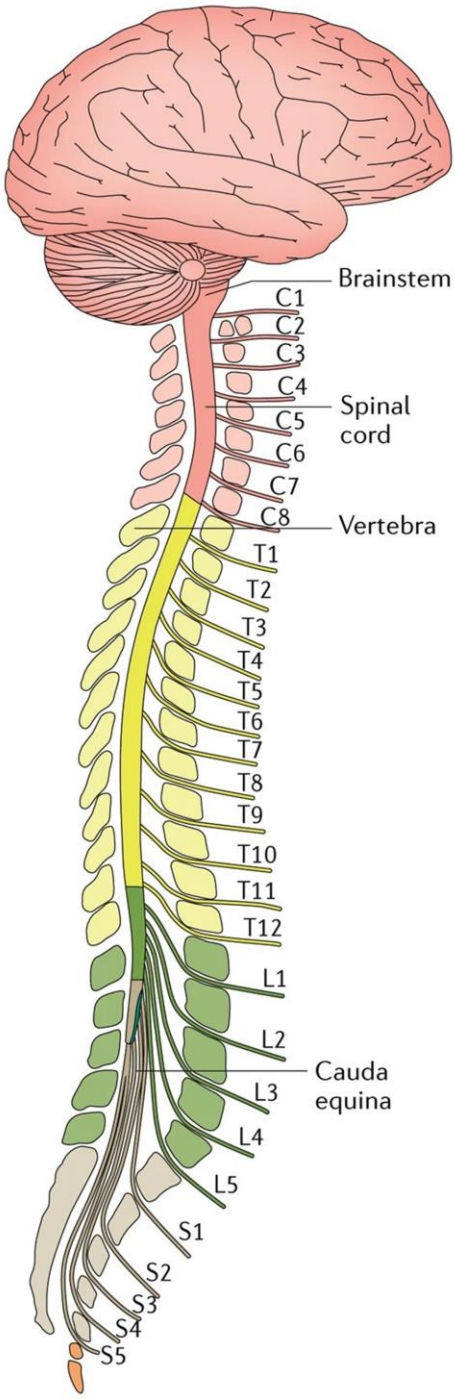

Figure 1.1: Anatomy of the spinal cord, showing the nerve pairs and vertebrae throughout the spinal cord. This figure was reproduced and modified with permission from Ahuja *et al.* (4)

1.1.2 Spinal Cord Blood Supply

The spinal cord receives blood supply from three major arteries: the single anterior spinal artery (ASA) and the two paired posterior spinal arteries (PSA). The ASA originates from the brainstem, longitudinally runs the length of the spinal cord and is the primary blood supply of the anterior two-thirds of the spinal cord (5). Both PSA travel the length of the spinal cord longitudinally, are derived from the vertebral arteries, and supply blood to one-third of the spinal cord (5). Segmental arteries aid both the ASA and PSA in supplying blood to the spinal cord. One type of segmental artery that travels along the nerve roots of the cord are known as the radicular arteries. Radiculo-medullary arteries are a subcategory of radicular arteries; they occur alongside the ventral nerve roots and provide a blood source for the ASA. Radiculo-pial arteries are another subcategory and travel alongside the dorsal nerve roots. A collection of these radiculo-pial arteries is called the pial plexus and provides blood to the peripheral region of the spinal cord, or the white matter. Note that in the spinal cord, gray matter is highly vascularized compared to white matter (6), and the ASA provides adequate blood to the gray matter.

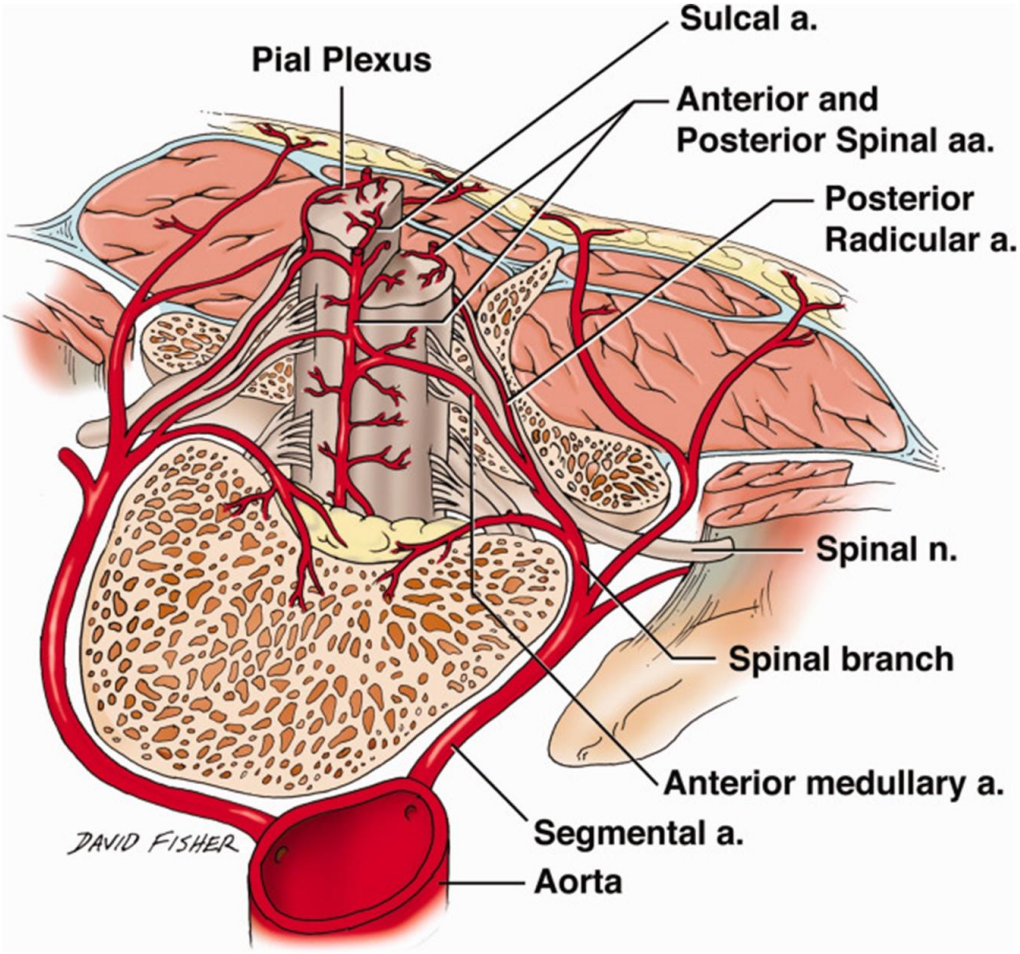

Figure 1.2: Schematic view of the blood supply of the spinal cord stemming from the aorta. *a.* stands for artery and *n.* stands for nerve. This figure was used with permission from Bosmia *et al.* (5)

1.2 Degenerative Cervical Myelopathy

Degenerative cervical myelopathy (DCM) is one of the leading causes of spinal cord dysfunction worldwide in adults. DCM is characterized by stenosis (or narrowing) of the cervical spinal canal due to the degeneration of the cervical spinal column, which can lead to chronic spinal cord compression. This is the most common form of spinal cord

dysfunction in adults over 55, with males being more predominately affected (7). Symptoms of DCM can range from mild dysfunction, such as dexterity/gait difficulties and numbness, to severe, such as incontinence and quadriparesis (7-10). When patients fail to respond to conservative treatment and symptoms are progressing, surgical intervention is required (10). However, studies have shown that some patients continue to deteriorate after surgery. This has created a need to identify predictors of outcome for DCM patients after decompression surgery.

1.2.1 Pathophysiology and Pathobiology of DCM

Degenerative changes to the spine components can occur from aging (10). The pathogenesis of DCM can be divided into three main components: static, dynamic, and histopathological (11). Static components are structural changes that cause canal narrowing. Deterioration of the intervertebral discs is typically the beginning of the degenerative cascade. Disc herniation occurs when the nucleus pulposus (center of the intervertebral disc) pushes against the annulus fibrosus (outer ring of the disc) (12). When the annulus is worn or injured, the nucleus can squeeze through, causing spinal canal compression or narrowing. Discs can also lose height as aging occurs. Disc height can collapse due to the loss of water content, drying the discs out and becoming stiffer. The vertebrae move closer, and bone spurs form around the disc to strengthen it, causing the spinal canal to narrow and compress. The ligamentum flavum can thicken and buckle into the spinal canal. Ossification of the posterior longitudinal ligament can also cause direct spinal cord compression. These changes often lead to a loss of the range of motion, and to compensate for this decreased motion, adjacent structures of the spine become hypermobile (11,13).

Dynamic components leading to DCM stem from abnormal repetitive cervical spine movement during flexion and extension (14). This repetitive movement can cause spinal cord compression. Hyperextension, or the over extension of the neck, can cause pinching of the spinal cord between the vertebral body anteriorly and the hypertrophied ligamentum flavum posteriorly (8,15), while flexion, or bending the neck towards the chest, may compress the cord against the anterior osteophytes and intervertebral discs (16,17).

Both the static and dynamic factors lead to chronic spinal cord compression. This chronic spinal cord compression can lead to vascular changes, like regional malperfusion and deformation of the vessels, which can result in ischemia/hypoxia and neuroinflammation (7,8,10,11). Chronic cord compression may also lead to neuronal cell loss, gray and white matter degeneration, atrophy of the anterior horns, and endothelial damage, which results in a compromised blood-spinal cord barrier (10). The disruption of the blood-spinal cord barrier can permit the entry of inflammatory cells into the spinal cord parenchyma, which can also eventually lead to the neuroinflammatory process (8). Ischemia/hypoxia and neuroinflammation can activate the apoptotic pathway, causing progressive neuronal cell death (10,18). This has been suggested to affect the severity of the neurological deficits experienced by DCM patients (10,18,19). The pathophysiological process of DCM is summarized in Figure 1.3.

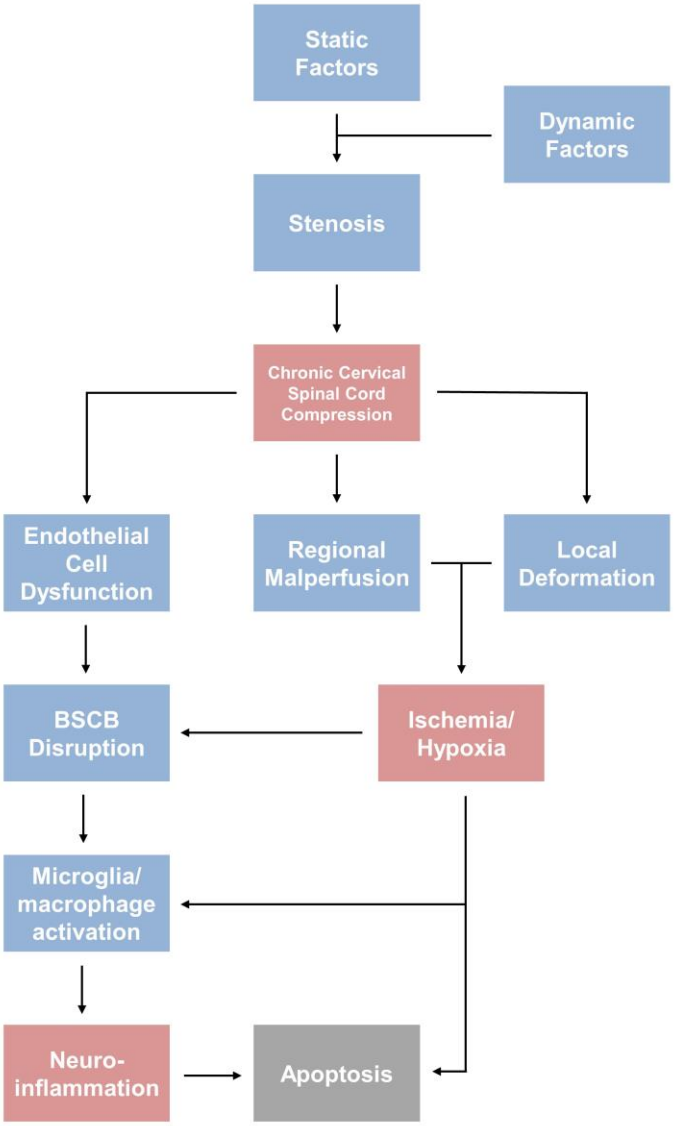

Figure 1.3: Flow graph of the pathophysiological process of degenerative cervical myelopathy (DCM). Static factors can cause stenosis of the spinal cord (narrowing of the cross-sectional area of the spinal cord), which is further exacerbated by dynamic factors during movement. This can cause compression of the spinal cord which can result in the disruption of the blood-spinal cord barrier (BSCB) via endothelial cell dysfunction or ischemia/hypoxia through regional malperfusion and vessel deformation. Both can eventually activate the apoptotic pathways, causing neuronal and oligodendroglial cell death. This figure was adapted with permission from Badhiwala *et al.* (8).

1.2.2 Clinical Assessment

Common symptoms can include neck pain or stiffness, weakness, pain or numbness in the upper limbs, loss of dexterity, weakness, numbness or stiffness in the lower limbs, gait unsteadiness, and loss of control of the bowel/bladder. The modified Japanese Orthopaedic Association (mJOA) is used to grade the functional impairment of DCM patients (13,20). This is a clinically administrated index specific to DCM patients. mJOA assesses functional abilities on an 18-point scale, which is divided into the subdomains of upper limb motor function, lower limb motor function, upper limb sensation, and sphincter function. This scale is used to classify patients into different severity categories, with a score >15 indicative of mild DCM, 12-14 indicating moderate DCM, and <11 indicating severe DCM (21). Table 1.1 shows how mJOA is assessed for DCM patients. This scale helps define whether patients are improving, either naturally or through surgical intervention.

Physical examinations of DCM patients can include assessment of balance and gait, cervical range of motion, and dexterity tests. The Graded Redefined Assessment of Strength, Sensibility, and Prehension – Version Myelopathy (GRASSP-M) is a dexterity assessment tool that can assess the function and hand impairments in DCM patients to characterize motor, sensory, and dexterity changes following compression (22,23). Assessing hand impairment can assist with patient monitoring and treatment planning.

Table 1.1: The modified Japanese Orthopaedic Scale (mJOA), modified with permission from Benzel *et al*. (20).

Type of Dysfunction	**Level of Dysfunction**	**Score**
Motor Dysfunction, upper extremity	Inability to move hands	0
	Inability to eat with a spoon, but able to move hands	1
	Inability to button shirt, but able to eat with a spoon	2
	Able to button shirt with great difficulty	3
	Able to button shirt with slight difficulty	4
	No dysfunction	5
Motor dysfunction, lower extremity	Complete loss of motor and sensory function	0
	Sensory preservation without ability to move legs	1
	Able to move legs, but unable to walk	2
	Able to walk on flat floor with a walking aid (cane or crutch)	3
	Able to walk up and/or down stairs with handrail	4
	Moderate-to-significant lack of stability, but able to walk up and/or down stairs without handrail	5
	Mild lack of stability, but walks with smooth reciprocation unaided	6
	No dysfunction	7
Sensory dysfunction, upper extremity	Complete loss of hand sensation	0
	Severe sensory loss or pain	1
	Mild sensory loss	2
	No sensory loss	3
Sphincter dysfunction	Inability to micturate voluntarily	0
	Marked difficulty with micturition	1
	Mild-to-moderate difficulty with micturition	2
	Normal micturition	3

1.2.3 Diagnostics Using Imaging

Computerized tomography (CT) scans of the cervical spine are useful when studying bone anatomy. Plain radiographs (X-rays) often are used to visualize how the spinal cord is narrowing, the degenerating discs and joints, and vertebral fusion (24,25). X-rays can be particularly useful in assessing the alignment of the cervical spinal cord when the patients are in an upright position under a physiological load. However, both CT scans and X-rays cannot provide information regarding the tissues and composition of the spinal cord.

To characterize both the structure and compression of the cervical spine, magnetic resonance imaging (MRI) is a useful diagnostic tool. MRI allows for high-resolution visualization of neural structures, ligaments, and bone structures (26) in three dimensions (sagittal, axial, and coronal). Qualitative MRI can detect diagnostic features of DCM, such as the location and source of the spinal cord compression, the nature and degree of the degenerative changes (i.e., hypertrophy, disc herniation, etc.), narrowing of the spinal canal, and spinal cord edema based on signal intensity changes within the spinal cord (10,16,27). T_2-weighted images typically demonstrate hyper-intensities, while T_1-weighted images typically demonstrate hypo-intensities, indicating atrophy of the spinal cord or spinal cord edema (28,29). MRI is also useful when trying to differentiate DCM from other conditions with similar presenting symptoms, like a tumour causing compression of the spinal cord (25,30).

Figure 1.4: Sagittal T_2-weighted MRI (acquired on a Siemens 3.0 T MAGNETOM Prisma Fit, 3D spin-echo sequence, repetition time (TR)/echo time (TE) = 1400/136 ms, 64 slices, isotropic resolution of 0.8 mm^3) of the spinal cord of a DCM patient. Arrow indicates presence of spinal cord compression.

1.2.4 Management

Clinical practice guidelines recommend that when DCM patients are classified as mild (mJOA score > 15), conservative management is suggested (31). Conservative, non-operative management can include neck bracing (32), manual therapy (33), bedrest and avoidance of risky activities and environments (34). The objective of conservative management is to treat the symptoms while protecting the spinal cord from any additional injury. There is debate about the efficacy of conservative management – studies have demonstrated that 23-54% of patients that were conservatively managed required follow up surgical intervention 29-74 months after initial management (8,32,35). Studies have also demonstrated that DCM patients who received conservative management showed

minimal improvement based on a nominal observed change in mJOA scores (observed change mostly between 0 and 1) (36).

Surgical intervention is recommended for DCM patients who are considered moderate (mJOA score 12-14) or severe (mJOA score <11) (31). Surgical intervention decompresses the spinal cord, with the goal of preserving the alignment of the vertebrae and preventing any further neurological decline. Newer evidence suggests that mild DCM patients could also benefit from surgical intervention as a substantial reduction in quality of life can also occur in this cohort (37). The main objective of decompression surgery is to maintain neurological function and prevent further deterioration. A previous study has demonstrated that one-third of patients typically improve following surgery, while 40% show no change and 25% worsen (10,13). However, predicting surgical outcomes in individuals is a challenge.

1.2.5 Predictors of Outcome

Many studies have attempted to identify clinical predictors of surgical outcomes after decompression surgery. Some suggested predictors of outcome that are associated with worse surgical outcomes are older age, longer duration of symptoms, and higher severity of myelopathy (25,38). Unfortunately, the last two predictors undermine the importance of early diagnosis of DCM before irreversible spinal cord damage has occurred. A study performed by Vidal *et al.* demonstrated that there is a need for early diagnosis; when delayed decompression occurred in rodent models of DCM, there was poorer neurological recovery (39). MRI features have also been studied to try to predict the outcomes of surgery in DCM patients. Studies have shown that high signal intensity (hyper-intensity) on T_2-weighted images, low signal intensity (hypo-intensity) on T_1-weighted images, the cross-sectional area of the spinal cord, and a combination of T_1 and T_2 signal changes are associated with poorer neurological surgical outcome (38,40,41). Unfortunately, these factors have been unreliable when trying to predict the outcome of surgery in individual DCM patients.

1.3 Ischemia and Hypoxia

Brain *et al.* first introduced ischemia as a pathophysiological mechanism that influences the progression of DCM (42). Compression of the spinal cord can result in the deformation of vasculature structures (i.e., PSA, ASA, and radicular arteries). Physical changes reduce blood flow to the spinal cord and can cause ischemic damage (8,43). A study performed by Mair & Druckman demonstrated that spinal compression, caused by the protrusion of the cervical interverbal discs, led to the thickening of arterial and small vessel walls at the site of compression, causing the major vessels to have a reduced blood flow velocity and impaired regional perfusion (44). Studies have also demonstrated that ischemic injury of the gray and white matter has occurred in patients with cervical spine compression due to the compressed intramedullary arteries causing malperfusion of gray and medial white matter (11,45). This ischemic injury in the gray and medial white matter can lead to inadequate blood flow to axonal pathways, including corticospinal tracts (46). Furthermore, Ellingson *et al.*, found a decrease in blood flow, measured using dynamic susceptibility contrast perfusion MRI, in the spinal cord region experiencing compression (47).

In animal models of DCM, ischemic injury has been shown. A study performed by Kurokawa *et al.* demonstrated that compared to non-compressed sites of the spinal cord, there was a blood flow reduction of 20% at the site of compression in a rat model (48). In a study using micro-computer tomography (micro-CT), the ASA and radicular arteries of rats were compressed, and the diameter was significantly decreased compared to non-compressed arteries; there was also a significant decrease in the microvasculature, depicted by the reduced density (49). Furthermore, Karadimas *et al.*, also demonstrated that in a DCM rat model of chronic compression, there were microvasculature changes in the cervical spinal cord, indicated by decreased staining for laminin, which is a protein of the basement membrane of blood vessels (50). Other studies have considered the effect of decompression surgery on ischemia. Interestingly, when blood flow is restored to the ischemic site following decompression surgery, a secondary injury can manifest and induces oxidative damage in neurons (39,51). Ischemia-reperfusion injury will be further discussed in Section 1.3.1.

1.3.1 Reperfusion Injury

It has been shown in a rodent model of DCM that a key factor that could explain neurological decline after decompression surgery is ischemia-reperfusion injury (39,51). Studies have demonstrated that reperfusion injury can contribute to the injury process of the central nervous system (CNS) by activating the immune system (52-54). One specific study demonstrated that after ischemic stroke, the increased activation of the immune system induced the recruitment of immune cells to the affected ischemic tissue, triggering an inflammatory response and increasing the infarct size (53). Ischemia-reperfusion injury can exacerbate the cellular damage that was already caused by ischemia/hypoxia. Post-revascularization causes a sudden increase in the blood and oxygen, which can activate the inflammatory response and cause further damage to the cells and membranes (55). A delay in decompression surgery in DCM patients could lead to an increase in neurological deficits and the absence of recovery post-surgery (51). Developing a measure of ischemia of hypoxia in the spinal cord could be informative when trying to diagnosis DCM patients early and determine who would benefit from decompression surgery instead of conservative management.

1.3.2 Acidity measured by pH

Naturally, water molecules (H_2O) tend to ionize or separate into a proton (H+) and hydroxyl ion (OH^-) (i.e., $H_2O \rightarrow H^+ + OH^-$). The dissociation constant of water (K_w) characterizes the product of ion concentrations at equilibrium:

$$K_w = [H^+][OH^-] \quad [1.1]$$

The logarithm form of K_w is known as pK_w:

$$pK_w = -log(K_w) \quad [1.2]$$

As an acid, H^+ can either donate a proton or accept an electron pair; as a base, the hydroxyl ion can either accept a proton or donate an electron pair. To quantify how basic or acidic a solution is, Soren Sorensen developed the concept of pH:

$$pH = -log[H^+] \quad [1.3]$$

where $[H^+]$ is the molar concentration of protons (56,57). In biological tissue, the $[H^+]$ in the intracellular (pH_i) and extracellular (pH_e) fluid can be calculated using equation 1.3. If pK_w is known, then $[OH^-]$ can be calculated:

$$[OH^-] = \frac{[H^+][OH^-]}{[H^+]} = \frac{10^{-pK_w}}{10^{-pH}} = 10^{pH-pK_w} \quad [1.4]$$

When ischemia and hypoxia occur, the cellular response includes the production of lactate and excess $[H^+]$ by anaerobic glycolysis, which alters the tissue pH homeostasis. More specifically, cellular glucose metabolism plays an important role in pH homeostasis. The breakdown of one glucose molecule causes the reduction of two co-enzymes called nicotinamide adenine dinucleotide (NAD^+) to NADH, the conversion of two adenosine diphosphate (ADP) molecules to two adenosine triphosphate (ATP) molecules, and the phosphorylation of two inorganic phosphates (P_i). Two water molecules and two protons are also produced.

$$Glucose + 2NAD^+ + 2ADP + 2P_i \rightarrow 2Pyruvate + 2NADH + 2H^+ + 2ATP + 2H_2O \quad [1.5]$$

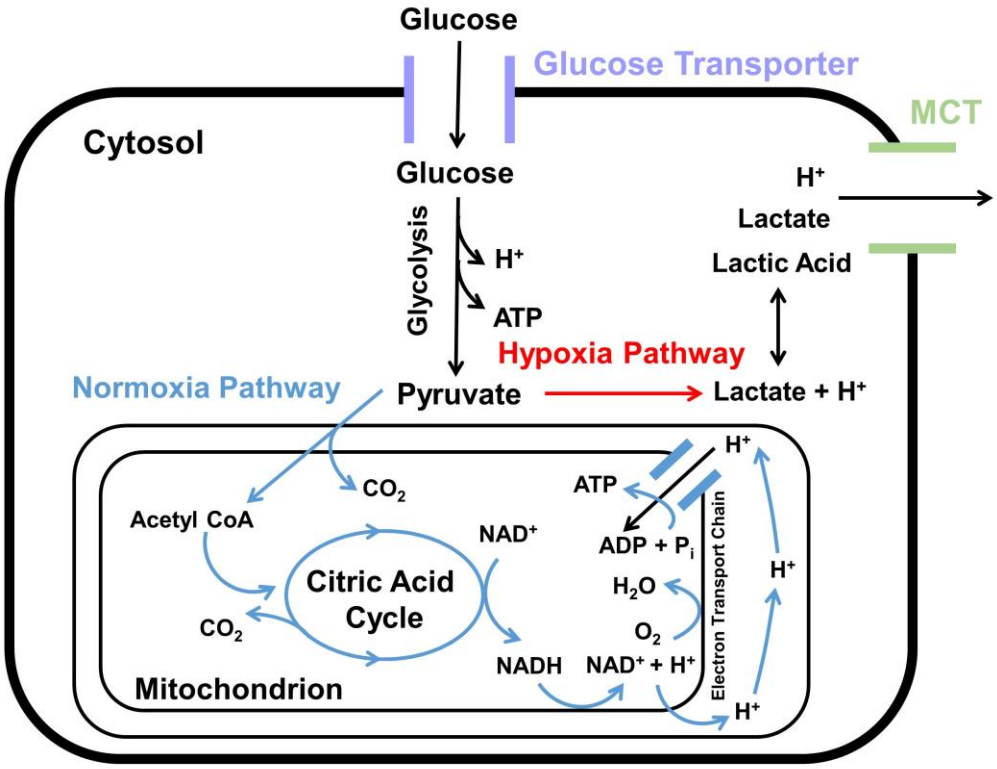

Figure 1.5: Schematic diagram of pH homeostasis. Normal cellular glucose metabolism in normoxic (blue) and hypoxic (red) conditions. The hypoxic pathway contributes to proton and lactate production. MCT – monocarboxylate transporters

In aerobic, or normoxic, conditions, pyruvate is transported to the mitochondrion and converted to acetyl co-enzyme a (acetyl-CoA) and CO_2. Acetyl-CoA enters the citric acid cycle in the mitochondrion, producing more CO_2 and reducing NAD+ to NADH. Then, the electron transport chain oxidizes NADH to NAD^+ (oxidized form), with O_2 acting as the final electron acceptor. Consequently, a proton gradient is established across the inner mitochondrial membrane, producing ATP through oxidative phosphorylation (58).

In hypoxic conditions, both the citric acid cycle and electron transport chain are inhibited, causing glycolysis to elevate to meet the energy demands. To meet the energy

demands, lactic acid fermentation occurs to create a sufficient supply of NAD^+ for glycolysis.

$$Pyruvate + NADH + H^+ \rightarrow Lactate + NAD^+ \quad [1.6]$$

At physiological pH values, lactic acid mostly dissociates into the lactate anion and a proton, leading to acidification in hypoxic conditions (59).

$$Lactic\ acid \leftrightarrow Lactate^- + H^+ \quad [1.7]$$

As well, the hydrolysis of the ATP that is produced in the mitochondria during hypoxia can contribute to the decrease in cellular pH if the cells cannot export the protons quickly enough (59).

$$ATP + H_2O \leftrightarrow ADP + HPO_4 + H^+ \quad [1.8]$$

These metabolic acids like protons, lactate and CO_2 can be transported to the extracellular space through membrane transporters to avoid acidosis (60,61). The metabolic acids can diffuse into local blood vessels and are carried to the lungs (CO_2) or the kidneys (via urine) for removal. Normal human tissue can maintain a healthy balance of acid-base in many conditions, including brief periods of hypoxia. When tissue does not have sufficient oxygen to meet the metabolic demands (i.e., spinal cord compression), the elevated lactate and proton concentration can lead to an acidic pH. Furthermore, many

macromolecules, proteins, and peptides have pH dependent activities and structures (61,62), meaning that pH could be a fundamental marker of pathological progression.

Cellular pH can be considered either intracellular (pH_i) or extracellular (pH_e). Both provide highly valuable information when assessing disease progression, investigating pathogenesis, and monitoring disease response. A study has demonstrated that pH_e decreases correlated with immune response in acute infection and chronic inflammatory disease (63). Disruption in pH_i has been demonstrated in cell proliferation and cellular death (64). Studies have shown that the acidification of lysosomes is a marker of ageing and several neurodegenerative diseases (65,66). However, it has been shown that pH_i is more resistant to pH changes than pH_e and less sensitive to metabolic alterations (67). As previously mentioned, this is due to the regulation of intracellular pH through transporters and channels – metabolic acids in cells can be transported to the extracellular space, influencing the pH_e. Both pH_i and pH_e are dependent on each other.

1.3.3 Imaging of pH

There are several magnetic resonance spectroscopy (MRS) techniques that have been proposed to measure tissue pH. A study performed by Moon and Richards was the first to demonstrate that intracellular pH could be quantified using ^{31}P MRS (68). They demonstrated that the inorganic phosphate (P_i) chemical shift resonance was pH dependent. Because concentrations of P_i are higher in the intracellular space compared to the extracellular space (2-3 mM compared to 1 mM, respectively), P_i is weighted towards intracellular pH changes. The 3-aminopropylphosphate (3-APP) resonance in ^{31}P MRS has been used to measure extracellular pH in mice tumour models (69). A major limitation of ^{31}P MRS is its low sensitivity, which leads to long acquisition times and low spatial resolution. Specially designed hardware is also required, including a dedicated phosphorous coil. However, ^{31}P is the gold standard of MR pH measurements because of its extensive validation with microelectrode measurements and reliability (70).

^{19}F has a higher gyromagnetic ratio, leading to greater MRS signal sensitivity over ^{31}P (71). A study performed by Deutsch and Taylor demonstrated the development of ^{19}F probes to measure intracellular pH (72). The advantages are that ^{19}F has a

relatively large chemical shift dispersion and an almost total lack of endogenous signal in normal tissue. Exogenous agents can then be resolved easily. Limitations include the instability of fluorinated compounds and the inability to measure other compounds simultaneously (70). Hyperpolarized ^{13}C MRS is an emerging method to measure pH. It has shown that hyperpolarized ^{13}C bicarbonate ratio to $^{13}CO_2$ can be used to measure extracellular pH (67,73). However, because the hyperpolarized signal decreases quickly due to T_1 relaxation, measurements must be completed within 1-2 minutes of sample preparation and injection, and typically have low spatial resolution (70). In ^{1}H MRS, the lactate peak can be measured at the chemical shift of 1.33 ppm as a doublet peak (74). In normal, non-hypoxia conditions, the lactate concentration is very low and is rarely detected above the baseline noise; however, when concentrations of lactate are increased (i.e., hypoxic conditions), the lactate doublet can appear above the baseline at short echo times (TE), or as a phase inverted doublet below baseline at longer echo times (i.e., TE = 135 ms) (75). Unfortunately, differentiation between lactate and lipid peaks can be problematic at short echo times and sensitivity needs to be improved.

Radionuclide detection of hypoxia has also been studied using hypoxia positron emission tomography (PET) specific tracers ^{18}F-labelled nitroimidazoles and Cu-labelled diacetyl-bis (N4-methylthiosemicarbazone) analogues (76). 2-Nitroimidazole compounds enter cells through passive diffusion and undergo reduction forming a reactive intermediate species. Under normoxic conditions, the compounds are reoxidized and diffuse out of the cell. In hypoxic conditions, the compounds further reduce and become irreversibly trapped in the hypoxic cell. One of the most extensively study tracers is ^{18}F-fluoromisaonidazole (^{18}F-FMISO); however, it has a slow pharmacokinetic profile, with limited clearance from normal tissue, causing limited hypoxic contrast (76). Cu with diacetyl-bis (N4-methylthiosemicarbazone) (ATSM) can rapidly diffuse into cells and undergo intracellular reduction of Cu(II) to Cu(I). Under hypoxic conditions, Cu(I)-ATSM can dissociate into Cu(I) and ATSM, causing the Cu(I) ion to be trapped. When oxygen is present, the compound can reoxidized to the parent compound and efflux from the cell (77). However, there is limited availability of the Cu isotope. PET imaging also has low resolution and cannot resolve very small point sources (78).

Optically, near-infrared spectroscopy (NIRS) can continuously monitor regional tissue oxygenation. NIRS can differentiate the absorption spectra from three important chromophores: oxygenated hemoglobin (O_2Hb), deoxygenated hemoglobin (dHb), and cytochrome (cyt). The NIRS technique can achieve a quantitative measure of oxygenation saturation and hemoglobin content in tissue by utilizing the spectral differences in these chromophores (79,80). This technique is non-invasive, easy to apply, and has the potential for good temporal and spatial resolution. However, NIR light is also absorbed by skin and subcutaneous fat, causing individuals with high-fat deposition to have decreased signals. NIRS can only detect oxygenation approximately 2-3 cm deep (81), limiting this technique to superficial structures. Utilizing NIRS to measure spinal cord oxygenation could also be challenging due to the optical properties of the surrounding bone (i.e., absorption and scattering), causing the spinal cord signal to be attenuated (82).

1.4 Introduction to Magnetic Resonance Imaging (MRI)

The nuclear magnetic resonance (NMR) phenomenon arises from the quantum mechanical properties of protons and neutrons of the atomic nuclei (83,84). Magnetic resonance imaging (MRI) typically exploits the interaction between the hydrogen nucleus (^1H) as the nucleus of interest and the magnetic fields produced by the MR scanner, to generate a detectable localized signal and produce contrast associated with the bulk water in soft tissue. This section outlines the basic principles of MRI to help develop an understanding of functional MRI (fMRI) and chemical exchange saturation transfer (CEST) MRI techniques, which are used in the remainder of the thesis.

1.4.1 Magnetic Moments

A ^1H nucleus is comprised of a positively charged proton and will be called a proton in this thesis. The angular momentum of the proton is characterized by the fundamental property called spin. I is the nuclear spin quantum number, which is equal to ½ for protons. The angular momentum of the proton generates a magnetic field, which is known as the nuclear magnetic moment, μ. Protons are placed into a static external magnetic field (B_0) which has a fixed axis, considered to be the z or longitudinal axis.

The precession about B_0 when placed in the external magnetic field is caused by torque (τ).

$$\frac{d}{dt}\vec{\mu} = \vec{\mu} \times \vec{B}_0 \qquad [1.9]$$

with the solution describing the magnetic moment rotating about B_0 in the clockwise direction:

$$\vec{\mu} = \vec{\mu}_0 e^{-i\gamma \vec{B}_0 t} \qquad [1.10]$$

The magnetic moment rotates with an angular frequency equal to the Larmor frequency (rads s^{-1}):

$$\vec{\omega}_0 = \gamma \vec{B}_0 \qquad [1.11]$$

where γ is the gyromagnetic ratio (106 rad s^{-1} T^{-1}) and B_0 is the main external magnetic field (in T) (85).

When there is no external magnetic field present, the individual nuclear magnetic dipole moments are typically distributed randomly, resulting in the absence of net magnetization. Introducing B_0 causes the distribution of the proton magnetic moments to align slightly in favour of the direction of B_0, causing the net magnetization to be in the

same direction. In a hypothetical system where proton interactions are absent, proton magnetic moments precess in two possible orientations about B_0: parallel or anti-parallel (86). In actuality, protons undergo continuous collisions with their surroundings, causing them to align in various orientations, with a slight majority favoring alignment in the direction of B_0 (Figure 1.6). For the purpose of this thesis, the hypothetical spin system will be described. More specifically, a group of spins will be described, which are known as isochromats, where the net magnetization of the group aligns along the direction of B_0 (86).

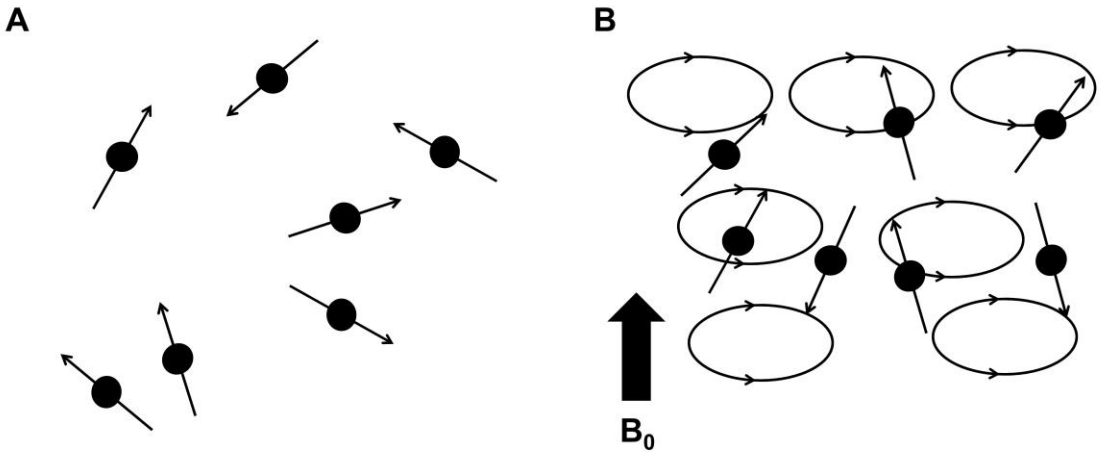

Figure 1.6: A. Protons spin in random orientation in the absence of a magnetic field. **B.** In the presence of a magnetic field (B_0), the proton spins have a slight excess of magnetic moments aligned in parallel to the external field, leading to a net magnetization M_0.

As mentioned, magnetic moments are characterized by energy states either aligning parallel (low-energy - E_L) or anti-parallel (high-energy - E_H) with B_0. The system's inclination is towards the lower-energy state, which involves alignment parallel to the external magnetic field. The energy difference between the two states is equal to:

$$\Delta E = \gamma \frac{h}{2\pi} \vec{B}_0 \quad [1.12]$$

where h is Planck's constant (84). The distribution of the protons between the two energy states is described by the Boltzmann distribution:

$$\frac{N_-}{N_+} = e^{-\left(\frac{\Delta E}{kT}\right)} \quad [1.13]$$

where N_- and N_+ represent the number of protons in the lower and higher energy states, respectively, k is the Boltzmann constant (1.38 x 10^{-23} J/Kelvin), and T is the absolute temperature in Kelvin. The fraction of excess protons in the lower energy state accounts for the net polarization, P:

$$\vec{P} = \frac{N_- - N_+}{N_- + N_+} = \frac{e^{\left(\frac{\Delta E}{kT}\right)} - e^{-\left(\frac{\Delta E}{kT}\right)}}{e^{\left(\frac{\Delta E}{kT}\right)} + e^{-\left(\frac{\Delta E}{kT}\right)}} \quad [1.14]$$

However, at room temperature, Curie's Regime states that $e^{\left(\frac{\Delta E}{kT}\right)} \ll 1$, therefore, polarization can be approximated as:

$$\vec{P} \approx \frac{\gamma h \vec{B}_0}{4\pi kT} \quad [1.15]$$

As mentioned, net magnetization, M_0, is produced when there is an excess of protons in the lower energy state:

$$\vec{M}_0 = N \cdot \vec{\mu} \cdot \vec{P} \quad [1.16]$$

where N is the number of proton nuclei per unit volume. This net magnetization is parallel with the fixed axis of the external magnetic field, or the z-axis. Therefore, the summation of all magnetic moments produces an equilibrium net longitudinal magnetization, denoted as $\vec{M}_z^0$:

$$\vec{M}_z^0 = \frac{N \cdot \left(\gamma \frac{h}{2\pi}\right) \cdot \vec{B}_0}{4kT} \quad [1.17]$$

$\vec{M}_z^0$ is comprised of magnetic moments precessing at the same Larmor frequency, so there is no phase coherence in the xy or transverse plane at equilibrium (84). Therefore, there is no net transverse magnetization.

1.4.2 Excitation

Faraday's law of induction states that a rotating magnetization induces a corresponding voltage in the electric radiofrequency (RF) receive coils (87), which allows for MR signal detection. More specifically, the RF receive coils are in the transverse plane and can detect the magnetization rotating in the transverse plane (transverse magnetization $\vec{M}_{xy}$). The net magnetization vector $\vec{M}_z^0$ aligned with B_0 (described in Section 1.4.1), as shown

in Figure 1.7A, is excited or tipped into the transverse plane by an additional external magnetic field B_1. This external magnetic field is produced when a RF pulse is applied perpendicular (i.e., in the transverse plane) to the main magnetic field (85). Once the net magnetization vector is tipped into the transverse plane, the B_1 field is removed, creating a transverse magnetization $\vec{M}_{xy}$, as shown in Figure 1.7B. The RF receive coils receive the voltage generated by the transverse magnetization undergoing precession around B_0 at the Larmor frequency. This produced voltage is proportional to the amplitude net magnetization and the square of the magnetic field strength B_0 (83).

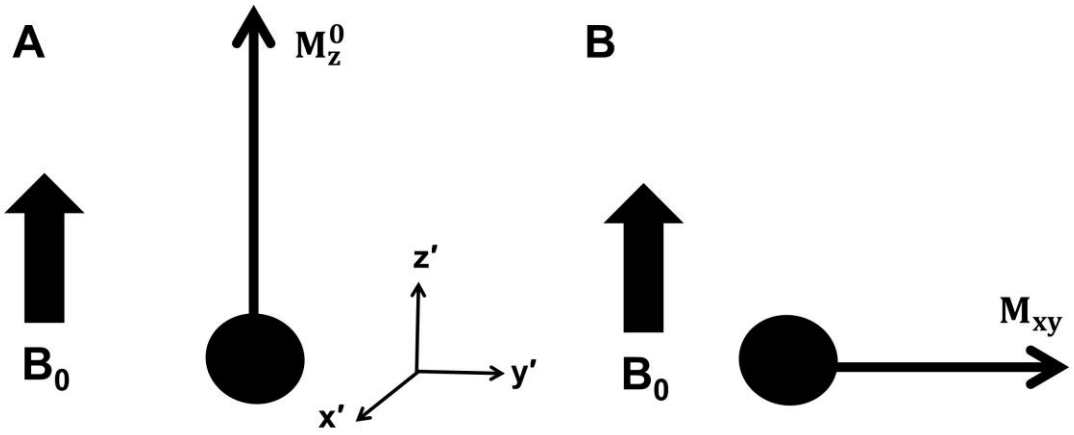

Figure 1.7: Protons spin in the rotating reference frame. **A.** In the presence of an external magnetic field (B_0), the protons tend to orient either parallel or anti-parallel with B_0, leading to a net magnetization vector ($\vec{M}_z^0$). **B.** Upon the application of an RF excitation pulse along the x′-axis, protons become evenly distributed between parallel and anti-parallel orientations and phase in alignment along the y′-axis. Figure was recreated from de Graaf with permission (84).

Based on Faraday's Law, the RF coils not only receive magnetic signals but also produce magnetic fields. These magnetic fields, known as RF pulses, are used to excite

spins, and create transverse magnetization $\vec{M}_{xy}$. An oscillating magnetic field with B_1 amplitude and frequency ω_{RF} is created by the RF pulses. Criteria to achieve the tipping of the net magnetization into the transverse plane are: 1) the applied B_1 field must be applied perpendicular to the external field B_0, and 2) the applied B_1 field must be tuned to the Larmor frequency (i.e $\omega_{RF} = \omega_0$). In a rotating frame of reference (x′ y′ z′ – rotating in a clockwise direction about the longitudinal axis), the motion of the net magnetization can be described by:

$$\frac{d}{dt}\vec{M} = \vec{M} \times \gamma\vec{B}_1 \qquad [1.18]$$

Analogous to how the magnetic moment μ preccesses about the main magnetic field B_0, the net magnetization vector rotates around $\vec{B}_1$, or x′-axis, towards the y′-axis in the transverse plane. The angle at which the net magnetization vector tips away from the longitudinal axis and to the transverse plane is know as the flip angle, α, and is determine by the duration and amplitude of the RF pulse (83):

$$\alpha = \gamma B_1 T \qquad [1.19]$$

where B_1 is the amplitude of the applied magnetic field and T is the RF pulse duration. In simple experiments, α is 90° and the net transverse magnetization vector aligns along the y′ axis and precesses about the main magnetic field B_0 (83). Note that in a quantum mechanics perspective, protons are equally distributed in both orientations (i.e., energy states), but in phase coherence along the y′ axis.

1.4.3 Relaxation

Following the excitation RF pulse, transverse magnetization begins to decrease in amplitude due to dephasing of the magnetic moments and the return of magnetization to the equilibrium magnetization $\vec{M}_z^0$. This process where magnetization comes back to equilibrium is called relaxation.

Longitudinal or spin-lattice relaxation is where the longitudinal component of the magnetization returns to equilibrium after any perturbation, like excitation from an RF pulse. This relaxation is initiated by dipole-dipole interactions between neighbouring protons, leading to a net transfer of energy from an excited magnetic moment (spin) to its surrounding environment (lattice) (84). Transverse or spin-spin relaxation is the process in which magnetic moments dephase and transverse magnetization decays to zero. This relaxation is the loss of phase coherence from the energy exchange between spins. As an example, when excitation occurs, high energy spin may transfer energy to low energy spin, causing both spins to change states and lose phase coherence.

$$\vec{M}_z(t) = \vec{M}_z(0)\left(1 - e^{-t/T_1}\right) \quad [1.20]$$

$$\vec{M}_{xy}(t) = \vec{M}_{xy}(0) \cdot e^{-t/T_2} \quad [1.21]$$

where $\vec{M}_z(0)$ is the magnitude of the longitudinal relaxation at time t = 0, T_1 is the spin-lattice (longitudinal) relaxation time constant, $\vec{M}_{xy}(0)$ is the magnitude of the transverse relaxation at time t = 0, and T_2 is the spin-spin (transverse) relaxation time constant (84).

In a biological sample, transverse magnetization decays more quickly than what is explained by the T_2 time constant after an excitation pulse which is due to time-independent local magnetic field variations within the sample being imaged. In this environment, spins will experience a slightly different magnetic field depending on their location and have a range of Larmor frequencies. This range of Larmor frequencies causes dephasing of the transverse magnetization and addition loss of magnetization. This dephasing from local magnetic field inhomogeneities is described as the decay constant T_2'.

$$\vec{M}_{xy}(t) = \vec{M}_{xy}(0) \cdot e^{-t/T_2^*} \quad [1.22]$$

where the apparent transverse relaxation is described as:

$$\frac{1}{T_2^*} = \frac{1}{T_2} + \frac{1}{T_2'} \quad [1.23]$$

To summarize, following an RF pulse excitation, magnetization begins to regrow in the longitudinal direction and dephase in the transverse direction.

1.4.4 Signal Detection and Localization

As mentioned in Section 1.4.2, the MR signal is detected based on Faraday's Law. The observed signal immediately following an RF excitation pulse is called the free induction decay (FID) signal (84). The FID signal can be manipulated to generate an echo, which can be generated in two different ways: a spin echo generated by a refocusing pulse, usually with a 180° flip angle; or a gradient echo, which is generated by a gradient reversal.

The spin echo is generated by using two successive RF pulses, usually with flip angle of 90° and 180°, respectively (83). The first RF pulse will tip the net magnetization into the transverse plane and generate the FID. The spins then begin to dephase due to T_2 and T_2' mechanisms, and after a short delay period where some transverse magnetization has dephased, the second RF pulse is applied, and the spins are flipped in the transverse plane. In the equivalent short delay period following the flip, all dephased spins rephased, producing a spin echo at a time defined as the echo time (TE). A gradient echo is generated using the magnetic field gradients of the MRI scanner. After applying the RF pulse and generating the FID, a negative gradient lobe creates a calibrated spatially dependent dephasing of the spins, causing accelerated dephasing of the transverse magnetization and attenuation of the FID signal. This is followed by a positive gradient lobe, which is equal in area to the negative lobe, to rephase the spins and generate the gradient echo (88).

While the FID signal or echo generates a signal in the RF coil, it alone is insufficient to produce an image. Localization of the generated signals is needed through the use of external magnetic field gradients (i.e., magnetic field with spatially varying strength). Gradient amplitudes are deliberately varied in a linear way along a particular axis (x, y, and z), which makes the spins precess at different frequencies (i.e., slower or faster than the Larmor frequency). In this way, their precession frequency encodes their position along the gradient axis (83,85). The following equation describes the frequency of the spins as a function of gradient strength:

$$\vec{\omega}(r) = \vec{\omega}_0 + \gamma \vec{G}_r(r) \cdot r \qquad [1.24]$$

where $\vec{G}_r$ is amplitude of the external magnetic field gradient along direction r and r is the location of the spin as described by x, y, or z. In MRI, gradients are used to spatially encode the transverse magnetization. To localize the signal and to create an image,

gradients are used for three purposes: slice selection, frequency encoding, and phase encoding.

Slice selection is the excitation of a specific slab to isolate the signals (83). The slice selection gradient, which can be applied along any direction, causes the spins to precess at different frequencies along its axis. The slice is selected by simultaneously applying the magnetic gradient and an RF excitation pulse, which has a bandwidth equal to BW_{RF}. The bandwidth of the RF pulse represents a range of frequencies centered at the RF pulse frequency (ω_{RF}) that are excited by the pulse. In short, only the spins matching the frequency of the RF pulse bandwidth are excited and only the spins within the selected slice will produce transverse magnetization (83). Other spins outside the selected slice will remain aligned with B_0. For example, a slice of thickness Δz in a slice on the xy plane can be selected using an RF pulse with BW_{RF} and a magnetic gradient in the z direction:

$$\Delta z = \frac{BW_{RF}}{\frac{\gamma}{2\pi}\vec{G}_z} \qquad [1.25]$$

After the slice has been selected the transverse magnetization must be spatially encoded using phase and frequency encoding gradients, which are orthogonal G_x and G_y gradients. Specifically, the y-direction of k-space k_y is defined as the phase direction while the x-direction of k-space k_x is defined as the frequency direction.

$$\vec{k}_x(t) = \frac{\gamma}{2\pi}\int_0^t \vec{G}_x(x,\tau)d\tau \qquad [1.26]$$

$$\vec{k}_y(t) = \frac{\gamma}{2\pi}\int_0^t \vec{G}_y(y,\tau)d\tau \quad [1.27]$$

These spatially dependent integrals of the gradients represent points in the k-space domain. When the phase-encoding gradient G_y is applied, this causes the spins to precess at different frequencies based on position y. During the time the gradient is on, the phase of the spins is altered as a function of their position (83). Prior to the acquisition of the signal, the phase-encoding gradient is turned off, causing the spins to precess at their initial frequency (i.e., Larmor frequency) but the y-dependent phase accumulated shift remains. Therefore, the spins are now "phase-encoded" (83). The frequency-encoding gradient G_x is then applied, causing the spins to precess at different frequencies based on their position in x. These gradients are applied throughout signal acquisition, and like phase-encoding, G_x spatially encodes the x position of the spins through an x-dependent phase accumulation. Transverse magnetization is altered after the application of the phase-encoding and frequency encoding gradients:

$$\vec{M}_{xy}(t) = \vec{M}_{xy}(0) \cdot e^{-1/T_2^*} \cdot e^{-i2\pi(\vec{k}_x(t)x + \vec{k}_y(t)y)} \quad [1.28]$$

where $2\pi(\vec{k}_x(t)x + \vec{k}_y(t)y)$ is the total phase accrued through the application of the phase-encoding and frequency encoding gradients.

The signal that we acquire can be decomposed into individual parts each representing a unique spatial frequency by Fourier theory. Fourier transforms of the signal can separate the individual frequency and spatial contributions, where the frequency and phase contribute to different spatial positions as described previously. This

information is stored in k-space, which is a raw Fourier space where each data point represents a unique spatial frequency and amplitude represents the relative contribution of that spatial frequency to the resultant image. Outer rows of k-space contribute to image resolution and correspond to high-order phase-encodings and high spatial frequencies; inner rows provide information on image contrast and correspond to low-order phase-encodings and low spatial frequencies (89,90). An MR image is a 2D inverse Fourier transform of the whole k-space.

1.5 Functional MRI

Functional MRI (fMRI) is an MRI technique used to measure brain activity by detecting changes in the MRI signal caused by alterations in local blood flow and oxygenation. Blood oxygen level-dependent (BOLD) contrast is used to detect changes in local blood oxygenation and from the coupling between cerebral blood flow and neuronal activation.

1.5.1 Neurovascular Coupling

Neurovascular coupling denotes the intricate interplay between metabolism, cerebral blood flow, and neural activity. More specifically, there is an increase in blood flow when tissues are active. This heightened blood flow response is a consequence of elevated neuronal activity, involving a complex signaling mechanism cascade involving neurons, astrocytes, and energy metabolism (91). Under typical resting conditions, the brain's primary energy source is adenosine triphosphate (ATP), primarily generated by glycolysis (anaerobic – 2 molecules) and oxidative glucose metabolism (aerobic – 36 molecules) (91). Cerebral metabolism predominately relies on the aerobic process; cerebral blood flow can supply the required continuous supply of glucose and oxygen. When neural activation occurs, the cerebral metabolic rate of glucose increases, prompting an increase in cerebral blood flow. This causes an overcompensation of the amount of oxygen supplied, as shown in Figure 1.8. This is the basis of the BOLD signal.

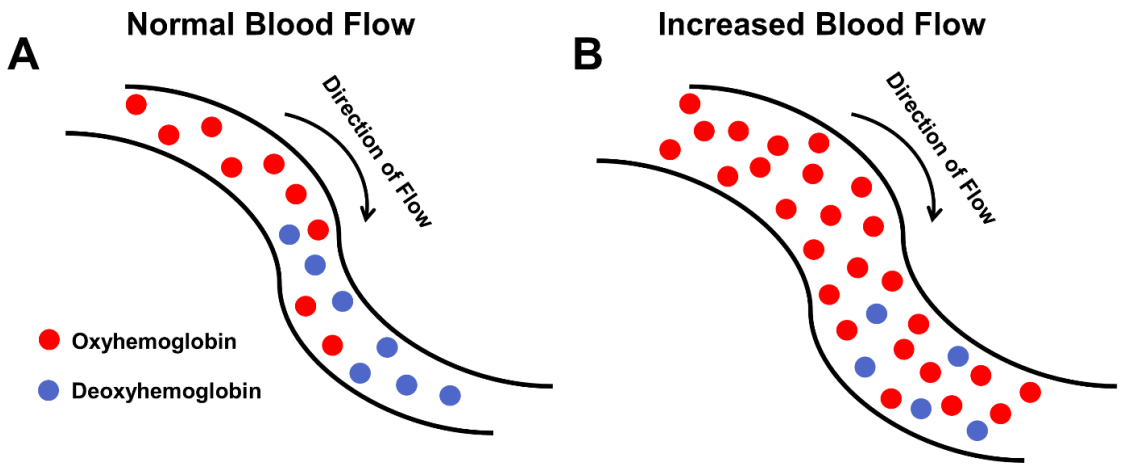

Figure 1.8: A. Blood flow during rest; oxygen is extracted from the hemoglobin at a constant rate. **B.** Blood flow during neural activity; glucose and oxygen consumption triggers an increase in blood flow and the dilation of the capillary, overcompensating for the oxygen being extracted. The BOLD contrast occurs due to changes in the relative concentration of deoxyhemoglobin.

Several signaling pathways organize the communication of increased blood flow requirements to nearby blood vessels. Initially, a feedback mechanism is triggered by various ions and metabolic by-products, including nitric oxide (NO), potassium (K^+), adenosine, carbon dioxide, low levels of oxygen, and arachidonic acid (92,93). The energy demand directly influences alterations in blood flow through this mechanism (92,93). Activation or inhibition of the vascular smooth muscle cells modulates blood flow through the direct or indirect change in vessel diameter. A secondary pathway involves a feedforward mechanism, where signaling occurs via neurotransmitters. Astrocytes release vasoactive messengers that influence blood flow through either vasoconstriction or vasodilation of the vascular smooth muscle cells (94). Astrocytes are glial cells that act as the communication connection between the vascular and neuronal systems. This pathway relies on glial pathways rather than energy consumption. Lastly, the third mechanism involves the direct neuronal innervation of smooth muscle cells on

the blood vessels themselves. It is likely that these mechanisms work together to mediate neurovascular coupling (92,93).

1.5.2 Hemoglobin

Hemoglobin, a protein that is iron rich, plays a crucial role in oxygen transportation throughout the bloodstream. Hemoglobin has magnetic properties contingent on its oxygen binding status (95). Oxygen-bound hemoglobin (Hb) is diamagnetic. However, naturally, hemoglobin is paramagnetic due to the lack of bound oxygen molecules, making it deoxygenation hemoglobin (dHb). This can be exploited using MRI. When a magnetic field is present, blood vessels containing Hb show minimal or no distortions to the magnetic field. In contrast, the presence of dHb in capillaries or veins causes magnetic field distortions, leading to T_2* based signal loss (96,97). As blood flow increases in response to neural activity, the relative amount of dHb decreases, resulting in an increase in T_2* relaxation rate and an elevated MRI signal intensity relative to the normal resting state (96,97). This phenomenon by which dHb modulates the MRI signal intensity is called the blood oxygen level-dependent (BOLD) effect.

1.5.3 Blood oxygen level-dependent (BOLD) contrast

It was recognized that Hb and dHb yield different MRI signal intensities by Ogawa and colleagues, making them suitable to measure brain physiology (98). Specifically, Ogawa *et al.* manipulated blood oxygen levels in rats by adjusting the inhaled amounts of oxygen and carbon monoxide (98). When the rats inhaled normal air, areas with signal loss corresponded to blood vessels containing dHb. Increasing the amount of dHb caused blood vessels to be more prominent in T_2*-weighted images. This signal change was attributed to the dephasing of tissue water signal induced by the paramagnetic deoxyhemoglobin (98). In comparison to Hb, the presence of dHB reduced the MR signal on T_2* images and could be used non-invasively to monitor the blood oxygen levels in the brain.

1.5.4 Hemodynamic Response

The utilization of the BOLD contrast to observe alterations in cerebral metabolic rate of oxygen, cerebral blood flow, and cerebral blood volume relies on the exploitation of the hemodynamic response (HDR). The HDR refers to the signal changes in T_2* weighted images induced by neural activity (99). Given the predictable nature of the BOLD contrast response, fMRI sequence design and analysis can be used to manipulate it (91).

When neural activity increases in a specific brain region, there is a corresponding increase in blood flow to satisfy the elevated demands for oxygen and glucose (100). Studies have reported a delay in the onset of the HDR (approximately 2 seconds), which reflects the time required for blood to travel from the arteries to the capillaries (101). Following the onset of neural activity, there is a momentary decrease in the MRI signal, called the "initial dip"; this dip reflects the delay in the cerebral blood flow response relative to oxygen extraction, resulting in a higher proportion of dHb (i.e., decreased signal) (101,102). Subsequently, the increased blood flow and hemoglobin supply lead to an over-compensatory response (i.e., increase in signal) to meet the heightened metabolic demands of increased activity. This will reach a plateau after 6-12 seconds. When neural activity ceases, there is an excess of oxygen, causing the BOLD signal to decrease below the baseline in a phenomenon known as post-stimulus undershoot (102). This undershoot occurs as cerebral blood flow returns to baseline more rapidly than the blood volume. This is depicted in Figure 1.9.

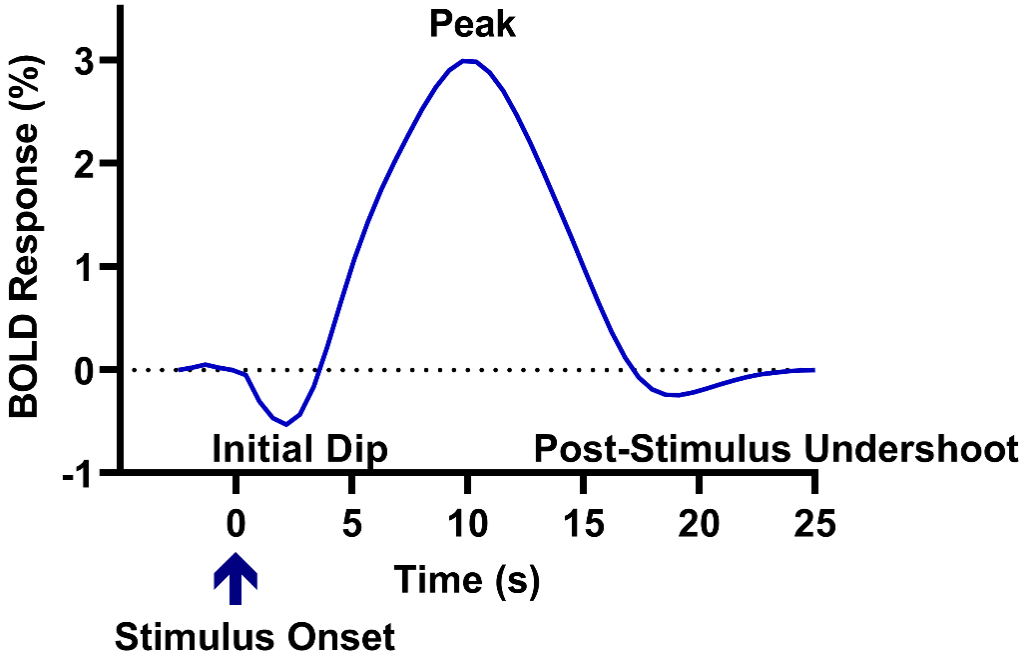

Figure 1.9: At the stimulus onset, an initial dip occurs, leading to a temporary increase in deoxyhemoglobin (dHb) concentration due to heightened oxygen consumption. In response to the elevated demand for glucose and oxygen, both cerebral blood flow and blood volume increases. This surplus of oxygen exceeds the actual consumption, resulting in a relative decrease in dHb and elevation in BOLD signal. Once the activity subsides, the BOLD signal decreases below baseline, a phenomenon referred to as post-stimulus undershoot. This occurs due to the blood flow decreasing more rapidly than cerebral blood volume.

1.5.5 fMRI Applications in DCM and Spinal Cord Injury

In clinical applications, functional MRI (fMRI) can be used to map cortical regions (like sensory and motor areas) when performing simple tasks, like tapping of the fingers. fMRI can also be used to identify differences between two populations or monitor the effects of a treatment or intervention of one clinical population. In response to brain or spinal cord injury, cortical reorganization has the potential to influence functional recovery or may

be a compensatory mechanism to minimize functional deficits (103-105). Many studies have demonstrated that DCM patients experience a cortical reorganization of the brain's motor areas. Holly *et al.* demonstrated that there was an expansion of neuronal activity in the affected motor area when performing either a wrist extension task or ankle dorsiflexion task compared to healthy controls (104). Duggal *et al.* illustrated that reversible spinal cord compression increases the primary motor cortex (M1) activation volume compared to controls (103). In this study, decompression surgery resulted in cortical reorganization in the primary motor cortex (M1) and a significant return of clinical function. Furthermore, Bhagavatula *et al.* showed that compared to healthy controls, DCM patients had larger M1 volumes of activation. After decompression surgery, the activation decreased but remained higher than in the control group (106). Previous work in our lab has shown differences in activation between mild and moderate DCM patients. Mild patients demonstrated an increase in the volume of activation of the M1 compared to moderate patients, while six months post decompression surgery, activation between the two patient groups was no longer significantly different (107).

Cortical reorganization is still not fully understood. The expansion of the activated motor areas when performing a hand task may be related to the rewiring of axons from the lower extremities to the hand regions (104). This can include modifying pre-existing connections and/or developing new circuity to preserve neurological function (108,109). This is primarily driven by using the less affected part to compensate for any difficulty with the instructed hand task. Spinal cord injury studies have previously shown this effect, with increased activation in a handgrip task in the medial precentral gyrus, which is consistent with leg representation (110). It has been proposed that cortical reorganization arises from the development of new lateral connections rather than the previously dormant connections (111). Henderson *et al.* studied complete thoracic spinal cord injury patients and controls and brushed their hands with a plastic brush. The SCI group demonstrated medial displacement of auricular finger activation toward the lower body representation, with patients of a longer time since injury demonstrating the greatest displacement of activation. In conjunction with the reorganization of the primary somatosensory cortex (S1), noticeable alterations in cortical anatomy were observed,

implying that substantial shifts in activation may be due to the growth of new connections (111).

1.6 Chemical Exchange Saturation Transfer

Chemical exchange saturation transfer (CEST) is a relatively new MRI contrast that exploits the selective saturation, or a state with no net magnetization, of a slowly exchanging group with a chemical shift distinct from water, leading to a transfer of the magnetization to the bulk water via chemical exchange (112,113). Chemical shift, or δ, is the Larmor frequency of the slowly exchanging group relative to the bulk water Larmor frequency. CEST was first introduced by Balaban and Ward, who described a new class of contrast agents that were sensitive to the surrounding environment (114). Typical exchanging groups of interest are endogenous protons like amide (NH), amine (NH_2), and hydroxyl (OH). One unique advantage of CEST contrast is the ability to switch the contrast on and off using an RF saturation pulse. Because chemical exchange can be sensitive to the environment, the CEST effect can be used to image physiological parameters, such as pH and metabolite levels.

1.6.1 CEST Mechanism

CEST contrast is generated by the saturation of a solute (S) proton pool that is 1) resonating at a different frequency from water and 2) in chemical exchange with bulk water (W) protons. The exchanging solute proton pool is saturated using frequency selective RF irradiation at the frequency of the solute, and the energy is transferred to bulk water via chemical exchange. The transfer of energy causes a decrease in the magnetization (and thus the signal) of the water (as shown in Figure 1.10). One powerful advantage of CEST is that the continuous transfer of energy between the solute and water pools amplifies the observable signal change. The solute is typically low in concentration (~μM to mM range) and not observable with standard MR detection methods.

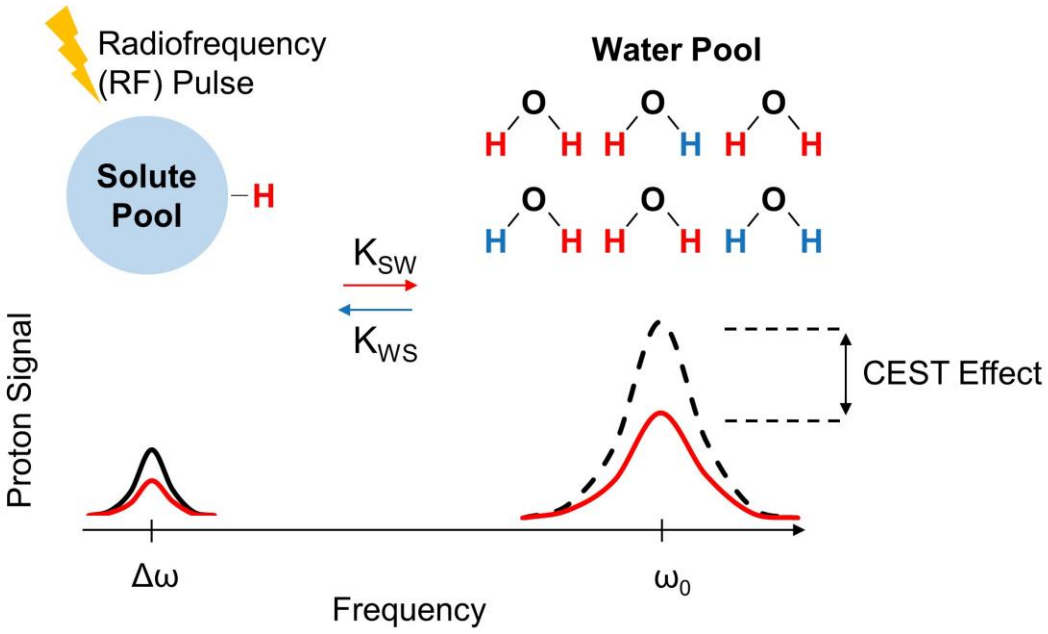

Figure 1.10: Schematic illustration of the basic chemical exchange saturation transfer (CEST) MRI principles. Solute protons (red) are saturated at their specific resonance frequency by a radiofrequency (RF) saturation pulse. This saturation is transferred to bulk water at exchange rate k_{SW} and non-saturated protons (blue) return. After a period of time, the CEST effect becomes visible on the water signal and is an indirect measure of the solute concentration and the rate of exchange.

As previously stated, the solute pool must be chemically shifted from the water pool. A chemical shift can be defined as the difference in the Larmor frequency of the two pools. As defined in Section 1.4.1, the Larmor frequency is the product of the nucleus-specific gyromagnetic ratio γ and the main magnetic field B_0. For protons, the gyromagnetic ratio is identical; however, the local magnetic field depends on the proton's chemical environment (i.e., the solute molecule the proton is associated with). The electron clouds enveloping the nucleus act as a shield against B_0, resulting in an effective main magnetic field (B_0'), causing the protons to have unique Larmor frequencies ($\vec{\omega}_s$):

$$\vec{\omega}_s = \gamma\vec{B}_0(1-\sigma_s) = \gamma\vec{B}_0' \quad [1.29]$$

where σ_s is the solute-dependent shielding coefficient. In applications of CEST, the Larmor frequency of bulk water protons is defined as the reference frequency ω_{ref}. The frequency offset of the solute protons, or chemical shift from bulk water protons, is defined in ppm as:

$$\delta = \frac{\omega_s - \omega_{ref}}{\omega_{ref}} \cdot 10^6 \quad [1.30]$$

To saturate the magnetization of the solute in a CEST experiment, RF pulses are used. The z-component of the proton magnetic moments (μ_z) tend to align parallel to the direction of the static external magnetic field (B_0). Protons that are parallel with B_0 (i.e., in the low energy state) are slightly more excessive than protons anti-parallel with B_0 (i.e., in the high energy state). When an RF excitation pulse with equal energy to the energy difference between the two protons energy states is applied, saturation can be achieved after some time. The RF pulse drives low-energy protons to the high-energy state until the population of each energy state is equal. The applied RF pulse frequency ω_{RF} must be equal to the Larmor frequency:

$$h\vec{\omega}_{RF} = \Delta\vec{E} = \gamma h\vec{B}_0 = h\vec{\omega}_0 \quad [1.31]$$

The RF pulse is used to saturate the magnetization of a pool of solute protons resonating at a Larmor frequency (ω_S) distinct from that of the bulk water protons. When

applying an RF pulse of amplitude B_1 and at the frequency offset of the solute proton pool (i.e., $\omega_{RF} = \omega_S$), net excitation occurs of protons in the lower energy state to the higher energy state. When the number of protons in the lower energy state equalizes with the higher energy state ($E_H=E_L$), the proton pool has reached a state of saturation.

For CEST, chemical exchange occurs either through the exchange of protons, molecular exchange, or a combination of both. A common example of proton exchange is when an exchangeable proton from the amide group (NH) moves to bulk water (H_2O). To observe the CEST effect, the chemical exchange must satisfy the slow-to-intermediate exchange condition:

$$\overrightarrow{\Delta\omega_s} \geq k_{sw} \qquad [1.32]$$

where k_{sw} is the chemical exchange rate from the solute to the bulk water pool and $\overrightarrow{\Delta\omega_s}$ in the frequency offset between the solute and bulk water protons. Both the chemical exchange rate k_{sw} and frequency offset $\overrightarrow{\Delta\omega_s}$ depend on temperature and pH.

To summarize, chemical exchange contrast can occur in an environment with a chemically shifted solute proton pool and bulk water proton pool. Applying a frequency selective RF saturation pulse can saturate the solute proton pool, creating the conditions for a transfer of high energy protons (aligned anti-parallel) from the saturated solute pool to the bulk water pool. The high-energy protons will accumulate in the bulk water pool, leading to partial magnetic saturation when there is a long saturation period. Therefore, saturation of the bulk water proton pool is limited by longitudinal relaxation. Simultaneous solute saturation and relaxation of the bulk water pool drives the system to a steady state (M_{SS}^W):

$$\frac{M_{SS}^{W}(\omega)}{M_{0}^{W}} = \frac{1}{(1 + kfT_{1w})} \quad [1.33]$$

where M_0^W is the bulk water magnetization without saturation, k is the solute proton exchange rate, and f is the mole fraction of solute protons (solute protons/water protons) (115). The CEST effect can be characterized by the partial saturation of the bulk water proton pool due to the saturation of the solute proton pool.

CEST effects are often quantified using the magnetization transfer ratio (MTR):

$$CEST(\omega) = 1 - \frac{M_{SS}^{W}(\omega)}{M_{0}^{W}} \quad [1.34]$$

This quantifies the CEST effect by calculating the reduced steady bulk water magnetization relative to the equilibrium magnetization. CEST is a sensitive measurement, especially compared to MRS, because of the accumulation of the bulk water saturation throughout long RF saturation periods, which amplifies bulk water signal reduction.

1.6.2 Z-Spectrum/CEST Spectrum

A Z-spectrum (or CEST spectrum) is a plot of the water signal intensity as a function of the saturation RF pulse offset frequency. For example, the signal intensity at one offset frequency will differ from the signal intensity measured at another. When acquiring an image following a saturation preparation pulse, a Z-spectrum can be obtained for each pixel in the image. More specifically, the normalized MRI signal intensity ($\frac{M_{SS}^{W}(\omega)}{M_{0}^{W}}$, Section 1.6.1, Equation 1.33) is plotted a function of the saturation pulse frequency offset relative to the bulk water resonance. The average Z-spectra is often plotted for a region-

of-interest (ROI) to depict the CEST effects occurring, as shown in Figure 1.11. A reduction in the MRI signal intensity ('CEST peak') can be observed in a CEST spectrum if appropriate experimental parameters are used and an exchangeable proton group is present.

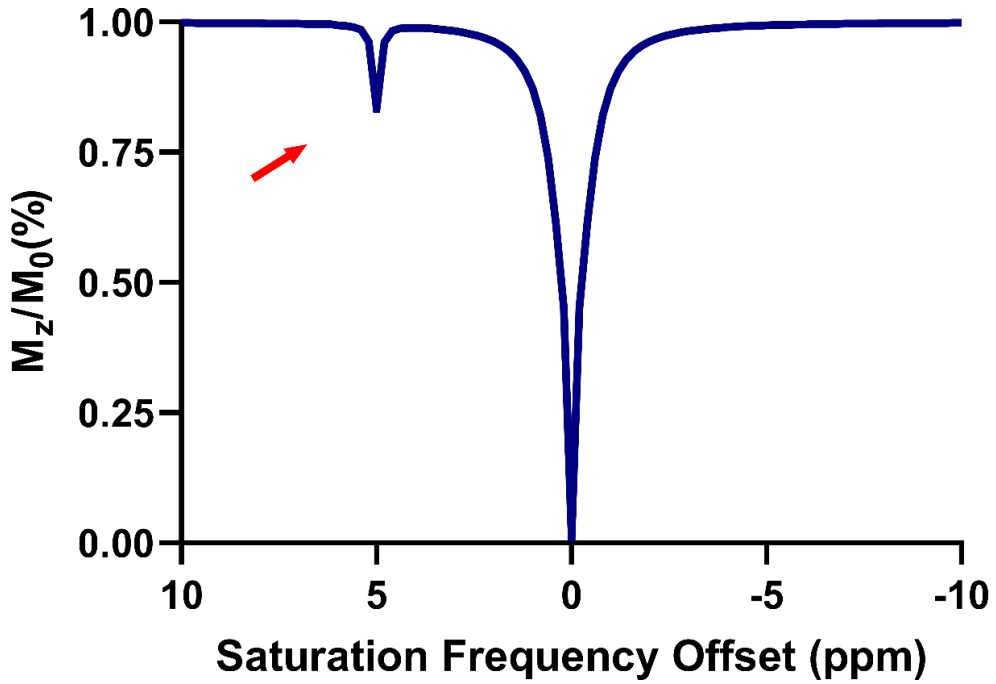

Figure 1.11: An example of a CEST spectrum. The CEST peak (or CEST effect) is observed at 5ppm, highlighted with the red arrow. The peak due to direct saturation of the bulk water protons by the RF saturation pulse is demonstrated at 0 ppm.

Using the CEST spectrum, several different CEST contrasts can be calculated. The simplest CEST contrasts read data points from the CEST spectrum, like asymmetry analysis. Other contrasts can be calculated using fitting approaches. Fitting based on the Bloch-McConnell equations can be used to quantify the metabolite concentration and exchange rate. Fitting raw data using a Lorentzian based approach can also be used to quantify metabolite concentration while minimizing the bulk water effect and

macromolecule saturation. The pools to fit in the model are chosen based on experimental parameters, like the magnetic field strength, RF pulse strength, and sampling of frequencies. An example of a Lorentzian fitted spectrum (6-pool model) is in Figure 1.12.

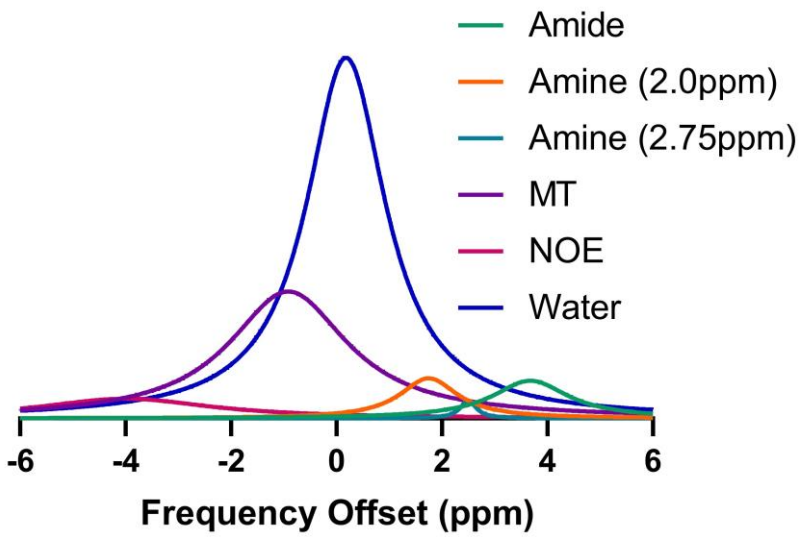

Figure 1.12 An example of one pixel's CEST spectrum fitted using a 6-pool model.

1.6.3 CEST Contrast

Endogenous CEST contrast depends on several parameters, including solute proton concentration and exchange rate, incorporating factors that also affect exchange rate like temperature and pH. The CEST effect also depends on magnetic field strength, bulk water relaxation time constants (T_1 and T_2), and experimental saturation parameters. Proton pools must have protons in a fairly high concentration to produce CEST contrast; however, continuous saturation allows for the detection of solutes in the range of µM to mM (116). Endogenous CEST contrast is also affected by the size of the molecule and the bulk water relaxation rate. There is a T_1 relaxation rate dependency on the CEST effect because signal reduction caused by saturation transfer is reduced by longitudinal

relaxation of the bulk water signal (117). Furthermore, T_2 relaxation affects the direct saturation of the bulk water signal (118).

CEST measurements also become more sensitive at higher field strengths. The amount of bulk magnetization increases proportionally to the field strength due to the Boltzmann distribution. T_1 also lengthens at higher field strengths, which causes an increase in the length of time that saturation persists in the bulk water proton pool before appreciable longitudinal relaxation occurs. This results in a lower steady-state water signal, which leads to greater detection sensitivity. Increasing the magnetic field strength also increases the chemical shift separation between proton pools (i.e., better adherence to the slow-exchange condition), making it easier to selectively saturate proton pools with different frequency offsets (117). Experimental saturation parameters, including B_1 saturation power, pulse type, pulse duration, interpulse delay, can also affect the measured CEST contrast (119).

1.6.4 Proton Exchange Rate and pH

The CEST proton exchange rate affects the magnitude of the CEST effect. The proton exchange rate k_{ex} is pH-sensitive for many exchangeable protons, including amide and amine groups. The pH-dependent exchange rate is described as follows:

$$k_{ex} = k_0 + k_a[H^+] + k_b[OH^-] = k_0 + k_a 10^{-pH} + k_b 10^{pH-pk_w} \quad [1.35]$$

where k_0 is the rate constant of spontaneous proton exchange between amide and water, k_a is the rate constant of the acid-catalyzed protonation of the amide, k_b is the rate constant of the base-catalyzed proton exchange between hydroxyl and the amide, and pK_w is the ionization constant of water (pK_w = 15.4 at 37°C). Proton exchange is predominately base-catalyzed for both amide and amine protons and the expression can be simplified to:

$$k_{ex} = k_b 10^{pH-pK_w} \quad [1.36]$$

CEST contrast is dependent on the proton exchange rate and is inherently sensitive to pH (115,120). The CEST effect, however, can also depend on other factors, including temperature, B_1 amplitude, solute proton concentration, and bulk water relaxation time constants (T_1 and T_2), as described in Section 1.6.3. Isolation of the pH contribution on the CEST effect has been challenging. It is tedious to accurately measure pH from CEST contrast accounting for other contributing factors. For example, increasing pH can cause the CEST contrast to increase; however, increased solute proton concentration can induce near identical increases in the CEST effect. Macromolecule MT effects can further complicate the isolation of pH effects contributing to the CEST contrast because the exact solute proton concentration is unknown in vivo. Different methods have been developed to measure pH with endogenous CEST.

1.6.5 Endogenous pH Measurements

Endogenous CEST uses protons that exist with endogenous solutes present in tissue, which can include proteins, peptides, or metabolites. Endogenous CEST is advantageous compared to CEST generated using exogenous contrast agents because it is non-invasive and ideal for longitudinal studies as there is no concern about contrast agent accumulation or clearance (113,121). The most common endogenous CEST contrast used to measure pH is that from amide protons resonating at 3.50 ppm (122), which are associated with mobile proteins and peptides. Zhou *et al.* first developed amide proton transfer (APT), which has been used to endogenously measure intracellular pH (122). However, there are several limitations to this method.

First, the asymmetric magnetization transfer ratio (MTR_{asym}) is used to subtract the macromolecule MT effect from the CEST effect. This is done by subtracting the

negative frequency offsets from the positive frequency offsets of the Z-spectrum, with bulk water referenced to 0 ppm (Equation 1.37).

$$MTR_{asym}(\Delta\omega) = \frac{M_Z(\Delta\omega) - M_Z(-\Delta\omega)}{M_Z(-\Delta\omega)} \quad [1.37]$$

$$MTR_{asym}(\Delta\omega) = MTR'_{asym}(\Delta\omega) + APTR \quad [1.38]$$

where $M_Z(\Delta\omega)$ is the bulk water magnetization after saturation at the frequency offset $\Delta\omega$ and $MTR'_{asym}(\Delta\omega)$ is inherently pH-insensitive, including the nuclear Overhauser enhancements (NOE) of aliphatic protons in mobile macromolecules and semi-solid magnetization transfer effect. The MTR_{asym} curve was defined as the combination of a pH-sensitive amide proton transfer ratio (APTR) (equation 1.39) and the inherent pH-insensitive curve (MTR'_{asym}).

$$APTR = \frac{k_{ex}[amide\ proton]}{R_{1W}[water\ proton]} \cdot [1 - e^{-R_{1w}t_{sat}}] \quad [1.39]$$

where R_{1W} is the spin lattice relaxation rate of water, and t_{sat} is the length of the saturation time. However, APTR is affected not just by pH but by amide proton concentration, longitudinal relaxation, and cellular water content. Secondly, this asymmetrical measurement may be contaminated by NOEs that occur between -2.0 and -4.0 ppm, which opposes the amide protons at 3.50 ppm. All these factors can make the pH measurements using APT susceptible to errors (122-124).

Another study has also shown that glutamate CEST (GluCEST) and creatine CEST (creCEST) are also sensitive to pH and have the potential to produce pH-weighted maps. Cai *et al.* demonstrated amine protons were sensitive to pH changes (125), while other groups have also demonstrated hydroxyl protons have a pH dependent exchange rate with water (126-128). A limitation of all these endogenous CEST contrasts is that the CEST effect is not just affected by pH but also by longitudinal relaxation.

1.6.6 Amine/Amide Concentration Independent Detection

Ward and Balaban developed a ratiometric *exogenous* CEST approach where the CEST effects at two distinct frequencies were used to quantify pH independent of bulk water T_1 and exchange site concentration (115). Previous work in our lab by McVicar *et al.* has focused on the development of a measure of absolute tissue pH using the *endogenous* CEST effects of both amide (3.50 ppm) and amine (2.75 ppm) protons within mobile peptides and proteins (129,130). Amine and amide protons have been shown to have different k_b, therefore, they have different responses to pH changes (131,132). As pH increases, amide (k_{amide} = 5.57 x $10^{pH-6.4}$) and amine (k_{amine} = $10^{pH-4.2}$) base-catalyzed exchange rates increase. Saturation of the amide proton pool causes $\frac{M_{SS}^{W}(\omega)}{M_0^W}$ (see section 1.6.1, equation 1.33) to reduce as pH increases, causing an increase in the amide CEST effect. However, the amine CEST effect appears to decrease as pH decreases, which defies the theoretical equations. This, however, occurs because the amine proton exchange rate increases into the fast-exchange regime ($k>\omega$) when pH increases above ~6.5.

The method proposed by Ward and Balaban used a ratiometric approach to measure pH using the CEST effects from two different exchange sites (i.e., site 1 and site 2) on the same CEST solute (115). This approach was proposed due to the difficulty of direct pH measurement using the CEST effect of a single solute proton pool due to the impact of saturation pulse amplitude and duration, T_1 relaxation, and solute concentration on the measured CEST effect. Using equation 1.33 (from Section 1.6.1) and knowing $f = [\text{solute protons}]/[\text{water protons}]$, Equation 1.40 is determined for either exchange site:

$$\frac{(M_0 - M_S)^{Site1,2}}{M_S^{Site1,2}} = k^{Site1,2} T_{1w} \left[\frac{solute\ protons}{water\ protons}\right]^{Site1,2} \quad [1.40]$$

The T_1 relaxation effects and solute concentration effects cancel, leaving only a ratio of the pH-dependent exchange rates when taking the ratio of Equation 1.40 for the two different exchange sites:

$$\frac{M_S^{Site2}(M_0 - M_S)^{Site1}}{M_S^{Site1}(M_0 - M_S)^{Site2}} = \frac{k^{Site1} T_{1w} \left[\frac{solute\ protons}{water\ protons}\right]^{Site1}}{k^{Site2} T_{1w} \left[\frac{solute\ protons}{water\ protons}\right]^{Site2}} \quad [1.41]$$

In the approach developed by McVicar *et al.*, amine protons resonating at 2.75 ppm and amide protons resonating at 3.50 ppm on endogenous proteins were considered as site 1 and site 2, respectively. A common reference saturation frequency of 6.0 ppm was used because there are no observed CEST effects or NOEs at this frequency. This approach avoided contamination from NOEs and minimized endogenous macromolecule MT-related signal loss. Any significant signal modulations at the reference frequency (i.e., from T_2 relaxation or MT) cancel in the ratiometric equation, thus justify the choice of a single reference point (129). Also, because the CEST effects of the amide and amine change in opposite directions with increasing pH, the ratio of the two is more sensitive to pH than using a single CEST effect. Figure 1.13 depicts how the CEST effects of amide and amine change at different pH values.

$$AACID = \frac{M_Z(3.50\ ppm) \times (M_Z(6.0\ ppm) \times M_Z(2.75\ ppm))}{M_Z(2.75\ ppm) \times (M_Z(6.0\ ppm) \times M_Z(3.50\ ppm))} \quad [1.42]$$

In vitro studies using solutions of varying pH with different concentrations of bovine serum albumin (BSA) demonstrated that AACID was linearly dependent on pH, while AACID had little dependence on solute concentration and temperature (129). Animal models of both ischemic stroke and brain tumor also demonstrated that AACID was sensitive to changes in pH (129,130).

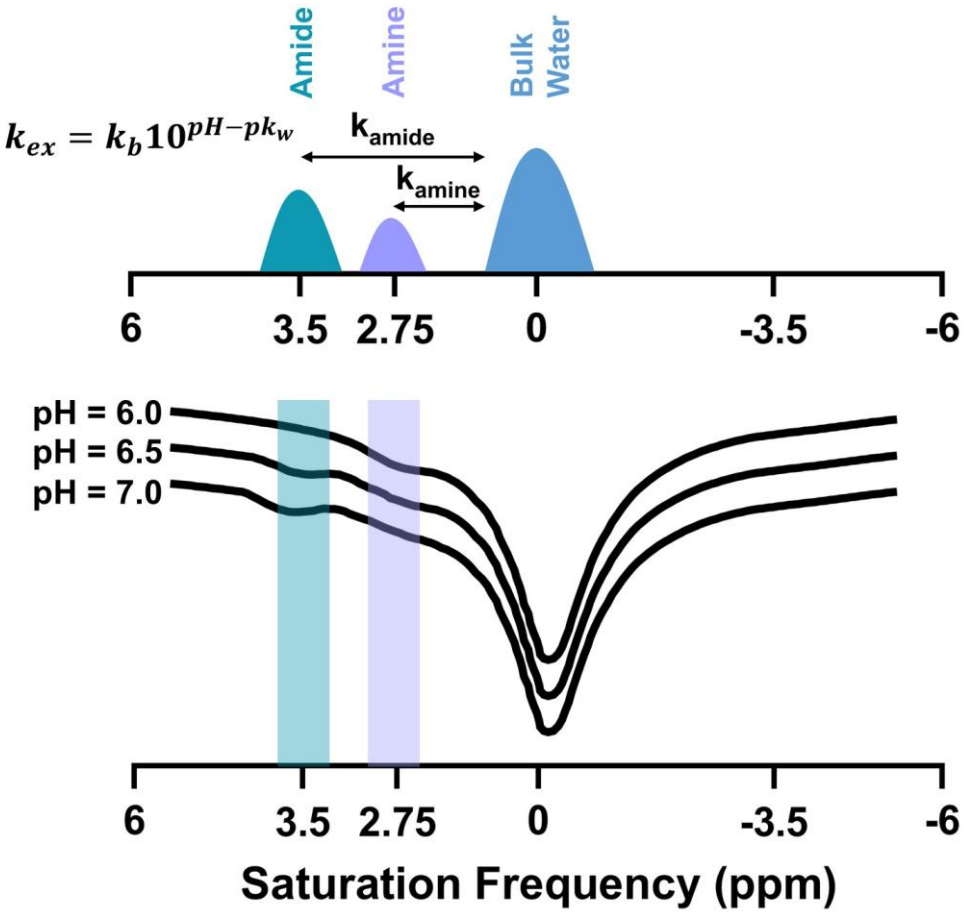

Figure 1.13: Schematic diagram demonstrating the effect of pH on the amine and amide CEST effects. The top schematic demonstrates both the amide and amine proton pools that are chemically shifted from the bulk water pool. The bottom schematic demonstrates CEST spectra measured at different pH (6.0, 6.5, and 7.0), showing the amide and amine pH dependent changes highlighted in blue and purple, respectively. This figure has been adapted with permission from McVicar *et al.* (129).

1.6.7 Nuclear Overhauser Enhancement

Non-exchangeable protons can transfer magnetization to nearby dipolar-coupled protons via cross-relaxation, which is known as the nuclear Overhauser effect (NOE). Examples of non-exchangeable protons are protons from carbon-bound aliphatic and aromatic

groups. Cross-relaxation can transfer energy due to dipolar interactions between spins that are in close proximity. Dipole-dipole interactions occur when two protons/spins are in close proximity and can be influenced by each other's magnetic field. When two protons (interesting spin (I) and source spin (S)) are in close proximity, the thermal motion of proton S causes a local oscillating magnetic field that can induce the relaxation of the proton I.

To recall in Section 1.4.1, spins have two energy levels, m = +1/2 and m = -1/2, which are associated with the lower (spin-up) and higher (spin-down) energy levels, respectively. When a spin pool is fully saturated, there are an equal number of spins in the spin-up and spin-down energy states, causing a population difference of zero. There are several pathways in which this energy can be transferred, including single spin flips (single quantum transitions) or mutual spin flips. Mutual spin flips are the pathways corresponding to the NOE. This can include double quantum transitions, which involves a pair of spin-up nuclei flipping to spin-down, or vice-versa, and zero quantum transitions, which involves the flipping of a pair of opposite spins. These energy exchanges are shown in Figure 1.14. The probability of any of these transitions occurring depends on the gyromagnetic ratios, rotational correlation time of the spins, and the energy of the dipolar interaction (84).

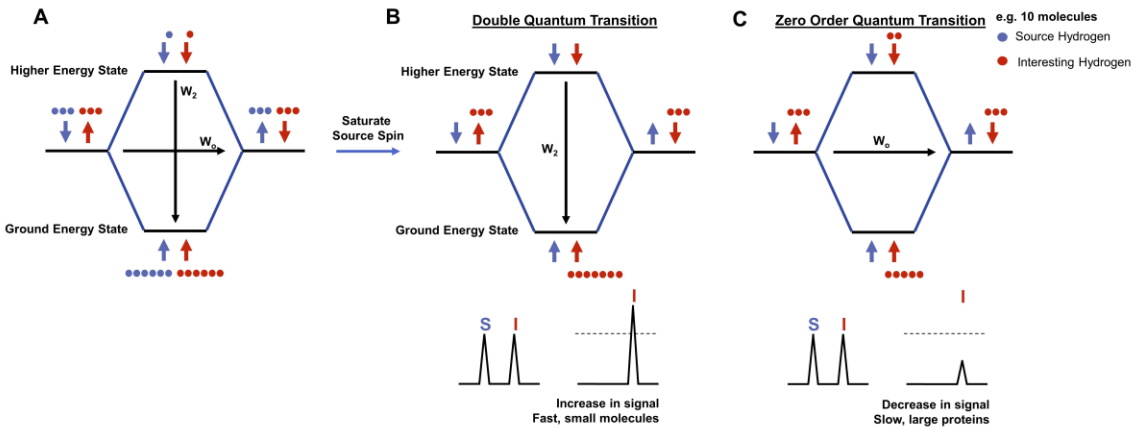

Figure 1.14: Schematic diagram illustrating the different mutual spin flips that are the pathways corresponding to the NOE. **A.** Energy level diagram for a dipolar coupled two spin system, I spin population difference of 5. **B.** A double quantum transition involves a pair of spin-up nuclei flipping to spin-down, or vice-versa, and causes an increase in the signal of the proton of interest. When spin S relaxes back to equilibrium, the coupled spin I flips from higher energy to the ground state, increasing the population difference (i.e., difference of 7). **C.** Zero order quantum transitions involve the flipping of a pair of opposite spins and causes a decrease in the signal of the proton of interest. When spin S relaxes back to equilibrium, the coupled spin I flips from low energy to the ground state, decreasing the population difference (i.e., difference of 3).

Proton-proton NOE cannot attain a very considerable signal enhancement. Enhancement resulting from the NOE can be achieved through a relayed transfer process to other, exchangeable protons. The saturation of the non-exchangeable proton pool is continuous, and the effect can be relayed and incorporated into the larger, coupled exchangeable proton pool. This effect is called exchange relayed NOE (rNOE) (133). rNOE can be simplified as a two-step process, where saturation of the non-exchangeable protons is transferred via dipole-dipole interactions (cross-relaxation) to a neighbouring exchangeable proton, and then transferred to water via chemical exchange (as shown in Figure 1.15):

$$H_a \underset{\sigma_{en}}{\overset{\sigma_{ne}}{\rightleftharpoons}} H_e \underset{k_{we}}{\overset{k_{ew}}{\rightleftharpoons}} H_W \qquad [1.43]$$

where H_a, H_e are the non-exchangeable aliphatic proton and neighbouring exchangeable proton, respectively.

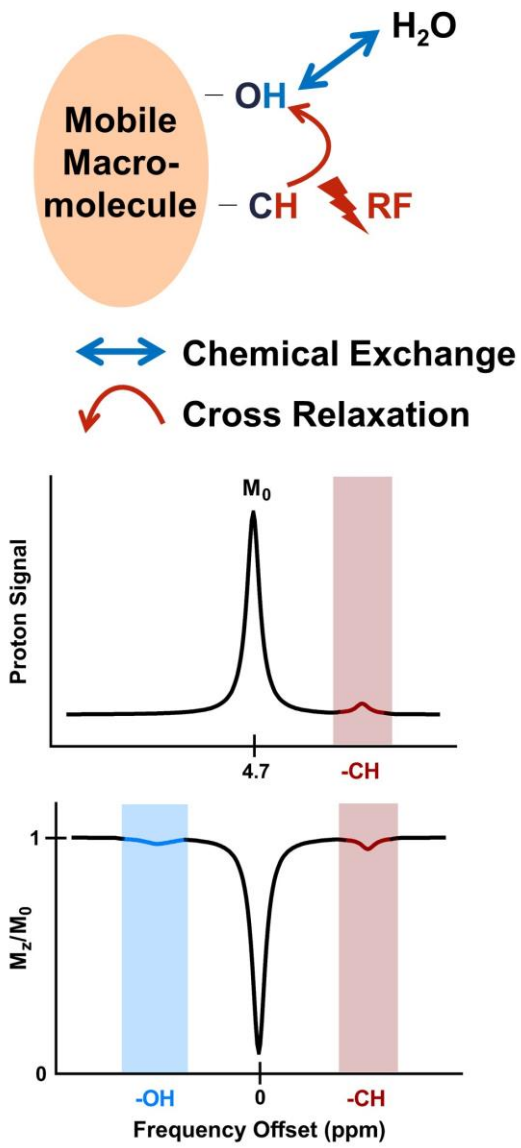

Figure 1.15: Schematic illustrating the irradiation if a nonexchangeable proton pool with a radiofrequency (RF) pulse, which causes the bulk water pool signal to decrease through relayed nuclear Overhauser effect (rNOE). This figure has been recreated and adapted with permission from Zhou *et al.* (134)

The rNOE signal depends on both the cross-relaxation rate and the chemical exchange rate. However, if there is a large rate difference, the rNOE signal will depend

on the signal rate-limiting step (i.e., the slowest) (134). When the cross-relaxation is the rate limiting step, the following relationship holds:

$$k_{ew} \gg |\sigma_{ea}| \approx \rho_e \qquad [1.44]$$

where σ_{ea} is the dipolar cross-relaxation rate and ρ_e is the longitudinal relaxation rate of the exchangeable proton. When cross-relaxation is the rate-limiting step in rNOE processes, the mobility of molecules is necessary to understand how the signal appears in the Z-spectra. For small molecules, cross-relaxation is dominated by the double-quantum transition and σ_{ea} is positive. Cross-relaxation is small for these molecules, so the rNOE signal is negligible on the Z-spectra. For large molecules or those that have limited mobility (i.e., semisolid), the zero-quantum transition dominates, and cross-relaxation is negative and can be very large. It is important to note, that in semisolid components, the T_2 relaxation times are extremely short, causing a broad signal and the magnetization transfer contrast (MTC) can begin to show in the Z-spectra, merging with any rNOE signal (134).

Like the CEST effect, rNOE signal can depend on several different factors. The signal can increase with the concentration of the molecules or the density of the non-exchangeable protons and neighbouring exchangeable protons. In a more complex macromolecular structure, only the exchangeable protons that are in close proximity affect the signal (134). pH could also affect the rNOE signal measured; however, studies have shown different results. Some studies have shown that rNOE does have a dependence on pH (133,135,136), but others have failed to demonstrate this relationship (124,135,137). Cross-relaxation is not directly affected by pH, any pH dependence on the rNOE signal is due to the proton chemical exchange, which has been shown to be pH dependent (see Section 1.6.4). Therefore, it can be speculated that the rNOE signal could be pH sensitive when the chemical exchange rate is the rate-limiting step in the rNOE process (120). Temperature can also affect the rNOE signal observed. Increasing

temperature will reduce cross-relaxation rates (molecular thermal motion is faster at higher temperatures) and water longitudinal relaxation rates (138), however, it will increase proton exchange rates. Thus, when cross-relaxation is the rate-limiting step, rNOE signal can be insensitive to temperature changes because cross-relaxation and longitudinal relaxation change in opposite directions on the same scale of magnitude (139). When chemical exchange is the rate-limiting step, temperature can affect rNOE signal in the same way that it affects the CEST signal (see Section 1.6.3).

1.6.8 Spinal Cord MR Imaging Challenges

Unfortunately, non-invasive investigation of spinal cord function and structure is limited by the inaccessibility of the cord. MRI is a non-invasive approach to assess the function and structure of the spinal cord. However, there are some inherent challenges when trying to perform MRI in the spinal cord: a spatially inhomogeneous magnetic field when in an MRI system, the small diameter of the cord cross-section (widest cervical enlargement only ~1.5 cm (140)), and physiological motion.

Differences in the magnetic susceptibility between soft tissue, bone, and air can result in image distortion and signal intensity loss. Unfortunately, the spinal cord is very small and comprised of all three components. Shimming the magnetic field (i.e., making the field more uniform) can be employed within the spinal cord to increase uniformity. The small dimension of the spinal cord also requires high in-plane spatial resolution (typically 1 mm x 1 mm) and relatively thin slices (1-2 mm) to accurately depict the anatomical features. Axial imaging allows for the highest resolution to be in the spinal cord cross section, where spinal cord anatomy is more varied (see Section 1.2.6). However, a large number of slices must be acquired to view the full inferior to superior extent of the cord, which significantly increases the scan time. The pulsation of the CSF flow can also cause artefacts in spinal cord images. Respiratory motion can also cause periodic motion in the spinal cord. Artefacts caused by motion can be distributed in the phase-encoding direction. Consequently, choosing the phase-encoding direction so artefacts do not spread across the spinal cord can improve image quality. Periodic motion can be reduced by harmonizing the acquisition with cardiac and respiratory cycles, (i.e., gating is performed). However, this causes a dramatic increase in acquisition time.

1.6.9 CEST in the Spinal Cord

Very few studies of CEST MRI have been performed in the cervical spinal cord of humans. The first study was performed by Dula *et al.* in the cervical spinal cord at 7.0 T (141). Using simulated optimal CEST saturation parameters, CEST imaging of the spinal cord was performed in 10 healthy controls and 10 patients with multiple sclerosis (MS) using both asymmetry analysis (MTR_{asymm}) and a Lorentzian fitting method. It was found that there was increased asymmetry around the amide proton resonance in MS patients, but the measurement was complicated by NOE signal upfield in the Z-spectra. Lorentzian differences for lesions and normal-appearing white matter were also distinct from healthy white matter. Following this study, By *et al.* performed APT CEST in the cervical spinal cord of 10 healthy controls and 10 MS patients at 3.0 T (142). This study found that incorporating a respiratory correction created more reproducible Z-spectra in white matter. Normal-appearing white matter of the MS patients was also significantly different than the healthy controls.

As mentioned in Section 1.6.8, there are many challenges in spinal cord MR imaging, and these exist also for CEST in the spinal cord. As the study performed by By *et al.* demonstrated, incorporating a respiratory correction could improve the reproducibility of the measurements in the spinal cord (142). It has been shown that field shifts caused by respiration can distort the B_0 field and cause temporal signal fluctuations, up to 0.58 ppm at the seventh cervical vertebra (C7) level (143). Advanced shimming is important when trying to mitigate field inhomogeneities in spinal cord CEST to ensure spectrally accurate RF irradiation to generate the CEST contrast. B_1 inhomogeneity can also be prevalent in the spinal cord, which can directly affect CEST contrast and the B_1 saturation pulse amplitude. It should also be noted that while in spinal cord imaging, it is recommended to have relatively thin slice thickness to accurately depict the structures of the spinal cord, CEST imaging in the spinal cord improves with thicker slices to maximize the signal-to-noise ratio (SNR) and contrast-to-noise (CNR). However, a thick slice can lead to partial volume effects and limited spatial resolution for CEST spinal cord imaging.

1.6.10 CEST Reproducibility

Reproducibility in MRI is of upmost importance to ensure valid quantitative measurements, quality assurance of protocols, and to assist with transition to clinical practice. Quantification of reproducibility (i.e., producing the same results when repeated by a different team), variability (i.e., divergence of data from its center of distribution), and repeatability (i.e., producing the same results when repeated in the same circumstances) are essential for CEST research. More specifically, CEST contrast depends on the saturation parameters and exchange rate (see Section 1.6.3). Reproducible CEST measurements are needed in healthy tissue to begin to transition this technique to clinical populations. In the context of DCM patient outcomes, evaluating the reproducibility of CEST contrasts can help determine if non-invasive biomarkers of the recovery of pH and hypoxia can be established. CEST reproducibility studies have begun to emerge in brain research (144-147). 3D APT CEST was found to have high reproducibility in the supratentorial locations of the brain compared to the infratentorial locations in 19 healthy volunteers, 15 glioma patients, and 12 acute stroke patients (145). APT CEST reproducibility was found to be high in 21 healthy volunteers and 6 glioma patients for whole-brain, within-session, and between-day evaluations (147). Another study found good single-slice APT reproducibility in brain tumours between sessions in 13 patients (146). Unsurprisingly because of the lack of CEST studies performed in the spinal cord, the only study examining CEST reproducibility in the spinal cord was performed by By *et al.* at a single cervical slice centred at the C3/C4 level (142).

1.7 Thesis Overview

DCM is a highly prevalent spinal cord disease and can cause motor and sensory function disruptions. While decompression surgery is the recommended treatment for DCM, some patients still have neurological decline post-operatively. Identifying biomarkers for surgical and functional success is of the utmost importance.

The main objective of this thesis was the development of pH-weighted MRI measurements of the cervical spinal cord in DCM patients using CEST MRI. Very few studies have implemented CEST MRI in the human spinal cord, and no studies have

attempted to measure pH using CEST in the spinal cord. Initially, fMRI was used to determine if cortical reorganization of the motor areas in the brain were correlated with compression severity in DCM patients. Following the completion of this work, CEST MRI was optimized for pH-weighted contrast, and reproducibility was evaluated in the more stable brain structure. 3D pH-weighted CEST was then implemented in the cervical spinal cord of healthy subjects, and reproducibility was evaluated, leading to the use of pH-weighted CEST MRI in DCM patients.

Chapter 1 of this thesis provides a literature review of degenerative cervical myelopathy and how ischemia and hypoxia could affect the surgical outcomes of these patients. Furthermore, an introduction to CEST MRI and how it can be exploited to measure hypoxia indirectly through pH-weighted measurements is discussed.

Chapter 2 of this thesis presents work adapted from an original research manuscript titled “Spinal cord compression is associated with brain plasticity in degenerative cervical myelopathy”. The objective of this study was to determine if compression severity, used as a proxy for hypoxia, was correlated with increased activation of the motor areas in DCM patients while they performed a controlled tapping task during fMRI. The study showed that when the spinal cord was more severely compressed, larger regions of the primary motor cortex were activated, suggesting that cortical reorganization had occurred. This expansion of cortical activity may be due to brain plasticity and the rewiring of axons from the lower limb extremities into the hand region to compensate for difficulty with the instructed finger-tapping task.

Chapter 3 of this thesis presents work from an original research manuscript entitled “Reproducibility of 3D Chemical Exchange Saturation Transfer (CEST) Contrasts in the Healthy Brain at 3T”. This study evaluated the reproducibility of different 3D CEST contrasts, including AACID, in the brain. 3D CEST was successfully optimized and implemented at 3.0 T, and within-subject and between-subject reproducibility was evaluated in both gray and white matter. Results demonstrated that AACID and NOE contrasts were the most reproducible in both tissue types.

Chapter 4 of this thesis presents work from an original research manuscript entitled "Reproducibility of 3D pH-Weighted Chemical Exchange Saturation Transfer Contrast in the Healthy Cervical Spinal Cord". This study continues the work presented in Chapter 3, and successfully implemented 3D AACID CEST in the healthy cervical spinal cord. The objective of this study was to evaluate the reproducibility of AACID along the cervical spinal cord and determine which post-processing scheme produced the most reproducible measurement. This study showed that 3D AACID was the most reproducible measurement at the centre of the volume when also applying a B_1-correction.

Chapter 5 of this thesis presents work from an original research manuscript titled "Spinal Cord pH-weighted CEST MRI Suggests Hypoxia in Degenerative Cervical Myelopathy Patients". This study continues from work within Chapter 4, now utilizing 3D AACID CEST MRI in the spinal cord of DCM patients and controls, while incorporating a B_1-correction. The objective of this pilot study was to determine whether AACID measurements at the site of compression in the spine were significantly different compared to healthy controls. Preliminary results indicate that DCM patients have significantly higher AACID values in the compressed spinal cord, which is associated with a lower pH and indicative of hypoxia occurring in the spinal cord at the compression site of these patients.

Chapter 6 of this thesis summarizes the work presented in the thesis, followed by the potential future work related to this thesis.

Chapter 2

2 Spinal Cord Compression is Associated with Brain Plasticity in Degenerative Cervical Myelopathy

The work presented in this chapter is from:

Alicia E Cronin, Sarah A Detombe, Camille A Duggal, Neil Duggal, Robert Bartha, Spinal cord compression is associated with brain plasticity in degenerative cervical myelopathy. Brain Communications, Volume 3, Issue 3, 2021, fcab131, https://doi.org/10.1093/braincomms/fcab131

Permission to reuse this article has been obtained. Please see Appendix B.

2.1 Introduction

Cortical reorganization, in response to brain or spinal cord injury, may influence functional recovery and provide a compensatory mechanism to minimize functional deficits (104). Many functional magnetic resonance imaging (fMRI) studies have demonstrated that there is increased cortical activity in patients with spinal cord injuries in response to hand movement tasks (103,104,106,148,149). Studies in patients with spinal cord injuries have also found increased levels of activation in subcortical areas compared to controls (148,150,151). However, it is unclear if the plasticity occurring in these patients is associated with the severity of spinal cord compression and if severity of spinal cord compression influences functional recovery.

Degenerative cervical myelopathy (DCM) is one of the most common forms of spinal cord dysfunction, with the yearly incidence and prevalence in North America estimated to be 41 and 605 per million, respectively (152). It is a unique model of spinal cord injury that becomes increasingly prevalent with age (153), can result in compression of the spinal cord (7), and can lead to neurological dysfunction (154). Surgical intervention, in the form of decompression surgery, is universally accepted as a preferred treatment option (155) in patients with moderate to severe DCM (156,157). In many patients, surgical intervention can effectively prevent progression of neurological decline

and improve functional outcome (157,158). In fact, approximately two thirds of patients demonstrate some neurological recovery (e.g. upper limb function, lower limb function, and sphincter recovery) post-surgery (158). Unfortunately, select patients do not improve following surgery and some can continue to deteriorate. Identifying patients that do not respond to surgical intervention is a major unmet clinical need.

Predicting functional recovery and surgical outcome based on patient demographic factors such as age (159,160), level(s) of compression (161), or duration of symptoms (162) has proven unreliable. Magnetic resonance imaging (MRI) parameters in the spine, such as hyper-intensity on T_2-weighted images (29) and hypo-intensity on T_1-weighted images (28) have proven equally unreliable in predicting response to surgery and functional recovery. Interestingly, some studies have demonstrated that plasticity can occur in the brain when tissue damage occurs within the ascending and descending spinal cord fiber tracts (105,148). This finding suggests that the severity of spinal cord compression could be a useful prognostic indicator. To improve the prognostic determinates of DCM, the relationship between localized compression in the spinal cord, neuronal damage, cortical reorganization, and functional performance before and after surgery must be better understood.

Most fMRI studies in DCM have made group level comparisons between DCM patients and healthy controls, which treats DCM patients as a homogenous group (103,104,106,149,163). The aim of the current study was to determine if cortical activity differences in individual DCM patients, measured by fMRI, were associated with the severity of spinal compression. Understanding the relationship between spinal compression and brain plasticity may help to develop an objective prognostic indicator of surgical response. The overall goal of the current study was to determine if brain activity variations in individual DCM patients, measured by fMRI, were associated with the severity of spinal cord compression and neurological dysfunction, measured by validated clinical outcomes scores. We hypothesized that cortical and subcortical reorganization would be greater in patients with more severe spinal cord compression, and that patients with severe compression would have more impaired neurological function despite increased fMRI measured cortical activity.

2.2 Materials and Methods

2.2.1 Participants and Clinical Evaluation

This study was approved by the Western University Health Sciences Research Ethics Board. Informed consent was obtained from each patient prior to the start of the study. Twenty-five patients (14 men, mean age (± SD) 63 ± 13.1 years, 24 right-handed) with symptoms of DCM and no other neurological disorders were recruited from November 2018 to February 2020 and participated in a 3.0 T MRI session before decompression surgery. All patients completed the validated measure for assessing disability resulting from myelopathy, called the modified Japanese Orthopaedic Association (mJOA) outcome measure (164). This metric measures the severity of clinical symptoms in patients with myelopathy by assessing motor dysfunction in the upper and lower extremities, bladder function, and sensory function in the upper extremities. Patients were graded on an 18 point scale, where upper motor function was scored out of 5, lower motor function was scored out of 7, upper sensory function was scored out of 3, and bladder function was scored out of 3 (164). To be included in this study, DCM patients must have demonstrated some degree of hand dysfunction (4/5 or lower on upper mJOA score). Coincidently, all DCM patients also had varying degrees of gait dysfunction.

2.2.2 Imaging Protocol

Imaging was performed in DCM patients prior to their decompression surgery on a Siemens 3.0 T Prisma Fit MRI scanner using a 64-channel head and neck coil to acquire all data. Anatomical head images were acquired for each patient using a sagittal T1-weighted 3D magnetization-prepared rapid acquisition gradient echo sequence (9˚ flip angle, matrix size 256 x 256, number of slices = 175, 1 mm slice thickness, and repetition time/echo time 2300/2.98 ms). Blood oxygen level-dependent (BOLD) images were acquired using an interleaved echo planar imaging pulse sequence (720 x 720 acquisition matrix, 52 slices per volume, slice thickness 2.3 mm, repetition time/echo time 1000/30 ms, 40˚ flip angle). The total acquisition time of the BOLD scan was 5 minutes and 30 seconds for 330 volumes. Field maps were acquired to correct for signal distortions (slice thickness 3 mm, repetition time/echo time 500/4.92 ms, 60˚ flip angle). Finally,

anatomical neck and spine images were also acquired for each patient using a T_2-weighted sagittal 3D spin-echo sequence (slice thickness 0.9 mm, repetition time/echo time 2170/135 ms, flip angle 140˚, number of averages = 2).

2.2.3 Study Design

To activate the motor pathway, a block paradigm task, which included 11 segments (six resting and five active), was performed. All patients were instructed to perform a fingers-to-thumb pinch (duck quack) with their right hand in a button box. To control the frequency that patients were performing the task, visual cues were presented every 3 seconds during the 30 second task period. Compliance was ensured by the recording of the button presses using an in-house program created using MATLAB v.R2019b and Psychtoolbox v.3.0.15. This protocol was also repeated for the left hand.

2.2.4 Imaging Processing

Anatomical and functional images were preprocessed using the fMRI pipeline fmriprep version 1.4.1 (165). Specifically, the anatomical T_1-weighted head images were corrected for intensity non-uniformity using N4BiasFieldCorrection v2.1.0 (166) and skull-stripped using antsBrainExtraction.sh v2.1.0. Spatial normalization was performed through nonlinear registration with the antsRegistration tool of ANTS v2.1.0 (167). The cerebrospinal fluid (CSF), white-matter (WM), and gray-matter (GM) were all segmented on the brain extracted image to assist with registration. The functional images were corrected for motion using mcflirt (FMRIB Software Library (FSL) v5.0.9) (168), slice timing corrections were applied using 3dTshift from AFNI v16.2.07 (169), and field distortion corrections (170) were performed. Co-registration to the corresponding T_1-weighted image using boundary-based registration (BBR) (171) with 9 degrees of freedom was executed. The anatomical and functional data were all converted and reported in MNI space. For further details of the fmriprep pipeline, please refer to the online documentation: https://fmriprep.readthedocs.io/en/1.4.1/.

To find brain activity related to our proposed block design, a general linear model of the whole brain was run separately for each of the patients. The data were spatially smoothed by convolving each slice with a 6 mm full-width-half maximum Gaussian

kernel in FSL v6.03 (172). We modeled the predictors of each patient by convolving the block paradigm boxcar function with a double-gamma hemodynamic response function and included the nuisance regressors to form the complete statistical model. The nuisance regressors were the motion related parameters, consisting of three regressors for each translation direction and rotation direction. Cluster-based thresholding was performed ($Z > 3.1$, $p = 0.001$), where the p value was corrected for multiple comparisons (173).

The cervical spinal cord was automatically segmented using the Spinal Cord Toolbox (SCT) v4.2.2 (174), specifically using the Deepseg module (175). This module is a deep-learning-based spinal cord segmentation module that uses two Convolutional Neural Networks (CNNs), where the first detects the spinal cord centerline and the second performs the segmentation (175). Quality of the segmentation was manually checked on every axial slice using the FSL viewer, FSLeyes. An example of the segmented cord is demonstrated in Fig. 2.1A. Using SCT, the cross-sectional area was found for each axial slice of the spinal cord. Using custom MATLAB code, the total volume of the spinal cord in the compressed region was measured by identifying the limits of the compressed region using the rate of change of cord area, then summing the areas of each slice within the compressed region, as shown in Fig. 2.1B. To measure the reliability of the spinal cord volume measurement, two raters performed repeated measurements of cord compression using the approach described above. The first rater developed the metric (A.E.C.) and therefore had significant previous experience using the tool and the second rater had no previous experience in performing imaging measurements (C.D.). Each performed the measurement three separate times on the full dataset. For each measurement, raters were blinded, and the data were scrambled. The intraclass correlation (ICC) was computed to determine the intra and inter-reliability.

2.2.5 Statistical Analysis

Brain regions of interest (ROIs) were selected based on previous studies using the same task block design and the demonstration of activation in these areas (106,163). The ROIs included were the cortical structures (primary motor cortex (M1), the primary somatosensory cortex (S1), the supplementary motor area (SMA), the premotor cortex (PMC)) and the subcortical structures (cerebellum, putamen, caudate, and thalamus). The

contralateral region of each of the cortical ROIs and bilateral subcortical ROIs were chosen for each of the scans (right and left hand). Cortical ROIs were obtained from the probabilistic Harvard-Oxford cortical structural atlas and subcortical ROIs from the MNI Structural Atlas. The extent of activation in these regions was quantified using beta weights, which represent how much BOLD signal is associated to the task (% BOLD signal), and the volume of activation (VOA).

Pearson's correlation coefficient (r) was used to test the hypothesis that the severity of spinal compression was correlated with neuronal activation characterized using % BOLD signal and VOA, and that the severity of spinal compression was correlated functionally using mJOA scores. Pearson's correlation coefficient (r) was also used to determine whether the duration of symptoms (Table 2.1) was correlated with neuronal activation (% BOLD signal and VOA).

2.3 Results

The measurement of spinal cord volume was found to be highly reproducible. Specifically, the reliability of the spinal cord volume measurements between the two raters were characterized with an ICC of 0.977. Similarly, the intra-rater reliability of each rater was also substantial, with the first rater (A.E.C.) achieving an ICC of 0.996 and the second, less experienced, rater (C.D.) achieving an ICC of 0.967. Fig. 2.1C provides the individual measurements for each subject to show the small variation observed.

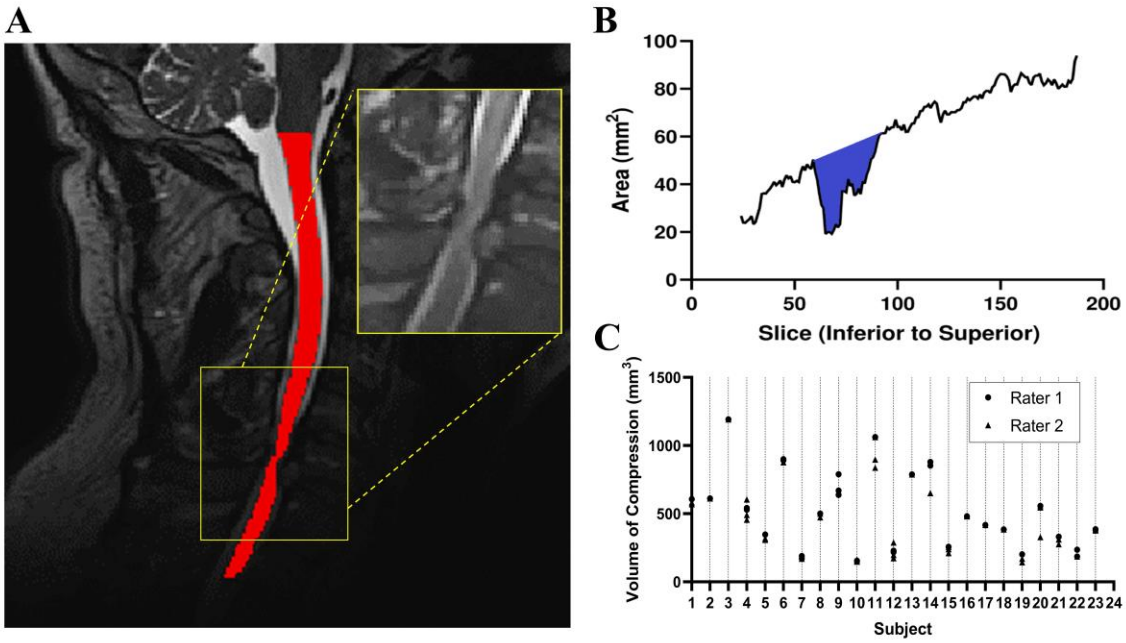

Figure 2.1: Volume of compression measurement. **A:** T_2-weighted image of the cervical spinal cord of a DCM patient showing the segmented cord in red, with the compression site displayed on the inset. **B:** Line graph displaying the area of each axial slice of the segmented cord, from inferior to superior, with the coloured region the total compression volume measurement. **C:** Dot plot of rater agreement, with an ICC of 0.977 for inter-rater reliability, first rater achieving an intra-rater reliability ICC of 0.996, and the second rater achieving an intra-rater reliability ICC of 0.967.

Two DCM patients were excluded from the study due to missing T_2-weighted spine images and differing fMRI parameters. Demographics of this cohort of included patients are provided in Table 2.1. Supplementary Fig. 2.1 highlights the differences in cortical activation patterns in individual participants with varying degrees of spinal cord compression. When DCM patients tapped with their left hand, motor network and subcortical activation was correlated with spinal cord compression volume. Specifically, in the contralateral M1, the % BOLD signal was significantly correlated with the total compression volume ($r = 0.49$, $p = 0.02$; Fig. 2.2A) and VOA was also significantly correlated with total compression volume ($r = 0.55$, $p = 0.006$; Fig. 2.3A). In the

contralateral S1, the % BOLD signal was significantly correlated with the total compression volume ($r = 0.49$, $p = 0.02$; Fig. 2.2B) and VOA was also significantly correlated with total compression volume ($r = 0.45$, $p = 0.03$; Fig. 2.3B). In the associated motor areas (SMA and PMC), the total compression volume was only significantly correlated with the PMC VOA ($r = 0.42$, $p = 0.04$; Fig. 2.3C). Regarding subcortical brain areas, there was a significant correlation between spinal compression volume and % BOLD signal in the cerebellum ($r = 0.56$, $p = 0.006$; Supplementary Fig. 2.2A), the putamen ($r = 0.57$, $p = 0.005$; Supplementary Fig. 2.2B), the caudate ($r = 0.67$, $p = 0.0004$; Supplementary Fig. 2.2C), and the thalamus ($r = 0.60$, $p = 0.003$; Supplementary Fig. 2.2D). There was also a significant correlation between spinal compression volume and VOA in the cerebellum ($r = 0.56$, $p = 0.006$; Supplementary Fig. 2.3A), the putamen ($r = 0.58$, $p = 0.004$; Supplementary Fig. 2.3B), the caudate ($r = 0.70$, $p = 0.0002$; Supplementary Fig. 2.3C), and the thalamus ($r = 0.63$, $p = 0.001$; Supplementary Fig. 2.3D).

Table 2.1: Demographic data and clinical characteristics of patients with DCM

Case	Age (mean 65 ± 13 years)	Sex	Site of Impairment[a]	Duration of Symptoms (months)	mJOA Score (mean 9.9 ± 2.1)				
					Upper Motor	Lower Motor	Upper Sensory	Bladder	Total Score (max 18)
1	70	M	C3-4	7	2	2	1	1	6
2	51	M	C6-7	4	3	4	1	1	9
3	68	M	C5-6	15	3	4	1	3	11
4	57	F	C5-6	30	2	4	1	1	8
5	81	M	C5-6	12	2	4	1	3	10
6	77	M	C4-5	4	3	4	1	2	10
7	74	M	C4-5	24	4	6	1	3	14
8	60	M	C5-6	36	4	4	1	3	12
9	52	F	C3-4	12	1	6	0	1	8
10	82	F	C3-4	12	4	6	2	3	15

11	52	M	C5-6	4	4	3	1	2	10
12	70	M	C3-4	22	3	4	1	2	10
13	72	M	C3-4	24	2	4	1	2	9
14	77	M	C3-4	5	2	3	1	2	8
15	51	F	C4-5	11	4	4	1	2	11
16	34	F	C4-5	16	3	5	1	2	11
17	84	M	C3-4	7	2	3	1	2	8
18	79	F	C4-5	6	2	3	1	2	8
19	45	M	C3-4	5	3	4	1	2	10
20	72	F	C3-4	24	2	3	1	3	9
21	67	F	C4-5	3	2	4	1	2	9
22	56	F	C3-4	7	4	4	2	3	13
23	73	M	C3-4	3	3	3	1	2	9

[a] Location of compression where surgery was performed, mJOA = modified Japanese Orthopaedic Association

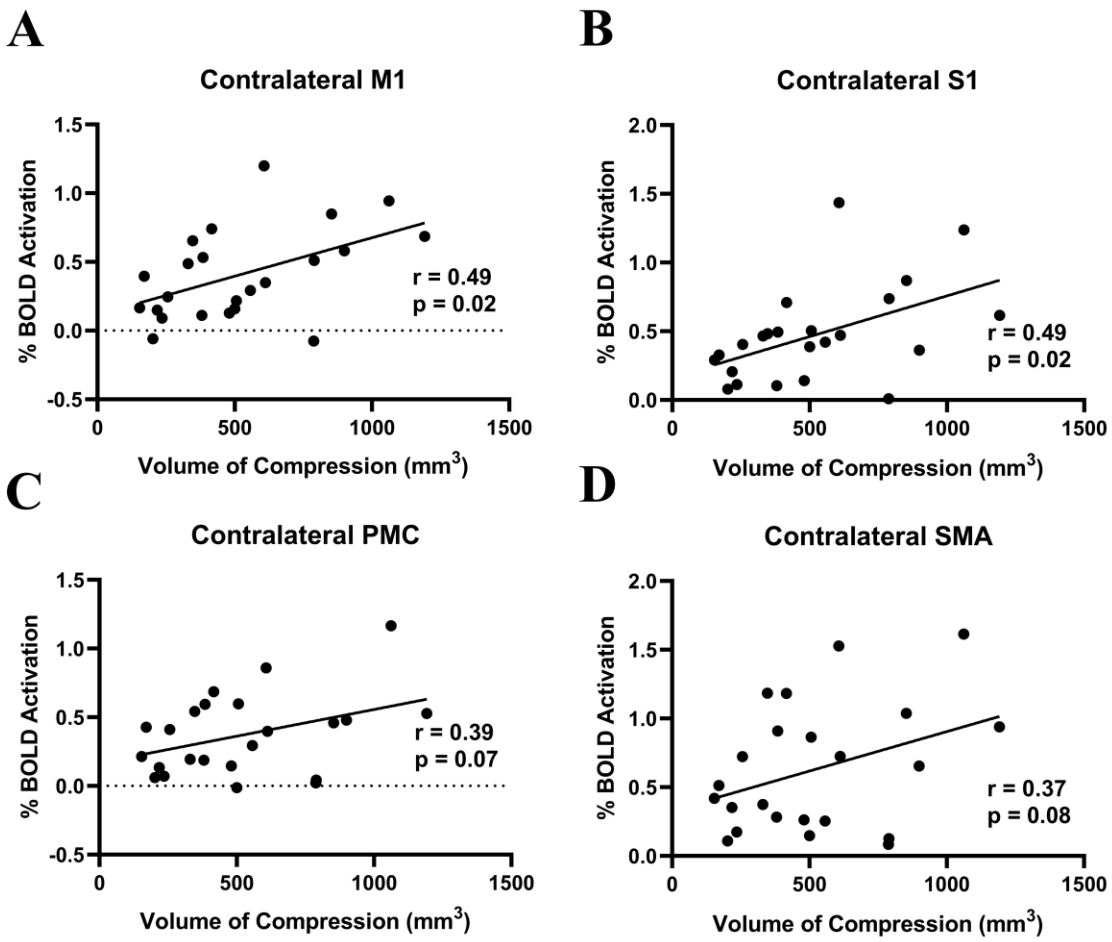

Figure 2.2: Left hand tapping BOLD signal and volume of compression. **A:** The correlation between the % BOLD signal of the contralateral M1 and the spinal cord compression volume. **B:** The correlation between the % BOLD signal of the contralateral S1 and the spinal cord compression volume. **C:** The correlation between the % BOLD signal of the contralateral PMC and the spinal cord compression volume. **D:** The correlation between the % BOLD signal of the contralateral SMA and the spinal cord compression volume.

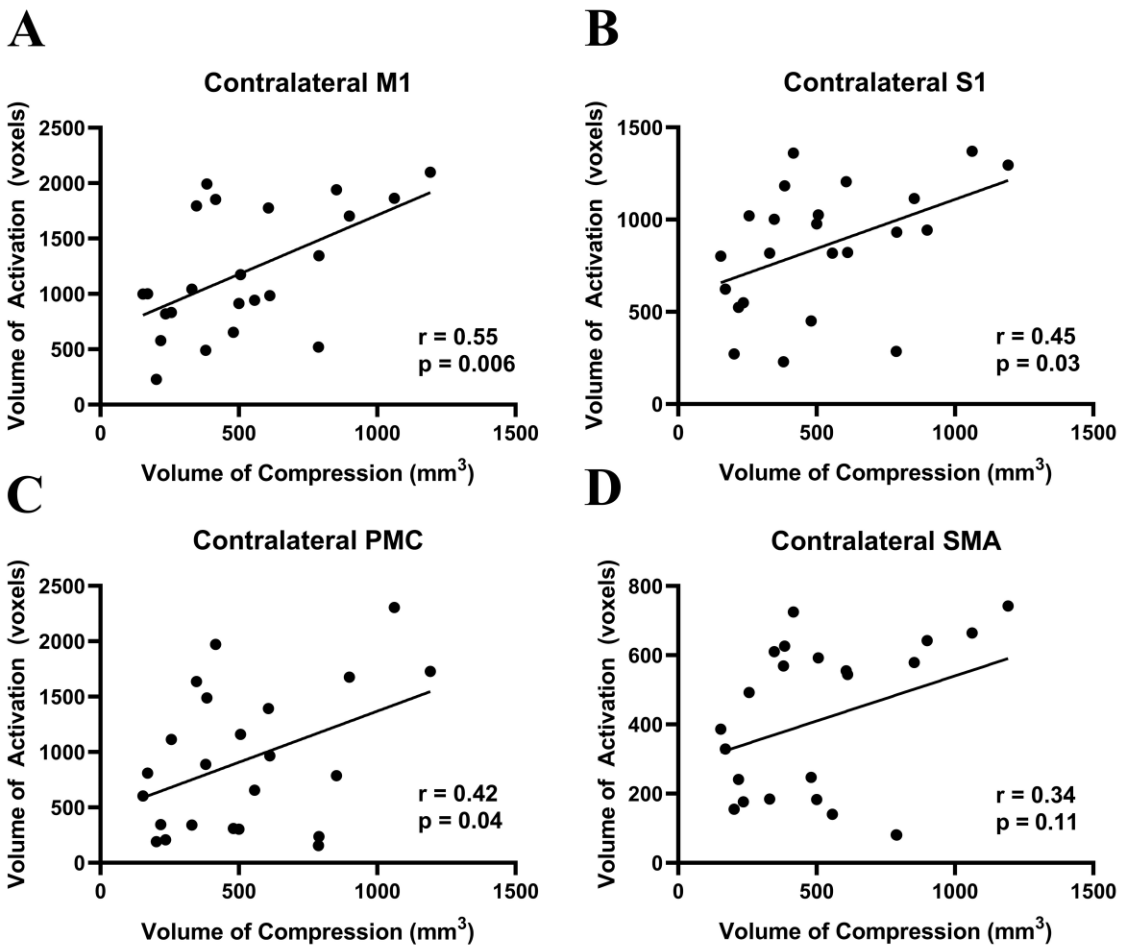

Figure 2.3: Left hand tapping volume of activation and volume of compression. **A:** The correlation between the VOA of the contralateral M1 and the spinal cord compression volume. **B:** The correlation between the VOA of the contralateral S1 and the spinal cord compression volume. **C:** The correlation between the VOA of the contralateral PMC and the spinal cord compression volume. **D:** The correlation between the VOA of the contralateral SMA and the spinal cord compression volume.

Similarly, when patients tapped with their right hand, cortical and subcortical activation was correlated with spinal cord compression volume. Specifically, in the contralateral M1 of the patients, a larger % BOLD signal was associated with a larger spine compression ($r = 0.56$, $p = 0.005$; Fig. 2.4A) and a larger VOA was also associated with a larger compression ($r = 0.45$, $p = 0.03$; Fig. 2.5A). In the contralateral S1, the % BOLD signal was significantly correlated with the total compression volume ($r = 0.53$, $p = 0.009$; Fig. 2.4B) and the VOA was close to significance with the total compression volume ($r = 0.41$, $p = 0.05$; Fig. 2.5B). In the contralateral PMC, the VOA was also significantly correlated with the total compression severity ($r = 0.50$, $p = 0.01$; Fig. 2.5C). Likewise, in the contralateral SMA, it was demonstrated that patients with a larger % BOLD signal also had a larger spine compression ($r = 0.46$, $p = 0.03$; Fig. 2.4D) and a larger VOA was also associated with a larger compression ($r = 0.47$, $p = 0.02$; Fig. 2.5D). Regarding the subcortical areas, a larger spinal cord compression volume was associated a higher % BOLD signal in the cerebellum ($r = 0.50$, $p = 0.02$; Supplementary Fig. 2.4A), the putamen ($r = 0.70$, $p = 0.0002$; Supplementary Fig. 2.4B), the caudate ($r = 0.65$, $p = 0.0007$; Supplementary Fig. 2.4C), and the thalamus ($r = 0.52$, $p = 0.01$; Supplementary Fig. 2.4D). Finally, total spinal cord compression volume was also significantly correlated with VOA in the cerebellum ($r = 0.53$, $p = 0.01$; Supplementary Fig. 2.5A), the putamen ($r = 0.71$, $p = 0.0001$; Supplementary Fig. 2.5B), the caudate ($r = 0.73$, $p = 0.0001$; Supplementary Fig. 2.5C), and the thalamus ($r = 0.59$, $p = 0.003$; Supplementary Fig. 2.5D).

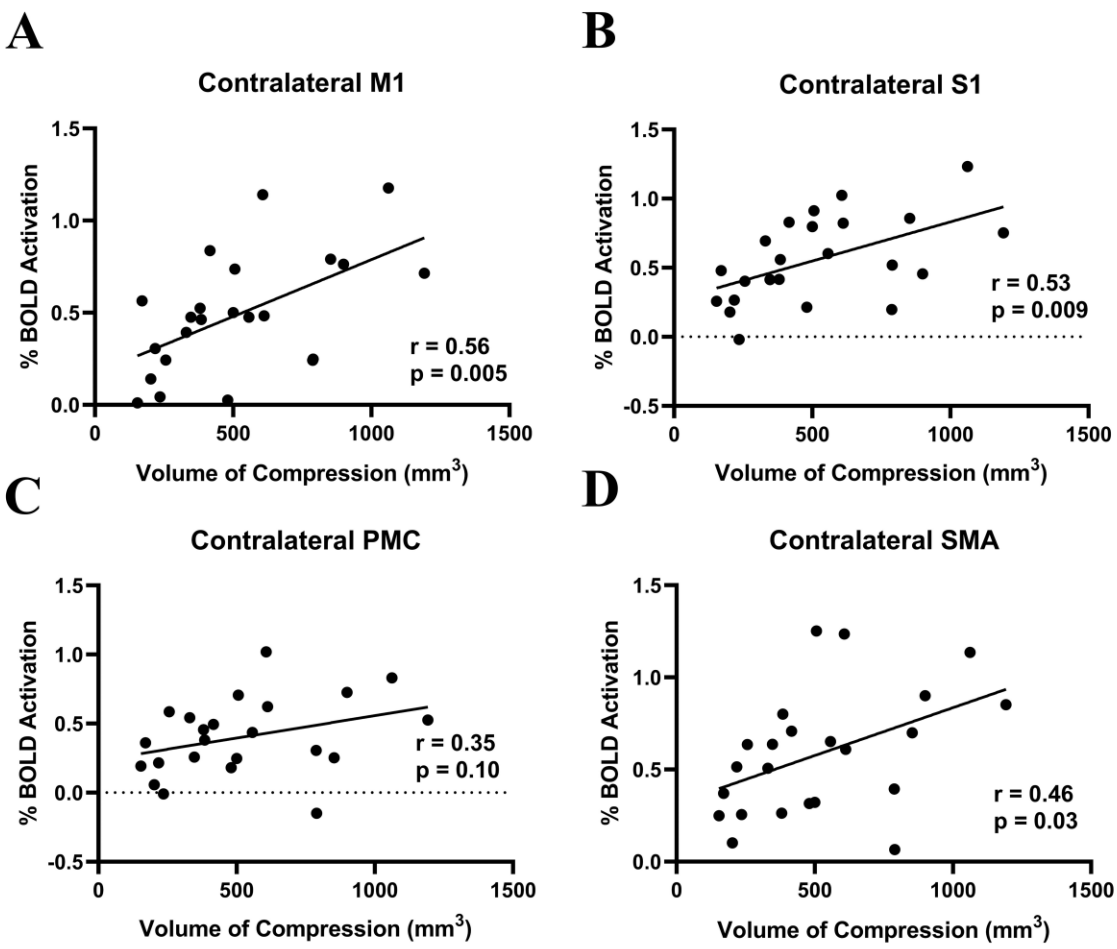

Figure 2.4: Right hand tapping BOLD signal and volume of compression. **A:** The correlation between the % BOLD signal of the contralateral M1 and the spinal cord compression volume. **B:** The correlation between the % BOLD signal of the contralateral S1 and the spinal cord compression volume. **C:** The correlation between the % BOLD signal of the contralateral PMC and the spinal cord compression volume. **D:** The correlation between the % BOLD signal of the contralateral SMA and the spinal cord compression volume.

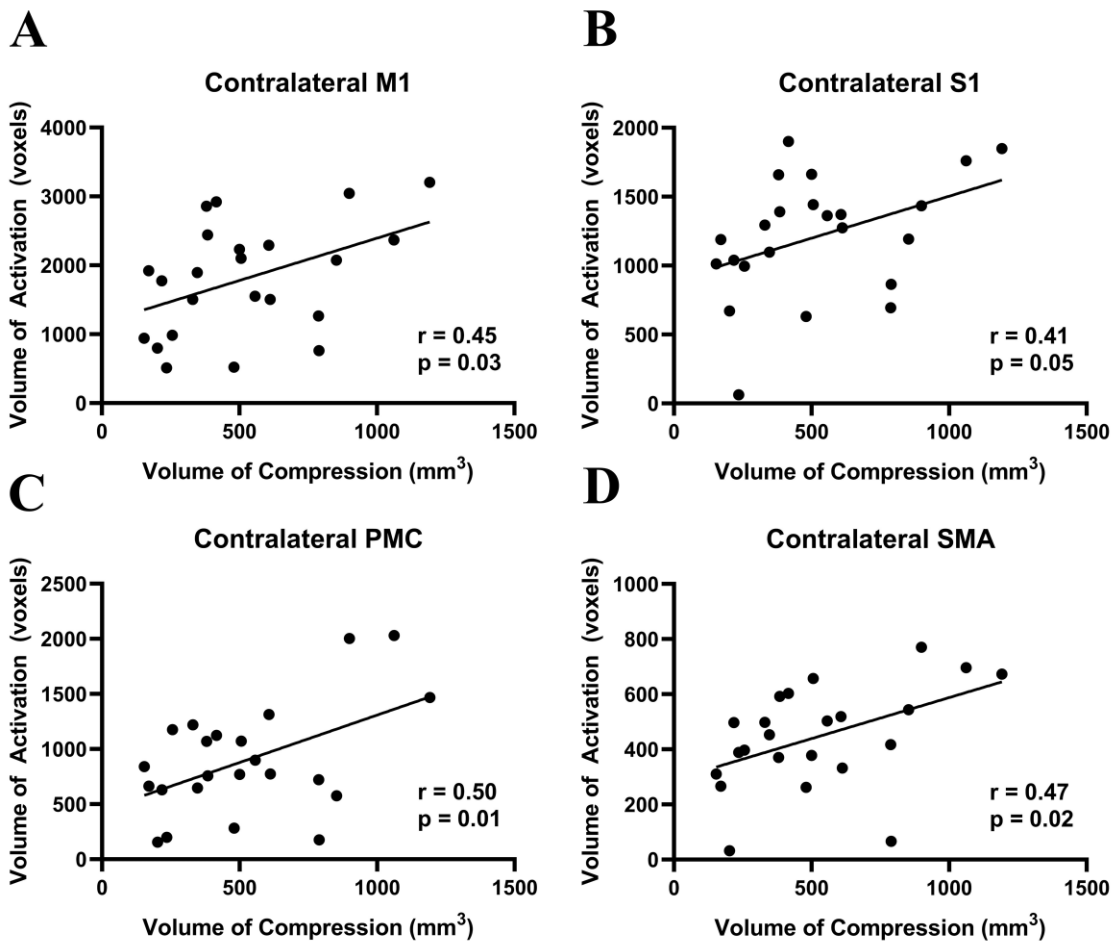

Figure 2.5: Right hand tapping volume of activation and volume of compression. **A:** The correlation between the VOA of the contralateral M1 and the spinal cord compression volume. **B:** The correlation between the VOA of the contralateral S1 and the spinal cord compression volume. **C:** The correlation between the VOA of the contralateral PMC and the spinal cord compression volume. **D:** The correlation between the VOA of the contralateral SMA and the spinal cord compression volume.

The mean mJOA score for the patient cohort was 9.9 ± 2.1 (mean ± SD). Analysis of compression severity and clinical scores (mJOA) did not demonstrate a significant relationship ($r = -0.36$, $p = 0.09$; Fig. 2.6). There was also no significant relationship between subcortical activation and clinical scores. However, analysis of the motor network and clinical scores (mJOA) demonstrated a significant relationship between

activation and function. When patients tapped with their left hand, the contralateral M1 % BOLD signal was significantly correlated with the mJOA score ($r = -0.44$, $p = 0.03$; Fig. 2.7A), indicating that a higher function is associated with a smaller signal change. Likewise, in the contralateral S1, a smaller % BOLD signal was associated with a higher mJOA score ($r = -0.48$, $p = 0.02$; Fig. 2.7C). Furthermore, when patients were tapping with their right hand, the same significant relationships were demonstrated (contralateral M1 % BOLD signal ($r = -0.50$, $p = 0.02$; Fig. 2.7B), contralateral S1 % BOLD signal ($r = -0.48$, $p = 0.02$; Fig. 2.7D)). There were no significant associations between any motor network activation and duration of symptoms.

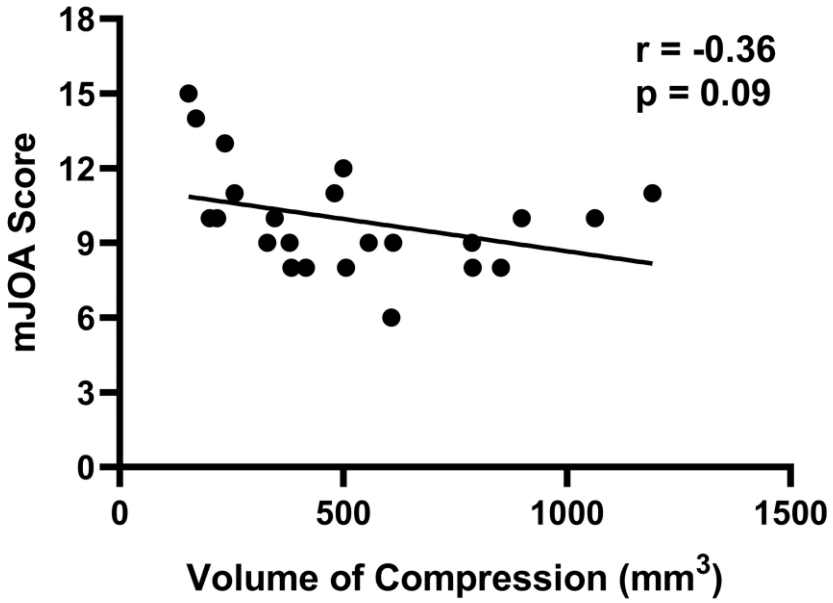

Figure 2.6: The association between the neurological function in DCM patients measured by the mJOA score and spinal cord compression volume.

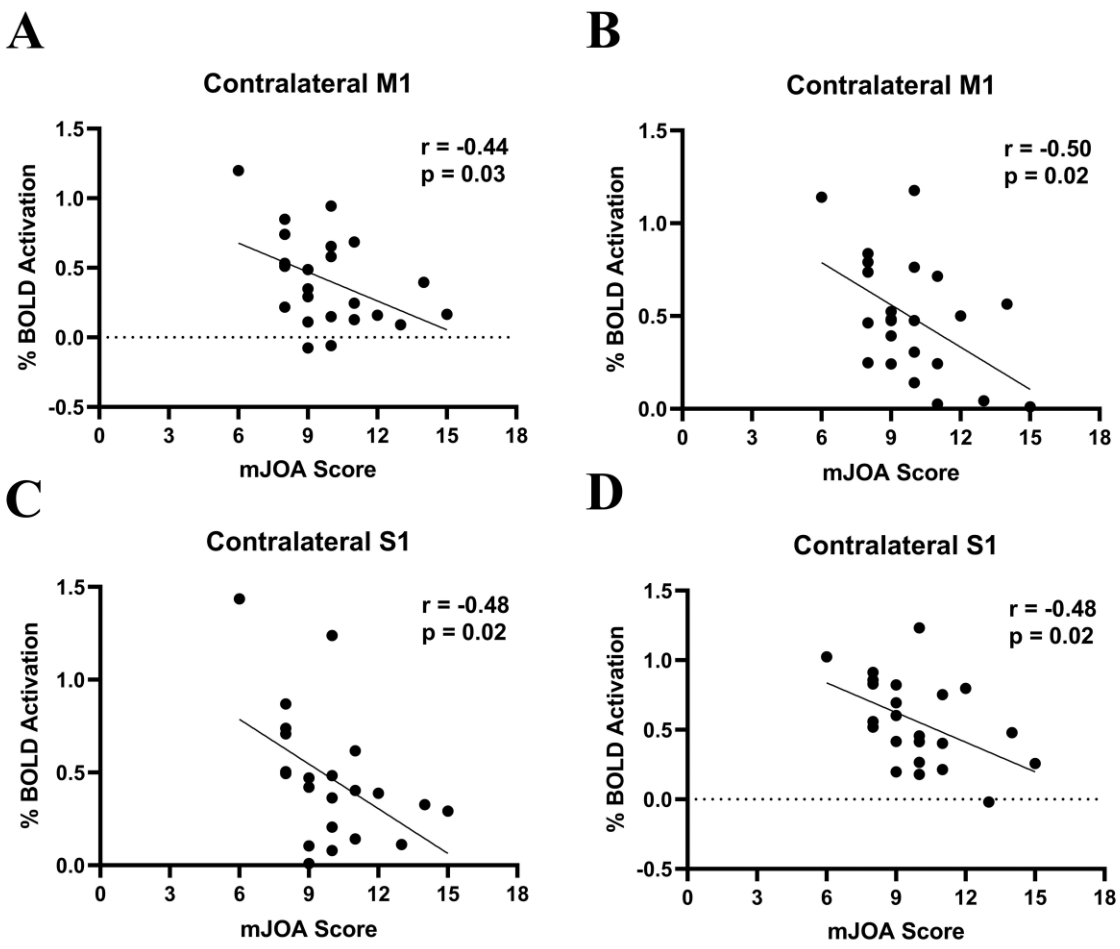

Figure 2.7: Correlation between % BOLD signal and mJOA. **A:** The correlation between the % BOLD signal of the contralateral M1when tapping with the left hand and neurological function of the CSM patients measured by the mJOA score. **B:** The correlation between the % BOLD signal of the contralateral M1 when tapping with the right hand and the mJOA score. **C:** The correlation between the % BOLD signal of the contralateral S1 when tapping with the left hand and the mJOA score. **D:** The correlation between the % BOLD signal of the contralateral S1 when tapping with the right hand and the mJOA score.

2.4 Discussion

In this study, conventional T_2-weighted MRI was used to quantify spinal cord compression severity in DCM patients using a newly developed method with high reproducibility. The association between spinal cord compression and motor function was assessed using clinical scores. In addition, the association between spinal cord compression and activation of the motor network of the brain was assessed using fMRI in response to a finger tapping task. The results indicate that total compression volume was positively correlated with the volume and magnitude of activation in several motor regions including the M1, S1, PMC, SMA, cerebellum, putamen, caudate, and thalamus. Additionally, mJOA scores were negatively correlated with the % BOLD signal in contralateral M1 and S1. To our knowledge, this is the first study in DCM that specifically explores the relationship between the severity of spinal cord compression and compensatory brain plasticity.

The current study demonstrates that DCM patients exhibit varying compensatory expansion of cortical activation *depending on the severity of spinal cord compression*. In many of the motor regions examined, there was a significant positive correlation between compression volume and activation levels, indicating that patients with greater spinal cord compression experience a larger compensatory expansion of activation or cortical recruitment. The expansion of the activated motor areas when DCM patients performed the controlled motor task may be related to rewiring of the axons of the lower limb extremities into the hand regions (176), which is driven by the use of the less affected part of the body to compensate for the difficulty with the instructed hand task. This effect has been shown in spinal cord injury patients, with an increase in handgrip related BOLD signal in the medial precentral gyrus, consistent with leg representation (110). The current study also demonstrated that patients with greater spinal cord compression have larger subcortical regions of activation. This increase in subcortical activation was previously suggested (151) to be due to the reduction of afferent input from the spinal cord, which could lead to more complex processing of the remaining input, leading to greater activation. Since the subcortical regions examined are part of circuits that

incorporate the cortical regions (177), activation pattern changes in subcortical regions could have a direct influence on the observed activation in the cortical regions.

There is mounting evidence from studies performing group-wise comparisons to control subjects or examining longitudinal changes in DCM subjects that DCM patients experience a reorganization of the motor areas in the brain. In one of the first studies demonstrating cortical reorganization in DCM patients, Holly *et al.* showed in four patients that there was an expansion of neuronal activity in the motor areas affected when performing either a wrist extension task or an ankle dorsiflexion task compared to healthy controls (104). Duggal *et al.* completed a study including 12 patients and 10 controls and performed both pre-operative and 6-month post-operative fMRI scans using a finger-tapping paradigm (103). It was found that patients demonstrated a larger VOA compared to controls in the precentral gyrus pre-operatively. Following surgery, this VOA difference between controls and DCM patients increased in this region. Hrabalek *et al.* completed a study involving seven patients and performed both pre-operative and 6-month post-operative fMRI scans using wrist flexions and extensions (149). It was found that there was significant activation in the dorsal M1, the adjacent secondary motor and sensory areas, and the cerebellum. Following surgery, there was a significant decrease in activation in the right parietal operculum and posterior temporal lobe.

In a larger study with 17 patients, Bhagavatula *et al.* also showed that compared to healthy controls, DCM patients had larger volumes of activation in their motor areas and cerebellum (106). Following decompression surgery, this cohort of patients demonstrated a decrease in activation compared to activation levels before surgery but remained higher than that of the control group. In a study that included 28 patients, Aleksanderek *et al.* demonstrated that there was a VOA difference pre-operatively between DCM patients with mild and moderate myelopathy, which was defined by mJOA (107). More specifically, the mild DCM patient group had a larger VOA in the postcentral gyrus compared to the moderate DCM group. This difference was no longer significant following surgery. Finally, Ryan *et al.* found that patients only exhibited a smaller VOA in the contralateral S1 compared to controls pre-operatively, which they attributed to the compression of the spinal cord attenuating signal transduction to the

cortical motor networks (163). Overall, these studies provide evidence to support the notion that there is a change in cortical activity in the motor areas of DCM patients pre-operatively.

We have demonstrated that DCM patients with larger spinal compression volumes also have greater activation levels within the motor regions of the brain. The compression of the spine may induce pathophysiological changes in the spine that could impact recovery after surgery. For example, both primary mechanical and secondary biological injury in the spinal cord have been acknowledged to cause functional deficits in DCM. However, cellular changes within the spine have not been well defined during disease pathogenesis. It has been hypothesized that ischemia and hypoxia, secondary to compression, are important pathophysiological mechanisms, however direct in-vivo measurement of these conditions has been challenging in humans. Studies involving animal models of DCM (48,50) and histological changes (24,44) have provided indirect evidence of these pathophysiological mechanisms. However, the role of ischemia and hypoxia in the spine in DCM disease progression and recovery is currently unknown.

The significant correlation between spinal compression volume and cortical plasticity is consistent with the presence of ischemia and hypoxia in the spine. Previous studies have demonstrated that cortical reorganization can occur in the brain when there is injury within the ascending and descending fiber tracts within the spinal cord (105,148). Ischemia and hypoxia can be caused by the disruption of vascular structures as a result of tissue compression. A study performed by Ellingson *et al.* found a decrease in blood flow in the region of the spinal cord that was compressed, supporting the hypothesis that spinal cord compression in DCM patients may result in ischemia and hypoxia (47). Since greater compression likely induces greater ischemia and hypoxia in the cord, it is reasonable to hypothesize that the observed cortical reorganization is a compensatory response to tissue damage in the spinal cord.

Our results also demonstrated that patients with a higher clinical score and functional ability, measured through mJOA, had lower activation in the brain motor areas. This result suggests that greater cortical recruitment may not necessarily translate

into functional gain pre-surgery. This effect has also been demonstrated in subjects with spinal cord injuries, where subjects with better upper limb function showed lower levels of activation in the primary motor cortex region (110). This has also been shown in stroke patients, where patients with increased cortical activation in the sensorimotor cortex also demonstrated increased functional impairment (178). They attributed this finding to the clinical changes indirectly reflecting injury-induced adaptive cortical recruitment of undamaged motor control pathways (178).

There are several limitations of the current study that are important to note. First, due to the high dimensionality and complexity of fMRI data, it is challenging to interpret single subject results. One intermediate approach between group level analysis and individual analysis is to perform clustering of subgroups with similar activation characteristics. This method could be used to identify differences in DCM patients without the complexity of interpreting the single subject data. In the future, this approach could be used to determine if one subgroup of patients demonstrates neurological recovery following decompression surgery. However, for this method to work effectively, a larger cohort of patients is needed. Second, this study included participants with compression sites ranging from C3-C4 to C6-C7. The site of compression may also account for some variance in the functional measures, and future studies with larger cohorts should examine this effect. Third, this in-vivo study was not designed to identify the extent and pathogenesis of cellular injury in the spinal cord. Future studies should be performed to directly quantify the extent of ischemia and hypoxia in the cord and examine the relationship to tissue compression. Finally, it is currently unknown whether spinal cord compression measures, combined with measures of brain activation, could predict who will not respond favourably to spinal decompression surgery, but a longitudinal study should be performed to investigate.

2.5 Conclusion

The current study indicates that DCM patients recruit larger regions of the motor cortex and subcortical areas to tap their fingers when spinal cord compression is more severe. This adaptation may compensate for neurological injury in the spine. Interestingly, the relationship between motor cortex activation patterns and function showed an inverse

relationship indicating individuals with larger activation patterns had worse function. Taken together, this data suggests that individuals with more severe spinal cord compression exhibit larger brain activation patterns to complete motor tasks, but that this does not translate into improved function. Future studies should determine whether larger activation patterns confer an advantage for recovery following decompression surgery.

2.6 Acknowledgements

The authors thank all participants for their contribution to this project. We also thank Scott Charlton and Oksana Opalevych (CFMM, Robarts Research Institute, The University of Western Ontario) for facilitating MRI acquisitions.

2.7 Funding

This study was funded by Canadian Institutes of Health Research (CIHR) (grant no: PJT 169100); Canada First Research Excellence Fund (BrainsCAN); Ontario Neurotrauma Foundation (grant no: 2016-RHI-RECOV-1018); and Academic Medical Organization of Southwestern Ontario (grant no: INN19-002).

2.8 Supplementary Materials

2.8.1 Results

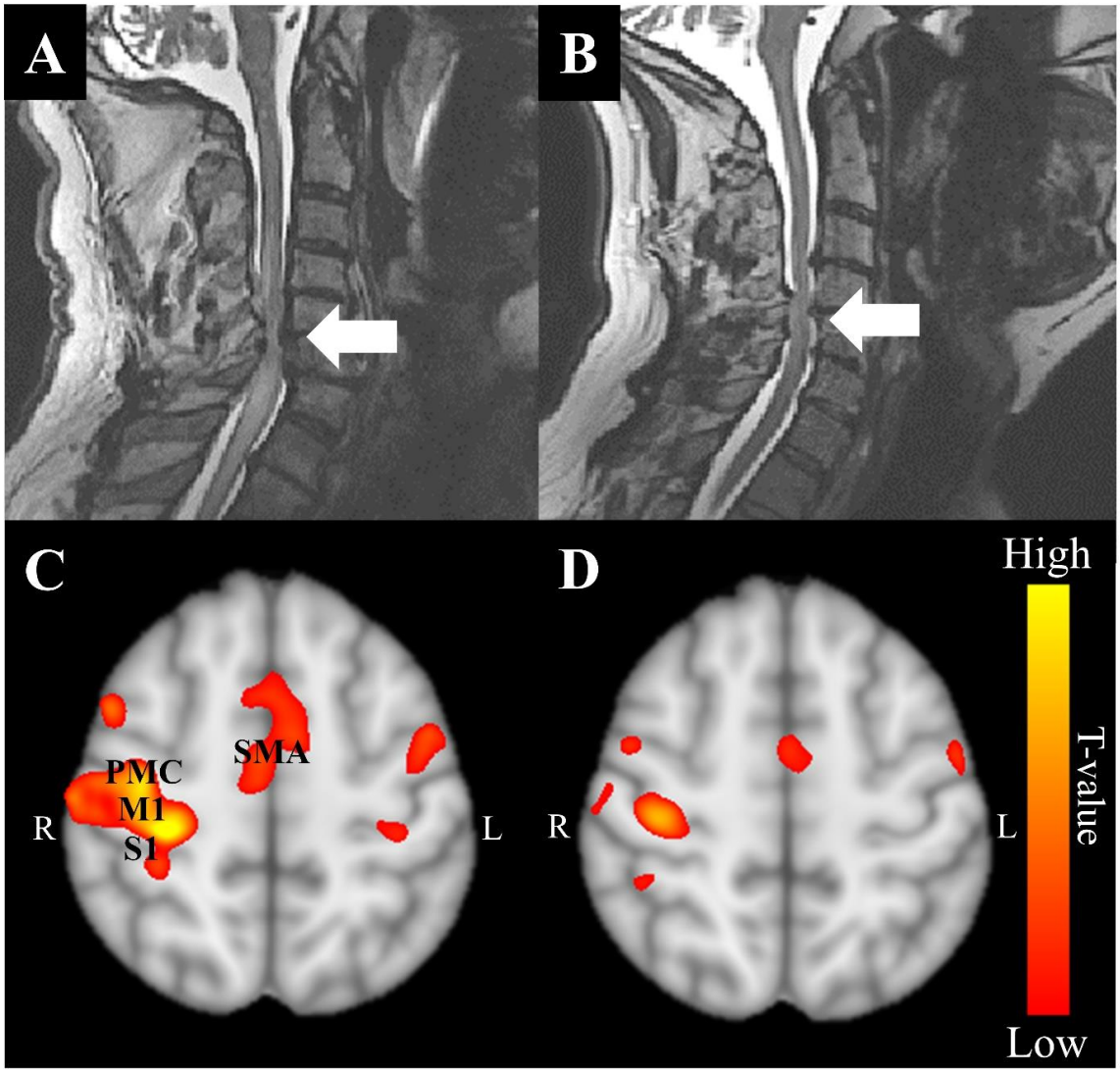

Supplementary Figure 2.1: fMRI activation map variations associated with spinal cord compression severity. **A:** Participant with a significant compression site (white arrow). **B:** A symptomatic participant with a lesser degree of spinal cord compression (white arrow). **C:** The corresponding fMRI activation map (left hand tapping) for the participant with severe compression. **D:** The corresponding fMRI activation map (left hand tapping) for the participant with less compression.

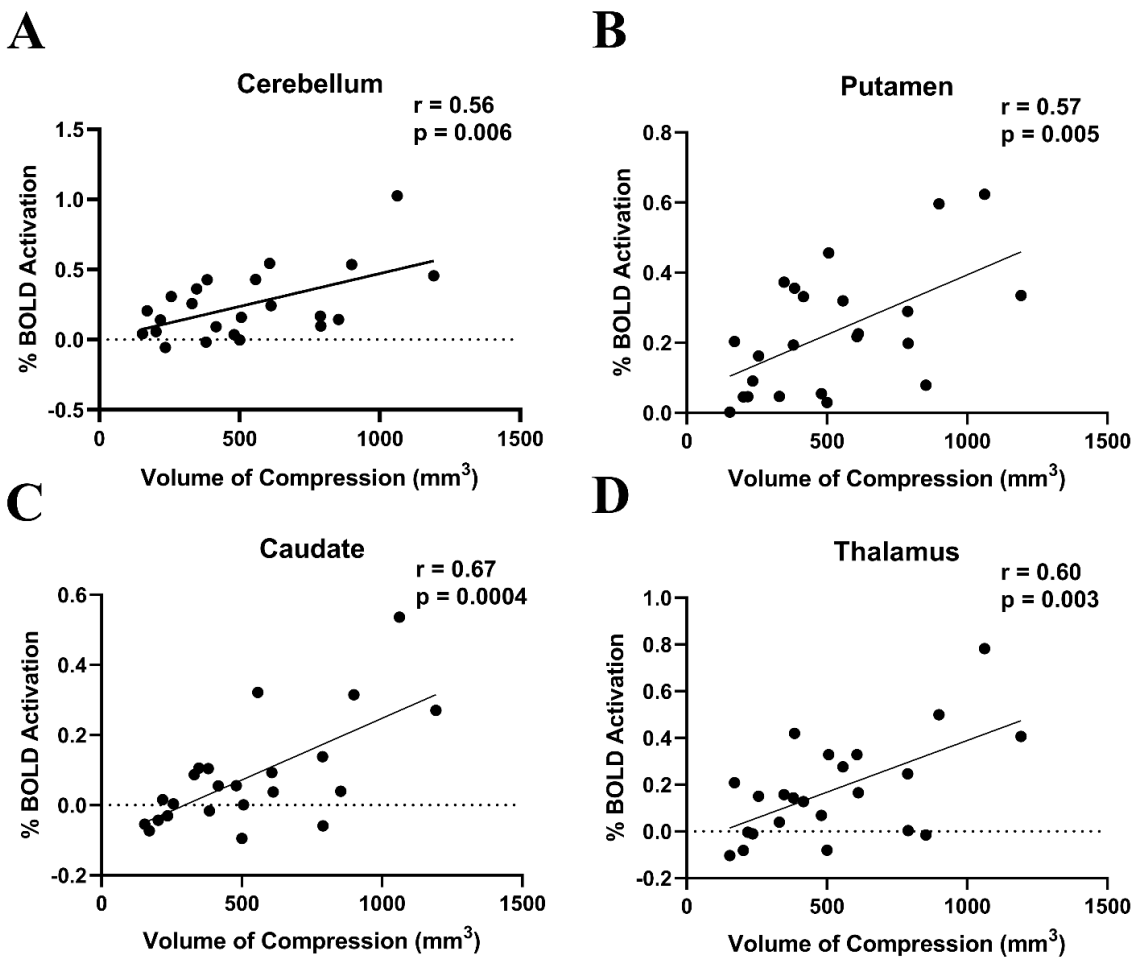

Supplementary Figure 2.2: Left hand tapping BOLD signal and volume of compression. **A:** The correlation between the % BOLD signal of the cerebellum and the spinal cord compression volume. **B:** The correlation between the % BOLD signal of putamen and the spinal cord compression volume. **C:** The correlation between the % BOLD signal of the caudate and the spinal cord compression volume. **D:** The correlation between the % BOLD signal of the thalamus and the spinal cord compression volume.

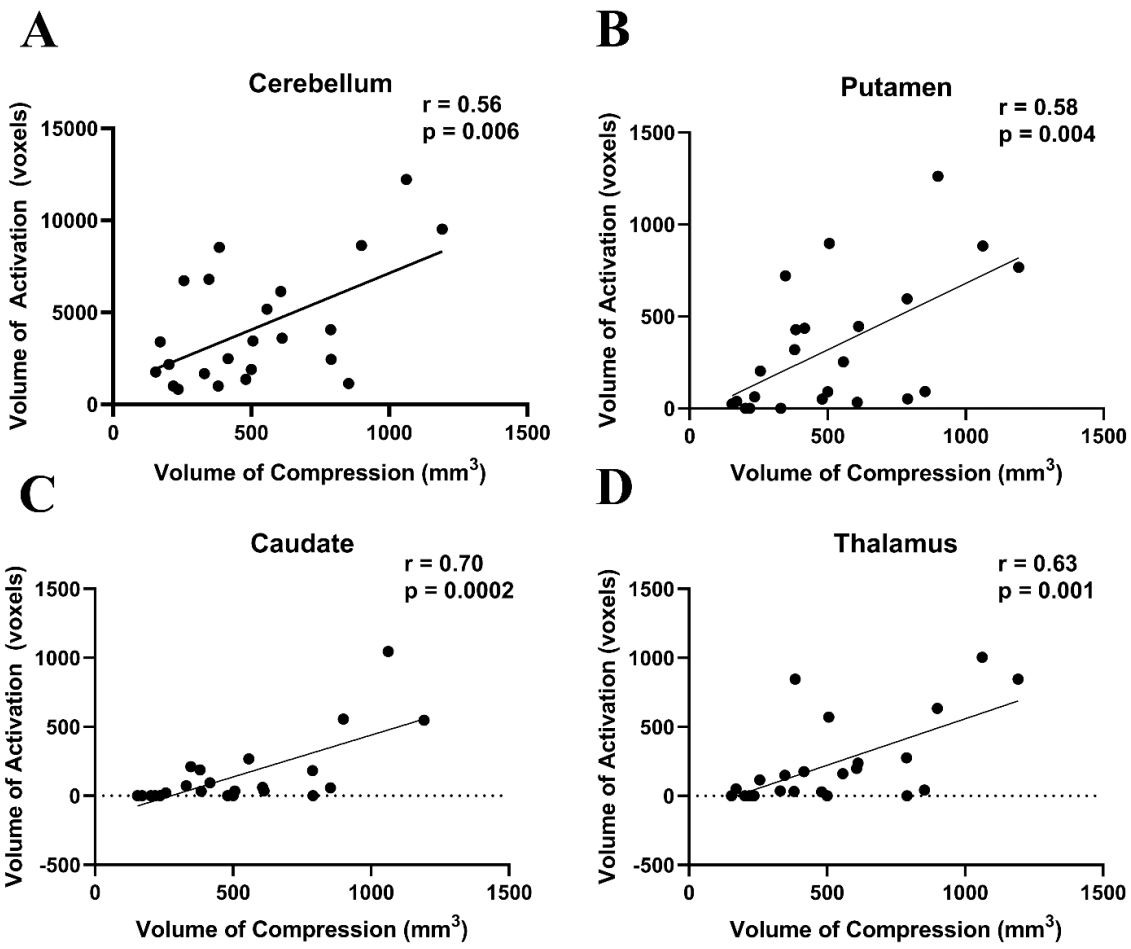

Supplementary Figure 2.3: Left hand tapping volume of activation (VOA) and volume of compression. **A:** The correlation between the VOA of the cerebellum and the spinal cord compression volume. **B:** The correlation between the VOA of putamen and the spinal cord compression volume. **C:** The correlation between the VOA of the caudate and the spinal cord compression volume. **D:** The correlation between the VOA of the thalamus and the spinal cord compression volume.

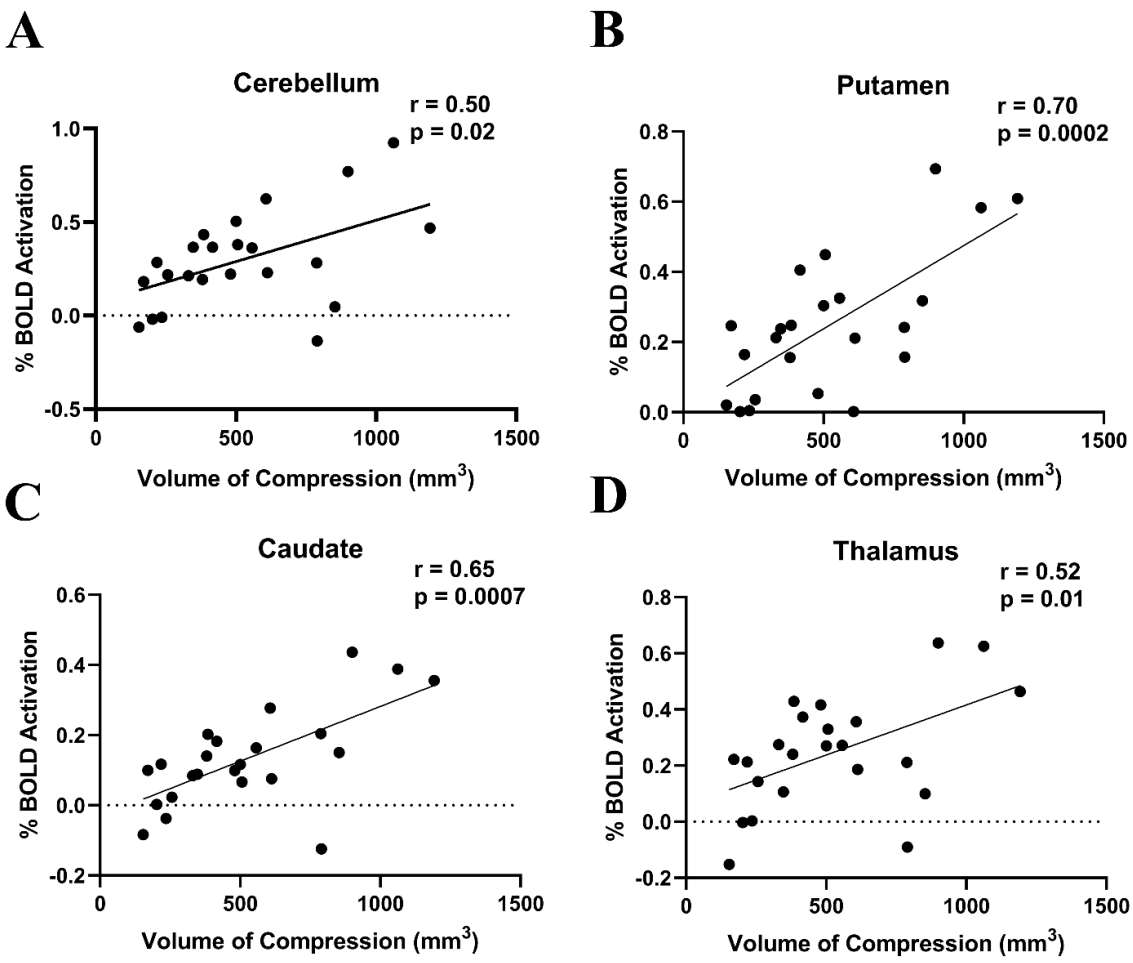

Supplementary Figure 2.4: Right hand tapping BOLD signal and volume of compression. **A:** The correlation between the % BOLD signal of the cerebellum and the spinal cord compression volume. **B:** The correlation between the % BOLD signal of putamen and the spinal cord compression volume. **C:** The correlation between the % BOLD signal of the caudate and the spinal cord compression volume. **D:** The correlation between the % BOLD signal of the thalamus and the spinal cord compression volume.

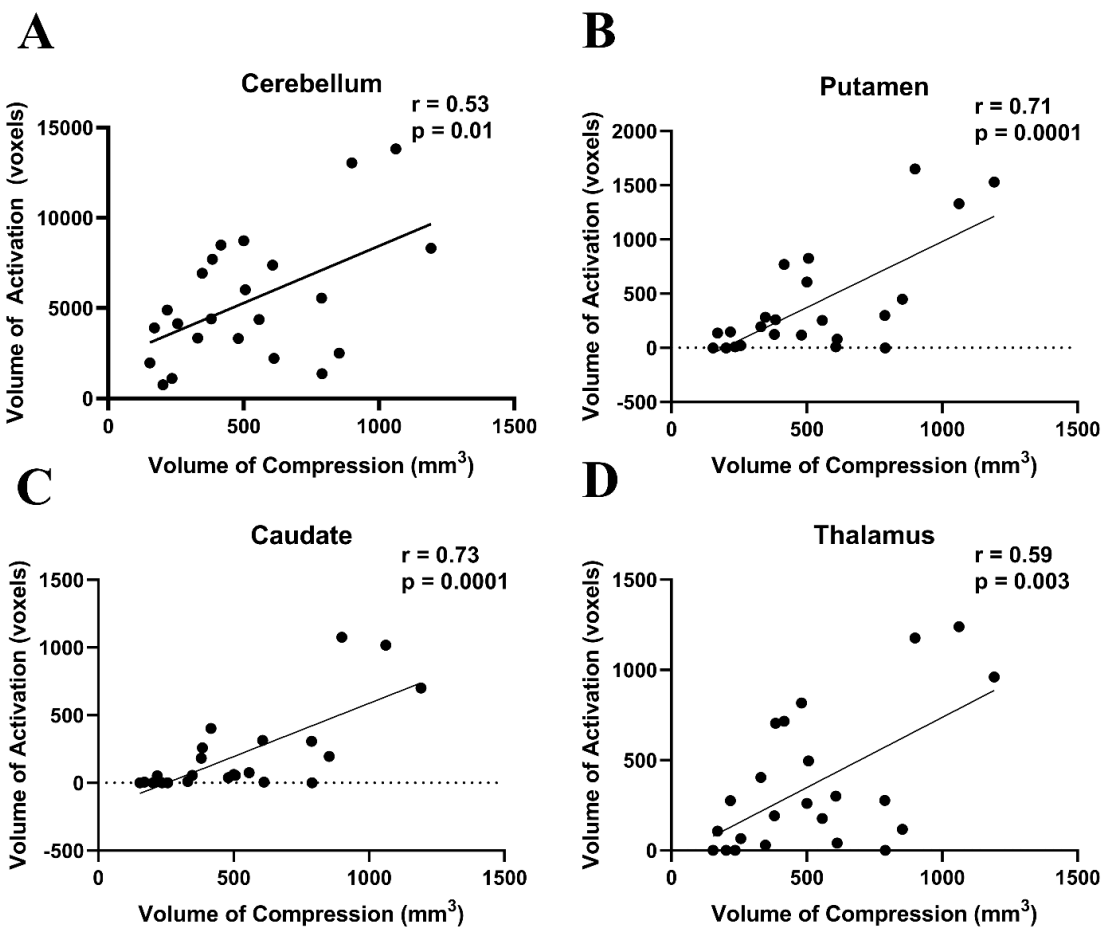

Supplementary Figure 2.5: Right hand tapping volume of activation (VOA) and volume of compression. **A:** The correlation between the VOA of the cerebellum and the spinal cord compression volume. **B:** The correlation between the VOA of putamen and the spinal cord compression volume. **C:** The correlation between the VOA of the caudate and the spinal cord compression volume. **D:** The correlation between the VOA of the thalamus and the spinal cord compression volume.

Supplementary Table 2.1: The measurements of the spinal cord compression volume (mm^3) found for each rater

Subject	Rater 1			Rater 2		
	Measure 1	Measure 2	Measure 3	Measure 1	Measure 2	Measure 3
1	607.3	607.3	607.3	582.0	626.7	569.9
2	611.8	611.8	611.8	611.8	611.8	611.8
3	1191.8	1191.8	1191.8	1191.8	1191.8	1191.8
4	542.2	529.4	529.4	604.2	491.0	455.4
5	346.8	346.8	346.8	317.9	314.9	308.0
6	899.3	892.4	892.4	876.4	875.4	905.7
7	170.7	189.2	189.2	169.8	169.8	189.2
8	500.5	500.5	500.5	500.5	499.7	472.6
9	789.4	669.0	638.7	662.2	660.9	660.9
10	153.9	153.9	153.9	148.6	162.9	153.9
11	1062.4	1062.4	1062.4	836.7	1062.4	896.8
12	217.9	228.1	228.1	173.2	196.5	288.1
13	788.2	788.2	788.2	788.2	788.2	788.2

14	852.6	852.6	879.8	651.0	651.0	879.8
15	256.7	256.7	256.7	239.1	256.7	210.4
16	480.6	480.6	486.6	480.6	486.6	480.6
17	416.7	416.7	416.7	416.7	416.7	417.3
18	384.2	384.2	384.2	384.2	384.2	384.2
19	201.8	201.8	201.8	143.5	143.5	168.9
20	557.2	557.2	557.2	545.7	328.5	557.2
21	330.6	330.6	330.6	310.4	276.2	279.2
22	235.4	186.0	235.4	186.0	186.0	186.0
23	380.4	385.9	385.9	385.9	376.7	373.8

Chapter 3

3 Reproducibility of 3D Chemical Exchange Saturation Transfer (CEST) Contrasts in the Healthy Brain at 3T

The work presented in this chapter is from the manuscript:

Alicia E Cronin, Patrick Liebig, Sarah A Detombe, Neil Duggal, Robert Bartha. Reproducibility of 3D Chemical Exchange Saturation Transfer (CEST) Contrasts in the Healthy Brain at 3T. *In preparation for submission.*

Optimization work is from the manuscript:

Alicia E Cronin, Patrick Liebig, Sarah A Detombe, Neil Duggal, Robert Bartha. Reproducibility of 3D pH-Weighted Chemical Exchange Saturation Transfer Contrast in the Healthy Cervical Spinal Cord. NMR in Biomedicine. 2024; 1-13. doi:10.1002/nbm.5103.

Permission to reuse this article has been obtained. Please see Appendix B.

3.1 Introduction

Chemical exchange saturation transfer (CEST) imaging can indirectly detect select metabolites and is sensitive to tissue physiological conditions including temperature and pH. CEST contrast is generated using the transfer of magnetic saturation from selectively excited endogenous or exogenous exchangeable protons to bulk water (112,113). Exchangeable protons include amide (NH) and amine (NH_2) protons, which are found in tissue metabolites, proteins, and peptides (121). Several prominent CEST effects including amide-CEST and nuclear Overhauser enhancement (NOE) CEST (179-186) have been previously used to study cohorts with various neurological conditions. For example, amide-CEST (exchangeable protons at 3.5 ppm) has been extensively studied for brain tumour grading (182,186), detecting early treatment effects (184,185), and monitoring pH effects during ischemia (180). NOE-CEST is an emerging contrast targeting non-exchangeable protons (i.e., carbon-bound aliphatic and aromatic protons)

that transfer magnetic saturation to nearby dipolar-coupled protons via cross-relaxation (187). NOE signals at the downfield frequency of -3.5 ppm are of particular interest and have been used to characterize tumour aggressiveness (181), discriminate between tumour regrowth and radiation necrosis (183), and linked to protein aggregation in an Alzheimer's disease mouse model (179). More recently, a ratiometric endogenous CEST contrast, called amine/amide concentration independent detection (AACID), has also emerged as a contrast sensitive to intracellular pH relying on the relative amide (3.5 ppm) and amine (2.75 ppm) CEST effects and has been used to track pH changes following ischemic stroke and in tumours (129,130).

However, future application of these novel contrasts in clinical settings to assess patients with neurological conditions requires characterization of reproducibility in healthy brain gray matter (GM) and white matter (WM) tissue. Reproducibility measures are necessary to compare contrast efficacy and estimate detectable effect sizes. Previous studies have evaluated the reproducibility of amide proton transfer (APT) CEST (144-147). A recent study demonstrated high whole-brain within-session, between-session, and between-day APT reproducibility in 21 healthy participants and 6 people with glioma using clinically feasible scan times at 3.0 T (147). Another study performed with 19 healthy volunteers, 15 people with glioma, and 12 people with acute stroke found that 3D APT CEST had higher reproducibility in the supratentorial locations of the brain compared to the infratentorial locations, regardless of disease condition (145). Another study found that single-slice APT reproducibility in brain tumours between sessions in 13 patients was characterized by an intraclass correlation coefficient (ICC) of 0.95 (146). Finally, a fourth study found the limit of agreement was below 20% for both APT and NOE CEST but only in two healthy volunteers (144). There have been no studies performed to date that have compared the reproducibility of different CEST contrasts in the healthy brain. Identifying CEST contrasts with high reproducibility will aid in clinical translation and the development of robust thresholds to identify pathological tissue.

The purpose of the current study was to develop an optimized CEST acquisition protocol to generate pH-weighted AACID contrast at 3.0 T. The current study characterized and compared the scan-rescan reproducibility of four different CEST

contrasts in healthy volunteers in both GM and WM at the clinically relevant field strength of 3.0 T. This study also aimed to quantify the difference in these contrasts in GM and WM tissue.

3.2 Material and Methods

3.2.1 Phantom Preparation

To optimize the in-vivo CEST acquisition and determine the AACID dependency on pH at 3.0 T, phantoms of differing pH were created using 100% liquid egg white and pH was adjusted by adding hydrochloric (HCl) acid (concentration 5N). Egg white phantoms were chosen based on the study by Yeung *et al.* that demonstrated that raw egg white is an appropriate material to model the pH sensitivity of amide and amine protons from mobile proteins (188). Ten samples were created (pH ranging from 9.17 – 5.82) and transferred into 50 mL conical tubes. The pH of the samples was measured using a pH meter (Orion Green pH Combination Electrode - GD9156BNWP, Thermo Fisher Scientific Inc., Waltham, MA, USA).

3.2.2 Participants

This study was approved by the Western University Health Sciences Research Ethics Board and informed consent was obtained from all participants prior to the first scan. Twelve healthy participants were included in this study (7 females, mean age (± SD) 26 ± 4 years). The inclusion criteria were (1) age >18 years, and (2) no clinical or MRI evidence of brain pathologies. Participants with contra-indications to 3.0 T MRI were excluded. Each participant was scanned twice (10 ± 4 days between scans) to determine the reproducibility of each CEST contrast in the brain.

3.2.3 Image Acquisition

All participants were scanned using a Siemens 3.0 T MAGNETOM Prisma Fit MRI scanner (Siemens, Erlangen, Germany) equipped with a 64-channel head and neck coil to collect the necessary data. The prototype CEST sequence consisted of a series of selective saturation pulses to produce CEST contrast followed by a rapid 3D gradient-echo readout using a centric spiral k-space sampling. The saturation scheme used in the

current study consisted of a train of 30 Gaussian-shaped RF pulses with length (t_{pulse}) of 100 ms and an interpulse delay (t_{delay}) of 1 ms, resulting in a total saturation time of 3.03s. A recovery time of 2 s was utilized after each readout period. It should be noted that for the brain optimization experiments, a 2D prototype CEST sequence was used, which consisted of the same saturation scheme as previously stated, followed by a 2D gradient-echo readout.

The optimum B_1 amplitude of the saturation pulses was assessed in both phantoms and human participants. For the optimization of B_1 amplitude in phantoms, Z-spectra were obtained at 66 frequency offsets from -6.5 ppm to 6.5 ppm, in 0.2 ppm increments, and an additional frequency was acquired at -300 ppm as a control frequency. The imaging parameters included matrix size = 112 x 112 x 8, nominal resolution = 2.0 x 2.0 x 5.0 mm^3, repetition time (TR)/echo time (TE) = 3.35/1.16 ms, and GRAPPA acceleration factor = 2. The total CEST scan time was 7 minutes and 54 seconds. For the optimization of B_1 amplitude in the brain, three additional participants were scanned, and Z-spectra were obtained at 131 frequency offsets from -6.5 ppm to 6.5 ppm, in 0.1 ppm increments, and an additional frequency was acquired at -300 ppm as a control frequency. The imaging parameters for the brain optimization experiment included matrix size = 96 x 96, field of view = 19.2 cm, slice thickness = 2 cm, TR/TE = 3.35/1.16 ms, and GRAPPA acceleration factor = 2. The total CEST scan time was 6 minutes and 50 seconds. Both the phantom and brain scans were performed at six different B_1 amplitudes (0.1 µT, 0.2 µT, 0.5 µT, 1.0 µT, 1.5 µT, and 2.0 µT). In all cases, the height of the amide peak was used to determine which B_1 amplitude was optimal. Note that this optimization protocol was created for the contrast AACID.

To evaluate the reproducibility in the brain, a whole-brain 3D MPRAGE T_1-weighted scan was acquired including the following scan parameters: TR of 2300 ms, TE of 2.98 ms, inversion time (TI) of 900 ms, flip angle (FA) of 9°, matrix size of 256 x 256 x 176, producing a 1 mm^3 isotropic nominal pixel size. Based on the optimization, a selective saturation scheme was employed that used a series of 30 Gaussian-shaped RF pulses ($B_{1,mean}$ = 0.5 µT) with a t_{pulse} of 100 ms and a t_{delay} of 1 ms. The total saturation time was 3.03 s, followed by a 2 s recovery time after each readout. CEST images were

acquired at 45 pre-saturation frequency offsets ranging from -6.5 ppm to 6.5 ppm (with uneven increments, emphasizing the amide and NOE features, see Supplementary Table 3.1 for specific details) and an additional frequency was acquired at -300 ppm for normalization. The 3D CEST volume was positioned superior to the ventricles in the brain of all participants, with imaging parameters set at a matrix size of 96 x 96 x 8, a nominal pixel size of 2.0 x 2.0 x 5.0 mm^3, a TR/TE of 3.35/1.16 ms, and a GRAPPA acceleration factor of 2. The total CEST imaging scan time was 3 minutes and 38 seconds. To ensure the 3D volume between scans was positioned in the same location, an automated slice positioning scout sequence (Siemen's AutoAlign) was employed during the first scan. The AutoAlign images were acquired by 3D FLASH using the following parameters: TR/TE = 3.15/1.37 ms, 1.6 mm^3 isotropic, FA = 8°, acquisition time = 14 s. AutoAlign references a 3D MR brain atlas, and automatically aligns the follow-up scan slice positions in a standardized manner.

A water saturation shift referencing (WASSR) scan was also acquired for B_0 correction (189). For WASSR saturation, a train of 5 Gaussian pulses with t_{pulse} = 50 ms, t_{delay} = 40 ms, and $B_{1,mean}$ = 0.5 μT was used and sampled at 25 frequency offsets from -2.5 ppm to 2.5 ppm, in increments of 0.2 ppm. The total WASSR scan time was 1 minute and 4 seconds.

3.2.4 CEST Postprocessing

For each scan, the whole-brain T_1-weighted images were automatically segmented using the FMRIB Software Library (FSL) v.6.0. Specifically, for whole-brain extraction and creation of GM and WM binary regions-of-interest (ROIs), optiBET was used (190). Registration of the 3D CEST images to the T_1-weighted image was performed using FMRIB's Linear Image Registration Tool (FLIRT) and the whole-brain, GM, and WM masks were transformed into CEST space for further analysis by applying the inverse transformation matrix obtained from the previous CEST to T_1-weighted anatomical image registration. All acquired and registered CEST data was loaded into MATLAB R2021a (Mathworks, Natwick, MA, USA) custom code. To correct for B_0 inhomogeneities, the corresponding Z-spectrum of each pixel was frequency-shifted

using the corresponding WASSR spectrum (189). For each pixel, the Z-spectrum was fitted with a five-pool Lorentzian model including water, amide, amine, NOE, and magnetization transfer (MT) pool contributions. More information regarding the fitting is available in the Supplementary Materials. Starting points and boundaries of the fit are given in Supplementary Table 3.2. To minimize the effect of fat signal contamination on the NOE side of the Z-spectrum (191), any pixel that had a residual mean between the fit and raw data below -0.2 (from -4 ppm to -3 ppm), was eliminated because the Lorentzian model was not designed to fit a positive peak.

Different CEST contrasts were calculated to compare the between-subject and within-subject reproducibility. AACID (Equation 3.1) is the ratio of the amine proton CEST effect at 2.75 ppm and the proton amide CEST effect at 3.50 ppm, normalized by MT effects after saturation at 6.0 ppm. This CEST contrast has been shown to have only a small dependence on temperature, bulk water T_1 relaxation, and macromolecular concentration (129,130).

$$AACID = \frac{M_z(3.50\ ppm) \times \left(M_z(6.0\ ppm) - M_z(2.75\ ppm)\right)}{M_z(2.75\ ppm) \times \left(M_z(6.0\ ppm) - M_z(3.50\ ppm)\right)} \quad [3.1]$$

where M_z is the bulk water magnetization. Jin *et al.* introduced a three-offset contrast method (Equation 3.2), which reduces the effect of MT asymmetry by using two boundary frequencies, with minimal CEST effect from other mobile macromolecules. This technique assumes that the two boundary frequencies can be approximated by a straight line, which eliminates the Z-spectra fitting approach by calculating the difference between the amide CEST effect and the line segment (124).

$$Amide^* = \left(\frac{M_z(3.0\ ppm) + M_z(4.0\ ppm)}{2}\right) - M_z(3.5\ ppm) \quad [3.2]$$

Finally, studies have shown spillover and MT effects can be corrected by inversely subtracting the Lorentzian fit of the Z-spectrum consisting of all pools except that of pool *i* ($Z_{ref,i}$) from the complete Lorentzian fit of the Z-spectrum (Z_{lab}), yielding MTR_{Rex} (Equation 3.3) (192). This contrast was calculated when the amide pool was of interest (*i* = 3.5 ppm), and the NOE pool was of interest (*i* = -3.5 ppm).

$$MTR_{Rex}(\delta_i) = \frac{1}{Z_{lab}(\delta_i)} - \frac{1}{Z_{ref,i}(\delta_i)} \quad [3.3]$$

where δ_i is the displacement from the frequency of the bulk water protons. To determine the CEST contrast values in both GM and WM, the binary GM and WM ROIs were applied to the 3D CEST contrast maps, and the average contrast values were calculated for both GM and WM.

3.2.5 Statistics

Pearson's correlation coefficient (r) was used to determine whether the measured AACID values from the pH phantoms were correlated with pH at the 3.0 T field strength.

A repeated measures t-test was performed to compare the GM and WM measurements (at both timepoints) for all CEST contrasts at a significance level of $p = 0.05$. CEST contrast scan-rescan reproducibility was characterized for both GM and WM using the coefficient of variation (CV) and percent difference of the contrast measurements. The CV is indicative of both the reproducibility and repeatability of a measurement, while the percent difference represents the reproducibility between scans. Between-subject and within-subject reproducibility was quantified using between-subject CV and within-subject CV, respectively. Between-subject CV was calculated for each scan as the standard deviation divided by the mean value across all subjects. The two

between-subject CVs were averaged to find the mean between-subject CV for both GM and WM. Within-subject CV was calculated as the standard deviation divided by the mean of the two scans for each subject separately. Mean within-subject CV was found for both GM and WM by averaging the 12 within-subject CVs together. Percent difference was calculated for each subject by finding the absolute difference between the scans and dividing it by the average of the two scans, multiplied by 100. The 12 individual percent difference measurements were averaged to determine the mean percent difference for both GM and WM of each contrast. All these calculations were performed for each CEST contrast. To determine if there were any differences in reproducibility between tissue, a repeated one-way ANOVA (corrected for multiple comparisons (Tukey), $p<0.05$) was performed for between-subject CV, within-subject CV, and percent difference. CV and percent difference calculations were performed in MATLAB R2021a, and all tests of significance were performed using GraphPad Prism 9 (San Diego, CA). To standardize the different contrasts for visualization, contrasts of one subject were converted to Z-score maps (Figure 3.1), which describe each pixel's relationship to the mean of the contrast. Z-scores for each contrast were calculated using Equation 3.4:

$$Z = \frac{(x - \mu)}{\sigma} \qquad [3.4]$$

where x is the contrast value of a pixel, μ is the mean of the contrast of one subject, and σ is the standard deviation of the contrast of one subject.

3.3 Results

In the egg white phantoms at all pH values studied, it was found that the amide signal amplitude was maximized when using Gaussian saturation pulse amplitude B_1= 0.5 μT. This result is demonstrated in Figure 3.2A for pH in the physiological range. AACID maps (Figure 3.2B) demonstrate the homogeneity of the measurements throughout the egg white phantoms. Using the optimal B_1 amplitude of 0.5 μT, the measured AACID

values of each pH phantom were found to be strongly linearly correlated with the measured pH value ($p < 0.01$, $r = -0.98$, Figure 3.2C). Similarly, in the three healthy control brains, the average amide signal amplitude was also maximized when using Gaussian saturation pulse amplitude $B_1 = 0.5$ μT, as shown in Figure 3.3A. A typical transverse slice through the healthy human brain (Figure 3.3B) shows the variation of the amide signal amplitude.

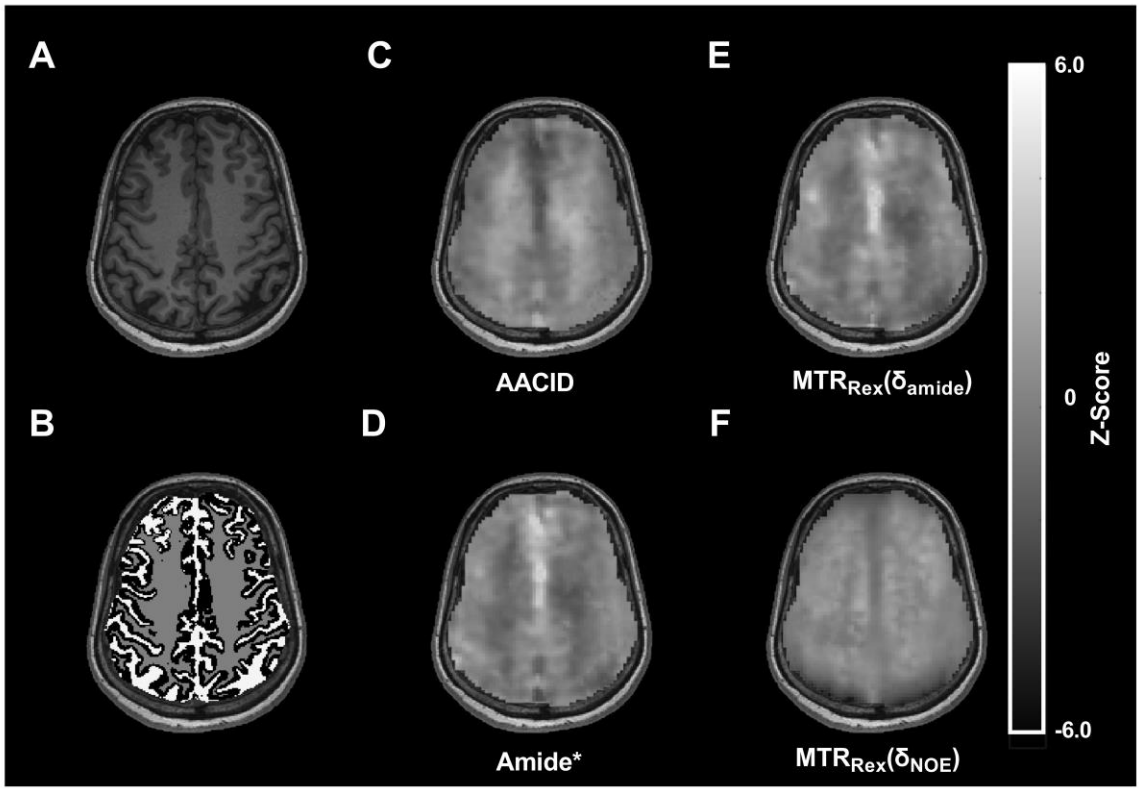

Figure 3.1: A: Axial T_1-weighted slice of the brain of a healthy participant corresponding to the center of the 3D volume (slice 4). The same T_1-weighted axial image with overlayed **B:** segmented gray matter (black), white matter (grey), and cerebrospinal fluid (white) regions of interest; **C:** amine/amide concentration independent detect (AACID) Z-Score map; **D:** Amide* Z-Score map; **E:** $MTR_{Rex}(\delta_{amide})$ Z-Score map, and **F:** $MTR_{Rex}(\delta_{NOE})$ Z-Score map.

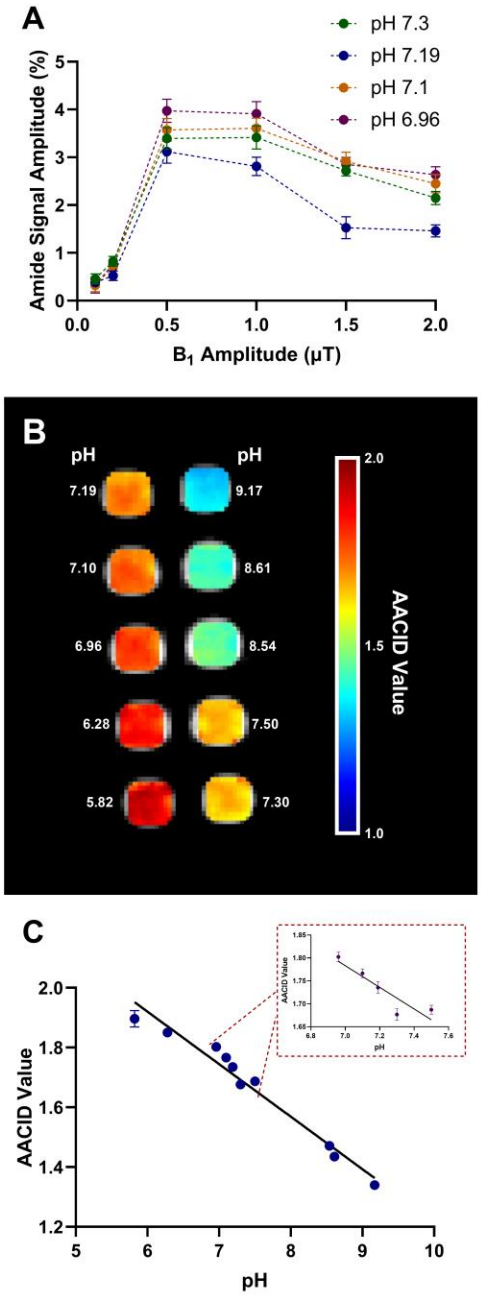

Figure 3.2: A. B_1 amplitude optimization using egg white phantoms (values represent mean amide signal of control egg white phantom map ± standard deviation of the map), demonstrating maximized amide signal amplitude at B_1 = 0.5 μT. Although all phantoms demonstrated a similar pattern of change as a function of pH, only data from the four phantoms that encompass the physiological pH range are shown. **B.** Average amine/amide concentration independent detection (AACID) maps (slices = 8) for the ten

egg white phantoms ranging in pH from 5.82-9.17 when using a B_1 amplitude of 0.5 μT. **C.** The correlation between the measured AACID value and the pH of each egg white phantom, demonstrating a significant linear relationship ($p < 0.001$, $r = -0.98$). The line of best fit has a slope of -0.176. pH accounts for 97% of the total variation in AACID. The inset represents the data in the physiological range, also demonstrating a significant linear relationship ($p < 0.05$, $r = -0.91$) and slope of -0.236. AACID values represent the mean AACID value of each phantom map ± standard deviation of the map.

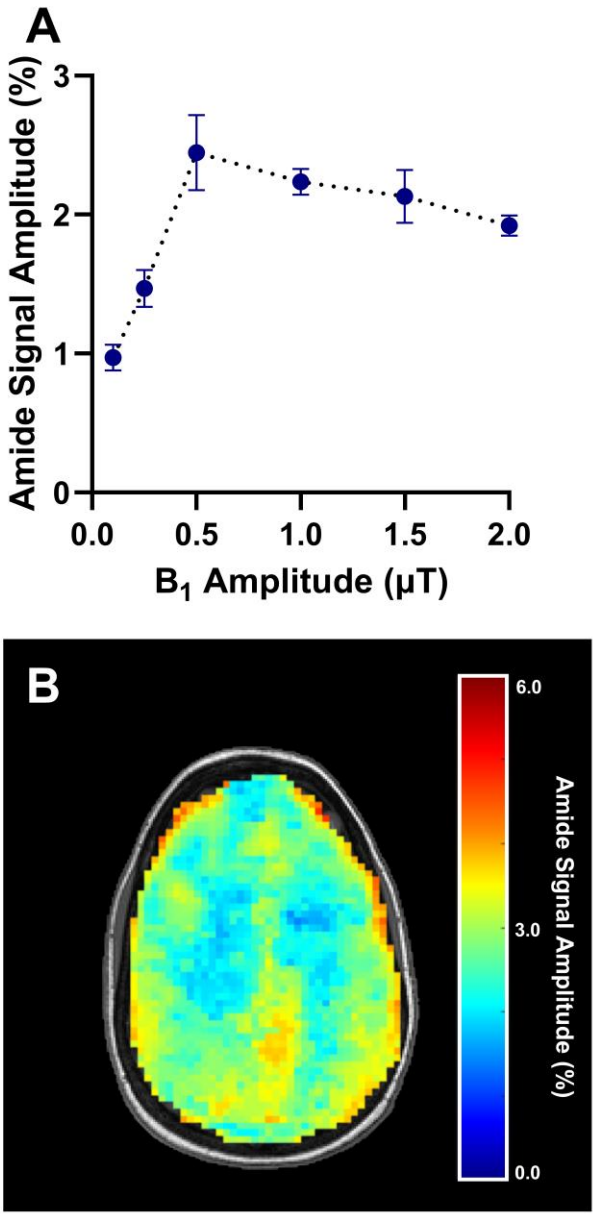

Figure 3.3: A. B_1 amplitude optimization in the human brain in three healthy participants (values represent mean amide signal of the three volunteers ± standard deviation), showing maximum amide signal amplitude at B_1 = 0.5 μT. **B.** Axial slice amide signal amplitude map through the brain of one healthy participant using B_1 amplitude = 0.5 μT.

Figure 3.1A shows the T_1-weighted brain image of an exemplary axial slice from one healthy subject with the corresponding GM (black), WM (gray), and cerebrospinal fluid (CSF) (white) segmentations overlayed on Figure 3.1B. The corresponding CEST slice contrast Z-score maps are shown as follows: AACID (Figure 3.1C), Amide* (Figure 3.1D), $MTR_{Rex}(\delta_{amide})$ (Figure 3.1E), and $MTR_{Rex}(\delta_{NOE})$ (Figure 3.1F). To compare the differences between GM and WM, the different brain tissue was compared for each of the four different CEST contrasts, as illustrated in Figure 3.4. It was found that the AACID value was significantly greater in WM compared to GM (2.60% difference, Figure 3.4A, $p<0.0001$) as was the $MTR_{Rex}(\delta_{NOE})$ value (4.90% difference, Figure 3.4D, $p<0.0001$) measures. It was also found that the Amide* value was significantly lower in WM compared to GM (31.0% difference, Figure 3.4C, $p<0.05$) and as was the $MTR_{Rex}(\delta_{amide})$ value (4.27% difference, Figure 3.4B, $p<0.0001$) measures. Table 3.1 provides the mean GM (± SD) and mean WM (± SD) contrast values for all participants.

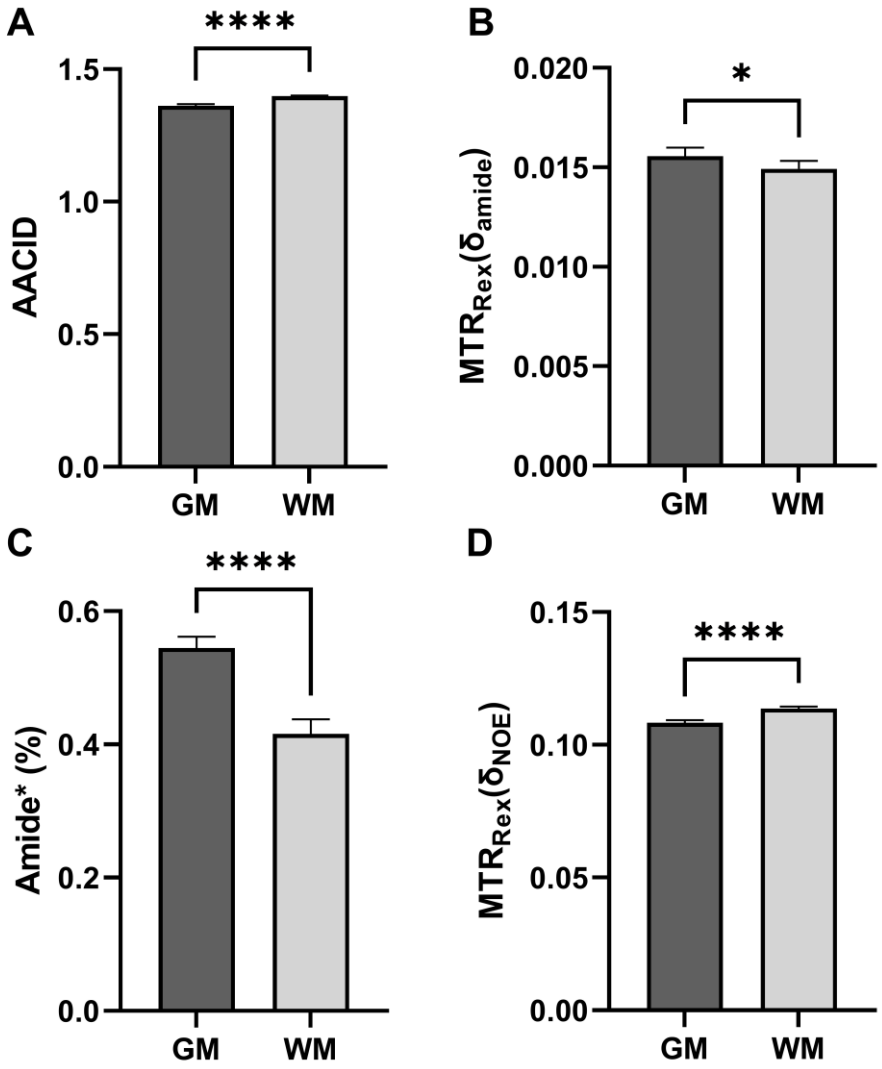

Figure 3.4: A: Mean amide/amine concentration independent detection (AACID) values (with standard deviation) for gray matter (GM) and white matter (WM), with WM significantly greater than GM ($p < 0.0001$). **B.** Mean $MTR_{Rex}(\delta_{amide})$ values (with standard deviation) for GM and WM, with GM significantly greater than WM ($p < 0.05$). **C.** Mean Amide* values (with standard deviation) for GM and WM, with GM significantly greater than WM ($p < 0.0001$). **D.** Mean $MTR_{Rex}(\delta_{NOE})$ values (with standard deviation) for GM and WM, with WM significantly greater than GM ($p < 0.0001$). Means were calculated from all subjects and both time points (24 measurements).

Table 3.1: Summary of the mean values in both gray matter and white for each of the four contrasts (amine/amide concentration independent detection (AACID), Amide*, $MTR_{Rex}(\delta_{amide})$, and $MTR_{Rex}(\delta_{NOE})$) at each time point (with standard deviation).

		Gray Matter (mean ± SD)	White Matter (mean ± SD)
AACID	Scan 1	1.37 ± 0.03	1.40 ± 0.02
	Scan 2	1.36 ± 0.02	1.40 ± 0.02
Amide*	Scan 1	0.56 ± 0.07	0.44 ± 0.08
	Scan 2	0.53 ± 0.09	0.39 ± 0.13
$MTR_{Rex}(\delta_{amide})$	Scan 1	0.015 ± 0.002	0.015 ± 0.002
	Scan 2	0.016 ± 0.002	0.015 ± 0.002
$MTR_{Rex}(\delta_{NOE})$	Scan 1	0.11 ± 0.005	0.11 ± 0.004
	Scan 2	0.11 ± 0.005	0.11 ± 0.003

Figure 3.5A illustrates an axial slice of a CEST image of one healthy participant. Figure 3.5B shows the AACID map from the first scan, while Figure 3.5C is the AACID map from the second scan, both from the same slice. Visually, the similarities between the AACID values of the two scans in both the GM and WM tissue is apparent. Figure 3.6 provides histograms of the distribution of the measurements of all CEST contrasts in GM (top row) and WM (bottom row) for the same healthy participant showing the initial scan and rescan overlayed.

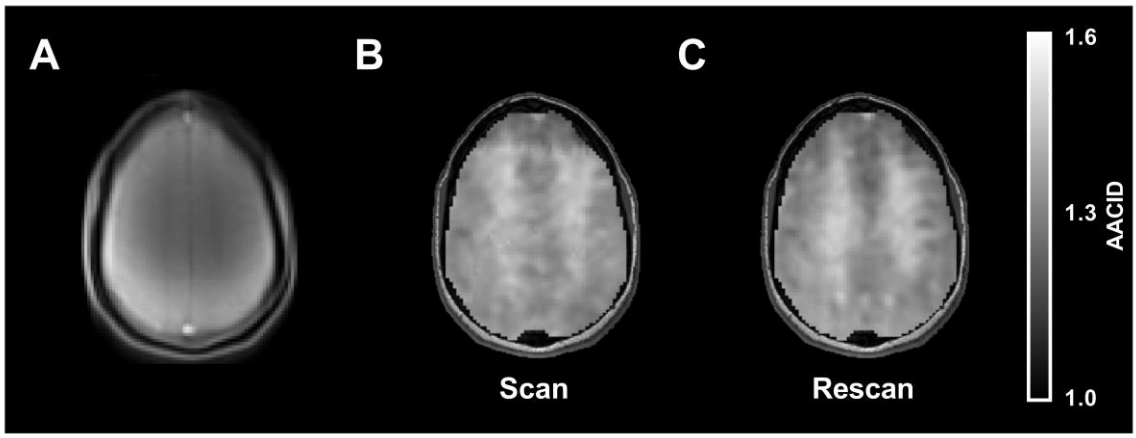

Figure 3.5: A. Axial CEST image of one slice (corresponding to the center of the 3D volume) of one healthy participant. **B-C.** Amide/amine concentration independent detection (AACID) map of the same healthy participant for the first scan (**B**) and second scan (**C**), with both overlayed onto the corresponding T_1-weighted axial slice.

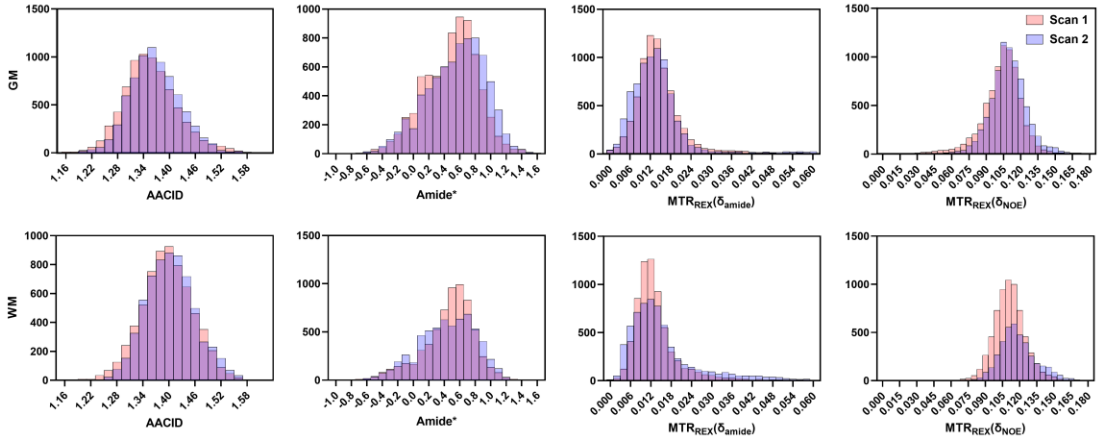

Figure 3.6: Histograms of the four different calculated contrasts of one healthy participant (amide/amine concentration independent detection (AACID), Amide*, $MTR_{Rex}(\delta_{amide})$, and $MTR_{Rex}(\delta_{NOE})$) for both the scan (pink) and rescan (blue) conditions. The top row shows the histograms for the gray matter region-of-interests (ROIs), while the bottom row shows the histograms for the white matter ROIs. The overlap of the two scans is demonstrated in purple and visually, the histograms show good reproducibility between scans for all calculated contrasts.

Between-subject reproducibility of all CEST contrasts was characterized using between-subject CV. Figure 3.7A demonstrates the between-subject CV of the different CEST contrasts for both GM and WM. AACID between-subject CV was 2.0% for GM compared to 1.3% for WM. In comparison, $MTR_{Rex}(\delta_{amide})$ demonstrated a between-subject CV for GM of 13.3% and a similar CV of 13.2% for WM. $MTR_{Rex}(\delta_{NOE})$ GM between-subject CV was 4.6% compared to 3.2% for WM. Finally, Amide* showed a between-subject CV in GM of 15.3% and 25.4% in WM.

Within-subject reproducibility for all CEST contrasts was characterized using both within-subject CV and percent difference. Figure 3.7B shows the within-subject CV of all CEST contrasts for both GM and WM. Within-subject CV for AACID was 1.2% for GM and 1.0.% for WM. Within-subject CV for $MTR_{Rex}(\delta_{amide})$ was 6.2% for GM and 5.5% for WM. Within-subject CV for $MTR_{Rex}(\delta_{NOE})$ was 1.3% for GM and 1.9% for WM. Finally, Amide* demonstrated within-subject CV of 10.7% for GM and 17.4%. for WM. Figure 3.7C illustrates the percent difference between the timepoints for all subjects in GM and WM showing all CEST contrasts. For GM, the lowest percent difference was 1.7% for AACID and 1.9% for $MTR_{Rex}(\delta_{NOE})$, followed by $MTR_{Rex}(\delta_{amide})$ with percent difference of 8.8%, and Amide* with percent difference of 15.9%. For WM, lowest percent difference was 1.4% for AACID and 2.7% for $MTR_{Rex}(\delta_{NOE})$, followed by $MTR_{Rex}(\delta_{amide})$ with percent difference of 7.8%, and Amide* with percent difference of 24.5%.

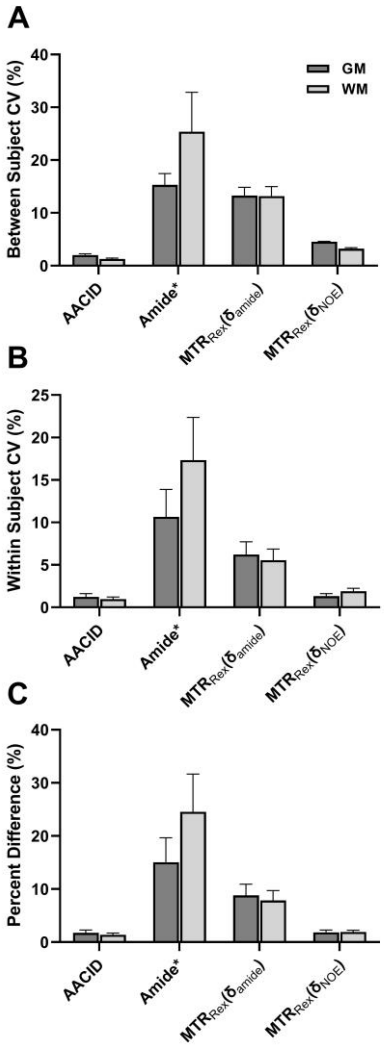

Figure 3.7: A. Mean between-subject coefficients of variation (CV) for each calculated contrast for both gray matter (GM) and white matter (WM). Between-subject CV values represent the mean ± standard error of the mean across the 12 participants (averaged over the two time points). **B.** Mean within-subject CV for each calculated contrast for both GM and WM. Within-subject CV values represent the mean ± standard error of the mean between the two time points (averaged across the 12 participants). **C.** Mean percent difference for each calculated contrast for both GM and WM. Percent difference represents the mean ± standard error of the mean between the two time points (averaged across the 12 participants).

3.4 Discussion

The goal of this study was to measure the reproducibility of four common CEST contrasts in healthy subjects in the brain at 3.0 T, which were acquired within a clinically feasible scan time. In egg-white phantoms and healthy human brain, it was found that the B_1 amplitude to maximize the amide CEST contrast was 0.5 μT when using a 3 s long train of 100 ms Gaussian pulses for selective saturation. The AACID measurement was shown to be linearly dependent on pH in egg white phantoms at 3.0 T, demonstrating that AACID CEST is sensitive to pH changes at this magnetic field strength. Overall, scan-rescan reproducibility within the same subject (within-subject CV and percent difference) was consistently better than the reproducibility between different subjects (between-subject CV) for both GM and WM tissue. Furthermore, both between-subject and within-subject reproducibility were similar in GM and WM for each of the different CEST contrasts; however, there were significant differences in the measured contrast between GM and WM among the four CEST contrasts. Finally, the results indicate that AACID CEST and $MTR_{Rex}(\delta_{NOE})$ were the most reproducible imaging biomarkers at 3.0 T in both GM and WM for the top portion of the cerebrum, which includes both the frontal and parietal lobes. Interestingly, the reproducibility differed greatly between $MTR_{Rex}(\delta_{amide})$ and Amide*, with the inverse fitting MTR approach having greater reproducibility.

The maximum amide signal in both the egg white phantom and healthy brain slices was obtained when using a pulse train with B_1 amplitude of 0.5 μT. A train of Gaussian pulses is commonly used at clinical field strengths such as 3.0 T, where the absolute frequency separation between resonances of interest is small compared to higher fields, leading to challenges in resolving specific CEST signals. Previous work at 3.0 T has shown that slow-exchanging pools (i.e., amide protons) do show greater detection sensitivity and spectral selectivity when using lower saturation powers (193), consistent with the current results. The high spectral sampling allows for several CEST effects to be discerned using the multi-pool Lorentzian model. This lower-power, high-spectral resolution approach has been used in previous studies (193,194), where it was shown that lower powers were optimal for isolating the amide CEST effect at 3.5 ppm. Despite the

sub-optimal saturation power used in the current study to detect the more quickly exchanging amine protons, the AACID measurement was found to be linearly dependent on pH at 3.0 T. While higher field strength studies have found that AACID has an inverse relationship with pH in stroke and tumor mouse models (129,130) when using higher power saturation to increase sensitivity to the amine CEST effect (125), the current results indicate that AACID is also sensitive to tissue pH at 3.0 T using saturation power levels optimized for amide CEST detection.

Consistent with previously published amide CEST studies (193,195,196), it was found that both $MTR_{Rex}(\delta_{amide})$ and Amide* had significantly higher signal in GM compared to WM. Similarly, the CEST-NOE signal ($MTR_{Rex}(\delta_{NOE})$) was found to be significantly greater in WM compared to GM, agreeing with previous literature (137,193,196). The CEST amide signal arises primarily from mobile proteins and peptides (122). Since GM contains a higher concentration of proteins compared to WM, as well as a higher density of cells, it is reasonable to expect that the resultant amide CEST effect would be larger in WM. On the contrary, the CEST NOE signal also has contributions from mobile lipids (197), which have a higher concentration in WM (198). Interestingly, a previous animal study of AACID found no significant AACID value differences between GM and WM in the mouse brain (129). However, the current study in the human brain showed that AACID was significantly greater in WM compared to GM, albeit the magnitude of the difference was small. The discrepancy may be due to differences in the composition or density of GM and WM in the mouse brain compared to the human brain, or may be due to methodological limitations in the mouse brain analysis, due to the very small WM area (corpus callosum) that may have been susceptible to partial volume contamination from surrounding GM. The field strength of the measurements was also very different than the current study.

Both the between-subject and within-subject reproducibility assessments demonstrated that AACID and $MTR_{Rex}(\delta_{NOE})$ measurements were the most reproducible. While the proton exchange rate is pH dependent, it is also a function of the bulk water T_1-relaxation rate. Zaiss *et al*. introduced the concept of AREX, or apparent exchange-dependent relaxation compensated CEST, and concluded that amide-CEST

contrast in the brain is influenced by the inherent water T_1-relaxation tissue properties (192) and a T_1 correction is necessary to achieve measurements independent of T_1. T_1 differences have been observed in human GM and WM (196,199), indicating the importance of a T_1 correction to produce CEST contrasts that are more accurate to a metabolite of interest. In the current study, T_1-relaxation was not considered in any of the CEST contrast calculations, except AACID, which demonstrated the highest reproducibility of the calculated CEST contrasts. Since AACID utilizes a ratiometric approach as well as a reference to normalize MT effects, AACID has been shown to have minimal dependence on temperature, bulk water T_1-relaxation, and macromolecule concentration (129,130).

Interestingly, between-subject reproducibility was also greatest for AACID and $\mathrm{MTR_{Rex}}(\delta_{\mathrm{NOE}})$ measurements, indicating that these contrasts may be the most robust of these imaging biomarkers. Studies of $\mathrm{MTR_{Rex}}(\delta_{\mathrm{NOE}})$ have shown that at 3.0 T in a glioma model, the tumour region was hypointense compared to the control region (200). AACID studies at a higher field strength have also shown that in animal models of ischemia, AACID values are consistently higher in regions of ischemia (129), and in glioma models, AACID measurements are consistently lower in the tumour regions compared to controls (130). Multiple studies have demonstrated that these individual contrasts significantly differ between normal tissue and various pathologies (i.e., ischemia and cancer). Therefore, these contrasts, which also demonstrate excellent between-subject reproducibility, would be preferred for clinical application to monitor changes in brain pathologies.

Amide* had poorer within-subject and between-subject reproducibility compared to the other calculated CEST contrasts. While the Amide* method has the benefit of being simple, it seems to underestimate the full extent of the amide CEST effect (201), lowering accuracy. In the current study, a pulse train with B_1 amplitude of 0.5 μT was used. Using a low power allows for several CEST effects to be discerned when using the multi-pool Lorentzian model, which is ideal when calculating $\mathrm{MTR_{Rex}}$, for both amide and NOE. Fitting allows for the removal of confounding components, like direct water saturation and MT (118), allowing for the $\mathrm{MTR_{Rex}}$ measurements to be a more accurate

representation of a metabolite of interest. This could explain why $MTR_{Rex}(\delta_{amide})$ had greater reproducibility than Amide*. The overall higher within- and between-subject CV value and percent difference of the $MTR_{Rex}(\delta_{NOE})$ contrast compared to $MTR_{Rex}(\delta_{amide})$ is likely due to the larger NOE effect compared to the amide effect at low saturation power levels. Studies have also previously demonstrated that low-power NOE CEST has larger observed effects at 3.0 T compared to amide CEST (135,193,194,202). This could produce a higher signal-to-noise (SNR) for the NOE effect in comparison to the amide effect, contributing to the reproducibility differences between $MTR_{Rex}(\delta_{NOE})$ and $MTR_{Rex}(\delta_{amide})$.

As with any study, there are several limitations that should be considered. First, it should be noted that optimization was performed using Lorentzian line fitting and the amplitude of the amide signal because AACID cannot be optimized based on power. Second, while no apparent signs of denaturing of the proteins occurred in the egg white phantoms, one should consider using a lower concentration of HCl to ensure minimum protein aggregation and conformational when performing optimization experiments. Slow-exchanging pools, like amide pools, show greater spectral selectivity and detection sensitivity at lower saturation powers (193,194), which also limits the MT effect and direct water saturation (118) and is beneficial for fitting-based approaches. A limitation that needs to be considered is that the B_1 amplitude was optimized based on the amide fit amplitude and was not optimized for each contrast. Asymmetry analysis also was not performed due to the low power chosen, which causes NOE to be a confounding factor in the contrast calculation. Also, Amide* relies on clear delineation of the raw data amide peak (124), which would be easier to distinguish at a higher field strength and may have improved the reproducibility of this contrast.

The current study also only investigated the reproducibility within a four cm 3D volume of tissue positioned at the upper portion of the cerebrum, containing the frontal and parietal lobes. Reproducibility measurements in the future should include more inferior regions and deep brain structures by performing whole-brain 3D CEST. While reproducibility was favourable in the current study, reproducibility may be different in some regions of the brain with lower signal to noise. It is possible that reproducibility

would be reduced for all the CEST contrasts in the lower regions of the brain, especially areas around the sinuses and ear cavities, like the orbitofrontal cortex. We would expect lower reproducibility in these areas due to the presence of greater B_0-inhomogeneities, which would impact the Z-spectrum and our calculated contrasts (203). Robust B_0-inhomogeneity correction would be of upmost importance when extending the coverage to full brain.

Spatial resolution of the CEST images (in-plane resolution of 2.0 x 2.0 mm) could also be improved in future studies to mitigate partial volume effects at the junction between the GM, WM, and CSF tissue. Although the regions were automatically segmented using the anatomical image and transformed to CEST space, CEST space ROIs could have included some contributions from different tissue types. While the AACID measurements had minimal dependence on T_1-relaxation, the other CEST contrast measurements were potentially affected by T_1, which could also affect their reproducibility and reliability as incorporating relaxation properties can lead to more accurate quantification due to the mitigation of any errors arising from variations in relaxation times between different tissues and subjects (192). Incorporating AREX (192) has been shown to be more sensitive to metabolite concentration and exchange rate without the confounding effects from MT- and T_1-relaxation (192,199,204) and only a T_1 map is needed to implement this correction. Incorporating this correction may improve the reproducibility and reliability of the other contrasts, especially the amide CEST contrasts. Finally, this study only measured the reproducibility in young participants at two time points on the same scanner. Increasing the number of repeated measures and extending the measurements to healthy older participants would provide a more robust measure of reproducibility. Reproducibility between scanners/vendors is also of interest when aiming for clinical implementation, as scanning on the same scanner is not always clinically feasible for follow up sessions.

3.5 Conclusion

The findings of this study indicate that AACID and $MTR_{Rex}(\delta_{NOE})$ measurements made using a 3D CEST sequence had the highest within-subject reproducibility for both GM

(CV of 1.2% and 1.3%, respectively) and WM (CV of 1.0% and 1.9%, respectively) at the clinically relevant field strength of 3T. Both contrasts could have the potential to be used to determine clinically relevant differences between brain tissue pathologies.

3.6 Acknowledgements

The authors thank all participants for their contribution to this project. We also thank Scott Charlton and Oksana Opalevych (CFMM, Robarts Research Institute, Western University) for facilitating MRI acquisitions.

3.7 Funding

NSERC Discovery Grant (RGPIN/05290-2020), Canada First Research Excellence Fund (BrainsCAN – https://brainscan.uwo.ca/). A.E. Cronin was supported in part by the NSERC Canada Graduate Scholarships Doctoral (CGS-D) program.

3.8 Supplementary Materials

3.8.1 CEST Acquisition

Supplementary Table 3.1: Offsets (measured in ppm) sampled to acquired Z-spectrum for all healthy participants (read left to right, top to bottom)

-300	-6.5	-6.0	-5.5	-5.0	-4.5	-4.3	-4.1	-3.9	-3.7
-3.5	-3.3	-3.1	-2.9	-2.5	-2.0	-1.5	-1.0	-0.5	-0.3
-0.1	0	0.1	0.3	0.5	1.0	1.5	1.7	1.9	2.1
2.3	2.5	2.7	2.9	3.1	3.3	3.5	3.7	3.9	4.1
4.3	4.5	5.0	5.5	6.0	6.5				

3.8.2 Fitting

Fitting was performed in MATLAB using the Levenberg-Marquardt algorithm using the following equation:

$$\frac{M_z(\Delta\omega)}{M_z^0(\Delta\omega)} = Z(\Delta\omega) = Z_{base} - \sum_i L_i\,(\Delta\omega) \qquad [1]$$

with

$$L_i(\Delta\omega) = A_i\,\frac{{\Gamma_i}^2/_4}{{\Gamma_i}^2/_4 + (\Delta\omega - \delta_i)^2} \qquad [2]$$

Each Lorentzian function (L_i) is defined for each offset ($\Delta\omega$) by amplitude A_i, full-width at half maximum (FWHM) Γ_i, and displacement from the frequency of bulk water protons δ_i. Z_{base} corrects for constant signal reduction.

Supplementary Table 3.2: Starting points and boundary values of all fit parameters of the five-pool Lorentzian fit. Chemical shift (δ) and FWHM (Γ) are given in ppm.

	Start	**Lower**	**Upper**
Zbase	95	50	100
A_{water}	67	2	100
Γ_{water} (ppm)	1.8	0.3	10
δ_{water} (ppm)	0	-1.0	1.0
A_{MT}	15	0	50
Γ_{MT} (ppm)	10	30	60
δ_{MT} (ppm)	-2.0	-2.5	0
A_{NOE}	40	0	20
Γ_{NOE} (ppm)	-1.0	0.4	6.0
δ_{NOE} (ppm)	-3.5	-4.0	-3.0
$A_{amide(3.50ppm)}$	5	0	20
$\Gamma_{amide(3.50ppm)}$ (ppm)	4.5	0.4	6.0
$\delta_{amide(3.50ppm)}$ (ppm)	3.5	3.2	3.8
$A_{amine(2.75ppm)}$	5	0	10
$\Gamma_{amine(2.75ppm)}$ (ppm)	1.0	0.4	6.0
$\delta_{amine(2.75ppm)}$ (ppm)	2.75	2.5	3.0

Chapter 4

4 Reproducibility of 3D pH-Weighted Chemical Exchange Saturation Transfer Contrast in the Healthy Cervical Spinal Cord

The work presented in this chapter is from the manuscript:

Alicia E Cronin, Patrick Liebig, Sarah A Detombe, Neil Duggal, Robert Bartha. Reproducibility of 3D pH-Weighted Chemical Exchange Saturation Transfer Contrast in the Healthy Cervical Spinal Cord. NMR in Biomedicine. 2024; 1-13. doi:10.1002/nbm.5103.

Permission to reuse this article has been obtained. Please see Appendix B.

4.1 Introduction

Magnetic resonance imaging (MRI) of the human spinal cord non-invasively provides essential structural information to help diagnose spinal cord disease and dysfunction. However, advanced functional and metabolic MRI remains a challenge due to the inaccessibility, anatomy, and motion of the spinal cord and its surrounding structures including the lungs, heart, and cerebrospinal fluid (CSF). Non-invasive assessment of ischemia and/or hypoxia is of particular interest in disease assessment because these conditions can lead to irreversible cell death. Ischemia and hypoxia of the spinal cord can be caused by compression (48,49), injury (205), vascular alterations (206), and multiple sclerosis (MS) (207). The prevalence of degenerative cervical myelopathy is particularly high in the aging population, with rates in North America approximated at 605 per million (152). Although surgery is the standard treatment for spinal cord compression, it remains difficult to identify patients, prior to surgery, who will not respond to the treatment. However, the presence of ischemia in the cord has been hypothesized as an important contributing factor to surgical response (48,49). Although methods to measure ischemia (i.e., arterial spin labeling) and hypoxia (i.e., magnetic resonance spectroscopy) are commonly used in the brain (208,209), such methods have not easily translated to the spinal cord. Recently, chemical exchange saturation transfer (CEST) MRI has been

utilized to measure altered pH in the brain caused by ischemia (180,210) and has shown promise for implementation in the spinal cord (141,142).

CEST is an MRI contrast that exploits the transfer of magnetic saturation from selectively excited endogenous or exogenous exchangeable protons to bulk water protons (112,113). These exchangeable protons can include but are not limited to, amide (NH) and amine (NH_2) protons, which can be found in tissue proteins and peptides (121). These exchangeable protons have distinct chemical shifts, allowing frequency-selective saturation through the application of narrow bandwidth radiofrequency (RF) irradiation. Given sufficient time, selectively saturated protons can exchange with protons in the bulk water pool, reducing the bulk water magnetization and creating image contrast (112,113,121). The exchange rate between these pools has been shown to be pH-dependent, creating an opportunity to produce pH-dependent contrast (122,211). Cellular response to ischemia and hypoxia includes the production of lactate and excess [H+] by anaerobic glycolysis altering tissue pH homeostasis (212). Consequently, pH-weighted CEST contrasts could identify ischemic and/or hypoxic tissue. It should be noted that studies have shown intracellular pH dynamically decreases due to ischemia and hypoxia, and when no reperfusion occurs, the level of pH reduction is maintained (213). The produced CEST effect is also dependent on magnetic field strength, with a greater CEST effect generally visible at high fields ($\geq$ 7.0 T) (113).

Several pH-weighted CEST contrasts have been developed and demonstrated in the brain, including amide proton transfer (APT) (122) and glucose CEST (glucoCEST) (126). Studies have previously shown that the ratio of the CEST effects from amide protons at 3.5 ppm and amine protons at 2.75 ppm produces a linear pH-dependence in the physiologic range. This ratiometric endogenous CEST contrast, called amine/amide concentration independent detection (AACID), is primarily sensitive to intracellular pH changes while having only a small dependence on temperature, bulk water T_1 relaxation, and macromolecule concentration (129,130). While the amine and amide CEST effects contributing to the AACID measurement represent the average tissue signal, they are heavily weighted to the intracellular compartment. The method has been used to track pH

changes in the brains of animals following ischemia and within tumours at 9.4 T (129,130).

Given the prevalence of spinal cord compression from degenerative disc disease, particularly in the elderly population, and the lack of measures that predict functional outcomes following surgical treatment, there is a need to develop more specific imaging biomarkers at clinically accessible field strengths (i.e., 3.0 T). AACID contrast could provide valuable information about spinal cord tissue hypoxia and ischemia, however, several challenges have limited in-vivo application. The spinal cord has a small diameter and is close to the lungs and heart, which creates problematic motion artefacts. Previously, Jones *et al.,* introduced a postprocessing correction scheme that can mitigate artefacts caused by signal drift, which can be induced by respiratory motion (137). Additionally, there is a potential for B_1 inhomogeneity in the spinal cord (214), which impacts AACID contrast as the CEST effect depends on the B_1 amplitude of the selective RF irradiation (215). Windschuh *et al.* previously introduced a B_1-inhomogeneity correction that improved CEST image quality in the brain at 7.0 T (216). Combining these corrections could improve the reproducibility of the CEST contrast along the healthy cervical spinal cord at 3.0 T.

The scan-rescan reproducibility of the AACID measurement was assessed at 3.0 T along the cervical spinal cord of healthy volunteers and AACID measurements were compared between levels of the cervical spinal cord. Furthermore, the current study evaluated previously introduced signal drift and B_1-inhomogeneity corrections to determine if they improved the reliability of quantitative AACID CEST measurements in the cervical spinal cord at 3.0 T.

4.2 Methods

4.2.1 Participants

The study was approved by the Western University Health Sciences Research Ethics Board. Informed consent was obtained from each healthy volunteer prior to the first scan. Participants with a previous diagnosis of any spinal cord pathologies, including

compression, injury, or MS were excluded. Twelve healthy young volunteers participated in the spinal cord reproducibility study (7 females, mean age (± SD) 26 ± 4 years). Each volunteer was scanned twice (10 ± 4 days between scans) to determine the reproducibility of the AACID CEST measurement at different levels of the cervical spinal cord.

4.2.2 Imaging Acquisition

Imaging was performed on a Siemens 3.0 T MAGNETOM Prisma Fit MRI scanner (Siemens, Erlangen, Germany) using a 64-channel head and neck coil to acquire all the data. The prototype CEST sequence consisted of a series of selective saturation pulses to produce CEST contrast followed by a rapid 3D gradient-echo readout using a centric spiral k-space sampling. The saturation scheme used in the current study consisted of a train of 30 Gaussian-shaped RF pulses ($B_{1,mean}$ = 0.5 μT) with length (t_{pulse}) of 100 ms and an interpulse delay (t_{delay}) of 1 ms, resulting in a total saturation time of 3.03s. A recovery time of 2 s was utilized after each readout period. This was chosen based off previous optimization experiments performed in the healthy brain and egg whites (Chapter 3).

To measure AACID CEST reproducibility in the spinal cord of human participants high-resolution (resolution parameters 0.8 x 0.8 x 0.8 mm^3) anatomical neck and spine images were acquired in each subject using a T_2-weighted sagittal 3D spin-echo sequence (repetition time(TR)/echo time(TE) = 1400/136 ms, flip angle (FA) 140°, number of slices = 64, number of averages = 2). The shim adjust volume (“shimbox”) was manually placed over the spinal cord area of interest to maximize the static magnetic field homogeneity. CEST images were obtained at each of 45 pre-saturation frequency offsets from -6.5 ppm to 6.5 ppm (densely sampled increments of 0.2 ppm around areas of interest (amide, amine, water, and nuclear Overhauser enhancement (NOE)), with 0.5 ppm increments elsewhere), and an additional frequency was acquired at -300 ppm as a control frequency. Non-saturated (S_0) acquisitions, achieved by applying saturating far off resonance at 100 ppm, were interleaved after every third frequency offset (total of 16 S_0 scans). See Supplementary Table 4.1 for specifics. In total, 62 image sets were acquired. The 3D CEST imaging volume was centered at the C4 level of the spinal cord for all subjects. The same saturation was used as previously described, with total

saturation time of 3.03s. The imaging parameters were matrix size = 96 x 96 x 14, nominal resolution = 2.0 x 2.0 x 5.0 mm^3, TR/TE = 3.35/1.16 ms, and GRAPPA acceleration factor = 2. The total CEST imaging scan time was 8 minutes and 14 seconds. Additionally, CEST images were acquired at three different B_1 amplitudes (the optimized B_1 value of 0.5 μT and two surrounding B_1 values of 0.2 μT and 0.8 μT) to implement a B_1 amplitude correction (216). To acquire the three Z-spectra at different B_1 amplitudes, the total scan time was 24 minutes and 42 seconds. A 2D flip angle map was also acquired in the same region for each participant using a gradient-echo sequence utilizing a turbo-FLASH readout. The imaging parameters were TR/TE = 5000/1.99 ms, 5 mm thickness, 8 slices (5 mm gap between slices), and a total acquisition time of 10 seconds. Since the flip angle map was 2D, interpolation between the slices was performed using an in-house MATLAB R2021a code (Mathworks, Natwick, MA, USA) to transform it into a 3D flip angle map.

A water saturation shift referencing (WASSR) scan was also acquired for B_0 correction (189). For WASSR saturation, a train of 5 Gaussian pulses with t_{pulse} = 50 ms, t_{delay} = 40 ms, and B_1 amplitude = 0.5 μT was used. Z-spectra were obtained using 25 frequency offsets from -2.5 ppm to 2.5 ppm, in increments of 0.2 ppm. The total WASSR scan time was 1 minute and 36 seconds. To ensure the 3D CEST volume was aligned between scans, an automated slice positioning scout sequence (Siemen's AutoAlign) was used during the first scan. AutoAlign was acquired using 3D FLASH using TR/TE = 3.30/1.27 ms, 1.7 mm^3 isotropic, FA = 8°, and acquisition time = 19 s. AutoAlign automatically aligned the follow-up 3D CEST volume position in a standardized manner.

4.2.3 CEST Postprocessing

For each time point, the T_2-weighted cervical spinal cord images were automatically segmented using the Spinal Cord Toolbox (SCT) v.5 (174). The segmentation quality was checked manually using the FMRIB Software Library (FSL) v.6.0 viewer, FSLeyes. The spinal cord vertebrae were automatically labelled using SCT, and the spinal cord level regions of interest (ROI) (C2-C6) were created. Registration of the 3D CEST images to the T_2-weighted image was also performed using the SCT, specifically using a multi-step,

non-rigid registration process. The spinal cord level ROIs were transformed into the CEST space for further analysis by applying the inverse transformation matrix obtained from the previous CEST image to T_2-weighted anatomical image registration.

All acquired and registered CEST data were loaded into MATLAB for further analysis using custom MATLAB code. All corrections and analyses were performed on Z-spectra produced for each pixel in the CEST image. To correct for any signal drift caused by respiratory motion in the spinal cord CEST scans, a signal drift correction first introduced by Jones *et al.* was implemented (137). To summarize, the signal intensities of the 16 S_0 offsets were spline-interpolated as a function of time in each pixel, and the spline-interpolated data was used to normalize the signal intensity of the other saturation frequency offsets to account for any signal drift. Henceforth, this will be called the signal drift correction.

To correct for B_0 field inhomogeneities, the Z-spectrum corresponding to each pixel was frequency shifted using the corresponding WASSR spectrum (189). Z-spectra from each pixel were then fitted with a six-pool Lorentzian model including water, amide, amine (2.75 ppm), amine (2.0 ppm), NOE, and MT pools. Fitting parameters can be found in Supplementary Table 4.2. For the spinal cord CEST scans, the three-point Z-B_1-correction method was implemented, which was first proposed by Windschuh *et al.* (216) and used to ensure all offsets of the Z-spectra had a signal corresponding to the signal associated with the optimized B_1 value.

The AACID value is the ratio of the amine proton CEST effect at 2.75 ppm and the amide proton CEST effect at 3.50 ppm, normalized by MT effects after saturation at 6.0 ppm (129). AACID was calculated using Equation 4.1:

$$AACID = \frac{M_z(3.50\,ppm) \times \left(M_z(6.0\,ppm) - M_z(2.75\,ppm)\right)}{M_z(2.75\,ppm) \times \left(M_z(6.0\,ppm) - M_z(3.50\,ppm)\right)} \quad [4.1]$$

where M_z is the bulk water magnetization. To determine AACID values at the different cervical spinal cord levels, the individual spinal cord level ROIs (C2-C6) were applied to the 3D cervical spinal cord AACID map, and the AACID values were averaged for each level.

4.2.4 Statistics

AACID measurement scan-rescan reproducibility was characterized for the different spinal cord levels using the coefficient of variation (CV) and the absolute difference of the AACID measurements for the following post-processing schemes: (1) signal drift correction and B_1 correction, (2) signal drift correction with no B_1 correction, (3) no signal drift correction with a B_1 correction, and (4) neither signal drift nor B_1 correction. The CV reflects both the variability and reproducibility of a measurement, while the absolute difference in AACID measurements reflects the reproducibility between scans. CVs were calculated between subjects and within subjects to quantify both the between-subject and within-subject repeatability and reproducibility, respectively. Between-subject CV was calculated for each time point separately as the standard deviation divided by the mean value across all subjects. The two time point CV values were averaged for the mean between-subject CV of each spinal cord level. Within-subject CV was calculated as the standard deviation divided by the mean of the two time points for each subject separately. The 12 within-subject CVs were averaged to determine the mean within-subject CV for each spinal cord level. The absolute difference of AACID measurements was calculated separately for each subject by taking the absolute difference of the AACID measurements of each time point. The 12 absolute AACID difference measurements were averaged to determine the mean absolute difference of each spinal cord level.

To compare the reproducibility of the four post-processing correction schemes, the mean absolute AACID difference between time points was compared between the different correction schemes for the spinal cord levels C3 – C5 using a Repeated One-Way ANOVA (corrected for multiple comparisons (Tukey), $p < 0.05$). To determine if AACID measurements significantly changed throughout the healthy spinal cord, the

average AACID measurements for each spinal cord level (C3 – C5) for both time points were compared using a Repeated One-Way ANOVA (corrected for multiple comparisons (Tukey), $p < 0.05$). This comparison was performed for each of the four different post-processing schemes. CV calculations were performed in MATLAB (R2021a), while all tests of significance and correlation were performed using GraphPad Prism 9 (San Diego, CA).

4.3 Results

Figure 4.1A illustrates the different cervical spine ROIs (labeled C2-C6) segmented using the SCT overlaid on the T_2-weighted anatomical image of one participant. The positions of slices 5 (through C3), 7 (through C4), and 10 (through C5) corresponding to the 3D CEST axial-oblique acquisition are outlined in yellow. Figures 4.1B-3D show the corresponding CEST images acquired at slices 5 (Figure 4.1B), 7 (Figure 4.1C), and 10 (Figure 4.1D), at the different spinal cord levels, using the optimized B_1 Gaussian saturation pulse amplitude of 0.5 μT (frequency offset = 100 ppm). The AACID maps of the spinal cord for each slice are overlayed on the corresponding T_2-weighted anatomical images (Figures 4.1E-4.1G). Figures 4.1H-4.1J provide the corresponding average uncorrected CEST spectra from the cord in slices 5, 7, and 10, respectively, with the 6-pool Lorentzian fit model overlayed.

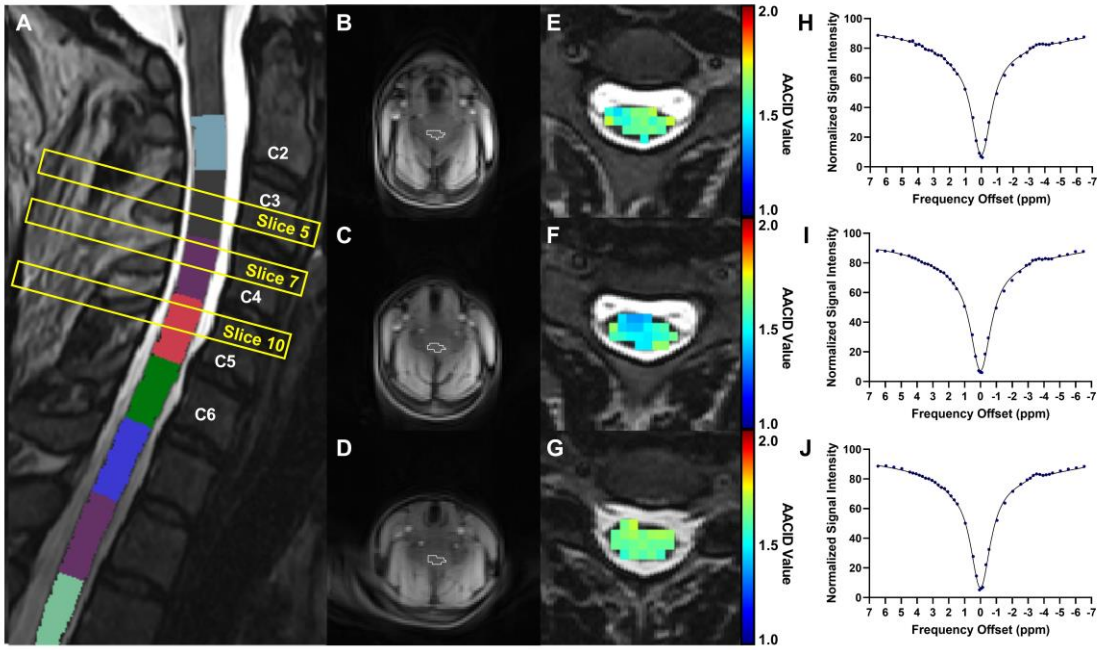

Figure 4.1: A. Sagittal T_2-weighted image of the cervical spinal cord of a healthy participant showing the segmented and labelled spinal cord levels (C2-C6), with the positions of corresponding CEST slices of interest overlayed in yellow. **B-D.** Axial oblique CEST images from the same participant corresponding to slices 5, 7, and 10 respectively in the 3D volume, shown by the yellow outlines in panel A. Each CEST image shows the spinal cord ROI outlined in white. The ROI was created by transforming the segmented cord into the CEST space. **E-G.** Amine/amide concentration independent detection (AACID) maps of the spinal cord corresponding to slices 5, 7, and 10, overlayed onto the corresponding T_2-weighted anatomical axial oblique image. **H-J.** Average raw CEST spectra (blue points) for all pixels within the cord in slices 5, 7, and 10, respectively, with the average 6-pool Lorentzian model fitted line overlayed.

Between-subject reproducibility of the AACID measurements was characterized using CV. Figure 4.2 demonstrates the between-subject CV of the AACID measurements at each spinal cord level, for each post-processing scheme. Spinal cord levels C3, C4, and C5, exhibited lower between-subject CVs (ranging between 5.6-10.7%) compared to spinal cord levels C2 and C6 (ranging between 14.7-25.1%). The middle of the stack of reconstructed CEST slices corresponds to the C4 level of the spinal cord, which had the lowest between-subject CVs (ranging between 5.6-6.3%) for all post-processing schemes. The specified ranges represent the minimum and maximum between-subject CVs obtained across all participants and post-processing schemes.

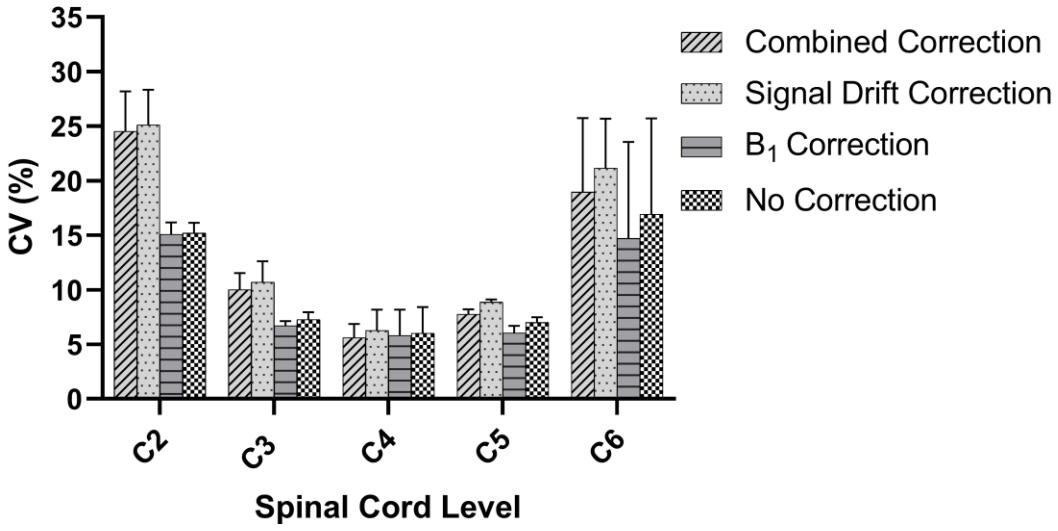

Figure 4.2: Mean between-subject coefficients of variation (CV) for each of the post-processing schemes at each spinal cord level (C2-C6). Between-subject CV values represent the mean ± standard deviation across the 12 participants (averaged over the two time points).

Within-subject reproducibility of the AACID measurements was characterized using both CV and absolute AACID differences. Figure 4.3A shows the within-subject CV of the AACID measurements at each spinal cord level, for each post-processing scheme. As with the between-subject CV, spinal cord levels C3, C4, and C5, demonstrated lower within-subject CVs (ranging between 4.1-7.4%) compared to C2 and C6 (ranging between 7.8-27.5%). The C4 spinal cord level also demonstrated the lowest within-subject CVs (ranging between 4.1-4.3%). These ranges represent the minimum and maximum within-subject CVs for the 12 participants at both time points, across all post-processing schemes. Figure 4.3B shows the average absolute AACID difference between the time points for all subjects at all spinal cord levels and post-processing schemes. The middle levels of the spinal cord (C3, C4, and C5) also exhibited lower absolute AACID difference values (ranging between 0.09–0.16, or 5.8-10.5% difference), with the very middle level (C4), demonstrating the lowest difference values (ranging from 0.089–0.093, 5.8-6.1% difference), compared to the spinal cord levels C2 and C6 (ranging from 0.16–0.55, 10.7-36.0% difference). These ranges represent the minimum and maximum absolute AACID difference across all participants and post-processing schemes. A summary of all CV and absolute difference measurements can be found in Supplementary Table 4.3.

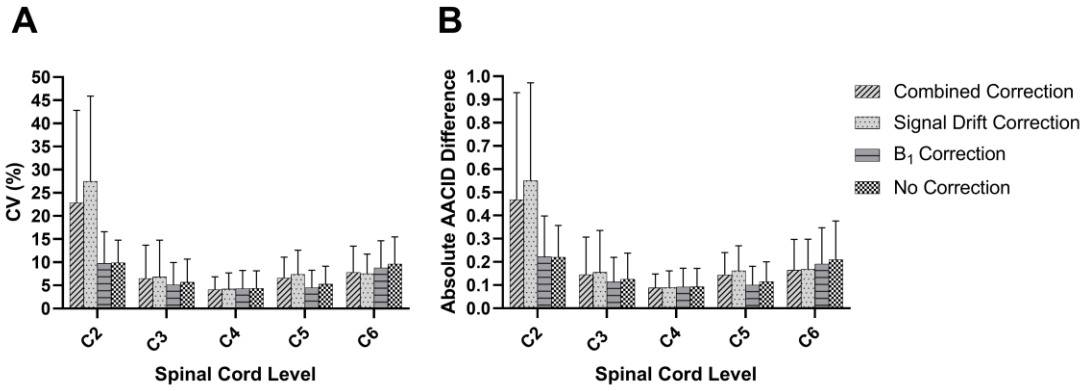

Figure 4.3: A. Mean within-subject coefficients of variation (CV) for each of the post-processing schemes at each spinal cord level (C2-C6). Within-subject CV values represent the mean ± standard error of the mean between the two time points (averaged across the 12 participants). **B.** Mean within-subject absolute amine/amide concentration independent detection (AACID) difference for each post-processing scheme at each spinal cord level (C2-C6). Absolute AACID difference values represent the mean difference ± standard deviation between the two time points (averaged across the 12 participants). A typical AACID value is ~1.5 in healthy spine.

To compare the four post-processing schemes and their effectiveness, the absolute AACID difference in the spinal cord was compared between time points using levels C3, C4, and C5, as illustrated in Figure 4.4. The B_1 correction significantly decreased AACID differences across time (adjusted p-value = 0.002) compared to using no correction. Compared to B_1 correction alone, the signal drift correction produced similar results ($p = 0.34$). When adding the B_1 correction with the signal drift correction (combined correction), no additional benefit was observed compared to B_1 correction alone ($p = 0.58$). Compared to using no correction, neither the signal drift correction ($p = 0.59$) or the combined correction showed any improvement ($p = 0.85$). The combined correction also did not show any significant AACID changes across time compared to the signal drift correction alone ($p = 0.29$). These data suggest that the B_1 correction alone was the most effective approach to improve reliability.

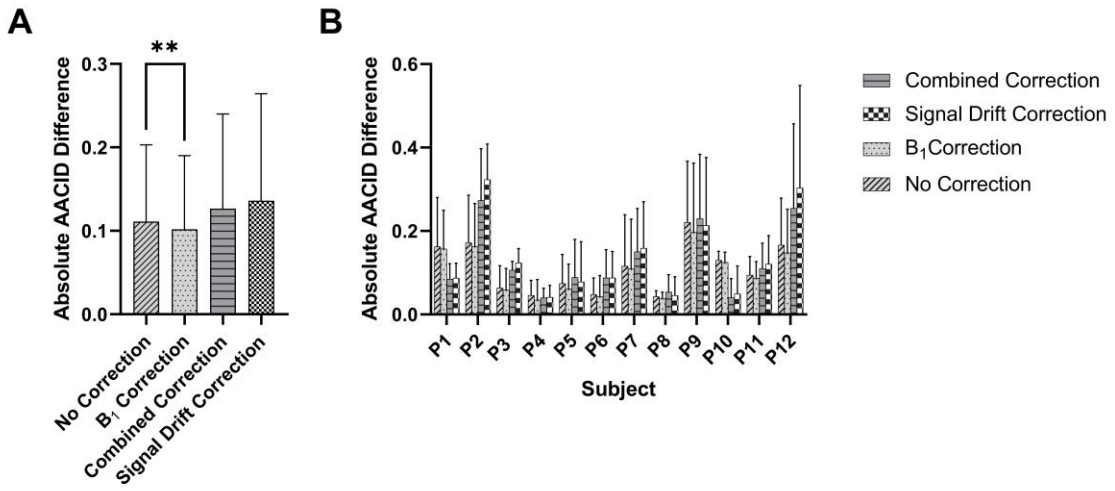

Figure 4.4: A. Mean absolute amine/amide concentration independent detection (AACID) difference between the two time points (with standard deviation) comparing the four different post-processing schemes at the spinal cord levels C3, C4, and C5. The B_1 correction significantly decreased AACID changes across time (adjusted p-value = 0.002) compared to no correction. Neither the signal drift correction nor the combined correction showed any improvement compared to no correction. **B.** Mean AACID difference between the two time points (with standard deviation) for all participants comparing the different post-processing schemes at spinal cord levels C3, C4, and C5.

To determine if the AACID measurements differed along the healthy cervical spinal cord, the average AACID values for both time points were compared between the spinal cord levels for all post-processing schemes. Figure 4.5 illustrates the results obtained for the B_1 correction post-processing scheme, showing that average AACID values were the same at each level (all adjusted p values were non-significant). The average AACID value across C3, C4, and C5 (the most reproducible spinal cord levels) following B_1 correction was 1.54 ± 0.09 (mean AACID ± SD). Similar results (data not shown) were obtained when comparing AACID values between segments after combined

correction, signal drift correction alone, and when using no correction. A summary of the AACID values for all subjects and post-processing schemes can be found in Supplementary Table 4.4. It should be noted that all results are depicted in AACID and not pH due to the inability to perform a calibration experiment at 3.0 T as done at 9.4 T in the mouse brain (129) because no ^{31}P-MRS experiments were performed in the spinal cord. AACID is inversely related to the tissue pH, where higher AACID values are associated with lower pH.

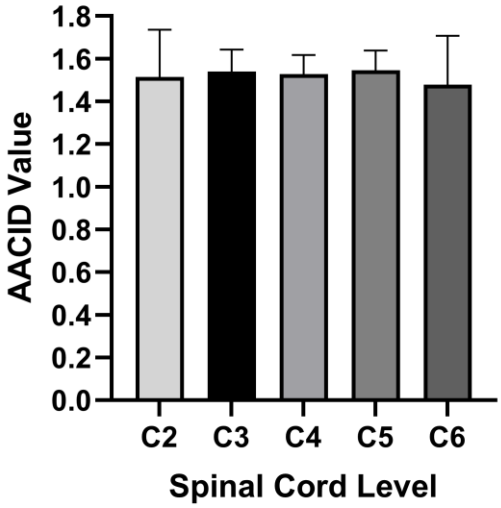

Figure 4.5: Average amine/amide concentration independent detection (AACID) values (with standard deviation) within different spinal cord levels. No significant differences in AACID values were observed between the cervical spinal cord levels for the B_1 correction post-processing scheme. Similar results were obtained for combined correction, signal drift correction alone, and when using no correction (not shown).

4.4 Discussion

The goal of this study was to measure the reproducibility of CEST contrast along the healthy cervical spinal cord at 3.0 T. In particular, the pH-sensitive AACID CEST measurement was made using a prototype 3D CEST sequence incorporating B_1-field inhomogeneity and signal drift post-processing corrections. AACID measurements were

found to be most reproducible at the center of the 3D CEST volume, corresponding to the spinal cord levels C3, C4, and C5, when considering both between-subject CVs, within-subject CVs, and absolute AACID differences measured over time. Absolute AACID percent difference was smallest at the C4 level at ~6%, demonstrating that the center of the CEST volume has the greatest reproducibility. Overall, within-subject CVs were lower than between-subject CVs for all spinal cord levels, indicating less variability within subjects for AACID scan-rescan measurements. While the use of B_1 corrections increased the reliability of repeated AACID measurements, the signal drift correction did not. Finally, AACID measurements did not differ between the C3, C4, and C5 spinal cord levels, suggesting that AACID values are consistent throughout the healthy cervical spinal cord.

The center of the CEST volume, corresponding to image slices at spinal cord levels C3 – C5, produced the most reproducible AACID measurements for all post-processing correction schemes. This result is not unexpected for several reasons. The CEST volume was centered at the C4 level in all participants, ensuring images at C4 were perpendicular to the spinal cord to minimize partial volume effects (214). However, when not perfectly perpendicular, a loss of spatial resolution can result in the blurring of adjacent structures. Most participants had some natural spinal cord curvature, causing slices at the edges of the CEST volume (i.e., in C2 and C6) to not be perfectly perpendicular to the cord. This misalignment could lead to some blurring in the CEST images due to partial volume effects which may affect the contrast and consequently the AACID measurements.

AACID reproducibility in the spinal cord was investigated at different cervical spine levels, incorporating previously published B_1 inhomogeneity correction and signal drift correction schemes. The signal drift correction scheme has been previously applied in the spinal cord at 3.0 T to examine the reproducibility of APT CEST measurements in five healthy controls; however, the study explored only a single slice centred at the C3/C4 level (142). The B_1 inhomogeneity correction method was first applied to CEST brain imaging at 7.0 T (216) and has now been implemented in multiple studies (217,218), including studies at 3.0 T (144,219). The B_1 inhomogeneity correction scheme

has not been previously tested in the cervical spinal cord, and the combination of the B_1 inhomogeneity and signal drift correction has not been explored. Use of the B_1 inhomogeneity correction resulted in a significant improvement in reproducibility compared to using no corrections. CEST contrast depends on the B_1 amplitude of the saturation pulses (215). Consequently, any spatial inhomogeneity in the applied B_1 can affect the contrast-to-noise ratio (CNR) of the CEST signal. The B_1 field is produced by a large body coil on the 3.0 T Siemens scanner used in the current study and is expected to be homogeneous within small tissue volumes. However, the spinal cord is long and surrounded by vertebral bodies, that can lead to B_1 non-uniformities as the vertebral bodies differ in electrical permittivity from the spinal cord (214). Furthermore, when extending coverage over a 3D volume, CEST effects become more sensitive to any inhomogeneity of B_1 irradiation (219). B_1 inhomogeneity correction could be of even greater importance in patient populations, which could introduce additional variability in tissue homogeneity due to edema and myelomalacia of neural tissue in the spinal cord (207).

Incorporating the signal drift correction to correct for signal changes due to respiratory motion did not demonstrate any significant improvement in the reproducibility of the AACID. Although a previous study has shown that the signal drift method slightly improved the reproducibility of ATP measurements in the spinal cord shown demonstrated by an improved intraclass correlation coefficient (ICC) value (142), our study used a different method to quantify reproducibility (CV and difference in AACID value). The lack of improvement in the current study could also be due to the level of the spine that was studied. Previous studies have shown that the greatest impact from respiratory motion occurs in the region of the cervicothoracic junction (220), which suggests that the largest signal fluctuations will occur in the C7 and upper thoracic regions, which correspond to the rostral portion of the lungs (143). Since magnetic field shifts and motion are more significant at spinal cord levels below those investigated in the current study, including this correction may improve AACID reproducibility and should be considered when examining lower levels of the spine.

The current study also found that AACID values were consistent between different levels of the cervical spine. For the cervical spinal cord, it has been shown that the structure (221) and MRI signal intensity (222) remain relatively constant throughout its length. It is also noteworthy that a previous study of AACID values found no significant AACID value differences between gray and white matter in the mouse brain (129). Since AACID value are expected to show little difference in gray and white matter, AACID values were expected to be consistent throughout the cervical spinal cord. As described by van Belle (223), the between-subject CVs of the C4 level can be used to determine the sample size required to detect a defined biological effect at a 95% significance level and power of 80%. In a previous study, ischemic tissue was estimated to have an AACID value that was ~5% higher than normal tissue (129). To detect a minimum change of 5% at the C4 level, a sample size of 19 is required in each group (ischemic and control). In comparison, to detect a change of 10%, a sample size of 5 is required in each group.

As with any study, there are several limitations that should be considered. First, the spatial resolution of the CEST images (in-plane resolution of 2.0 x 2.0 mm) was sufficient to identify the cord but resulted in some partial volume effects at the edges of the cord that could impact on the AACID measurements. Although the spinal cord ROIs were automatically segmented using the anatomical image and transformed into the CEST space, an ROI could include some pixels with CSF contributions. The small cross-sectional area of the cord (the widest part of the cervical cord is only ~1.5 cm in diameter) (140) would benefit from higher-resolution imaging to minimize partial volume effects. Increasing the spatial resolution would also allow for AACID to be measured in both gray and white matter.

Secondly, the CEST acquisition used in the current study was designed to maximize the CEST effect and signal-to-noise (SNR), and consequently scan time was not optimized. Implementation of the B_1 correction required that the CEST scan was repeated three times, resulting in a total CEST acquisition time of ~30 minutes. Future work in the spine should increase the resolution of the CEST images, while also implementing strategies to reduce the total scan time. Scan time could be shortened by

reducing the number of slices acquired, particularly in studies only interested in AACID measurements at one spinal cord level corresponding to the site of a spinal cord compression or injury and more sophisticated reconstruction methods, like compressed sensing. Another opportunity to reduce scan time is use a different B_1 correction method called the contrast-B_1-correction method (216). The contrast-B_1-correction method has been shown to provide better results with few scans (as few as two points compared to the Z-B_1-correction method) (216), which would reduce scan time.

In the future, collection of respiratory motion data using bellows and incorporating the bellows data with the drift correction, first implemented by By *et al.* (142), may significantly improve AACID reproducibility. Finally, the current study was designed to examine reproducibility in young participants using only two data points separated in time by approximately 10 days. A more robust measure of reproducibility would be made by increasing the number of repeated measures and extending the measurement to healthy older participants that are more representative of the patient populations who are likely to suffer degenerative disc disease causing spinal cord compression. Subject motion may be more problematic in elderly participants who are not comfortable lying down for extended periods of time.

4.5 Conclusion

This study successfully demonstrated that pH-weighted AACID measurements made using a 3D CEST sequence and incorporating B_1-inhomogeneity correction were reproducible within subjects (CV ~4%) along the healthy cervical spinal cord at the clinically relevant field strength of 3.0 T. Optimal image quality was achieved in the center of the 3D CEST volume, which should be centered over the spinal level of interest in future clinical studies.

4.6 Acknowledgements

The authors thank all participants for their contribution to this project. We also thank Scott Charlton and Oksana Opalevych (CFMM, Robarts Research Institute, Western University) for facilitating MRI acquisitions. We also thank Dr. Seth Smith (Vanderbilt

University) and Dr. Julian Cohen-Adad (Polytechnique University) for the insightful discussions on CEST in the spinal cord and spinal cord image processing, respectively.

4.7 Funding

This study was supported by the NSERC Discovery Grant (RGPIN/05290-2020) and the Canada First Research Excellence Fund (BrainsCAN – https://brainscan.uwo.ca/). A.E. Cronin was supported in part by the NSERC Canada Graduate Scholarships Doctoral (CGS-D) program.

4.8 Supplementary Materials

4.8.1 CEST Acquisition

Supplementary Table 4.1: Offsets (measured in ppm) sampled to acquired Z-spectrum for all healthy participants (read left to right, top to bottom), with non-saturated scan (S_0) of 100 ppm interleaved after every third frequency offset.

-300	100	-6.5	-6.0	-5.5	100	-5.0	-4.5	-4.3	100
-4.1	-3.9	-3.7	100	-3.5	-3.3	-3.1	100	-2.9	-2.5
-2.0	100	-1.5	-1.0	-0.5	100	-0.3	-0.1	0	100
0.1	0.3	0.5	100	1.0	1.5	1.7	100	1.9	2.1
2.3	100	2.5	2.7	2.9	100	3.1	3.3	3.5	100
3.7	3.9	4.1	100	4.3	4.5	5.0	100	5.5	6.0
6.5	100								

4.8.2 Fitting

Fitting was performed in MATLAB using the Levenberg-Marquardt algorithm using the following equation:

$$\frac{M_z(\Delta\omega)}{M_z^0(\Delta\omega)} = Z(\Delta\omega) = Z_{base} - \sum_i L_i\,(\Delta\omega) \qquad [4.8.1]$$

with

$$L_i(\Delta\omega) = \frac{A_i}{1 + \left(\frac{\Delta\omega - \delta_i}{\Gamma_i}\right)^2} \quad [4.8.2]$$

Each Lorentzian function (L_i) is defined for each offset ($\Delta\omega$) by amplitude A_i, full width at half maximum (FWHM) Γ_i, and displacement from the frequency of bulk water protons δ_i. Z_{base} corrects for constant signal reduction.

Supplementary Table 4.2: Starting points and boundary values of all fit parameters of the six-pool Lorentzian fit. Chemical shift (δ) and FWHM (Γ) are given in ppm.

	Start	**Lower**	**Upper**
Zbase	100	80	100
A_{water}	90	2	100
Γ_{water} (ppm)	1	0.03	2
δ_{water} (ppm)	0	-2	1.0
A_{MT}	10	2	20
Γ_{MT} (ppm)	10	7	100
δ_{MT} (ppm)	-2	-3	0
A_{NOE}	-2	-10	10
Γ_{NOE} (ppm)	0.8	0.1	2
δ_{NOE} (ppm)	-4	-4.25	-3.5
$A_{amide(3.50ppm)}$	1	0	10
$\Gamma_{amide(3.50ppm)}$ (ppm)	0.3	0.1	1
$\delta_{amide(3.50ppm)}$ (ppm)	3.5	3.25	3.75
$A_{amine(2.75ppm)}$	1	0	10
$\Gamma_{amine(2.75ppm)}$ (ppm)	0.3	0.1	1
$\delta_{amine(2.75ppm)}$ (ppm)	2.75	2.5	3.0
$A_{amine(2.0ppm)}$	1	0	10
$\Gamma_{amine(2.0ppm)}$ (ppm)	0.3	0.1	1
$\delta_{amine(2.0ppm)}$ (ppm)	2.0	1.75	2.5

4.8.3 Results

Supplementary Table 4.3: Summary of the mean between-subject coefficients of variation (CV), within-subject CV, and absolute amine/amide concentration independent detection (AACID) difference for each spinal cord level (C2-C6) for all post-processing schemes (averaged across the 12 healthy participants ± standard deviation).

		Combined Correction	Signal Drift Correction	B_1 Correction	No Correction
C2	Between-Subject CV	24.5 ± 3.6 %	25.1 ± 3.2 %	15.1 ± 1.1 %	15.2 ± 0.9 %
	Within-Subject CV	22.9 ± 19.9 %	27.5 ± 18.4 %	9.8 ± 6.8 %	9.9 ± 4.9 %
	AACID Absolute Difference	0.47 ± 0.46	0.55 ± 0.42	0.22 ± 0.18	0.22 ± 0.14
C3	Between-Subject CV	10.0 ± 1.5 %	10.7 ± 1.9 %	6.7 ± 0.4 %	7.3 ± 0.7 %
	Within-Subject CV	6.5 ± 7.2 %	6.9 ± 7.9 %	5.2 ± 4.8 %	5.7 ± 5.0 %
	AACID Absolute Difference	0.15 ± 0.16	0.16 ± 0.18	0.11 ± 0.11	0.13 ± 0.11
C4	Between-Subject CV	5.6 ± 1.3 %	6.3 ± 1.9 %	5.8 ± 2.4 %	6.0 ± 2.4 %
	Within-Subject CV	4.1 ± 2.8 %	4.2 ± 3.5 %	4.3 ± 3.9 %	4.3 ± 3.8 %
	AACID	0.09 ± 0.06	0.09 ± 0.07	0.09 ± 0.08	0.09 ± 0.08

	Absolute Difference				
C5	Between-Subject CV	7.8 ± 0.4 %	8.9 ± 0.2 %	6.1 ± 0.6 %	7.0 ± 0.5 %
	Within-Subject CV	6.6 ± 4.5 %	7.4 ± 5.2 %	4.5 ± 3.7 %	5.3 ± 3.9 %
	AACID Absolute Difference	0.15 ± 0.1	0.16 ± 0.11	0.10 ± 0.08	0.11 ± 0.08
C6	Between-Subject CV	19.0 ± 6.8 %	21.2 ± 4.5 %	14.7 ± 8.8 %	16.9 ± 8.8 %
	Within-Subject CV	7.8 ± 5.7 %	7.5 ± 4.2 %	8.8 ± 5.8 %	9.7 ± 5.8 %
	AACID Absolute Difference	0.16 ± 0.13	0.17 ± 0.13	0.19 ± 0.16	0.21 ± 0.17

Supplementary Table 4.4: Summary of the mean amine/amide concentration independent detection (AACID) for each time point (with standard deviation), comparing the four different post-processing schemes for each spinal cord level (C2-C6).

		Combined Correction	Signal Drift Correction	B_1 Correction	No Correction
C2	Scan 1	1.33 ± 0.36	1.31 ± 0.36	1.48 ± 0.23	1.47 ± 0.23
	Scan 2	1.55 ± 0.34	1.57 ± 0.36	1.55 ± 0.22	1.56 ± 0.23
C3	Scan 1	1.59 ± 0.18	1.60 ± 0.19	1.56 ± 0.10	1.56 ± 0.10
	Scan 2	1.53 ± 0.14	1.53 ± 0.14	1.52 ± 0.11	1.52 ± 0.12
C4	Scan 1	1.53 ± 0.07	1.53 ± 0.08	1.52 ± 0.11	1.53 ± 0.12
	Scan 2	1.55 ± 0.07	1.55 ± 0.12	1.53 ± 0.06	1.53 ± 0.07
C5	Scan 1	1.56 ± 0.13	1.56 ± 0.09	1.54 ± 0.10	1.54 ± 0.11
	Scan 2	1.58 ± 0.12	1.59 ± 0.14	1.56 ± 0.09	1.55 ± 0.10
C6	Scan 1	1.48 ± 0.35	1.49 ± 0.36	1.48 ± 0.31	1.51 ± 0.35
	Scan 2	1.52 ± 0.22	1.54 ± 0.28	1.48 ± 0.13	1.47 ± 0.16

Chapter 5

5 Spinal Cord pH-weighted CEST MRI Suggests Hypoxia in Degenerative Cervical Myelopathy

The work presented in this chapter is from the manuscript:

Alicia E Cronin, Patrick Liebig, Sarah A Detombe, Neil Duggal, Robert Bartha. Spinal Cord pH-weighted CEST MRI Suggests Hypoxia in Degenerative Cervical Myelopathy. *In preparation for submission.*

5.1 Introduction

Degenerative cervical myelopathy (DCM) is one of the leading causes of spinal cord dysfunction in adults over 55 years of age worldwide (7). The onset of DCM is often gradual and progresses stepwise (156,224), and the recommended treatment is surgical intervention by means of decompression surgery (10). The main objective of decompression surgery is to maintain neurological function and prevent further deterioration. Unfortunately, it has been observed that only about one-third of patients demonstrate improvement following surgery, while 40% maintain function and 25% worsen (10,13). These inconsistent results have created a need to identify predictors of surgical outcomes for potential surgical candidates to determine which patients would benefit from surgery and when.

Predictors of surgical outcomes have been extensively studied, with some predictors, like older age, longer duration of symptoms, and higher myelopathy severity, associated with worse outcomes (25,38). However, there is controversy surrounding the validity of these predictors, with queries surrounding the strength and direction of the relationship to surgical outcome (38). Imaging biomarkers have also been studied to predict outcomes in DCM patients. Studies have tried to associate poorer neurological recovery with hyper-intensity on T_2-weighted images (29), hypo-intensity on T_1-weighted images (28), and a combination of both T_1 and T_2 signal changes (28,38). Unfortunately,

these imaging measures undermine the importance of early diagnosis in these patients as these features probably reflect tissue that have already experienced neural injury.

Interestingly, ischemia and hypoxia in the spinal cord have been shown to be pathophysiological mechanisms that influence the progression of DCM (42) and recovery following decompression surgery (39,51). Therefore, the presence of ischemia and hypoxia could also be a predictor of surgical outcomes in this cohort of patients. Chemical exchange saturation transfer (CEST) MRI can be utilized to measure altered tissue pH in the brain and spinal cord (129,130,225,226). CEST exploits the transfer of magnetic saturation from selectively excited exchangeable protons to bulk water protons (112,113). Because the exchange rate between the exchangeable protons and bulk water protons is pH-dependent, pH-dependent contrast can be produced (122,211). pH-weighted CEST contrasts could identify ischemic and hypoxic tissue in the spinal cord due to the excessive production of lactate and [H+] by anaerobic glycolysis when the tissue is ischemic/hypoxic (212). Previous studies have demonstrated that the ratiometric endogenous CEST contrast, amine/amide concentration-independent detection (AACID), which is the ratio of the CEST effects from the amide protons at 3.5 ppm and amine protons at 2.75 ppm, produces a CEST contrast that is linearly dependent on pH in the physiological range (129). In the healthy cervical spinal cord at 3T, AACID CEST has been shown to be homogeneous and highly reproducible (225).

The purpose of the current study was to measure AACID values in the spinal cord of DCM patients and determine: (1) if there is a difference between AACID values at the compression site of DCM patients and the spinal cord of healthy control participants, (2) if AACID values change throughout the cord of DCM patients, and (3) if compression severity, which has previously been used as a proxy for hypoxia, is correlated with AACID measurements. It was hypothesized that DCM patients would exhibit higher AACID values at the site of compression compared to the healthy control participants, which is indicative of a lower tissue pH and hypoxic tissue.

5.2 Materials and Methods

5.2.1 Subjects

This study was approved by the Western University Health Sciences Research Ethics Board. Informed consent was obtained from each DCM patient and healthy control participant prior to the start of the study. Six patients (6 females, mean age (± SD) 53 ± 10 years) with symptoms of DCM and no other neurological disorders were recruited from October 2022 to July 2023. Five healthy older controls (4 males, mean age (± SD) 56 ± 16 years) with no history of neurological disorders were also recruited. Twelve younger healthy controls (7 females, mean age (± SD) 26 ± 4 years), with no history of neurological disorders, were also scanned at two different time points (10 ± 4 days between scans). The results from this younger control group have been previously published (225) and are included in this current study as an additional control group.

5.2.2 Imaging Acquisition

All imaging was performed on a Siemens 3.0 T MAGNETOM Prisma Fit MRI scanner (Siemens, Erlangen, Germany) equipped with a 64-channel head and neck coil to acquire all the data. T_2-weighted sagittal 3D spin-echo anatomical images of the neck and spine were acquired with the following scan parameters: repetition time (TR) of 1400 ms, echo time (TE) of 136 ms, flip angle of 140°, number of slices = 64, producing a 0.8 mm^3, number of averages = 2. The shim adjust volume ("shimbox") was manually placed over the spinal cord region of interest to maximize the static magnetic field homogeneity. A Siemens prototype CEST sequence was used, which consisted of a series of selective saturation pulses to produce CEST contrast, followed by a rapid 3D gradient-echo readout using a centric spiral k-space sampling. The selective saturation scheme consisted of 30 Gaussian-shaped RF pulses ($B_{1,mean}$ = 0.5 µT) with a pulse length (t_{pulse}) of 100 ms and an interpulse delay (t_{delay}) of 1 ms, resulting in a total saturation time of 3.03 s. A 2 s recovery time was employed after each readout. These parameters were chosen based on a previous optimization performed in both egg-white phantoms and brain data (225). CEST images were acquired at 45 pre-saturation frequency offsets ranging from -6.5 ppm

to 6.5 ppm (densely sampled increments of 0.2 ppm around areas of interest (amide, amine, water, and nuclear Overhauser enhancement (NOE), with 0.5 ppm increments elsewhere) and an additional frequency was acquired at -300 ppm for normalization. See Supplementary Table 5.1 for specific details.

In patients, the 3D CEST imaging volume was centered over the level of compression in the spinal cord. If the patient had more than one compression site, the 3D CEST imaging volume was centered between the compression sites. Table 5.1 provides demographic information of the patients, including compression site location. In controls, the 3D CEST imaging volume was either centered at the location of their matched patient (older healthy controls) or centered at the C4 level of the spinal cord (younger healthy controls). The imaging parameters were matrix size = 96 x 96 x 14, nominal resolution = 2.0 x 2.0 x 5.0 mm^3, TR/TE = 3.35/1.16 ms, and GRAPPA acceleration factor = 2. The total CEST imaging scan time was 8 minutes and 14 seconds. Additionally, CEST images were acquired at three different B_1 amplitudes (B_1 value of 0.5 μT and two surrounding B_1 values of 0.2 μT and 0.8 μT) to implement a B_1 amplitude correction (216), which has been shown to improve spinal cord CEST reproducibility (225). The total scan time to acquire three Z-spectra at different B_1 amplitudes was 24 minutes and 42 seconds. To implement the B_1 correction, a 2D flip angle map was acquired using a gradient-echo sequence utilizing a turbo-FLASH readout. The imaging parameters were TR/TE = 5000/1.99 ms, 5 mm thickness, 8 slices (5 mm gap between slices), and a total acquisition time of 10 seconds. Transformation to a 3D flip angle map was performed by interpolation between the slices using an in-house MATLAB R2021a code (Mathworks, Natwick, MA, USA).

A water saturation shift referencing (WASSR) scan was also acquired for B_0 correction (189). For WASSR saturation, a train of 5 Gaussian pulses with t_{pulse} = 50 ms, t_{delay} = 40 ms, and $B_{1,mean}$ = 0.5 μT was used and sampled at 25 frequency offsets from -2.5 ppm to 2.5 ppm, in increments of 0.2 ppm. The total WASSR scan time was 1 minute and 36 seconds.

Table 5.1: Demographic data and clinical characteristics of patients with degenerative cervical myelopathy (DCM).

Patient	Age Range 53 ± 10 years (Mean Age ± SD)	Sex	mJOA	Site of Compression
1	65+	F	12	C4/C5
2	30-49	F	17	C4/C5
3	30-49	F	15	C5/C6 C6/C7
4	30-49	F	15	C4/C5 C5/C6
5	50-64	F	16	C5/C6 C6/C7
6	50-64	F	15	C6/C7

mJOA = modified Japanese Orthopaedic Association

5.2.3 CEST Data Processing

The T_2-weighted cervical spinal cord images were automatically segmented using the Spinal Cord Toolbox (SCT) v.5 (174). Segmentation quality was manually checked using the FMRIB Software Library (FSL) v.6.0 viewer, FSLeyes. Registration of the 3D CEST images to the T_2-weighted image was performed by a multi-step, non-rigid

registration process utilizing the SCT. The spinal cord segmentation was transformed into the CEST space for further analysis by applying the inverse transformation matrix obtained from the previous CEST image to T_2-weighted anatomical image registration.

All acquired and registered CEST data was loaded into MATLAB custom code. All corrections and analyses were performed on Z-spectra produced for each pixel in the CEST image. To correct for B_0 inhomogeneities, the corresponding Z-spectrum of each pixel was frequency-shifted using the corresponding WASSR spectrum. For each pixel, the Z-spectrum was fitted with a six-pool Lorentzian model including water, amide, amine (2.75 ppm), amine (2.0 ppm), NOE, and magnetization transfer (MT) pools. More information regarding fitting is available in the Supplementary Materials, and specific fitting parameters can be found in Supplementary Table 5.2. To correct for B_1-inhomogeneities, the proposed method by Windschuh *et al.* (three-point Z-B_1-correction) was implemented (216).

AACID is the ratio of the amine proton CEST effect at 2.75 ppm and the amide proton CEST effect at 3.50 ppm, normalized by MT effects after saturation at 6.0 ppm (129). AACID was calculated using Equation 5.1:

$$AACID = \frac{M_z(3.50\ ppm) \times \left(M_z(6.0\ ppm) - M_z(2.75\ ppm)\right)}{M_z(2.75\ ppm) \times \left(M_z(6.0\ ppm) - M_z(3.50\ ppm)\right)} \quad [5.1]$$

where M_z is the bulk water magnetization. The AACID map of the slice corresponding to the site of compression was averaged to find the AACID value corresponding to compression for each patient. If the patient had multiple compression sites, the average AACID value was determined for each compression site. The AACID maps above the compression (slice 3), and below the compression (slice 11) were also averaged to find the corresponding AACID values. In healthy controls, the center slice AACID map was averaged to find the control AACID value.

5.2.4 Compression Measurement

The severity of compression was compared to the AACID measurements found at the compression site of each patient. The compression volume was measured using a previously published approach (227). In short, using the patient's segmented cord and custom MATLAB code, the total volume of the compressed region was measured by identifying the limits of the compressed region using the rate of change of the compressed cord area and then summing the areas of each slice within the compressed region (227). This spinal cord severity metric is total compression volume and is measured in units of mm^3. If a patient had more than one compression site, a separate measurement was made for each site.

5.2.5 Statistics

To determine if AACID measurements significantly differ in the spinal cord of DCM patients, the average AACID slice measurements for the compression site, above the compression, and below the compression site were compared using a repeated one-way ANOVA (corrected for multiple comparisons (Tukey), $p < 0.05$). To determine if AACID measurements at the site of compression in DCM patients were significantly different than the controls, two different Welch's t-tests ($p < 0.05$) were used: (1) DCM patient mean AACID compression value compared to younger control mean AACID value from slices 6-8, and (2) DCM patient mean AACID compression value compared to older control mean AACID value from slices 6-8. Multiple slices around the centre of the 3D volume were chosen as a previous study demonstrated that the centre had the most reproducible measurements and AACID did not significantly differ along the healthy cervical spinal cord (225). Pearson's correlation coefficient (r) was used to determine if the severity of spinal cord compression in DCM patients was correlated with the mean AACID value measured at the compression site.

5.3 Results

Three of the DCM patients had multiple sites of compression and AACID values were found for each site, resulting in 9 AACID compression measurements. Figure 5.1A and

5.1D demonstrate the T_2-weighted anatomical image of one DCM patient and their age-matched healthy control, respectively. The position of the center slice (slice 7) corresponding to the 3D CEST axial-oblique acquisition is outlined in yellow on both panels. The corresponding AACID maps of the spinal cord for the slice are overlayed on the corresponding T_2-weighted axial anatomical image for the DCM patient (Figure 5.1B) and healthy control (Figure 5.1E). Figures 5.1C and 5.1F provide the corresponding average CEST spectra for the patient and healthy control, respectively, with the 6-pool Lorentzian fit model overlayed. These example images highlight both the reduced size of the spinal cord at the site of compression and suggest that within this DCM participant, the AACID value is slightly higher (1.64 ± 0.09 (mean AACID ± SD)), than the average value in the control participant (1.53 ± 0.10).

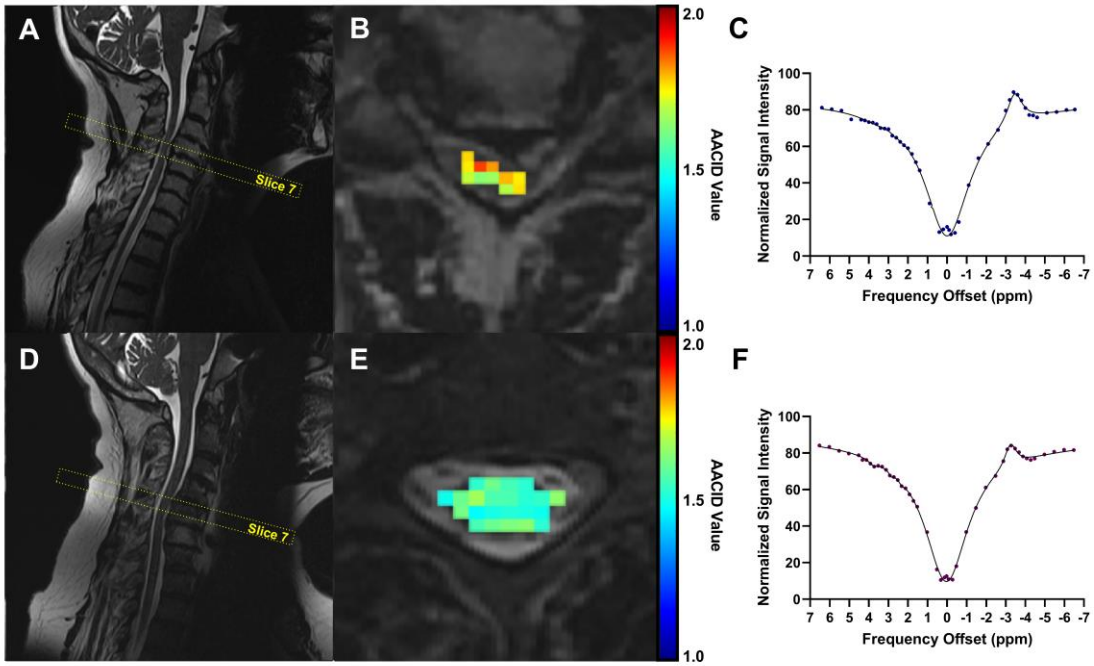

Figure 5.1: A. Sagittal T_2-weighted image of the cervical spinal cord of a degenerative cervical myelopathy (DCM) patient, with the position of CEST slice 7 overlayed in dotted yellow. **B.** Amine/amide concentration independent detection (AACID) map of the compressed spinal cord of the DCM patient, overlayed onto the corresponding T_2-weighted anatomical axial oblique image. **C.** Average raw CEST spectrum (blue points) for all pixels within the cord in slice 7 of the DCM patient, with the average 6-pool Lorentzian model fitted line overlayed. **D.** Sagittal T_2-weighted image of the cervical spinal cord of a healthy control, with the position of CEST slice 7 overlayed in dotted yellow. **E.** AACID map of the spinal cord, corresponding to slice 7, overlayed onto the corresponding T_2-weighted anatomical axial oblique image. **F.** Average raw CEST spectrum (purple points) for all pixels within the cord in slice 7 of the healthy control, with the average 6-pool Lorentzian model fitted line overlayed.

To determine if the AACID measurements differed along the cervical spinal cord of the DCM patients, the average AACID value of the slices at the sites of compression, above the site of compression, and below the site of compression were compared. Figure 5.2 illustrates the results of the comparison between the compression sites (n = 9) of the patients to other locations along the spinal cord (all adjusted p values were non-significant). Specifically, the difference was not significant between the compression site and above the compression (n = 6) (adjusted p-value = 0.85), or between the compression site and below the compression (n = 6) (adjusted p-value = 0.15). The average AACID value at the compression site was 1.64 ± 0.07 (mean AACID ± SD). Furthermore, the average AACID value above the compression site was 1.58 ± 0.19, and the average value below was 1.48 ± 0.17.

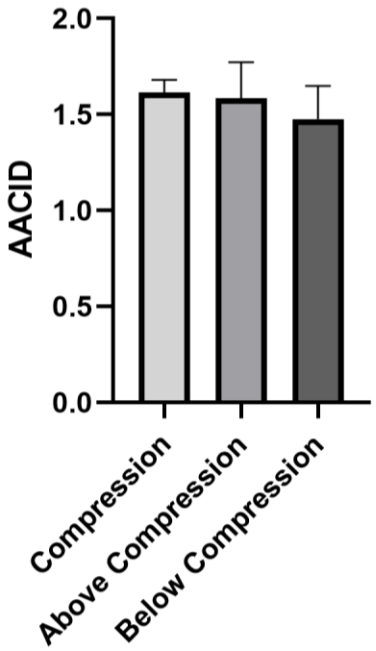

Figure 5.2: Mean single slice amine/amide concentration independent detection (AACID) (with standard deviation) corresponding to the compression site for degenerative cervical myelopathy (DCM) patients (n = 9), a single slice above the compression (slice 3) (n = 6), and a single slice below the compression (slice 11) (n = 6). No significant differences were observed throughout the spinal cord of DCM patients.

To evaluate if AACID measurements can distinguish the spinal cord of patients from the spinal cord of healthy subjects, AACID measurements at the site of compression were compared to the healthy participants, as illustrated in Figure 5.3. The average AACID value for the compression site of DCM patients ($n = 9$) was 1.64 ± 0.07 (mean AACID ± SD), 1.54 ± 0.10 for younger controls ($n = 24$, slices 6-8), and 1.55 ± 0.08 for older controls ($n = 5$, slices 6-8). The AACID measurement at the site of compression was significantly different compared to the younger controls ($p < 0.05$), as shown in Figure 5.3. Interestingly, the older controls did not have a significantly different AACID value than the patient compression value ($p = 0.16$), also demonstrated in Figure 5.3. Figure 5.4 illustrates the relationship between compression severity and the AACID measurement at the site of compression. Finally, there is no significant relationship between patient compression severity and AACID measurements at the site of compression ($p = 0.17$, $r = 0.51$).

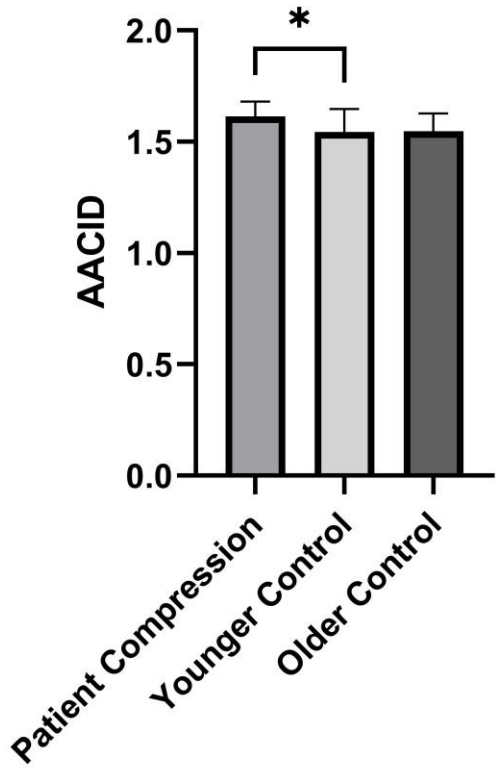

Figure 5.3: Mean amine/amide concentration independent detection (AACID) (with standard deviation) corresponding to the single slice at the compression site for degenerative cervical myelopathy (DCM) patients (n = 9), slices 6-8 for the younger healthy controls (n = 24), and slices 6-8 for older healthy controls (n = 5). DCM patients had a significantly higher AACID value than younger controls (p = 0.03).

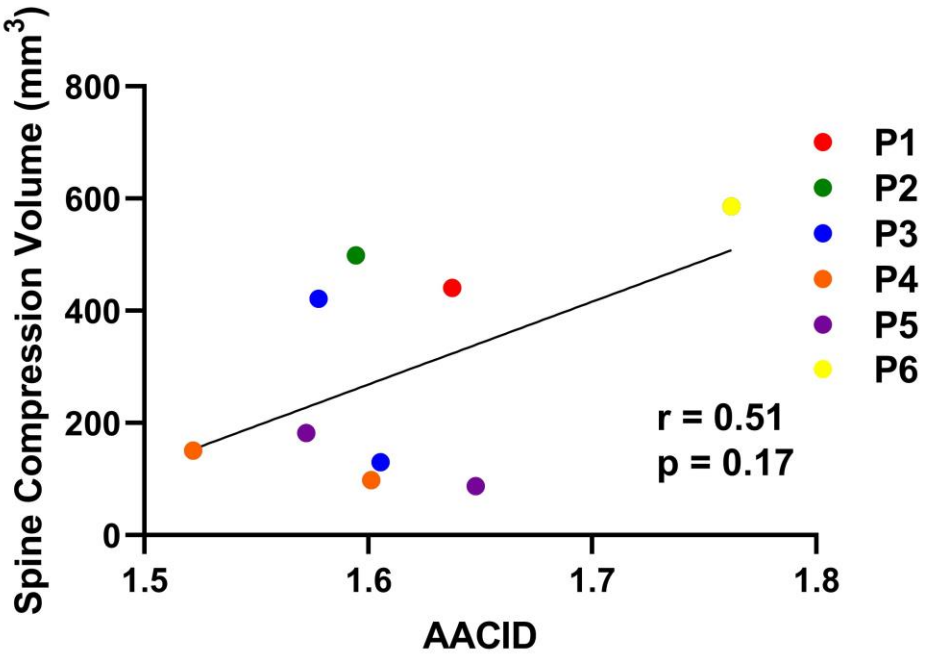

Figure 5.4: The correlation measured between the amine/amide concentration independent detection (AACID) value at the spinal cord compression of degenerative cervical myelopathy (DCM) patients and the associated spine compression volume, demonstrating a nonsignificant linear relationship ($p = 0.17$, $r = 0.51$).

5.4 Discussion

The goal of this study was to determine if AACID CEST, at the clinically relevant field strength of 3.0 T, could be used to detect an acidic tissue environment at the site of spinal compression in people with DCM compared to the spinal cord of healthy participants. Such data would provide evidence to support the hypothesis that tissue hypoxia may contribute to the pathology of DCM at the site of spinal compression. Based on a previous CEST reproducibility study in the spinal cord (225), the 3D CEST volume was centered at the site of compression for all patients and a B_1 magnetic field correction was performed. The current study suggests that AACID measurements were significantly higher at the site of spinal compression in people with DCM than that observed in healthy

young participants, but not different compared to older participants. Throughout the spinal cord of the people with DCM, it was found that the AACID values do not significantly differ between the compression site and that found above or below the compression site, suggesting that hypoxia might extend beyond the site of compression. Finally, AACID measurements at the site of spinal compression did not significantly correlate with the compression severity metric, indicating that the compression metric, which was used as a proxy for hypoxia in a previous study (227), might be too crude to capture subtle changes in hypoxia.

There is mounting evidence that ischemia and hypoxia are important pathophysiological mechanisms in the progression of DCM and recovery after decompression surgery. Direct in-vivo quantification of this tissue injury mechanism has been challenging in humans to date. However, several previous studies have provided evidence to support this theory. For example, Mair & Druckman demonstrated that spinal compression led to the thickening of the arterial and small vessel walls at the site of compression, causing reduced blood flow velocity and impaired regional perfusion (44). Similarly, a study performed by Ellingson *et al.* found decreased blood flow in the spinal cord area experiencing compression, which was measured using dynamic susceptibility contrast perfusion MRI (47). MR spectroscopy has also shown lactate peaks in the spinal cord of DCM patients, indicating that anaerobic metabolism is occurring, and ischemia and hypoxia are present (228). In addition, studies in animal models (48,50) and histological changes (24,44) have also provided indirect evidence of this pathophysiological mechanism occurring. Histopathological autopsy studies have shown necrosis and cystic cavitation in the central gray and white matter, which progresses to lacunae, gliosis, and anterior horn dropout (229). In agreement, animal studies have demonstrated that decreased blood flow in the compressed spinal cord is related to anterior-posterior spinal cord compression and microvessel changes (48). In the current study, pH-weighted (AACID) CEST contrast was measured at the site of spinal cord compression in humans to determine if pH changes were present, which is indicative of hypoxia. At the group level, it was found that AACID measurements at the site of compression in DCM patients were significantly higher than in young healthy participants but not from older healthy participants. This observation supports the

hypothesis that hypoxia exists in the spinal cord in DCM patients, as it has been demonstrated that a higher AACID value is associated with a lower pH (129,130). While no difference was observed between the patients and the older healthy participants, it is possible that an age effect may obscure the changes (230,231), but more likely it is simply a lack of statistical power as only five older healthy participants were included. The increase in AACID value (suggesting lower pH) in the spinal cord of people with DCM compared to young healthy participants is consistent with previous animal studies that have demonstrated spinal cord compression is associated with decreased spinal cord blood flow and ischemia.

The measurement of human spinal cord microcirculation during compression is beyond the scope of the current study. Interestingly, studies have shown that spinal cord ischemia can manifest differently depending on the nature of the compression. It has been reported that posterior cord compression reduces the central gray matter blood flow through intramedullary branches, while anterior cord compression reduces the blood flow of the anterior sulcus arteries through the transverse arterioles (11,45). Spinal cord compression has demonstrated localized ischemia and hypoxia at the site of compression (48), resulting in neurological dysfunction and neuronal cell apoptosis (10,18). However, ischemic damage may not be localized to the site of compression and have a more extensive effect above and below the site. The specific vascular anatomy of the compressed region could create more widespread ischemic effects around the compression site. While the anterior spinal artery supplies two-thirds of the blood supply to the spinal cord (5), both the posterior and anterior arteries are highly interconnected along the cord at a capillary level (232). The watershed areas of the spinal cord could also become hypoxic if nearby areas are subjected to compression (233). Watershed areas are created when opposing blood flow currents meet due to the highly complex haemodynamics of the cord, with blood flow being both ascending and descending (234). The current study demonstrated that there were no significant differences in the AACID measurements between the site of compression and the spinal cord above and below, suggesting that ischemia and hypoxia can have a widespread effect. This extensive ischemic effect could also make the spinal cord more vulnerable to vascular network

damage compared to the brain; tissue oxygen levels in the spinal cord are the same as in the brain (35-39 mmHg), but blood flow is 40-60% lower (235).

A previous study suggested that there was a significant correlation between spinal cord compression volume, which was used as a proxy for hypoxia, and cortical plasticity in the brain (227). The study hypothesized that the increased cortical plasticity observed in more severely compressed DCM patients was due to cortical reorganization, which is a compensatory response to tissue damage in the cord (110,227). This observation could be another indicator that ischemia and hypoxia may not just affect the site of compression or the spinal cord but could affect other parts of the body. However, this study used compression severity as a proxy for hypoxia. When AACID, which is a more direct measure of hypoxia, was correlated with compression severity in the current study, no significant correlation was found. The compression volume metric may not encompass the complexity of hypoxia in the spinal cord. Ramsey *et al.* performed a study in monkeys with controlled epidural compression using balloons, both anteriorly and posteriorly (236). Using selective spinal angiography, it was found that while severe compression resulted in significant blood flow reduction, moderate anterior compression also caused microvasculature deformation and reduced blood flow in the gray matter. This study indicates that compression severity might not be linearly correlated with blood flow and ischemia.

Limitations of this current study must also be considered. The spatial resolution of the CEST images (in-plane resolution of 2.0 x 2.0 mm) should be improved in the future as the spinal cord has a small cross-sectional area (cervical cord widest part is ~1.5 cm in diameter) (140), while, in people with DCM, the compressed cord is even smaller. Higher-resolution imaging would also be beneficial for mitigating partial volume effects. Interestingly, studies have demonstrated that ischemic injury of the gray and white matter occurs in DCM patients, causing malperfusion of the gray and medial white matter (11,45). Spinal cord ischemia can manifest differently; anterior spinal artery disruption causes ischemia to be limited to the bilateral or unilateral anterior horns and adjacent white matter (237) while posterior spinal artery disruption can cause ischemia to affect the posterior columns or the surrounding white matter (238). It has also been shown that

capillary network density is higher in gray matter compared to white matter (239), and while motor neurons are located in areas of lower density, there is a higher risk of damage due to vascular alterations. Increasing the spatial resolution of the CEST images would allow AACID to be measured in both tissue types to determine if ischemic injury is differentiable between tissues.

Second, the statistical power of this study must be increased. Due to the low numbers of patients and older controls, it is challenging to detect differences in the AACID measurements between the groups and along the spinal cord of the DCM patients. A previous study determined that to detect a minimum AACID change of 5%, a sample size of 19 in each group would be required (225). Also, the previous study found that while the center of the 3D volume has a variability of ~4%, moving above and below can increase the variability to ~10% (225). While the slices chosen to examine the AACID measurements along the cord in the 3D CEST volume have less variability than the first and last slices, the increased variability in the surrounding spinal cord AACID measurements is a limitation. To mitigate this problem, performing a variable slice angulation scheme that maintains slice perpendicularity to the spinal cord would be optimal, improving variability while mitigating partial volume effects.

In the future, a study utilizing both task-based functional MRI and AACID CEST should be performed to determine if ischemic injury in the cord leads directly to cortical reorganization in the brain to adapt to the functional deficits experienced by DCM patients (227). Also, the comparison of ischemia in mild, moderate, and severe DCM patients, based on mJOA scores, should be performed. Characterizing AACID changes along the spinal cord in patients with mild and severe symptoms could uncover if the contribution of ischemia/hypoxia differs between groups. Including a broader range of symptom severity would also help to determine how sensitive the AACID measurement is to functional changes. Finally, a study should be performed linking AACID measurements to outcomes following decompression surgery to determine if AACID could be utilized as a predictor of long-term functional outcomes for these patients. Such a biomarker could help to identify which and when patients should undergo surgery, with

the goal of fine-tuning patient selection to those that will improve or remain neurologically stable after decompression surgery.

5.5 Conclusion

The current study supports the hypothesis that spinal cord compression in DCM patients may result in both spinal cord ischemia and hypoxia. The extent of spinal cord ischemia could extend beyond the site of compression. Future work should correlate AACID measurements to neurological outcomes after decompression surgery to determine if the magnitude of pH change can predict long-term functional outcomes.

5.6 Acknowledgements

The authors thank all participants for their contribution to this project. We also thank Scott Charlton and Oksana Opalevych (CFMM, Robarts Research Institute, Western University) for facilitating MRI acquisitions. We would also like to thank Jennifer Murphy for all her help with patient recruitment.

5.7 Funding

NSERC Discovery Grant (RGPIN/05290-2020), Canada First Research Excellence Fund (BrainsCAN – https://brainscan.uwo.ca/). A.E. Cronin was supported in part by the NSERC Canada Graduate Scholarships Doctoral (CGS-D) program.

5.8 Supplementary Materials

5.8.1 CEST Acquisition

Supplementary Table 5.1: Offsets (measured in ppm) sampled to acquired Z-spectrum for all patients and healthy controls (read left to right, top to bottom), with non-saturated scan (S_0) of 100 ppm interleaved after every third frequency offset.

-300	100	-6.5	-6.0	-5.5	100	-5.0	-4.5	-4.3	100
-4.1	-3.9	-3.7	100	-3.5	-3.3	-3.1	100	-2.9	-2.5
-2.0	100	-1.5	-1.0	-0.5	100	-0.3	-0.1	0	100
0.1	0.3	0.5	100	1.0	1.5	1.7	100	1.9	2.1
2.3	100	2.5	2.7	2.9	100	3.1	3.3	3.5	100
3.7	3.9	4.1	100	4.3	4.5	5.0	100	5.5	6.0
6.5	100								

5.8.2 Fitting

Fitting was performed in MATLAB using the Levenberg-Marquardt algorithm using the following equation:

$$\frac{M_z(\Delta\omega)}{M_z^0(\Delta\omega)} = Z(\Delta\omega) = Z_{base} - \sum_i L_i\,(\Delta\omega) \qquad [5.8.1]$$

with

$$L_i(\Delta\omega) = \frac{A_i}{1 + \left(\frac{\Delta\omega - \delta_i}{\Gamma_i}\right)^2} \quad [5.8.2]$$

Each Lorentzian function (L_i) is defined for each offset ($\Delta\omega$) by amplitude A_i, full width at half maximum (FWHM) Γ_i, and displacement from the frequency of bulk water protons δ_i. Z_{base} corrects for constant signal reduction.

Supplementary Table 5.2: Starting points and boundary values of all fit parameters of the six-pool Lorentzian fit. Chemical shift (δ) and FWHM (Γ) are given in ppm.

	Start	**Lower**	**Upper**
Zbase	100	80	100
A_{water}	90	2	100
Γ_{water} (ppm)	1	0.03	2
δ_{water} (ppm)	0	-2	1.0
A_{MT}	10	2	20
Γ_{MT} (ppm)	10	7	100
δ_{MT} (ppm)	-2	-3	0
A_{NOE}	-2	-10	10
Γ_{NOE} (ppm)	0.8	0.1	2
δ_{NOE} (ppm)	-4	-4.25	-3.5
$A_{amide(3.50ppm)}$	1	0	10
$\Gamma_{amide(3.50ppm)}$ (ppm)	0.3	0.1	1
$\delta_{amide(3.50ppm)}$ (ppm)	3.5	3.25	3.75
$A_{amine(2.75ppm)}$	1	0	10
$\Gamma_{amine(2.75ppm)}$ (ppm)	0.3	0.1	1
$\delta_{amine(2.75ppm)}$ (ppm)	2.75	2.5	3.0
$A_{amine(2.0ppm)}$	1	0	10
$\Gamma_{amine(2.0ppm)}$ (ppm)	0.3	0.1	1
$\delta_{amine(2.0ppm)}$ (ppm)	2.0	1.75	2.5

Chapter 6

6 Conclusions

6.1 Thesis Summary

The primary goal of this thesis was to develop and assess the reproducibility of pH-weighted CEST MRI measurements in the human cervical spinal cord, which could eventually be applied in DCM patients to determine if hypoxia is an important predictor of outcome for surgical decompression treatment.

6.1.1 Spinal cord compression is associated with brain plasticity in degenerative cervical myelopathy

Before the development and implementation of AACID CEST MRI, Chapter 2 describes the results of the first exploratory study of motor area brain functional activation in twenty-three DCM patients to explore the relationship between spinal cord compression severity pre-operatively and functional activation patterns. Using task-based fMRI that utilized a structured finger-tapping paradigm, we observed that functional motor activity was increased in patients with more severely compressed cervical spinal cords, with the most significant correlation occurring in the contralateral primary motor cortex. This observation demonstrated that DCM patients exhibited varying compensatory cortical activation pattern expansion depending on the severity of the spinal cord compression. This expansion of cortical activity may be the result of brain plasticity and the rewiring of axons from the lower limb extremities into the hand region to compensate for the loss of motor hand function required to complete the finger-tapping task (176). In this study, spinal cord compression severity was used as a proxy for hypoxia as the assumption was made that compression of the spinal cord may induce pathophysiological changes, like hypoxia. Since greater compression likely induces greater ischemia/hypoxia in the spinal cord, we hypothesized that the observed cortical reorganization, manifested as increased functional activity, was a compensatory response to tissue damage in the spinal cord.

Overall, this was the first study to demonstrate that DCM patients recruit larger regions of the motor cortex to perform a structured finger-tapping task when spinal cord

compression is more severe. This recruitment may be a compensatory mechanism for neurological injury occurring in the spinal cord, which we hypothesize is associated with hypoxia.

6.1.2 Reproducibility of 3D Chemical Exchange Saturation Transfer (CEST) Contrasts in the Healthy Brain at 3T

AACID is a CEST contrast that has previously been shown to be pH-weighted and can detect changes in pH in different animal models at the higher magnetic field strength of 9.4 T (129,130). However, this specific CEST contrast has never been utilized at a lower field strength nor in humans.

In Chapter 2, it was hypothesized that the pathophysiological mechanism of ischemia/hypoxia occurs in the spinal cord of DCM patients; however, direct in-vivo quantification of hypoxia is challenging. However, when hypoxic conditions occur in tissue, there is an excess production of lactate and H^+, lowering the pH of the affected tissue. AACID CEST is a ratiometric approach using the endogenous CEST effects of both amide (3.50 ppm) and amine (2.75 ppm) exchangeable protons. AACID is sensitive to changes in intracellular pH while only exhibiting a small dependence on temperature, bulk water T_1 relaxation, and macromolecule concentration. Chapter 3 focused on the development and optimization of the AACID CEST MRI measurement in both egg-white phantoms and the healthy brain. The reproducibility of multiple 3D CEST contrasts, including AACID, was characterized in both gray and white matter.

Optimization of the in-vivo AACID acquisition was performed in both egg-white phantoms, which is an appropriate material to model the amide and amine CEST effect, and the healthy brain of three volunteers. It was found in both the phantom and healthy brain that the amide signal was maximized when using a Gaussian saturation pulse amplitude of B_1 = 0.5 μT (30 pulses, 100 ms each, 1 ms delay between each pulse, total saturation time of 3.03 s). Utilizing egg-white phantoms of differing pH, it was found that the linear relationship between pH and AACID was valid at the 3.0 T magnetic field strength.

Because the healthy brain is larger and experiences less physiological movement compared to the spinal cord, the brain was used to characterize the reproducibility of four different 3D CEST contrasts in healthy volunteers at 3.0 T. This strategy was used prior to optimization in the more difficult spinal cord. Two 3D CEST scans, which were positioned superior to the ventricles, were performed in 12 healthy subjects, approximately 10 days apart. The scan-rescan reproducibility was characterized both within-subject and between-subject in AACID, Amide*, $MTR_{Rex}(\delta_{amide})$, and $MTR_{Rex}(\delta_{NOE})$. Both AACID and $MTR_{Rex}(\delta_{NOE})$ had the highest within-subject and between-subject reproducibility for both tissue types. This result suggested that these contrasts would be the most sensitive and preferred for clinical applications in the brain. The high reproducibility of AACID in the healthy brain was a promising indicator that it would be feasible to implement this pH-weighted CEST contrast at lower magnetic field strength in the spinal cord.

6.1.3 Reproducibility of 3D pH-Weighted Chemical Exchange Saturation Transfer Contrast in the Healthy Cervical Spinal Cord

Having established in Chapter 3 that AACID CEST had a very high within-subject and between-subject reproducibility in the healthy brain, the application of AACID in the healthy cervical spinal cord was studied in Chapter 4. Additional challenges were present when translating CEST MRI from the brain to the spinal cord. The spinal cord is small in diameter and close to the heart and lungs, which can lead to problematic motion artefacts. The small diameter of the cord and the surrounding larger, bony vertebrae can also introduce B_0 and B_1 inhomogeneities in the spinal cord, which would also impact AACID measurements.

As this was the first study to develop and measure AACID CEST in the cervical spinal cord, there were two main objectives. The first objective was to evaluate the scan-rescan (both within-subject and within-subject) reproducibility of AACID measurements along the healthy cervical spinal cord at 3.0 T and determine if AACID measurements significantly differed between cervical spinal cord levels. The second objective of this study was to compare measurement reproducibility when utilizing different post-

processing schemes that incorporate a signal drift (respiratory) correction, B_1-inhomogeneity correction, or a combination of both.

Two 3D CEST scans were performed on 12 healthy subjects approximately 10 days apart, with the 3D CEST volume centered at the C4 level for all subjects. It was found that in the healthy cervical spinal cord, AACID measurements were not significantly different throughout the cord. The C4 level, or the level associated with the center of the 3D volume, demonstrated both the lowest within-subject and between-subject reproducibility for all post-processing schemes. Incorporating the B_1-correction significantly improved the reproducibility compared to no correction, while interestingly, the signal drift (respiratory correction) did not show any significant improvement. Overall, this study was the first to apply the pH-weighted AACID CEST contrast in the cervical spinal cord, and it was concluded that AACID measurements, while incorporating a B_1-inhomogeneity correction, were sufficiently reproducible for study of pathological conditions and that optimal image quality was achieved at the center of the 3D CEST volume.

6.1.4 Spinal Cord pH-weighted CEST MRI Suggests Hypoxia in Degenerative Cervical Myelopathy

Chapter 4 demonstrated that AACID measurements were most reproducible in the cervical spinal cord at the center of the 3D CEST volume while also incorporating a B_1-inhomogeneitiy correction. Chapter 5 describes preliminary work acquiring CEST scans in DCM patients and older volunteers. As a research group, we were interested in utilizing pH-weighted CEST contrast in the spinal cord of DCM patients to determine if hypoxia could be an indicator to tissue damage and potentially a predictor of surgical outcome. Surgical intervention, by means of decompression surgery, is the recommended treatment for DCM patients who are considered moderate or severe. However, studies have shown that 25% of patients will still worsen after surgery, creating a need to find reliable surgical outcome predictors (10,13). As previously mentioned, it has been hypothesized that ischemia/hypoxia is a pathophysiological mechanism that could influence the progression of DCM (42) and has the potential to be a measure of outcome.

The purpose of the study described in Chapter 5 was to determine: 1) if AACID values at the compression site of DCM patients significantly differed from healthy control subjects, 2) if AACID measurements changed throughout the spinal cord of DCM patients, and 3) if the compression severity metric from Chapter 2 significantly correlated with AACID measurements at the site of compression. For this initial pilot study, six DCM patients were recruited, along with five older controls and 12 younger controls. No differences were found in AACID measurements within the cord of DCM patients, possibly suggesting that hypoxia is not localized to the site of compression. Interestingly, AACID measurements at the site of compression in DCM patients did not significantly differ from the AACID values at the center of the 3D volume of the older controls but were significantly higher compared to the AACID measurements of the younger controls. This result could indicate that hypoxia may be present in DCM patients at the site of compression; an increased AACID measurement is associated with a more acidic pH. Comparing the compression severity metric from Chapter 2 to the AACID measurements at the site of compression did not demonstrate a significant correlation; however, the trend is beginning to show that patients with higher severity of compression also had a higher AACID value. The compression severity metric, however, could be too crude of a measurement to encompass the complexity of tissue hypoxia. Overall, this pilot study initially supports the hypothesis that spinal cord compression in DCM patients may result in both spinal cord ischemia and hypoxia.

6.2 Thesis Significance and Impact

Each of the presented studies offered novel information regarding cortical activity correlating with compression severity and the development of pH-weighted CEST MRI in the cervical spinal cord, which could be utilized in patients with DCM to determine if tissue hypoxia is present. The most important findings presented in this thesis are as follows: 1) functional activity is increased in the motor areas of the brain in DCM patients with more severe compression, which may be due to cortical reorganization occurring to compensate for functional deficits experienced during a structured tapping task; 2) pH-weighted AACID CEST can be successfully implemented at the clinically relevant field strength of 3.0 T and the linear relationship between AACID and pH still

holds; 3) AACID and $MTR_{Rex}(\delta_{NOE})$ are the most reproducible 3D CEST contrasts at 3.0 T in both gray and white matter in the healthy brain; 4) AACID CEST can be successfully measured in the healthy cervical spinal cord, with the center of the 3D volume, in conjunction with a B_1-inhomogeneity correction, producing the most reproducible results; and 5) preliminary data demonstrates higher AACID values in the spine at the site of compression in DCM patients compared to younger controls, indicating lower pH. Overall, this thesis demonstrated that AACID CEST can be utilized at a clinical field strength and can be implemented in the cervical spinal cord. All the studies in this thesis provide the groundwork to determine if hypoxia occurs in the spinal cord of DCM patients and to determine if it can be used as a predictor of outcome after decompression surgery. Ultimately, the work from this thesis has the potential to be used to increase the number of patients who either improve or remain neurologically unchanged following decompression surgery, overall, enhancing the care provided for DCM patients.

6.3 Future Directions

6.3.1 CEST Image Acquisition Improvements

The studies performed in Chapters 4 and 5 demonstrated the successful development and utilization of CEST MRI in the cervical spinal cord. However, one limitation of the current implementation of AACID in the spinal cord is the low spatial resolution, particularly in-plane resolution (2.0 x 2.0 mm). While the spatial resolution of the CEST images was sufficient to identify the cord, partial volume effects between the edges of the cord and the CSF are of particular concern. The concern about in-plane spatial resolution is even more prevalent in DCM patients, as the cross-sectional area of the spinal cord is even smaller in the compressed region. Higher spatial resolution would also allow for gray and white matter to be discerned in the spinal cord. It would be of interest to determine if hypoxia manifests differently in the different tissue types of the cervical spinal cord. One current concern about improving the in-plane spatial resolution, however, is the increase in scan time. Ideally, when scanning subjects, especially older subjects who are more prone to experience DCM, shorter scan times are preferred for clinical implementation. Future steps should also reduce scan time by either minimizing

the number of slices acquired or utilizing more sophisticated reconstruction methods, like compressed sensing.

Furthermore, the current slice thickness associated with the 3D CEST acquisition is 5 mm, which is necessary to provide adequate signal-to-noise (SNR), increase coverage, and improve sensitivity to detect small changes in the CEST effect. Unfortunately, a problem that is inherent to spinal cord imaging is the need to acquire axial slices along a curved structure. Increasing the sensitivity and SNR by increasing the thickness is only effective when axial slices are truly perpendicular to the cord. When slices are not perpendicular to the spinal cord, partial volume effects between tissue types and CSF can cause a loss in spatial resolution due to blurring. Unfortunately, a vast majority of people have natural curvature to their spinal cord and achieving slice perpendicularity is a challenge. Chapter 4 highlights this issue, as slices that were not perfectly perpendicular to the spinal cord (i.e., slices on the C2 and C6 levels) were not as reproducible as the center of the volume. To improve the accuracy of the AACID measurements throughout the 3D volume, an automatic slice angulation algorithm should be integrated into the acquisition. Using the Spinal Cord Toolbox (SCT) to identify the spinal cord on the scanner (174), the algorithm could automatically perform individual slice placements to ensure perpendicularity throughout the cord.

Finally, to improve the acquisition of 3D CEST in the cervical spinal cord, introducing a prospective motion correction could be beneficial. Chapter 4 incorporated a respiratory correction that leveraged the idea that CEST images acquired with no presaturation should have a consistent signal intensity. Any change in this non-saturated CEST signal intensity was ascribed to motion and should be normalized to reduce the effect. Ultimately, this signal drift correction did not provide any significant improvement to the reproducibility of the AACID measurements. However, introducing a more comprehensive 3D motion correction of the CEST images in the spinal cord may provide a more robust correction to any respiratory motion induced in the spinal cord. More specifically, introducing k-space navigators could prospectively measure the motion during the scan. MRI data is acquired in the k-space domain, so motion during acquisition (i.e., k-spacing filling) would result in blurring in the reconstructed CEST

images. K-space navigators can track this motion; navigators acquire portions of k-space at multiple time points throughout the acquisition, and when referenced to each other can be used to estimate motion. Future development should consider incorporating these navigators into the CEST sequence to robustly correct motion and potentially improve the accuracy of the CEST measurements. Through these various suggestions, the quality of spinal cord CEST imaging could be further improved, which would further increase its value in spinal cord MRI research.

6.3.2 DCM Study Continuation

Chapter 5 describes the initial pilot study utilizing AACID CEST MRI in the spinal cord of DCM patients. The preliminary results demonstrated that DCM patients had a significantly higher AACID value at the site of spinal cord compression compared to the spinal cord of younger controls, but the AACID value was not significantly different than older controls. However, the statistical power of this study must be increased. Because there is a low number of patients and older controls, detecting minor differences in AACID values between the two groups with the current data is challenging. Recruitment for this study must be continued to increase statistical power. Additionally, future recruitment should also focus on scanning and comparing DCM patients who are mild, moderate, and severe. The sensitivity of AACID CEST in the spinal cord could be evaluated to determine if ischemia/hypoxia is related to neurological changes occurring in these patients. Furthermore, a study should be performed that utilizes the task-based fMRI presented in Chapter 2 and AACID CEST. This study would be able to determine if ischemic injury in the spinal cord leads to cortical reorganization in the motor areas of the brain, which is what was hypothesized to be occurring in the Chapter 2 study.

Finally, to determine if hypoxia could be a measure of surgical outcome in DCM patients, a study will need to be performed that would determine if AACID measurements in the spinal cord of these patients correlate with outcomes following decompression surgery. This study would determine if AACID is a good predictor for neurological outcomes in DCM patients. Identifying a reliable predictor of surgical outcome in these patients would assist in determining which patients would benefit from decompression surgery and when surgery should be performed. Such a measure would

increase the number of patients who either improve or remain neurologically unchanged following decompression surgery.

References

1. Watson C, Bartholomaeus C, Puelles L. Time for Radical Changes in Brain Stem Nomenclature-Applying the Lessons From Developmental Gene Patterns. Front Neuroanat 2019;13:10.

2. Cramer GD, Darby SA, Cramer GD. Clinical anatomy of the spine, spinal cord, and ANS. St. Louis: Elsevier: 2014.

3. Khan YS, Lui F. Neuroanatomy, Spinal Cord. StatPearls. Treasure Island (FL): StatPearls Publishing; 2023.

4. Ahuja CS, Wilson JR, Nori S, et al. Traumatic spinal cord injury. Nature Reviews Disease Primers 2017;3(1):17018.

5. Bosmia AN, Hogan E, Loukas M, Tubbs RS, Cohen-Gadol AA. Blood supply to the human spinal cord: part I. Anatomy and hemodynamics. Clin Anat 2015;28(1):52-64.

6. Gillilan LA. The arterial blood supply of the human spinal cord. J Comp Neurol 1958;110(1):75-103.

7. Toledano M, Bartleson JD. Cervical spondylotic myelopathy. Neurol Clin 2013;31(1):287-305.

8. Badhiwala JH, Ahuja CS, Akbar MA, et al. Degenerative cervical myelopathy - update and future directions. Nat Rev Neurol 2020;16(2):108-124.

9. Bakhsheshian J, Mehta VA, Liu JC. Current Diagnosis and Management of Cervical Spondylotic Myelopathy. Global Spine J 2017;7(6):572-586.

10. Kalsi-Ryan S, Karadimas SK, Fehlings MG. Cervical spondylotic myelopathy: the clinical phenomenon and the current pathobiology of an increasingly prevalent and devastating disorder. Neuroscientist 2013;19(4):409-421.

11. Baptiste DC, Fehlings MG. Pathophysiology of cervical myelopathy. Spine J 2006;6(6 Suppl):190s-197s.

12. Humzah MD, Soames RW. Human intervertebral disc: structure and function. Anat Rec 1988;220(4):337-356.

13. Kato S, Fehlings M. Degenerative cervical myelopathy. Curr Rev Musculoskelet Med 2016;9(3):263-271.

14. White AA, 3rd, Panjabi MM. Biomechanical considerations in the surgical management of cervical spondylotic myelopathy. Spine (Phila Pa 1976) 1988;13(7):856-860.

15. Schneider RC, Cherry G, Pantek H. The syndrome of acute central cervical spinal cord injury; with special reference to the mechanisms involved in hyperextension injuries of cervical spine. J Neurosurg 1954;11(6):546-577.

16. Fehlings MG, Skaf G. A review of the pathophysiology of cervical spondylotic myelopathy with insights for potential novel mechanisms drawn from traumatic spinal cord injury. Spine (Phila Pa 1976) 1998;23(24):2730-2737.

17. Lebl DR, Hughes A, Cammisa FP, Jr., O'Leary PF. Cervical spondylotic myelopathy: pathophysiology, clinical presentation, and treatment. Hss j 2011;7(2):170-178.

18. Karadimas SK, Gialeli CH, Klironomos G, et al. The role of oligodendrocytes in the molecular pathobiology and potential molecular treatment of cervical spondylotic myelopathy. Curr Med Chem 2010;17(11):1048-1058.

19. Yu WR, Baptiste DC, Liu T, Odrobina E, Stanisz GJ, Fehlings MG. Molecular mechanisms of spinal cord dysfunction and cell death in the spinal hyperostotic mouse: implications for the pathophysiology of human cervical spondylotic myelopathy. Neurobiol Dis 2009;33(2):149-163.

20. Benzel EC, Lancon J, Kesterson L, Hadden T. Cervical laminectomy and dentate ligament section for cervical spondylotic myelopathy. J Spinal Disord 1991;4(3):286-295.

21. Tetreault L, Kopjar B, Nouri A, et al. The modified Japanese Orthopaedic Association scale: establishing criteria for mild, moderate and severe impairment in patients with degenerative cervical myelopathy. Eur Spine J 2017;26(1):78-84.

22. Kalsi-Ryan S, Beaton D, Curt A, et al. The Graded Redefined Assessment of Strength Sensibility and Prehension: reliability and validity. J Neurotrauma 2012;29(5):905-914.

23. Kalsi-Ryan S, Singh A, Massicotte EM, et al. Ancillary outcome measures for assessment of individuals with cervical spondylotic myelopathy. Spine (Phila Pa 1976) 2013;38(22 Suppl 1):S111-122.

24. Taylor AR. Mechanism and treatment of spinal-cord disorders associated with cervical spondylosis. Lancet 1953;1(6763):717-720.

25. Tetreault L, Goldstein CL, Arnold P, et al. Degenerative Cervical Myelopathy: A Spectrum of Related Disorders Affecting the Aging Spine. Neurosurgery 2015;77 Suppl 4:S51-67.

26. Nouri A, Martin AR, Mikulis D, Fehlings MG. Magnetic resonance imaging assessment of degenerative cervical myelopathy: a review of structural changes and measurement techniques. Neurosurg Focus 2016;40(6):E5.

27. Martin AR, Tadokoro N, Tetreault L, et al. Imaging Evaluation of Degenerative Cervical Myelopathy: Current State of the Art and Future Directions. Neurosurg Clin N Am 2018;29(1):33-45.

28. Yagi M, Ninomiya K, Kihara M, Horiuchi Y. Long-term surgical outcome and risk factors in patients with cervical myelopathy and a change in signal intensity of intramedullary spinal cord on Magnetic Resonance imaging. J Neurosurg Spine 2010;12(1):59-65.

29. Yukawa Y, Kato F, Yoshihara H, Yanase M, Ito K. MR T2 image classification in cervical compression myelopathy: predictor of surgical outcomes. Spine (Phila Pa 1976) 2007;32(15):1675-1678; discussion 1679.

30. Harrop JS, Naroji S, Maltenfort M, et al. Cervical myelopathy: a clinical and radiographic evaluation and correlation to cervical spondylotic myelopathy. Spine (Phila Pa 1976) 2010;35(6):620-624.

31. Fehlings MG, Kwon BK, Tetreault LA. Guidelines for the Management of Degenerative Cervical Myelopathy and Spinal Cord Injury: An Introduction to a Focus Issue. Global Spine J 2017;7(3 Suppl):6s-7s.

32. Yoshimatsu H, Nagata K, Goto H, et al. Conservative treatment for cervical spondylotic myelopathy. prediction of treatment effects by multivariate analysis. Spine J 2001;1(4):269-273.

33. Almeida GP, Carneiro KK, Marques AP. Manual therapy and therapeutic exercise in patient with symptomatic cervical spondylotic myelopathy: a case report. J Bodyw Mov Ther 2013;17(4):504-509.

34. Shimomura T, Sumi M, Nishida K, et al. Prognostic factors for deterioration of patients with cervical spondylotic myelopathy after nonsurgical treatment. Spine (Phila Pa 1976) 2007;32(22):2474-2479.

35. Matsumoto M, Chiba K, Ishikawa M, Maruiwa H, Fujimura Y, Toyama Y. Relationships between outcomes of conservative treatment and magnetic resonance imaging findings in patients with mild cervical myelopathy caused by soft disc herniations. Spine (Phila Pa 1976) 2001;26(14):1592-1598.

36. Tetreault LA, Rhee J, Prather H, et al. Change in Function, Pain, and Quality of Life Following Structured Nonoperative Treatment in Patients With Degenerative Cervical Myelopathy: A Systematic Review. Global Spine J 2017;7(3 Suppl):42s-52s.

37. Badhiwala JH, Witiw CD, Nassiri F, et al. Efficacy and Safety of Surgery for Mild Degenerative Cervical Myelopathy: Results of the AOSpine North America and International Prospective Multicenter Studies. Neurosurgery 2019;84(4):890-897.

38. Tetreault L, Palubiski LM, Kryshtalskyj M, et al. Significant Predictors of Outcome Following Surgery for the Treatment of Degenerative Cervical Myelopathy: A Systematic Review of the Literature. Neurosurg Clin N Am 2018;29(1):115-127.e135.

39. Vidal PM, Karadimas SK, Ulndreaj A, et al. Delayed decompression exacerbates ischemia-reperfusion injury in cervical compressive myelopathy. JCI Insight 2017;2(11).

40. Alafifi T, Kern R, Fehlings M. Clinical and MRI predictors of outcome after surgical intervention for cervical spondylotic myelopathy. J Neuroimaging 2007;17(4):315-322.

41. Fehlings MG, Ibrahim A, Tetreault L, et al. A global perspective on the outcomes of surgical decompression in patients with cervical spondylotic myelopathy: results from the prospective multicenter AOSpine international study on 479 patients. Spine (Phila Pa 1976) 2015;40(17):1322-1328.

42. Brain WR, Knight GC, Bull JW. Discussion of rupture of the intervertebral disc in the cervical region. Proc R Soc Med 1948;41(8):509-516.

43. Wilson JRF, Badhiwala JH, Moghaddamjou A, Martin AR, Fehlings MG. Degenerative Cervical Myelopathy; A Review of the Latest Advances and Future Directions in Management. Neurospine 2019;16(3):494-505.

44. Mair WG, Druckman R. The pathology of spinal cord lesions and their relation to the clinical features in protrusion of cervical intervertebral discs; a report of four cases. Brain 1953;76(1):70-91.

45. Karadimas SK, Gatzounis G, Fehlings MG. Pathobiology of cervical spondylotic myelopathy. Eur Spine J 2015;24 Suppl 2:132-138.

46. Gooding MR, Wilson CB, Hoff JT. Experimental cervical myelopathy. Effects of ischemia and compression of the canine cervical spinal cord. J Neurosurg 1975;43(1):9-17.

47. Ellingson BM, Woodworth DC, Leu K, Salamon N, Holly LT. Spinal Cord Perfusion MR Imaging Implicates Both Ischemia and Hypoxia in the Pathogenesis of Cervical Spondylosis. World Neurosurg 2019;128:e773-e781.

48. Kurokawa R, Murata H, Ogino M, Ueki K, Kim P. Altered blood flow distribution in the rat spinal cord under chronic compression. Spine (Phila Pa 1976) 2011;36(13):1006-1009.

49. Cheng X, Long H, Chen W, Xu J, Huang Y, Li F. Three-dimensional alteration of cervical anterior spinal artery and anterior radicular artery in rat model of chronic spinal cord compression by micro-CT. Neurosci Lett 2015;606:106-112.

50. Karadimas SK, Moon ES, Yu WR, et al. A novel experimental model of cervical spondylotic myelopathy (CSM) to facilitate translational research. Neurobiol Dis 2013;54:43-58.

51. Karadimas SK, Laliberte AM, Tetreault L, et al. Riluzole blocks perioperative ischemia-reperfusion injury and enhances postdecompression outcomes in cervical spondylotic myelopathy. Sci Transl Med 2015;7(316):316ra194.

52. Chen Y, Hallenbeck JM, Ruetzler C, et al. Overexpression of monocyte chemoattractant protein 1 in the brain exacerbates ischemic brain injury and is associated with recruitment of inflammatory cells. J Cereb Blood Flow Metab 2003;23(6):748-755.

53. Dimitrijevic OB, Stamatovic SM, Keep RF, Andjelkovic AV. Absence of the chemokine receptor CCR2 protects against cerebral ischemia/reperfusion injury in mice. Stroke 2007;38(4):1345-1353.

54. Gökce EC, Kahveci R, Gökce A, et al. Neuroprotective effects of thymoquinone against spinal cord ischemia-reperfusion injury by attenuation of inflammation, oxidative stress, and apoptosis. J Neurosurg Spine 2016;24(6):949-959.

55. Ikhlas M, Atherton NS. Vascular Reperfusion Injury. StatPearls. Treasure Island (FL): StatPearls Publishing; 2023.

56. Adeva-Andany MM, Carneiro-Freire N, Donapetry-García C, Rañal-Muíño E, López-Pereiro Y. The importance of the ionic product for water to understand the physiology of the acid-base balance in humans. Biomed Res Int 2014;2014:695281.

57. Myers RJ. One-Hundred Years of pH. Journal of Chemical Education 2010;87(1):30-32.

58. Fox SI. Human Physiology: McGraw-Hill: 2004.

59. Tannock IF, Rotin D. Acid pH in tumors and its potential for therapeutic exploitation. Cancer Res 1989;49(16):4373-4384.

60. Gatenby RA, Gillies RJ. Why do cancers have high aerobic glycolysis? Nat Rev Cancer 2004;4(11):891-899.

61. Webb BA, Chimenti M, Jacobson MP, Barber DL. Dysregulated pH: a perfect storm for cancer progression. Nat Rev Cancer 2011;11(9):671-677.

62. Srivastava J, Barber DL, Jacobson MP. Intracellular pH sensors: design principles and functional significance. Physiology (Bethesda) 2007;22:30-39.

63. Casimir GJ, Lefèvre N, Corazza F, Duchateau J, Chamekh M. The Acid-Base Balance and Gender in Inflammation: A Mini-Review. Front Immunol 2018;9:475.

64. Lagadic-Gossmann D, Huc L, Lecureur V. Alterations of intracellular pH homeostasis in apoptosis: origins and roles. Cell Death & Differentiation 2004;11(9):953-961.

65. Dehay B, Martinez-Vicente M, Caldwell GA, et al. Lysosomal impairment in Parkinson's disease. Movement Disorders 2013;28(6):725-732.

66. Nixon RA, Yang D-S. Autophagy failure in Alzheimer's disease—locating the primary defect. Neurobiology of Disease 2011;43(1):38-45.

67. Gallagher FA, Kettunen MI, Day SE, et al. Magnetic resonance imaging of pH in vivo using hyperpolarized 13C-labelled bicarbonate. Nature 2008;453(7197):940-943.

68. Moon RB, Richards JH. Determination of intracellular pH by 31P magnetic resonance. J Biol Chem 1973;248(20):7276-7278.

69. Gillies RJ, Liu Z, Bhujwalla Z. 31P-MRS measurements of extracellular pH of tumors using 3-aminopropylphosphonate. Am J Physiol 1994;267(1 Pt 1):C195-203.

70. Kim H, Krishnamurthy LC, Sun PZ. Brain pH Imaging and its Applications. Neuroscience 2021;474:51-62.

71. Ojugo AS, McSheehy PM, McIntyre DJ, et al. Measurement of the extracellular pH of solid tumours in mice by magnetic resonance spectroscopy: a comparison of exogenous (19)F and (31)P probes. Nmr Biomed 1999;12(8):495-504.

72. Deutsch CJ, Taylor JS. Intracellular pH as measured by 19F NMR. Ann N Y Acad Sci 1987;508:33-47.

73. Gallagher FA, Kettunen MI, Brindle KM. Imaging pH with hyperpolarized 13C. Nmr Biomed 2011;24(8):1006-1015.

74. Lange T, Dydak U, Roberts TP, Rowley HA, Bjeljac M, Boesiger P. Pitfalls in lactate measurements at 3T. AJNR Am J Neuroradiol 2006;27(4):895-901.

75. Allen PS, Thompson RB, Wilman AH. Metabolite-specific NMR spectroscopy in vivo. Nmr Biomed 1997;10(8):435-444.

76. Fleming IN, Manavaki R, Blower PJ, et al. Imaging tumour hypoxia with positron emission tomography. Br J Cancer 2015;112(2):238-250.

77. Dearling JL, Packard AB. Some thoughts on the mechanism of cellular trapping of Cu(II)-ATSM. Nucl Med Biol 2010;37(3):237-243.

78. Vaquero JJ, Kinahan P. Positron Emission Tomography: Current Challenges and Opportunities for Technological Advances in Clinical and Preclinical Imaging Systems. Annu Rev Biomed Eng 2015;17:385-414.

79. Macnab AJ, Gagnon RE, Gagnon FA. Near infrared spectroscopy for intraoperative monitoring of the spinal cord. Spine (Phila Pa 1976) 2002;27(1):17-20.

80. Rashnavadi T, Macnab A, Cheung A, Shadgan A, Kwon BK, Shadgan B. Monitoring spinal cord hemodynamics and tissue oxygenation: a review of the literature with special focus on the near-infrared spectroscopy technique. Spinal Cord 2019;57(8):617-625.

81. Giannotti G, Cohn SM, Brown M, Varela JE, McKenney MG, Wiseberg JA. Utility of near-infrared spectroscopy in the diagnosis of lower extremity compartment syndrome. J Trauma 2000;48(3):396-399; discussion 399-401.

82. Draghici AE, Potart D, Hollmann JL, et al. Near infrared spectroscopy for measuring changes in bone hemoglobin content after exercise in individuals with spinal cord injury. Journal of Orthopaedic Research 2018;36(1):183-191.

83. Constantinides C, Taylor, Francis. Magnetic Resonance Imaging: The Basics: CRC Press, Taylor & Francis Group: 2014.

84. de Graaf RA. In Vivo NMR Spectroscopy: Principles and Techniques. Chichester, UK: 2007.

85. McRobbie D.W. MEA, Graves M.J., Prince M.R. MRI from Picture to Proton: Cambridge University Press: 2017.

86. Hanson LG. Is quantum mechanics necessary for understanding magnetic resonance? Concepts in Magnetic Resonance Part A 2008;32A(5):329-340.

87. Eom HJ. Primary Theory of Electromagnetics. New York, New York: Spinger Dordrecht; 2013. p. 95-111.

88. Epstein FH, Mugler JP, 3rd, Brookeman JR. Spoiling of transverse magnetization in gradient-echo (GRE) imaging during the approach to steady state. Magn Reson Med 1996;35(2):237-245.

89. Gallagher TA, Nemeth AJ, Hacein-Bey L. An introduction to the Fourier transform: relationship to MRI. AJR Am J Roentgenol 2008;190(5):1396-1405.

90. Mezrich R. A perspective on K-space. Radiology 1995;195(2):297-315.

91. Phillips AA, Chan FH, Zheng MM, Krassioukov AV, Ainslie PN. Neurovascular coupling in humans: Physiology, methodological advances and clinical implications. J Cereb Blood Flow Metab 2016;36(4):647-664.

92. Attwell D, Buchan AM, Charpak S, Lauritzen M, Macvicar BA, Newman EA. Glial and neuronal control of brain blood flow. Nature 2010;468(7321):232-243.

93. Heeger DJ, Ress D. What does fMRI tell us about neuronal activity? Nat Rev Neurosci 2002;3(2):142-151.

94. Nair DG. About being BOLD. Brain Res Brain Res Rev 2005;50(2):229-243.

95. Pauling L, Coryell CD. The Magnetic Properties and Structure of Hemoglobin, Oxyhemoglobin and Carbonmonoxyhemoglobin. Proc Natl Acad Sci U S A 1936;22(4):210-216.

96. Buckner RL. Event-related fMRI and the hemodynamic response. Hum Brain Mapp 1998;6(5-6):373-377.

97. Matthews PM, Jezzard P. Functional magnetic resonance imaging. J Neurol Neurosurg Psychiatry 2004;75(1):6-12.

98. Ogawa S, Lee TM, Kay AR, Tank DW. Brain Magnetic Resonance Imaging with Contrast Dependent on Blood Oxygenation. Proc Natl Acad Sci USA 1990;87(24):9868-9872.

99. Huettel SA, Song AW, McCarthy G. Functional Magnetic Resonance Imaging. Sunderland, MA: Sinauer Associates: 2004.

100. Lindquist MA, Meng Loh J, Atlas LY, Wager TD. Modeling the hemodynamic response function in fMRI: efficiency, bias and mis-modeling. Neuroimage 2009;45(1 Suppl):S187-198.

101. Kwong KK, Belliveau JW, Chesler DA, et al. Dynamic magnetic resonance imaging of human brain activity during primary sensory stimulation. Proc Natl Acad Sci U S A 1992;89(12):5675-5679.

102. Buxton RB, Uludağ K, Dubowitz DJ, Liu TT. Modeling the hemodynamic response to brain activation. Neuroimage 2004;23 Suppl 1:S220-233.

103. Duggal N, Rabin D, Bartha R, et al. Brain reorganization in patients with spinal cord compression evaluated using fMRI. Neurology 2010;74(13):1048-1054.

104. Holly LT, Dong Y, Albistegui-DuBois R, Marehbian J, Dobkin B. Cortical reorganization in patients with cervical spondylotic myelopathy. J Neurosurg Spine 2007;6(6):544-551.

105. Raineteau O, Schwab ME. Plasticity of motor systems after incomplete spinal cord injury. Nat Rev Neurosci 2001;2(4):263-273.

106. Bhagavatula ID, Shukla D, Sadashiva N, Saligoudar P, Prasad C, Bhat DI. Functional cortical reorganization in cases of cervical spondylotic myelopathy and changes associated with surgery. Neurosurg Focus 2016;40(6):E2.

107. Aleksanderek I, Stevens TK, Goncalves S, Bartha R, Duggal N. Metabolite and functional profile of patients with cervical spondylotic myelopathy. J Neurosurg Spine 2017;26(5):547-553.

108. Ramachandran VS. Plasticity and functional recovery in neurology. Clin Med (Lond) 2005;5(4):368-373.

109. Takeuchi N, Oouchida Y, Izumi S. Motor control and neural plasticity through interhemispheric interactions. Neural Plast 2012;2012:823285.

110. Freund P, Weiskopf N, Ward NS, et al. Disability, atrophy and cortical reorganization following spinal cord injury. Brain 2011;134(Pt 6):1610-1622.

111. Henderson LA, Gustin SM, Macey PM, Wrigley PJ, Siddall PJ. Functional reorganization of the brain in humans following spinal cord injury: evidence for underlying changes in cortical anatomy. J Neurosci 2011;31(7):2630-2637.

112. Sherry AD, Woods M. Chemical exchange saturation transfer contrast agents for magnetic resonance imaging. Annu Rev Biomed Eng 2008;10:391-411.

113. Van Zijl PCM, Yadav NN. Chemical exchange saturation transfer (CEST): What is in a name and what isn't? Magn Reson Med 2011;65(4):927-948.

114. Ward KM, Aletras AH, Balaban RS. A new class of contrast agents for MRI based on proton chemical exchange dependent saturation transfer (CEST). J Magn Reson 2000;143(1):79-87.

115. Ward KM, Balaban RS. Determination of pH using water protons and chemical exchange dependent saturation transfer (CEST). Magn Reson Med 2000;44(5):799-802.

116. Zhou J, Zijl PCMv. Chemical exchange saturation transfer imaging and spectroscopy. Prog Nucl Magn Reson Spectrosc 2006;48(2):109-136.

117. Kim J, Wu Y, Guo Y, Zheng H, Sun PZ. A review of optimization and quantification techniques for chemical exchange saturation transfer MRI toward sensitive in vivo imaging. Contrast Media Mol Imaging 2015;10(3):163-178.

118. van Zijl PCM, Lam WW, Xu J, Knutsson L, Stanisz GJ. Magnetization Transfer Contrast and Chemical Exchange Saturation Transfer MRI. Features and analysis of the field-dependent saturation spectrum. Neuroimage 2018;168:222-241.

119. Sun PZ, Lu J, Wu Y, Xiao G, Wu R. Evaluation of the dependence of CEST-EPI measurement on repetition time, RF irradiation duty cycle and imaging flip angle for enhanced pH sensitivity. Phys Med Biol 2013;58(17):N229-240.

120. Liepinsh E, Otting G. Proton exchange rates from amino acid side chains--implications for image contrast. Magn Reson Med 1996;35(1):30-42.

121. Kogan F, Hariharan H, Reddy R. Chemical exchange saturation transfer (CEST) imaging: Description of technique and potential clinical applications. Curr Radiol Rep 2013;1(2):102-114.

122. Zhou J, Payen JF, Wilson DA, Traystman RJ, van Zijl PC. Using the amide proton signals of intracellular proteins and peptides to detect pH effects in MRI. Nat Med 2003;9(8):1085-1090.

123. Liu D, Zhou J, Xue R, Zuo Z, An J, Wang DJ. Quantitative characterization of nuclear overhauser enhancement and amide proton transfer effects in the human brain at 7 tesla. Magn Reson Med 2013;70(4):1070-1081.

124. Jin T, Wang P, Zong X, Kim S-G. MR imaging of the amide-proton transfer effect and the pH-insensitive nuclear overhauser effect at 9.4 T. Magn Reson Med 2013;69(3):760-770.

125. Cai K, Haris M, Singh A, et al. Magnetic resonance imaging of glutamate. Nat Med 2012;18(2):302-306.

126. Chan KW, McMahon MT, Kato Y, et al. Natural D-glucose as a biodegradable MRI contrast agent for detecting cancer. Magn Reson Med 2012;68(6):1764-1773.

127. Nasrallah FA, Pagès G, Kuchel PW, Golay X, Chuang KH. Imaging brain deoxyglucose uptake and metabolism by glucoCEST MRI. J Cereb Blood Flow Metab 2013;33(8):1270-1278.

128. Walker-Samuel S, Ramasawmy R, Torrealdea F, et al. In vivo imaging of glucose uptake and metabolism in tumors. Nat Med 2013;19(8):1067-1072.

129. McVicar N, Li AX, Gonçalves DF, et al. Quantitative tissue pH measurement during cerebral ischemia using amine and amide concentration-independent detection (AACID) with MRI. J Cereb Blood Flow Metab 2014;34(4):690-698.

130. McVicar N, Li AX, Meakin SO, Bartha R. Imaging chemical exchange saturation transfer (CEST) effects following tumor-selective acidification using lonidamine. Nmr Biomed 2015;28(5):566-575.

131. Desmond KL, Moosvi F, Stanisz GJ. Mapping of amide, amine, and aliphatic peaks in the CEST spectra of murine xenografts at 7 T. Magn Reson Med 2014;71(5):1841-1853.

132. Zong X, Wang P, Kim SG, Jin T. Sensitivity and source of amine-proton exchange and amide-proton transfer magnetic resonance imaging in cerebral ischemia. Magn Reson Med 2014;71(1):118-132.

133. Zhou Y, van Zijl PCM, Xu J, Yadav NN. Mechanism and quantitative assessment of saturation transfer for water-based detection of the aliphatic protons in carbohydrate polymers. Magn Reson Med 2021;85(3):1643-1654.

134. Zhou Y, Bie C, van Zijl PCM, Yadav NN. The relayed nuclear Overhauser effect in magnetization transfer and chemical exchange saturation transfer MRI. Nmr Biomed 2023;36(6):e4778.

135. Shen Y, Xiao G, Shen Z, et al. Imaging of nuclear Overhauser enhancement at 7 and 3 T. Nmr Biomed 2017;30(9).

136. Eliav U, Navon G. Multiple quantum filtered NMR studies of the interaction between collagen and water in the tendon. J Am Chem Soc 2002;124(12):3125-3132.

137. Jones CK, Huang A, Xu J, et al. Nuclear Overhauser enhancement (NOE) imaging in the human brain at 7T. Neuroimage 2013;77:114-124.

138. Simpson JH, Carr HY. Diffusion and Nuclear Spin Relaxation in Water. Physical Review 1958;111(5):1201-1202.

139. Zhou Y, Van Zijl PCM, Xu X, et al. Magnetic resonance imaging of glycogen using its magnetic coupling with water. Proc Natl Acad Sci USA 2020;117(6):3144-3149.

140. Stroman PW, Wheeler-Kingshott C, Bacon M, et al. The current state-of-the-art of spinal cord imaging: methods. Neuroimage 2014;84:1070-1081.

141. Dula AN, Pawate S, Dethrage LM, et al. Chemical exchange saturation transfer of the cervical spinal cord at 7 T. Nmr Biomed 2016;29(9):1249-1257.

142. By S, Barry RL, Smith AK, et al. Amide proton transfer CEST of the cervical spinal cord in multiple sclerosis patients at 3T. Magn Reson Med 2018;79(2):806-814.

143. Verma T, Cohen-Adad J. Effect of respiration on the B0 field in the human spinal cord at 3T. Magn Reson Med 2014;72(6):1629-1636.

144. Goerke S, Breitling J, Korzowski A, et al. Clinical routine acquisition protocol for 3D relaxation-compensated APT and rNOE CEST-MRI of the human brain at 3T. Magn Reson Med 2021;86(1):393-404.

145. Lee JB, Park JE, Jung SC, et al. Repeatability of amide proton transfer-weighted signals in the brain according to clinical condition and anatomical location. Eur Radiol 2020;30(1):346-356.

146. Togao O, Hiwatashi A, Keupp J, et al. Scan-rescan reproducibility of parallel transmission based amide proton transfer imaging of brain tumors. J Magn Reson Imaging 2015;42(5):1346-1353.

147. Wamelink I, Kuijer JPA, Padrela BE, et al. Reproducibility of 3 T APT-CEST in Healthy Volunteers and Patients With Brain Glioma. J Magn Reson Imaging 2023;57(1):206-215.

148. Cramer SC, Lastra L, Lacourse MG, Cohen MJ. Brain motor system function after chronic, complete spinal cord injury. Brain 2005;128(Pt 12):2941-2950.

149. Hrabálek L, Hluštík P, Hok P, et al. [Effects of spinal cord decompression in patients with cervical spondylotic myelopathy oncortical brain activations]. Rozhl Chir 2014;93(11):530-535.

150. Alkadhi H, Brugger P, Boendermaker SH, et al. What disconnection tells about motor imagery: evidence from paraplegic patients. Cereb Cortex 2005;15(2):131-140.

151. Bruehlmeier M, Dietz V, Leenders KL, Roelcke U, Missimer J, Curt A. How does the human brain deal with a spinal cord injury? Eur J Neurosci 1998;10(12):3918-3922.

152. Nouri A, Tetreault L, Singh A, Karadimas SK, Fehlings MG. Degenerative Cervical Myelopathy: Epidemiology, Genetics, and Pathogenesis. Spine (Phila Pa 1976) 2015;40(12):E675-693.

153. Irvine DH, Foster JB, Newell DJ, Klukvin BN. PREVALENCE OF CERVICAL SPONDYLOSIS IN A GENERAL PRACTICE. Lancet 1965;1(7395):1089-1092.

154. Nurick S. The natural history and the results of surgical treatment of the spinal cord disorder associated with cervical spondylosis. Brain 1972;95(1):101-108.

155. Ghogawala Z, Benzel EC, Riew KD, Bisson EF, Heary RF. Surgery vs Conservative Care for Cervical Spondylotic Myelopathy: Surgery Is Appropriate for Progressive Myelopathy. Neurosurgery 2015;62 Suppl 1(0 1 0 0):56-61.

156. Emery SE. Cervical spondylotic myelopathy: diagnosis and treatment. J Am Acad Orthop Surg 2001;9(6):376-388.

157. Furlan JC, Kalsi-Ryan S, Kailaya-Vasan A, Massicotte EM, Fehlings MG. Functional and clinical outcomes following surgical treatment in patients with cervical spondylotic myelopathy: a prospective study of 81 cases. J Neurosurg Spine 2011;14(3):348-355.

158. Cheung WY, Arvinte D, Wong YW, Luk KD, Cheung KM. Neurological recovery after surgical decompression in patients with cervical spondylotic myelopathy - a prospective study. Int Orthop 2008;32(2):273-278.

159. Lu J, Wu X, Li Y, Kong X. Surgical results of anterior corpectomy in the aged patients with cervical myelopathy. Eur Spine J 2008;17(1):129-135.

160. Tetreault L, Kopjar B, Côté P, Arnold P, Fehlings MG. A Clinical Prediction Rule for Functional Outcomes in Patients Undergoing Surgery for Degenerative Cervical Myelopathy: Analysis of an International Prospective Multicenter Data Set of 757 Subjects. J Bone Joint Surg Am 2015;97(24):2038-2046.

161. Fessler RG, Steck JC, Giovanini MA. Anterior Cervical Corpectomy for Cervical Spondylotic Myelopathy. Neurosurgery 1998;43(2):257-265.

162. Yamazaki T, Yanaka K, Sato H, Uemura K, Tsukada A, Nose T. Cervical spondylotic myelopathy: surgical results and factors affecting outcome with special reference to age differences. Neurosurgery 2003;52(1):122-126; discussion 126.

163. Ryan K, Goncalves S, Bartha R, Duggal N. Motor network recovery in patients with chronic spinal cord compression: a longitudinal study following decompression surgery. J Neurosurg Spine 2018;28(4):379-388.

164. Kato S, Oshima Y, Oka H, et al. Comparison of the Japanese Orthopaedic Association (JOA) score and modified JOA (mJOA) score for the assessment of cervical myelopathy: a multicenter observational study. PLoS One 2015;10(4):e0123022.

165. Esteban O, Markiewicz CJ, Blair RW, et al. fMRIPrep: a robust preprocessing pipeline for functional MRI. Nat Methods 2019;16(1):111-116.

166. Tustison NJ, Avants BB, Cook PA, et al. N4ITK: improved N3 bias correction. IEEE Trans Med Imaging 2010;29(6):1310-1320.

167. Avants BB, Epstein CL, Grossman M, Gee JC. Symmetric diffeomorphic image registration with cross-correlation: evaluating automated labeling of elderly and neurodegenerative brain. Med Image Anal 2008;12(1):26-41.

168. Jenkinson M, Bannister P, Brady M, Smith S. Improved optimization for the robust and accurate linear registration and motion correction of brain images. Neuroimage 2002;17(2):825-841.

169. Cox RW. AFNI: software for analysis and visualization of functional magnetic resonance neuroimages. Comput Biomed Res 1996;29(3):162-173.

170. Andersson JL, Skare S, Ashburner J. How to correct susceptibility distortions in spin-echo echo-planar images: application to diffusion tensor imaging. Neuroimage 2003;20(2):870-888.

171. Greve DN, Fischl B. Accurate and robust brain image alignment using boundary-based registration. Neuroimage 2009;48(1):63-72.

172. Mikl M, Marecek R, Hlustík P, et al. Effects of spatial smoothing on fMRI group inferences. Magn Reson Imaging 2008;26(4):490-503.

173. Friston KJ, Holmes AP, Worsley KJ, Poline J-P, Frith CD, Frackowiak RSJ. Statistical parametric maps in functional imaging: A general linear approach. Hum Brain Mapp 1994;2(4):189-210.

174. De Leener B, Lévy S, Dupont SM, et al. SCT: Spinal Cord Toolbox, an open-source software for processing spinal cord MRI data. Neuroimage 2017;145(Pt A):24-43.

175. Gros C, De Leener B, Badji A, et al. Automatic segmentation of the spinal cord and intramedullary multiple sclerosis lesions with convolutional neural networks. Neuroimage 2019;184:901-915.

176. Ghosh A, Haiss F, Sydekum E, et al. Rewiring of hindlimb corticospinal neurons after spinal cord injury. Nat Neurosci 2010;13(1):97-104.

177. Middleton FA, Strick PL. Basal ganglia and cerebellar loops: motor and cognitive circuits. Brain Res Brain Res Rev 2000;31(2-3):236-250.

178. Enzinger C, Johansen-Berg H, Dawes H, et al. Functional MRI correlates of lower limb function in stroke victims with gait impairment. Stroke 2008;39(5):1507-1513.

179. Chen L, Wei Z, Chan KWY, et al. Protein aggregation linked to Alzheimer's disease revealed by saturation transfer MRI. Neuroimage 2019;188:380-390.

180. Harston GW, Tee YK, Blockley N, et al. Identifying the ischaemic penumbra using pH-weighted magnetic resonance imaging. Brain 2015;138(Pt 1):36-42.

181. Heo HY, Jones CK, Hua J, et al. Whole-brain amide proton transfer (APT) and nuclear overhauser enhancement (NOE) imaging in glioma patients using low-power steady-state pulsed chemical exchange saturation transfer (CEST) imaging at 7T. J Magn Reson Imaging 2016;44(1):41-50.

182. Jiang S, Yu H, Wang X, et al. Molecular MRI differentiation between primary central nervous system lymphomas and high-grade gliomas using endogenous protein-based amide proton transfer MR imaging at 3 Tesla. Eur Radiol 2016;26(1):64-71.

183. Mehrabian H, Desmond KL, Soliman H, Sahgal A, Stanisz GJ. Differentiation between Radiation Necrosis and Tumor Progression Using Chemical Exchange Saturation Transfer. Clin Cancer Res 2017;23(14):3667-3675.

184. Mehrabian H, Myrehaug S, Soliman H, Sahgal A, Stanisz GJ. Evaluation of Glioblastoma Response to Therapy With Chemical Exchange Saturation Transfer. Int J Radiat Oncol Biol Phys 2018;101(3):713-723.

185. Meissner JE, Korzowski A, Regnery S, et al. Early response assessment of glioma patients to definitive chemoradiotherapy using chemical exchange saturation transfer imaging at 7 T. J Magn Reson Imaging 2019;50(4):1268-1277.

186. Yu H, Wen X, Wu P, et al. Can amide proton transfer-weighted imaging differentiate tumor grade and predict Ki-67 proliferation status of meningioma? Eur Radiol 2019;29(10):5298-5306.

187. Overhauser AW. Polarization of Nuclei in Metals. Physical Review 1953;92(2):411-415.

188. Yeung HN, Aisen AM. Magnetization transfer contrast with periodic pulsed saturation. Radiology 1992;183(1):209-214.

189. Kim M, Gillen J, Landman BA, Zhou J, van Zijl PC. Water saturation shift referencing (WASSR) for chemical exchange saturation transfer (CEST) experiments. Magn Reson Med 2009;61(6):1441-1450.

190. Lutkenhoff ES, Rosenberg M, Chiang J, et al. Optimized brain extraction for pathological brains (optiBET). PLoS One 2014;9(12):e115551.

191. Zhang S, Keupp J, Wang X, et al. Z-spectrum appearance and interpretation in the presence of fat: Influence of acquisition parameters. Magn Reson Med 2018;79(5):2731-2737.

192. Zaiss M, Xu J, Goerke S, et al. Inverse Z-spectrum analysis for spillover-, MT-, and T1 -corrected steady-state pulsed CEST-MRI--application to pH-weighted MRI of acute stroke. Nmr Biomed 2014;27(3):240-252.

193. Deshmane A, Zaiss M, Lindig T, et al. 3D gradient echo snapshot CEST MRI with low power saturation for human studies at 3T. Magn Reson Med 2019;81(4):2412-2423.

194. Desmond KL, Mehrabian H, Chavez S, et al. Chemical exchange saturation transfer for predicting response to stereotactic radiosurgery in human brain metastasis. Magn Reson Med 2017;78(3):1110-1120.

195. Dula AN, Asche EM, Landman BA, et al. Development of chemical exchange saturation transfer at 7T. Magnetic Resonance in Medicine 2011;66(3):831-838.

196. Khlebnikov V, Siero JCW, Wijnen J, et al. Is there any difference in Amide and NOE CEST effects between white and gray matter at 7T? J Magn Reson 2016;272:82-86.

197. Zu Z, Lin EC, Louie EA, et al. Relayed nuclear Overhauser enhancement sensitivity to membrane Cho phospholipids. Magn Reson Med 2020;84(4):1961-1976.

198. O'Brien JS, Sampson EL. Lipid composition of the normal human brain: gray matter, white matter, and myelin. J Lipid Res 1965;6(4):537-544.

199. O'Grady KP, Satish S, Owen QR, et al. Relaxation-Compensated Chemical Exchange Saturation Transfer MRI in the Brain at 7T: Application in Relapsing-Remitting Multiple Sclerosis. Front Neurol 2022;13:764690.

200. Wu Y, Wood TC, Arzanforoosh F, et al. 3D APT and NOE CEST-MRI of healthy volunteers and patients with non-enhancing glioma at 3 T. Magn Reson Mater Phys Biol Med 2022;35(1):63-73.

201. Zhang X-Y, Wang F, Li H, et al. Accuracy in the quantification of chemical exchange saturation transfer (CEST) and relayed nuclear Overhauser enhancement (rNOE) saturation transfer effects. Nmr Biomed 2017;30(7):e3716.

202. Paech D, Zaiss M, Meissner J-E, et al. Nuclear Overhauser Enhancement Mediated Chemical Exchange Saturation Transfer Imaging at 7 Tesla in Glioblastoma Patients. PLoS ONE 2014;9(8):e104181.

203. Jones CK, Schlosser MJ, van Zijl PC, Pomper MG, Golay X, Zhou J. Amide proton transfer imaging of human brain tumors at 3T. Magn Reson Med 2006;56(3):585-592.

204. Xu J, Zaiss M, Zu Z, et al. On the origins of chemical exchange saturation transfer (CEST) contrast in tumors at 9.4 T. Nmr Biomed 2014;27(4):406-416.

205. Ahuja CS, Martin AR, Fehlings M. Recent advances in managing a spinal cord injury secondary to trauma. F1000Research 2016;5:1-13.

206. Jellema K, Tijssen CC, van Gijn J. Spinal dural arteriovenous fistulas: a congestive myelopathy that initially mimics a peripheral nerve disorder. Brain 2006;129(Pt 12):3150-3164.

207. Martin R, McFarland HF, McFarlin DE. Immunological aspects of demyelinating diseases. Annu Rev Immunol 1992;10:153-187.

208. Haller S, Zaharchuk G, Thomas DL, Lovblad K-O, Barkhof F, Golay X. Arterial spin labeling Perfusion of the brain: Emerging clinical applications. Radiology 2016;281(2):337-356.

209. Graham GD, Blamire AM, Howseman AM, et al. Proton magnetic resonance spectroscopy of cerebral lactate and other metabolites in stroke patients. Stroke 1992;23(3):333-340.

210. Wang M, Hong X, Chang C-F, et al. Simultaneous detection and separation of hyperacute intracerebral hemorrhage and cerebral ischemia using amide proton transfer MRI. Magn Reson Med 2015;74(1):42-50.

211. Sun PZ, Benner T, Copen WA, Sorensen AG. Early experience of translating pH-weighted MRI to image human subjects at 3 Tesla. Stroke 2010;41(10 Suppl):S147-151.

212. Bakker J, Nijsten MW, Jansen TC. Clinical use of lactate monitoring in critically ill patients. Ann Intensive Care 2013;3(1):12.

213. Zha X-M, Xiong Z-G, Simon RP. pH and proton-sensitive receptors in brain ischemia. J Cereb Blood Flow Metab 2022;42(8):1349-1363.

214. Barry RL, Vannesjo SJ, By S, Gore JC, Smith SA. Spinal cord MRI at 7T. Neuroimage 2018;168:437-451.

215. Zaiss M, Bachert P. Exchange-dependent relaxation in the rotating frame for slow and intermediate exchange - modeling off-resonant spin-lock and chemical exchange saturation transfer. Nmr Biomed 2013;26(5):507-518.

216. Windschuh J, Zaiss M, Meissner JE, et al. Correction of B1-inhomogeneities for relaxation-compensated CEST imaging at 7T. Nmr Biomed 2015;28(5):529-537.

217. Zaiss M, Windschuh J, Goerke S, et al. Downfield-NOE-suppressed amide-CEST-MRI at 7 Tesla provides a unique contrast in human glioblastoma. Magn Reson Med 2017;77(1):196-208.

218. Paech D, Dreher C, Regnery S, et al. Relaxation-compensated amide proton transfer (APT) MRI signal intensity is associated with survival and progression in high-grade glioma patients. Eur Radiol 2019;29(9):4957-4967.

219. Mueller S, Stirnberg R, Akbey S, et al. Whole brain snapshot CEST at 3T using 3D-EPI: Aiming for speed, volume, and homogeneity. Magn Reson Med 2020;84(5):2469-2483.

220. Cai J, Sheng K, Sheehan JP, Benedict SH, Larner JM, Read PW. Evaluation of thoracic spinal cord motion using dynamic MRI. Radiother Oncol 2007;84(3):279-282.

221. Goto N, Otsuka N. Development and anatomy of the spinal cord. Neuropathology 1997;17(1):25-31.

222. Cohen-Adad J, Alonso-Ortiz E, Abramovic M, et al. Generic acquisition protocol for quantitative MRI of the spinal cord. Nature Protocols 2021;16(10):4611-4632.

223. van Belle G. Statistical rules of thumb. Hoboken, NJ: John Wiley and Sons; 2018. p. 27-51.

224. Matz PG, Anderson PA, Holly LT, et al. The natural history of cervical spondylotic myelopathy. J Neurosurg Spine 2009;11(2):104-111.

225. Cronin AE, Liebig, P., Detombe, S.A., Duggal, N., Bartha, R. . Reproducibility of pH-Weighted Chemical Exchange Saturation Transfer (CEST) Contrast in the Healthy Cervical Spinal Cord. ISMRM. Toronto, ON, Canada; 2023.

226. Cronin AE, Liebig, P., Detombe, S.A., Duggal, N., Bartha, R. . Reproducibility of Chemical Exchange Saturation Transfer (CEST) Contrasts in the Healthy Brain. WHATEVER ISMRM. Nashville; 2023.

227. Cronin AE, Detombe SA, Duggal CA, Duggal N, Bartha R. Spinal cord compression is associated with brain plasticity in degenerative cervical myelopathy. Brain Commun 2021;3(3):fcab131.

228. Holly LT, Freitas B, McArthur DDL, Salamon N. Proton magnetic resonance spectroscopy to evaluate spinal cord axonal injury in cervical spondylotic myelopathy: Laboratory investigation. Journal of Neurosurgery: Spine 2009;10(3):194-200.

229. Henderson FC, Geddes JF, Vaccaro AR, Woodard E, Berry KJ, Benzel EC. Stretch-associated injury in cervical spondylotic myelopathy: New concept and review. Neurosurgery 2005;56(5):1101-1112.

230. Agosta F, Laganà M, Valsasina P, et al. Evidence for cervical cord tissue disorganisation with aging by diffusion tensor MRI. Neuroimage 2007;36(3):728-735.

231. Terao S, Sobue G, Hashizume Y, Li M, Inagaki T, Mitsuma T. Age-related changes in human spinal ventral horn cells with special reference to the loss of small neurons in the intermediate zone: a quantitative analysis. Acta Neuropathol 1996;92(2):109-114.

232. Romanes GJ. THE ARTERIAL BLOOD SUPPLY OF THE HUMAN SPINAL CORD. Paraplegia 1965;2:199-207.

233. Bolton B. THE BLOOD SUPPLY OF THE HUMAN SPINAL CORD. J Neurol Psychiatry 1939;2(2):137-148.

234. Jellinger K. [Circulatory disorders of the spinal cord]. Wien Klin Wochenschr 1967;79(3):41-51.

235. Martirosyan NL, Feuerstein JS, Theodore N, Cavalcanti DD, Spetzler RF, Preul MC. Blood supply and vascular reactivity of the spinal cord under normal and pathological conditions. J Neurosurg Spine 2011;15(3):238-251.

236. Ramsey R, Doppman JL. The effects of epidural masses on spinal cord blood flow. An experimental study in monkeys. Radiology 1973;107(1):99-103.

237. Kumral E, Polat F, Güllüoglu H, Uzunköprü C, Tuncel R, Alpaydın S. Spinal ischaemic stroke: clinical and radiological findings and short-term outcome. Eur J Neurol 2011;18(2):232-239.

238. Novy J, Carruzzo A, Maeder P, Bogousslavsky J. Spinal cord ischemia: clinical and imaging patterns, pathogenesis, and outcomes in 27 patients. Arch Neurol 2006;63(8):1113-1120.

239. Zhang Z-A, Nonaka H, Hatori T. The microvasculature of the spinal cord in the human adult. Neuropathology 1997;17(1):32-42.

Appendices

Appendix A – Ethics Approval

Western Research

Date: 26 October 2023

To: Dr. Neil Duggal

Project ID: 108706

Review Reference: 2023-108706-85479

Study Title: Enhancing Recovery in Non-Traumatic Spinal Cord Injury: Implementation of an Integrated Program for the Assessment of Rehabilitation Therapies

Application Type: Continuing Ethics Review (CER) Form

Review Type: Delegated

Date Approval Issued: 26/Oct/2023 16:22

REB Approval Expiry Date: 01/Nov/2024

Dear Dr. Neil Duggal,

The Western University Research Ethics Board has reviewed the application. This study, including all currently approved documents, has been re-approved until the expiry date noted above.

REB members involved in the research project do not participate in the review, discussion or decision.

Western University REB operates in compliance with, and is constituted in accordance with, the requirements of the Tri-Council Policy Statement: Ethical Conduct for Research Involving Humans (TCPS 2); the International Conference on Harmonisation Good Clinical Practice Consolidated Guideline (ICH GCP); Part C, Division 5 of the Food and Drug Regulations; Part 4 of the Natural Health Products Regulations; Part 3 of the Medical Devices Regulations and the provisions of the Ontario Personal Health Information Protection Act (PHIPA 2004) and its applicable regulations. The REB is registered with the U.S. Department of Health & Human Services under the IRB registration number IRB 00000940.

Please do not hesitate to contact us if you have any questions.

Electronically signed by:

Mr. Joshua Hatherley, Ethics Coordinator on behalf of Dr. N. Poonai, HSREB Chair 26/Oct/2023 16:22

Reason: I am approving this document

Note: This correspondence includes an electronic signature (validation and approval via an online system that is compliant with all regulations).

Page 1 of 1

Western Research

Date: 21 September 2023

To: Dr. Neil Duggal

Project ID: 107497

Review Reference: 2023-107497-84030

Study Title: Advanced diagnosis and treatment of spinal cord compression

Application Type: Continuing Ethics Review (CER) Form

Review Type: Delegated

Date Approval Issued: 21/Sep/2023 10:59

REB Approval Expiry Date: 26/Sep/2024

Dear Dr. Neil Duggal,

The Western University Research Ethics Board has reviewed the application. This study, including all currently approved documents, has been re-approved until the expiry date noted above.

REB members involved in the research project do not participate in the review, discussion or decision.

Western University REB operates in compliance with, and is constituted in accordance with, the requirements of the Tri-Council Policy Statement: Ethical Conduct for Research Involving Humans (TCPS 2); the International Conference on Harmonisation Good Clinical Practice Consolidated Guideline (ICH GCP); Part C, Division 5 of the Food and Drug Regulations; Part 4 of the Natural Health Products Regulations; Part 3 of the Medical Devices Regulations and the provisions of the Ontario Personal Health Information Protection Act (PHIPA 2004) and its applicable regulations. The REB is registered with the U.S. Department of Health & Human Services under the IRB registration number IRB 00000940.

Please do not hesitate to contact us if you have any questions.

Electronically signed by:

Mr. Joshua Hatherley, Ethics Coordinator on behalf of Dr. N. Poonai, HSREB Chair 21/Sep/2023 10:59

Reason: I am approving this document

Note: This correspondence includes an electronic signature (validation and approval via an online system that is compliant with all regulations).

Appendix B - Copyright Permissions

CCC RightsLink

Spinal cord compression is associated with brain plasticity in degenerative cervical myelopathy

Author: Cronin, Alicia E; Detombe, Sarah A

Publication: Brain Communications

Publisher: Oxford University Press

Date: 2021-06-22

Copyright © 2021, © The Author(s) (2021). Published by Oxford University Press on behalf of the Guarantors of Brain.

Creative Commons

This is an open access article distributed under the terms of the Creative Commons CC BY license, which permits unrestricted use, distribution, and reproduction in any medium, provided the original work is properly cited.

You are not required to obtain permission to reuse this article.

JOHN WILEY AND SONS LICENSE
TERMS AND CONDITIONS

Feb 01, 2024

This Agreement between Alicia Cronin ("You") and John Wiley and Sons ("John Wiley and Sons") consists of your license details and the terms and conditions provided by John Wiley and Sons and Copyright Clearance Center.

License Number	5720511126279
License date	Feb 01, 2024
Licensed Content Publisher	John Wiley and Sons
Licensed Content Publication	NMR in Biomedicine
Licensed Content Title	Reproducibility of 3D pH-weighted chemical exchange saturation transfer contrast in the healthy cervical spinal cord
Licensed Content Author	Robert Bartha, Neil Duggal, Sarah A. Detombe, et al

WOLTERS KLUWER HEALTH, INC. LICENSE
TERMS AND CONDITIONS

Nov 03, 2023

This Agreement between Alicia Cronin ("You") and Wolters Kluwer Health, Inc. ("Wolters Kluwer Health, Inc.") consists of your license details and the terms and conditions provided by Wolters Kluwer Health, Inc. and Copyright Clearance Center.

License Number	5661490955179
License date	Nov 03, 2023
Licensed Content Publisher	Wolters Kluwer Health, Inc.
Licensed Content Publication	Clinical Spine Surgery
Licensed Content Title	Cervical Laminectomy and Dentate Ligament Section for Cervical Spondylotic Myelopathy
Licensed Content Author	Edward Benzel, John Lancon, Lee Kesterson, et al
Licensed Content Date	Sep 1, 1991
Licensed Content Volume	4
Licensed Content Issue	3

SPRINGER NATURE LICENSE
TERMS AND CONDITIONS

Nov 03, 2023

This Agreement between Alicia Cronin ("You") and Springer Nature ("Springer Nature") consists of your license details and the terms and conditions provided by Springer Nature and Copyright Clearance Center.

License Number	5661480056980
License date	Nov 03, 2023
Licensed Content Publisher	Springer Nature
Licensed Content Publication	Nature Reviews Neurology
Licensed Content Title	Degenerative cervical myelopathy — update and future directions
Licensed Content Author	Jetan H. Badhiwala et al
Licensed Content Date	Jan 23, 2020
Type of Use	Thesis/Dissertation
Requestor type	academic/university or research institute
Format	print and electronic

SPRINGER NATURE LICENSE
TERMS AND CONDITIONS

Nov 05, 2023

This Agreement between Alicia Cronin ("You") and Springer Nature ("Springer Nature") consists of your license details and the terms and conditions provided by Springer Nature and Copyright Clearance Center.

License Number	5662690203042
License date	Nov 05, 2023
Licensed Content Publisher	Springer Nature
Licensed Content Publication	Nature Reviews Disease Primers
Licensed Content Title	Traumatic spinal cord injury
Licensed Content Author	Christopher S. Ahuja et al
Licensed Content Date	Apr 27, 2017
Type of Use	Thesis/Dissertation
Requestor type	academic/university or research institute
Format	print and electronic

JOHN WILEY AND SONS LICENSE
TERMS AND CONDITIONS

Nov 03, 2023

This Agreement between Alicia Cronin ("You") and John Wiley and Sons ("John Wiley and Sons") consists of your license details and the terms and conditions provided by John Wiley and Sons and Copyright Clearance Center.

License Number	5661480551430
License date	Nov 03, 2023
Licensed Content Publisher	John Wiley and Sons
Licensed Content Publication	Clinical Anatomy
Licensed Content Title	Blood supply to the human spinal cord: Part I. Anatomy and hemodynamics
Licensed Content Author	Aaron A. Cohen-Gadol, R. Shane Tubbs, Marios Loukas, et al
Licensed Content Date	Jun 27, 2013
Licensed Content Volume	28

JOHN WILEY AND SONS LICENSE
TERMS AND CONDITIONS

Nov 03, 2023

This Agreement between Alicia Cronin ("You") and John Wiley and Sons ("John Wiley and Sons") consists of your license details and the terms and conditions provided by John Wiley and Sons and Copyright Clearance Center.

License Number	5661481030061
License date	Nov 03, 2023
Licensed Content Publisher	John Wiley and Sons
Licensed Content Publication	Wiley Books
Licensed Content Title	Basic Principles
Licensed Content Date	Dec 21, 2018
Licensed Content Pages	42
Type of use	Dissertation/Thesis
Requestor type	University/Academic

RightsLink

Quantitative Tissue Ph Measurement during Cerebral Ischemia Using Amine and Amide Concentration-Independent Detection (AACID) with MRI

Author: Nevin McVicar, Alex X Li, Daniela F Gonçalves, Miranda Bellyou, et al.
Publication: Journal of Cerebral Blood Flow & Metabolism
Publisher: SAGE Publications
Date: 2014-04-01

Copyright © 2014, © SAGE Publications

Gratis Reuse

Permission is granted at no cost for use of content in a Master's Thesis and/or Doctoral Dissertation, subject to the following limitations. You may use a single excerpt or up to 3 figures tables. If you use more than those limits, or intend to distribute or sell your Master's Thesis/Doctoral Dissertation to the general public through print or website publication, please return to the previous page and select 'Republish in a Book/Journal' or 'Post on intranet/password-protected website' to complete your request.

BACK CLOSE WINDOW

© 2023 Copyright - All Rights Reserved | Copyright Clearance Center, Inc. | Privacy statement | Data Security and Privacy | For California Residents | Terms and ConditionsComments? We would like to hear from you. E-mail us at customercare@copyright.com

JOHN WILEY AND SONS LICENSE
TERMS AND CONDITIONS

Nov 03, 2023

This Agreement between Alicia Cronin ("You") and John Wiley and Sons ("John Wiley and Sons") consists of your license details and the terms and conditions provided by John Wiley and Sons and Copyright Clearance Center.

License Number	5661490576365
License date	Nov 03, 2023
Licensed Content Publisher	John Wiley and Sons
Licensed Content Publication	NMR in Biomedicine
Licensed Content Title	The relayed nuclear Overhauser effect in magnetization transfer and chemical exchange saturation transfer MRI
Licensed Content Author	Nirbhay N. Yadav, Peter C. M. Zijl, Chongxue Bie, et al
Licensed Content Date	Jun 20, 2022
Licensed Content Volume	36

Curriculum Vitae

Alicia Cronin

Education

Ph.D. Candidate in Medical Biophysics
The University of Western Ontario
2018 - 2024

Bachelor of Science: Medical Physics, Minor in Mathematics
University of Guelph
2014-2018

Honours and Awards

NSERC Canada Graduate Scholarship - $105,000
May 2022 – April 2025

Ontario Graduate Scholarship – $15,000 (Declined)
May 2022 – Aug 2023

Deans Research Scholarship - $14,000 (Declined)
Sept 2022 – Aug 2023

Deans Research Scholarship - $14,000
Jan 2022 – Aug 2022

WHATEVER ISMRM Workshop Travel Award - $800 USD
Sept 18, 2023

Best Oral Presentation Award - $100
Imaging Network of Ontario (ImNO) 2023 Conference
Mar 24, 2023

CEST Workshop Travel Award - $500 USD
Aug 10, 2022

Best Oral Presentation Award - $250
Imaging Network of Ontario (ImNO) 2021 Conference
Mar 24, 2021

Top Oral Presentation Award - $100
Robarts Research Retreat 2020
June 19, 2020

Oral Presentation Honourable Mention - $100
Imaging Network of Ontario (ImNO) 2020 Conference
Mar 27, 2020

Western Graduate Research Scholarship
2018 - 2023

Harold E. Johns Medical Physics Award
Ontario Health (Cancer Care Ontario)
May 2017 – Aug 2017

Related Work Experience

Graduate T.A. – Radiation Physics
The University of Western Ontario – BIOPHYS 9712B
Jan 2023 – April 2023

Graduate T.A. – Medical Biophysics Float TA
The University of Western Ontario
Sept 2022 – Dec 2022

Graduate T.A. – Integrated Science 1001X Physics
The University of Western Ontario – INTEGSCI 1001X
Jan 2022 – April 2022

Graduate T.A. – Introduction to Biophysics for Advancing Medicine
The University of Western Ontario - MEDBIO 2500
Sept 2021 – Dec 2021

Graduate T.A. – First Year Biology
The University of Western Ontario
Jan 2021 – April 2021

Graduate Laboratory T.A. – First Year Physics Labs
The University of Western Ontario
Jan 2019 – April 2019, Jan 2020 – April 2020

Undergraduate T.A. – Math Learning Centre
University of Guelph
Fall 2017 – Spring 2018

Publications

1. **Cronin AE**, Liebig P, Detombe SA, Duggal N, Bartha R. Reproducibility of 3D pH-Weighted Chemical Exchange Saturation Transfer Contrast in the Healthy Cervical Spinal Cord. *NMR Biomed*. 2024; 1-13. https://doi.org/10.1002/nbm.5103.
2. Hunter SW, Motala A, **Cronin AE**, Bartha R, Viana R, Payne M. Cortical activation during imagined walking for people with lower limb loss: a pilot study. *Front Hum Neurosci.* 2023; 5(17). doi: 10.3389/fnhum.2023.1163526.
3. Mortuza R, Ching-Jonhson J, Yin H, O'Neil C, **Cronin AE**, Randhawa V, Nong Z, Hashi AA, Li AX, Bartha R, Chu MWA, Pickering G. Imaging of Glycosaminoglycans in Ascending Aortic Aneurysms with Chemical Exchange

Saturation Transfer MRI. *J Am Coll Cardiol Img.* 2022, 15(9), 1670-1672. https://doi.org/10.1016/j.jcmg.2022.04.009.

4. **Cronin AE**, Detombe SA, Duggal C, Duggal N, Bartha R. Spinal Cord Compression is Associated with Brain Plasticity in Degenerative Cervical Myelopathy. *Brain Commun*. 2021; 3(3): 1-12. https://doi.org/*10.1093*/*braincomms*/*fcab131*.

Conference Proceedings

1. **Cronin A**., Liebig P., Detombe S., Duggal N., & Bartha R. Reproducibility of Chemical Exchange Saturation Transfer (CEST) Contrasts in the Healthy Brain. Poster and power pitch presented at: ISMRM Workshop on WHATEVER 2023; September 18 – 20; Nashville, USA.
2. **Cronin A**., Liebig P., Detombe S., Duggal N., & Bartha R. Reproducibility of pH-Weighted Chemical Exchange Saturation Transfer (CEST) Contrast in the Healthy Cervical Spinal Cord. Digital poster presented at: 2023 ISMRM & SMRT Annual Meeting & Exhibition; June 3-8, 2023; Toronto, CA.
3. **Cronin A**., Liebig P., Detombe S., Duggal N., & Bartha R. Reproducibility of 3D pH-Weighted Chemical Exchange Saturation Transfer (CEST) MRI in the Spine. Oral presentation presented at: London Imaging Discovery Day 2023; June 1, 2023; London, CA.
4. **Cronin A**., Liebig P., Detombe S., Duggal N., & Bartha R. pH-Weighted Chemical Exchange Saturation Transfer (CEST) MRI Reproducibility in the Spinal Cord. Oral presentation presented at: 21st Annual Imaging Network Symposium (ImNO 2023); March 23-24, 2023; London, CA.
5. **Cronin A**., Liebig P., Detombe S., Duggal N., & Bartha R. Optimization of pH-Weighted CEST Contrast in the Spinal Cord. Oral presentation presented at: CEST 2022 Workshop; August 7-10, 2022; Atlanta, Georgia, USA.
6. Ibrahim P., **Cronin A**., Heidari H., Handsor S., Silverman M., Spicer E., Pasternak S., Sposato L., Fraser D., Tang A., Menon R., Baron C., Jurkiewicz M., Finger E., Mrkobrado M., Devlin M., Bartha R. Grey and White Matter

Differences in Tissue pH Measured by 7T Chemical Exchange Saturation Transfer MRI. Poster presentation presented at: London Health Research Day 2022; May 31, 2022; Virtual.

7. **Cronin A**., Liebig P., Detombe S., Duggal N., & Bartha R. Optimization of pH-Weighted Contrasts in the Spinal Cord using Chemical Exchange Saturation Transfer (CEST) MRI. Digital poster presented at: 2022 ISMRM & SMRT Annual Meeting & Exhibition; May 7-12, 2022; London, UK.
8. **Cronin A**., Liebig P., Detombe S., Duggal N., & Bartha R. Optimization of pH-Weighted Contrasts in the Spinal Cord using Chemical Exchange Saturation Transfer (CEST) MRI pH-Weighted MRI Optimization in the Spinal Cord. Power pitch & poster presented at: 20th Annual Imaging Network Symposium (ImNO 2022); March 22-24, 2022; Virtual.
9. **Cronin A**., Detombe S., Duggal C., Duggal N., and Bartha R. The Severity of Spinal Cord Compression is Associated with Functional Plasticity in Degenerative Cervical Myelopathy. Poster session presented at: Robarts Research Retreat; June 17, 2021; Virtual.
10. **Cronin A**., Detombe S., Duggal C., Duggal N., and Bartha R. Spinal Cord Compression is Associated with Brain Plasticity in Degenerative Cervical Myelopathy. Poster session presented at: 2021 ISMRM & SMRT Annual Meeting & Exhibition; May 15 - 20, 2021; Virtual.
11. **Cronin A**., Liebig P., Detombe S., Duggal N., and Bartha R. Determine Spinal Cord pH using Chemical Exchange Saturation Transfer (CEST) MRI. Poster session presented at: 2021 ISMRM & SMRT Annual Meeting & Exhibition; May 15 - 20, 2021; Virtual.
12. **Cronin A**., Detombe S., Duggal C., Duggal N., and Bartha R. Spinal Cord Compression Severity is Associated with Functional Plasticity in Degenerative Cervical Myelopathy. Poster session presented at: London Health Research Day 2021; May 11, 2021; Virtual.
13. **Cronin A**., Detombe S., Duggal C., Duggal N., and Bartha R. The Severity of Spinal Cord Compression is Associated with Functional Plasticity in

Degenerative Cervical Myelopathy. Oral presentation presented at: 19th Annual Imaging Network Symposium (ImNO 2021); March 24, 2021; Virtual.

14. **Cronin A**., Liebig P., Detombe S., Duggal N., and Bartha R. pH-Weighted Chemical Exchange Saturation Transfer (CEST) MRI in the Spine. Power Pitch presentation presented at: 19th Annual Imaging Network Symposium (ImNO 2021); March 24, 2021; Virtual.
15. **Cronin A**., Detombe S., Doyle-Pettypiece P., Kalsi-Ryan S., Speechley M., Duggal N., and Bartha R. Can Brain Activity Predict Manual Dexterity Improvement After Surgery in Cervical Myelopathy? Poster session presented at: The Organization of Human Brain Mapping 2020 (OHBM 2020); June 22 – July 3, 2020; Virtual.
16. **Cronin A**., Detombe S., Duggal N., and Bartha R. Spinal Cord Compression Leads to Cortical Reorganization in Patients with Cervical Spondylotic Myelopathy. Oral presentation presented at: Robarts Research Retreat; June 19, 2020; Virtual.
17. **Cronin A**., Detombe S., Doyle-Pettypiece P., Kalsi-Ryan S., Speechley M., Duggal N., and Bartha R. Can Brain Activity Predict Manual Dexterity Improvement After Surgery in Cervical Myelopathy? Oral presentation presented at: 18th Annual Imaging Network Symposium (ImNO 2020); March 27, 2020; Virtual.
18. **Cronin A**., Duggal N., and Bartha R. Correction of Respiration-Induced Magnetic Field (B_0) Fluctuations in the Spinal Cord. Oral presentation presented at: London Imaging Discovery Day 2019; June 12, 2019; London, ON.
19. **Cronin A**., Duggal N., and Bartha R. Correction of Respiration-Induced Magnetic Field (B_0) Fluctuations in the Spinal Cord. Poster session presented at: London Health Research Day 2019; April 30, 2019; London, ON.
20. **Cronin A**., Duggal N., and Bartha R. Correction of Respiration-Induced Magnetic Field (B_0) Fluctuations in the Spinal Cord. Poster session presented at: 17th Annual Imaging Network Ontario Symposium (ImNO 2019); March 28-29, 2019; London, ON.

21. Vandermeer, A., Mason, D. and **Cronin, A**. Improved Delivery Accuracy and Reduced Treatment Time Using DCAT with FFF Compared to VMAT for Lung SBRT Patients. Poster session presented at: Annual Meeting of The Canadian Organization of Medical Physicists; September 12-15, 2018; Montreal, QC.

Invited Talks

1. Cronin A.E. Can Biomarkers of Recovery be Determined Non-Invasively Using MRI in Degenerative Cervical Myelopathy Patients? Seminar presented at: Vanderbilt University Institute of Imaging Science Seminar Series; September 23, 2023; Nashville, USA.
2. Cronin A.E.. pH Imaging (Exogenous vs. Endogenous pH, limitations, and future developments). Group panel with presentation presented at: CEST 2022 Workshop; August 7-10, 2022; Atlanta, Georgia, USA.

Conference Session Moderators

1. ISMRM WHATEVER Workshop – CEST Discussion Leader and Moderator
   Sept 20, 2023
2. Imaging Network Ontario Symposium (ImNO) – Oral Session Moderator
   Mar 24, 2023
3. CEST Conference – Oral Session Moderator
   Aug 9, 2022
4. Imaging Network Ontario Symposium (ImNO) – Power Pitch Session Moderator
   Mar 24, 2022
5. Robarts Research Retreat – Oral Session Moderator
   June 17, 2021